Synthesis of Carbon Dots and Their Applications in Sensing, Optoelectronics, and Energy Storage Systems

A thesis submitted
in partial fulfilment of the requirements
for the degree of

Doctor of Philosophy

by

Rupam Sinha
(Roll No. 156107024)

Department of Chemical Engineering
Indian Institute of Technology Guwahati, Assam, 781039
May 2022

Dedicated

to

my Parents & my Sisters

Department of Chemical Engineering
Indian Institute of Technology Guwahati
Assam, 781039

Statement

I hereby declare that the thesis, entitled “**Synthesis of Carbon Dots and Their Applications in Sensing, Optoelectronics, and Energy Storage Systems**” contains original research work. Any content of this thesis has not been taken from anywhere else. This thesis has not been submitted elsewhere for obtaining the degree of Doctor of Philosophy.

May 2022

Rupam Sinha

Department of Chemical Engineering
Indian Institute of Technology Guwahati
Assam, 781039

Certificate

It is certified that the works described in this thesis, entitled "**Synthesis of Carbon Dots and Their Applications in Sensing, Optoelectronics, and Energy Storage Systems**" by **Mr. Rupam Sinha** (Roll No. 156107024) for the award of the degree of Doctor of Philosophy is an authentic record of the results obtained from the research work carried out under my supervision in the Department of Chemical Engineering, IIT Guwahati, India.

This thesis, in my opinion, has reached the standard fulfilling the requirements for the award of the degree of the Doctor of Philosophy in accordance with the regulations of the institute.

May 2022

Prof. Tapas K. Mandal
Professor
Department of Chemical Engineering
Indian Institute of Technology Guwahati
Guwahati, 781039

Acknowledgements

It has been an incredible journey from the moment I joined for my Ph.D. till the day I finally finished my thesis work. The completion of this thesis would never be possible without the help and support from many wonderful people. It is my genuine pleasure to express my deep sense of thanks and gratitude to every individual who has been a part of the journey towards the completion of this thesis.

First and foremost, I would like to thank my thesis supervisor ***Prof. Tapas Kumar Mandal*** *for allowing me to work in such an exciting area of research. I am very much grateful to him for his continuous guidance, valuable suggestions, and motivating discussion. Despite his busy schedule, he never hesitated to take out some extra time to discuss and analyze the problems and gave directions for the betterment of the works. His continuous faith and subtle push have helped me a lot to improve my presentation skills also. His "never say no" attitude will always inspire me. I consider myself fortunate enough to have a chance to work under his supervision. I whole-heartedly thank him for extending moral support as and when needed.*

I would like to thank my doctoral committee members, ***Prof. Raghavendra Gupta*** *and* ***Prof. Partho Sarathi Gooh Pattader****, Department of Chemical Engineering,* ***Prof. Dipankar Narayan Basu****, Department of Mechanical Engineering, for their valuable suggestions, time, and efforts during my thesis work.*

My sincere acknowledgement goes to the instrument facilities of IIT Guwahati, specifically, Analytical lab facility (Department of Chemical Engineering), Central Instrument Facility (CIF), Centre for Nanotechnology, Centre for the Environment, School of Energy Science and Engineering and Department of Biosciences and Bioengineering.

Further, I would like to acknowledge North East Institute of Science and Technology Jorhat, Indian Institute of Technology Kanpur, for helping me with the XPS facility required for the thesis.

My humble acknowledgement also goes to the ***faculty members and staff*** *of the Department of Chemical Engineering for providing the necessary facilities.*

A hearty thanks to all my friends for being there with me in my ups and downs. The constant emotional supports of them helped me to put myself up throughout this journey. I would also like to thank my colleagues, labmates for creating a pleasant and friendly working environment, which was very helpful for me to conduct myself properly in the lab and department.

Last but not least, I would certainly like to thank my parents, my sisters, and my brothers-in-law for being so patient with me. Their unconditional love and constant emotional support have been the key that helped to keep going throughout my Ph.D. journey.

Rupam Sinha

Abstract

Carbonaceous nanomaterials are one of the finest nanomaterials discovered to date. The most recent inclusion to the family of carbonaceous materials is carbon dots (CDs). CDs are the quantum dots that are derived from carbon-based precursor materials. They are identified as quasi 0D carbon materials with a size ranging from 1-10 nm. Their unique optical properties make the CDs one of the most desirable nanomaterials in the current scientific world. Apart from the unique optical properties, some other essential characteristics of CDs are their non-toxicity and high water solubility due to the presence of the functional groups such as –OH and –COOH. All these properties of CDs have made them desirable in different areas of applications such as sensing, optoelectronics, catalysis, energy storage systems, bioimaging, biomedicines, etc. In this context, the current thesis explores several natural resources employing different synthesis techniques to produce CDs. Thereafter, these CDs have been used in the applications of photoluminescence-based (PL-based) sensing, bioimaging, UV-photodetection, and energy storage systems. We targeted heavy metals (Cr^{6+} and Fe^{3+}) and explosive materials (picric acid; PA) to test the sensing abilities of the CDs, where potato and cigarette-tobacco have been used as the precursor materials, respectively. Both the synthesized CDs showed quite a good limit of detection (LOD) towards the sensing of heavy metals and explosive materials. These LOD values for the sensing of Cr^{6+} and Fe^{3+} are 0.012 μM and 0.000549 μM, respectively, whereas the LOD for the sensing of PA is 140 nM. Simple heating reaction and microwave assisted heating techniques were used to synthesize the CDs from potato and cigarette-tobacco, respectively. The synthesis techniques and the precursor material played an important role in the PL properties of the CDs as the quantum yield (QY) values of the CDs synthesized from potato (6.08%), and cigarette-tobacco (9.98%) were different. The CDs synthesized from potato were used for the bioimaging application also due to their non-toxic nature. This non-toxic nature of the CDs was confirmed via the cytotoxicity test. We have used the CDs (from cigarette-tobacco) in UV-photodetection applications (optoelectronics) as well. We have fabricated two devices for this application. One is a photoconductor, and the other is a Schottky diode. In the photoconductor, we attached the CDs with multi-walled carbon nanotube (MWCNT) and deposited the material in between two aluminium electrodes. In contrast, we attached the CDs on ZnO nanorods grown on a graphite-coated paper substrate for fabricating the Schottky diode. The photoconductor showed a rise and decay time of 0.38 and 0.42 s, respectively. In the case of the Schottky diode, the response and recovery times were ∼2 and ∼3.2 s, respectively. This device (Schottky diode) was able to be operated in self-powered condition as well. The responsivity and the specific detectivity of this fabricated UV detector were 9.57 mA/W and 4.27×10^8 Jones, respectively, at 330 nm wavelength, which is quite comparable with literature-reported values considering a self-powered photodetector. For the application in energy storage systems, we attached CDs with single-walled carbon nanotube (SWCNT)/ZnO composite to fabricate an optically responsive hybrid electrode material for a supercapacitor. It was observed that the areal capacitance of the supercapacitor got enhanced by ~41.38% at 50 mV/s scan rate. We also explored the working mechanism of the supercapacitor, and it was noted that the contribution towards the overall capacitance from pseudocapacitance and electric double layer capacitance (EDLC) were 30.65 and 69.35%, respectively. The occurrence of intercalation pseudocapacitance was also proven with justified shreds of evidence.

Graphical abstract

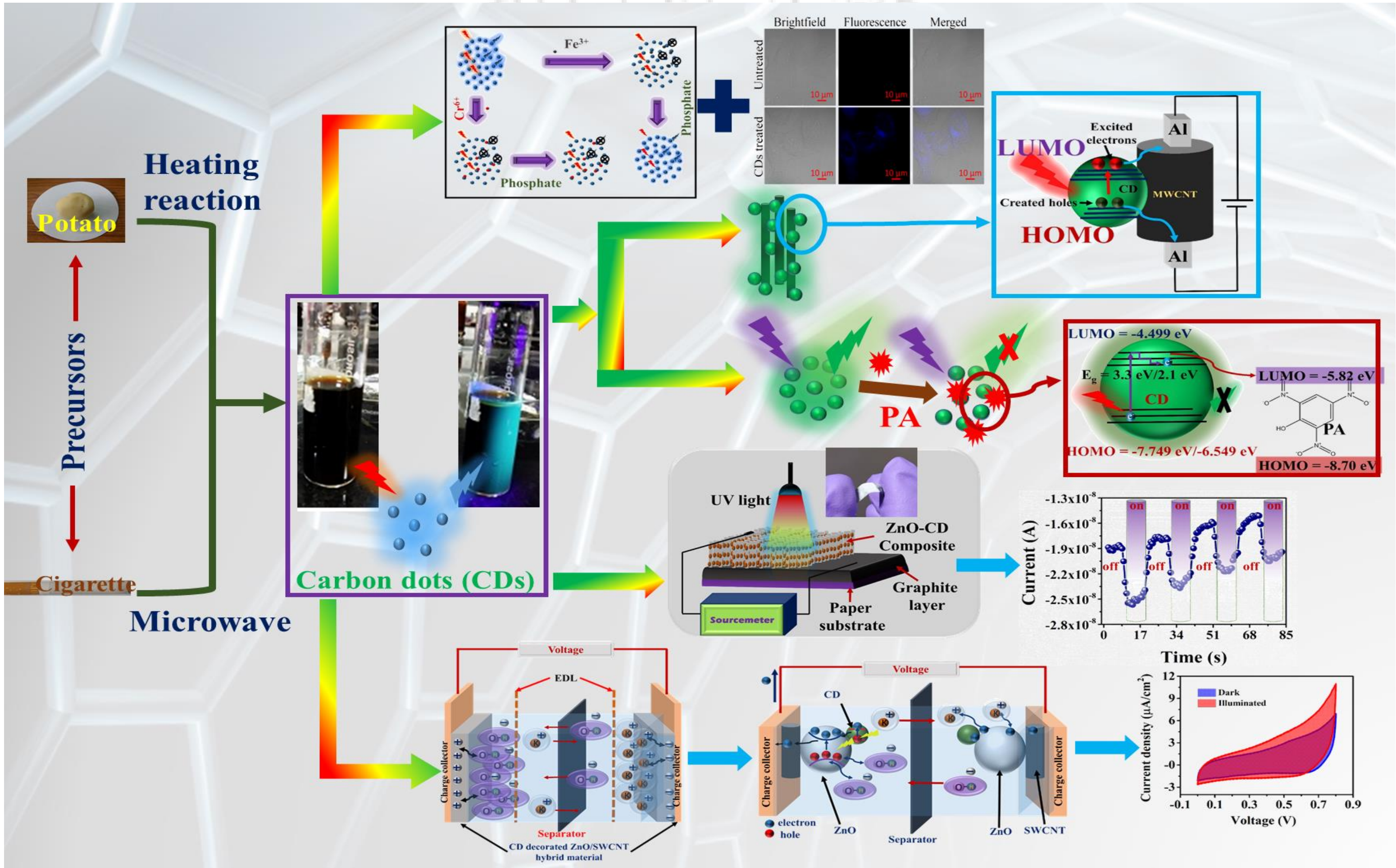

List of Figures

List of Schemes

List of Tables

Contents

Chapter 1: Introduction

Chapter 2: Synthesis of non-toxic Carbon dots from potato for the detection of Cr^{6+} and Fe^{3+} in water samples and bioimaging applications

Chapter 3: N-doped carbon dots from cigarette-tobacco: Picric acid sensing in real water sample and synthesis of CD-MWCNT nanocomposite for UV-photodetection

Chapter 4: Carbon dots and ZnO based flexible and self-powered Schottky diode for UV-photodetection

Chapter 5: Carbon dots decorated SWCNT/ZnO based hybrid electrode for optically responsive supercapacitor

Chapter 6: Summary and future scopes

Chapter 1

Introduction

Contents

Graphical abstract

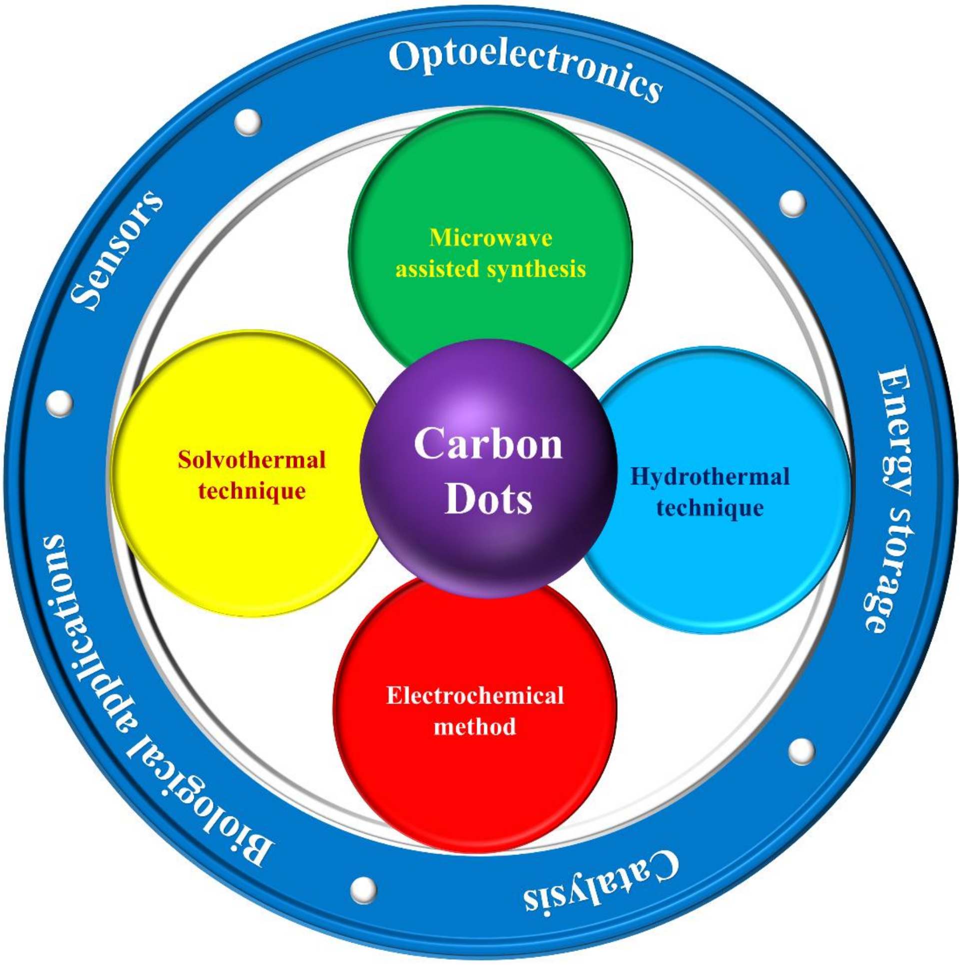

Abstract

Carbon dots (CDs) have gained a significant amount of attention over the past decade and a half. Optical characteristic such as the photoluminescence (PL) property of the CDs has made them unique from other carbonaceous nanomaterials. Different precursor materials and synthesis techniques help to tune the optical properties of the CDs. This chapter has focused on a detailed discussion of the different synthesis approaches and the precursor materials of CDs. A detailed discussion of the applications of CDs in the fields of sensing, optoelectronics, energy storage systems, catalysis, and bioscience has also been provided. In context with the extensive discussion, this chapter identifies the knowledge gaps and, based on the knowledge gaps, it finally introduces the problems and objectives of this thesis.

1.1. Overview

The smaller, the better. This has been the mantra for the researchers who are working on nanotechnology. The term nanotechnology is a combination of two words; the first one is the Greek word nano (means dwarf) which refers to a billionth, followed by the word technology [1]. Therefore, as the term suggests, nanotechnology deals with particles of a size below 100 nm. Nanotechnology does not limit itself to a particular discipline; instead, this is a field of science that combines several disciplines such as, Physics, Chemistry, Health care, and Engineering, etc. Owing to this, nanotechnology possesses a high potential that can lead to some of the most significant breakthroughs in real life. As this technology basically works on materials with dimensions in the range of nanometers, therefore these materials have been termed as nanomaterials by scientists. There have been numerous nanomaterials to date with which people have worked since the inception of nanotechnology. One such category of materials is carbonaceous nanomaterials. Some examples of these sorts of materials are single and multi-walled carbon nanotubes (SWCNT, MWCNT), graphene, and graphene oxides (GO), reduced graphene oxides (rGO), etc. [2, 3]. These nanomaterials are being used in almost every field of nanoscience and engineering. Some of their most practical applications can be cited in the areas of sensing, catalysis, capacitor, supercapacitor, field-effect transistors (FET), transparent conducting films (TCF), etc. [4-6] Because of the good electrical and mechanical properties, CNTs had an extraordinary demand amongst the scientists in the earlier days. Such characteristics of the CNTs influenced Xu *et al.* [7] to work with these nanomaterials. Hence this group started their experiments on the electrophoretic purification of SWCNTs. In doing so, they found out that the by-product in this process was showing fluorescence characteristics. The fluorescent band was then run electrophoretically into the anodic buffer followed by the dialysis (using a membrane of cut-off 12,500) method. N_2 was then blown to remove extra water from the fluorescent band before vacuum drying. This final fluorescent by-product was later termed as carbon dots (CDs) by the research fraternity.

CDs can be defined as the quantum dots which have the source of carbonaceous materials. They are quasi 0D carbon materials with a size ranging from 1-10 nm [8, 9]. They have an intrinsic property of PL, which is missing in the other carbonaceous nanomaterials. These nanoparticles show tunable PL emissions [9], i.e., they emit light in diverse colours, exactly like the other inorganic heavy-metal-based quantum dots. However, they completely outperform the inorganic quantum dots in terms of toxicity, as the inorganic quantum dots are highly toxic in nature. In contrast, CDs possess very low to no toxicity at all [10]. Apart from the PL property and the low toxicity, one more noteworthy characteristic of the CDs is high water solubility [9, 10]. The presence of functional groups on the surfaces, such as $-COOH$ and/or $-OH$ is responsible for the high water solubility of the CDs [10]. These properties of CDs make them attractive in several applications, where water solubility and toxicity act as challenges for other luminescent inorganic quantum dots.

1.2. Types of Carbon dots

CDs typically comprise of a core with mostly sp^2 hybridization, covered with several functional groups [11, 12]. CDs have been categorized into three different groups: carbon quantum dots (CQDs), graphene quantum dots (GQDs), and carbonized polymer dots (CPDs) (Figure 1). This classification is solely based on the formation mechanism, properties, and structure [8, 12]. At least one of the dimensions in all these three categories is < 10 nm in size. CQDs are characteristically spherical, with graphite-like structures being connected between multiple layers. The PL mechanism in CQDs is due to the quantum confinement and the intrinsic luminescence of the nanomaterials. The method of formation of CQDs follows the "bottom-up" technique. On the contrary, GQDs follow the "top-down" method for synthesizing. For example, GQDs are being synthesized by cutting the larger carbon materials like CNTs, carbon fibers, graphite, carbon rods, etc. [8, 13, 14] In GQDs, a few graphene structures are connected by the functional groups on the boundaries. A distinct characteristic of GQDs is that the horizontal dimension of the GQDs is larger than the longitudinal one. The observed average lattice gap is 0.24 nm. In the case of CPDs, there is a carbon core entangled with polymers (cross-linked)/ numerous functional groups [8, 12]. Owing to

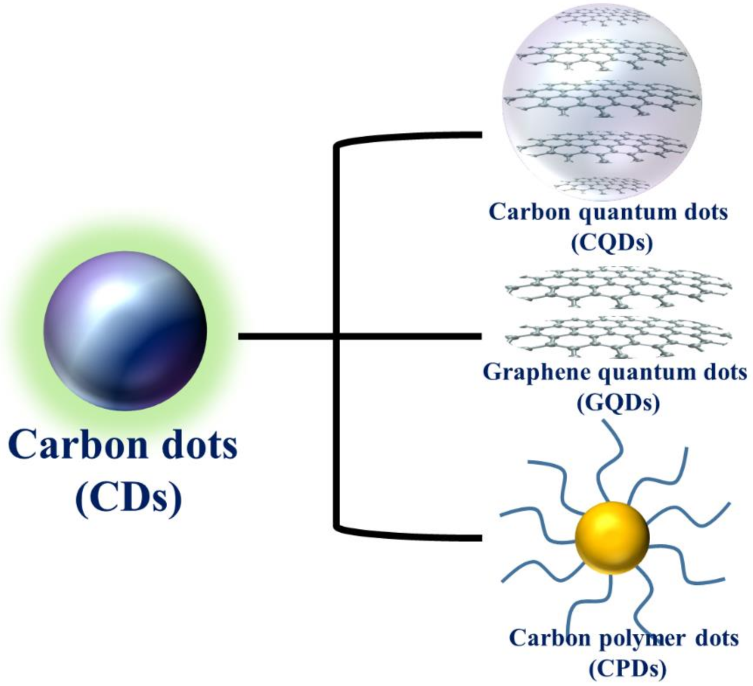

Figure 1.1. Types of CDs: CQDs, GQDs, and CPDs [12].

this, CPDs exhibit excellent water stability. Moreover, the presence of abundant functional groups on the surfaces provides a more extensive scope of doping with some heteroatoms like oxygen, nitrogen, etc. The external doping can help them to attain higher PL.

1.3. Synthesis techniques of Carbon dots

After the first discovery of the CDs in 2004, a great revolution in the research fraternity was witnessed as scientists from all around the globe were keen to identify and know more about this tiny nanomaterial. Therefore, rigorous research on CDs started afterward, which involved in synthesizing the same in many different ways. The synthesis techniques have been generalized into two categories; the “bottom-up” and “top-down” approaches.

1.3.1. “Bottom-up” approach

As the name suggests, the bottom-up approach involves synthesizing CDs from bottom to up, i.e., smaller groups of molecules get together to form a larger cluster. Some “bottom-up” approaches for CD synthesis are the hydrothermal treatment of citric acid or carbohydrates, pyrolysis, microwave, ultrasonic, solution chemistry, carbonization method, etc. [12, 15, 16] For instance, Zhu *et al*. [17] synthesized high QY CDs from citric acid and ethylenediamine (EDA) using the hydrothermal technique. Their highest reported QY of the synthesized product is 80%. They further used the CDs to detect Fe^{3+}. Wang *et al*. [18] also used the hydrothermal technique to synthesize high QY CDs (40%). They further used their synthesized CDs as fluorescence-based picric acid (PA) sensing probes. Their reported detection limit for PA is 0.041 µmol/L in a linear range of 0.5-30 µmol/L. Yuan *et al*. [19], on the other hand, used the solvothermal technique to synthesize

CDs from citric acid and diaminonaphthalene. They used EtOH/H_2SO_4 as the solvent, and the QY of their synthesized CDs was 75%. Zhuo *et al*. [20] used the pyrolysis method to synthesize extremely high QY CDs with excitation independent fluorescence. The use of glutathione with citric acid helped to obtain such a high QY. The lower toxicity of the synthesized CDs was then used for cell imaging purposes. Xu *et al*. [21] used microwave assisted synthesis technique to synthesize N, S-CDs using glycerol solvent and cysteine as the source of C, N, and S. They used the CDs as turn-on probes for fluorescence-based detection of Hg^{2+}. Li *et al*. [22], on the other hand, explored the ultrasonic technique using acid/alkali assisted glucose solution for the synthesis of fluorescent carbon nanoparticles. Their observation reports that the hydroxyl group-rich surface of the carbon nanoparticles helps to get higher hydrophilicity. However, there remains a difficulty in this technique, which is the aggregation during carbonization.

1.3.2. "Top-down" approach

The "top-down" approach involves the procedure of breaking larger particles into smaller ones. Several methods can be incorporated under this category, such as arc discharge, hydrothermal and solvothermal, laser ablation, acidic oxidation, stripping, electrochemical process, etc. [23]. Amongst these, the most popular ones are the hydrothermal method and the solvothermal method. The production of high QY CDs has been observed by the researchers using hydrothermal method [10]. However, to get better control on the size of the CDs, the electrochemical technique is preferred [23]. For example, Kalita *et al*. [24] explored the electrochemical method for the synthesis of GQDs. They used $LiClO_4$ in propylene carbonate as the electrolyte. The synthesized GQDs were used as sensing probes for the sensing of moisture in the soil. On the other hand, deYro *et al*. [25] synthesized CDs from biowaste with hydrothermal technique. The synthesized CDs were then used in bioimaging applications. However, the first evidence of CDs was obtained using a top-down approach, which was reported by Xu *et al*. [7] They used the arc discharge technique in their work.

The research regarding the synthesis techniques of CDs is currently not limited to the above-mentioned individual processes. There are examples where the combination of both methods has been used to obtain CDs. Calcination of organic molecules can result in producing fine carbon powder. This is a typical bottom-up technique. CDs are then formed by shearing the carbon powder, which is a typical top-down method [23].

1.4. Sources for precursor materials

One of the reasons that CDs have gained more advantages is the low price and easy availability of the raw materials/precursor materials. With the “top-down” technique, several carbonaceous raw materials have been used to synthesize CDs, and it has been reported that the raw materials used in this technique are less costly [23]. For example, GO [26], citric acid [17], pyrene [27], etc., are some of the reported materials which were used to synthesize CDs by the “top-down” technique. Having said so, the “bottom-up” approach has also been rigorously utilized to prepare CDs with more precision. Some raw materials used in this technique are salicylic acid [28], glucose [29], etc.

Moreover, there are several reports in which green materials or organic materials have also been used to synthesize CDs. For example, Picard *et al*. [30] synthesized fluorescent CDs from *Miscanthus* grass to detect Fe^{3+} ions. They used different dopants with the raw material to synthesize P-doped, N-doped, and dual-doped CDs. The detection limit of their synthesized CDs is 20 nM. Wang *et al*. [31] derived N, S, P-doped CDs from biomass waste. They also used the synthesized CDs to detect Fe^{3+} ions, and their reported limit of detection (LOD) value is 0.1 µM. In another report, Qiang *et al.* [32] showed the synthesis of CDs from potato-starch by acid-assisted ultrasonication method and used the CDs to detect Zn^{2+}. This synthesis probe showed an excellent detection limit of 1 nM. Not only this, there are numerous articles reporting the synthesis of CDs from many other precursor materials, such as eggshell, milk, banana peel, and banana stem, bamboo leaf, cow manure, paper [33-40] etc. Not only this, the researchers have not restricted themselves to the above-mentioned materials. They even used human hair to get CDs successfully and applied it for the detection of chloroform in water [41]. All these reported sources for CDs synthesis open a wide window for the researchers to explore further to obtain even higher QY CDs and use them in a wide range of applications.

1.5. Applications of Carbon dots

Since the discovery of CDs, there has been an enormous demand for CDs due to their distinct characteristics. Consequently, CDs have been used in a wide range of applications as well, from sensing to catalysis, from optoelectronics to biomedicines, etc. Therefore, for a robust understanding, the applications of CDs are categorized separately based on their applied areas. This classification is schematically shown in figure 1.2.

1.5.1. Sensors

The only property of CDs that differs from other carbon nanoparticles, i.e., the fluorescence property, makes CDs a potent candidate for fluorescence-based sensing applications. Based on the sensing mechanism, this section has also been divided into four subsections as photoluminescence-based (PL-based) sensors, chemiluminescence-based (CL-based) sensors, electrochemiluminescence-based (ECL-based) sensors, photoelectrochemiluminescence-based (PECL-based) sensors. This subdivision of the sensor is also presented in figure 1.2.

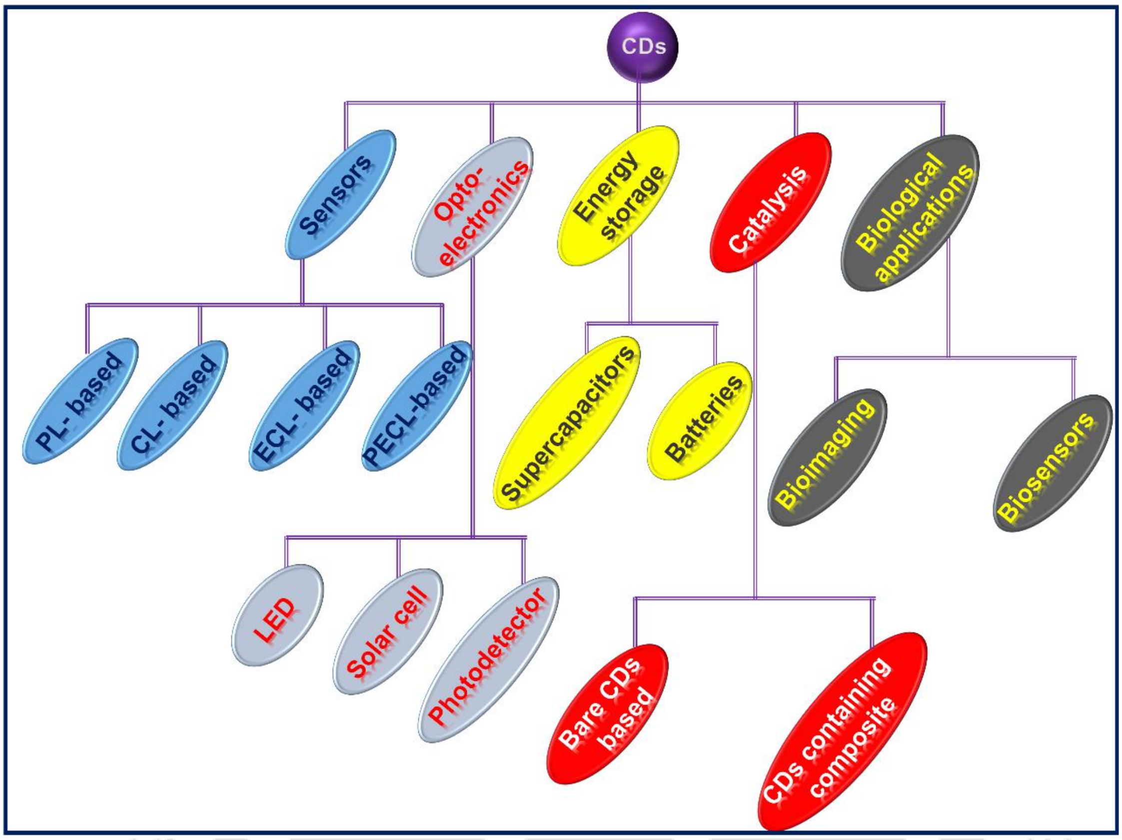

Figure 1.2. Different categories and sub-categories of the applications of CDs.

1.5.1.1. Photoluminescence-based (PL-based) Sensors

CDs have been used as a PL-based sensing probe for the detection of heavy metals, explosive nitro compounds, pesticides, and toxic compounds, etc. [42] To date; most research has been conducted on fluorescence-based heavy metal sensing applications. The metals reported in these works are Cr^{6+} [9, 43-45], Hg^{2+} [46-51], Fe^{3+} [9, 30, 31, 52-55], Pd^{2+} [56-58], Co^{2+} [59-62], Zn^{2+} [63-67], Cu^{2+} [68-74], Au^{3+} [75, 76], Cd^{2+} [77-79], Bi^{3+} [80-82], Al^{3+} [83-85], K^{+} [86], Sn^{2+} [87], Mn^{2+} [67, 88], Be^{2+} [85], Ag^{+} [89-94], Ni^{2+} [85], and Pd^{2+} [56, 58], etc. In the case of explosive materials also, CDs especially, the N or N/P doped CDs, have shown a potential side as sensors [42]. Some of the hazardous explosive materials are nitroethane (NE), nitrophenol (NP), nitromethane (NM), nitrotoluene (NT), nitroaniline (NA), 2,4,6-trinitrotoluene (TNT), picric acid (PA), etc.[10, 42, 95-99] Owing to the high solubility, these nitro group containing chemicals easily contaminate the groundwater and soil and thus create several health threats. Hence, detecting the presence of these materials in water and soil is also of great importance, which has been issued and resolved quite convincingly by the researchers using CDs. In most cases, the selectivity towards a particular metal ion/chemical relied on the precursor materials or the synthesis techniques. Having said so, it is worthwhile to mention some of the common sensing mechanisms such as d orbital transition of electrons, fluorescence resonance energy transfer (FRET), dual electron transfer (DET), electron interaction (EI), charge transfer complex (CTC), inner filter effect (IFE), photo-induced electron transfer (PET), etc. For example, Khan *et al*. [100] used N, S-CQDs for the detection of PA. The LOD of the sensor is 0.24 µM. It was observed in this report that the fluorescence of the CQDs got quenched when exposed to PA. The mechanism of this fluorescence quenching was reported to be FRET. Whereas, Li *et al*. [95] showed that the PA sensing mechanism was based on the charge transfer method and their reported LOD for PA sensing is 10 nM. Cheng *et al*.[101] also reported the sensing of PA by CDs; however, in their case, the sensing mechanism was based on IFE. Similarly, for metal detection, the quenching of fluorescence of the CDs due to the transfer of excited electrons to the vacant d orbitals of the metal ion is a popular concept. Zhang *et al*. [102] represented this concept in their work, in which they synthesized CDs to detect Fe^{3+} ions. Apart from heavy metals and explosive materials, CDs have been used as sensing probes to detect pesticides and other toxic materials as well. Several toxic chemicals such as carbamate pesticides, organophosphorus, etc. have been used rigorously as pesticides, which have an adverse impact on human health. Therefore, the identification of such chemicals in water and soil is also one of the important aspects. One such chemical that is used as a pesticide is methyl parathion (organophosphate). Lan *et al.* [103] detected this chemical by using N-CDs as sensing probe. They reported that the sensing mechanism for the same was based on IFE. Their reported LOD was as low as 1.87 ppb. Apart from pristine CDs, CD composites with metal nanoparticles also act as good sensing probes to detect pesticides. One such example is that, the composite made by attaching CDs with Au nanoparticles proved to be a colorimetric sensor for the identification of phoxim as reported by Zheng *et al.* [104] In another work, Yang *et al.* [105] targeted carbendazim as the analyte and they proposed the sensing mechanism to be based on FRET. Along with the pesticides, some chemical compounds detected with the help of CDs are acetic acid, acetone, NO, etc. [42] Overall, the PL property of the CDs has been widely utilized to use them as PL-based sensing probes.

1.5.1.2. Chemiluminescence-based (CL-based) Sensors

The fundamental mechanism for chemiluminescence involves the emission of light as a consequence of the reaction between two or more reactants. This particular mechanism has been adopted to prepare CL-based sensors using CDs. The advantages of CL-based sensors involve high precision, simple instrumentation, zero interference from the scattering light in the background [85]. Wang *et al.* [106] determined the presence of L-cysteine with the help of a CL-based sensor using CDs and lucigenin. They synthesized the CDs from starch hydrothermally. It was observed that there was no blue emission (CL) initially in the CDs and lucigenin mixture. However, upon the addition of L-cysteine in the system, it started showing a strong blue emission. They exploited this phenomenon to detect L-cysteine. The reported LOD is 8.8 µM. Hallaj *et al*. [107] demonstrated the CL property of a mixture, including $KMnO_4$ and S, N-doped CDs in the presence of indomethacin and thus used this as a CL-based sensor for indomethacin. The CDs were synthesized by hydrothermal treatment of a mixture of citric acid and L-cysteine. The reported LOD in their work is 65 µg/L. Glucose can also be detected using the CL property of the CDs as presented by Duan *et al*. [108] They synthesized CD from citric acid and doped it with Cu by using $Cu(NO_3)_2{\cdot}3H_2O$. The LOD of this sensor was as low as 0.32 µM. Apart from the above-mentioned chemicals, some other materials that were detected using a CL-based sensor are gallic acid [109], bromate [110], tannic acid and thiourea [111], adenosine [112], ranitidine [113], Mn(II) [114], metronidazole [115], etc.

1.5.1.3. Electrochemiluminescence-based (ECL-based) Sensors

The ECL process involves a chemical reaction of species in an electrolytic system (especially on the electrodes) that gets high energy during the reaction to eventually get excited and emit light [116]. Unlike PL and CL, in the case of ECL, the luminescence is controlled and tuned using appropriate applied potential [116, 117]. The CDs show ECL without using any surface passivation. Oxidized CDs are generally utilized as luminophores for ECL. In most cases, a PBS solution of pH 7 is used to get ECL signal by CDs. As the ECL signal using CDs is observed in both the potential area (positive and negative), both the radicals of CDs (anionic; $R^{\bullet-}$, cationic; $R^{\bullet+}$) should actively operate for the occurrence of ECL in the non-attendance of co-reactants. The charge transfer phenomenon occurs due to the collision between the radicals, and consequently, the CDs attain their excited state [118]. It has been reported that the emission maxima get red-shifted in the case of ECL compared to the PL maxima. The separation of energy for ECL is relatively less compared to the energy of band gap (for PL), which can be deemed responsible for the red-shift of ECL maxima compared to the PL maxima [119]. One example of such an ECL-based sensor application of significant impact is the use of it as a tumor marker. For example, Xu *et al*. [120] reported the synthesis and application of an ECL-based immunosensor to detect cancer samples, and their reported LOD is 0.00026 fg/ml. They used CDs and perylenetetracarboxilic acid as the luminophores, whereas graphene as nanocarriers. The co-reactants used in ECL sensors such as $S_2O_8^{2-}$ SO_3^{2-}. $S_2O_8^{2-}$ help to produce $SO_4^{\bullet -}$ radicals whereas SO_3^{2-} helps to produce $SO_3^{\bullet -}$ radicals. In the latter case, the $SO_3^{\bullet -}$ radicals further react with dissolved oxygen and form $SO_4^{\bullet -}$. On the other hand, the CDs get reduced (electrochemically) in the cathodes to form $CDs^{\bullet -}$. This $CDs^{\bullet -}$ then react with the $SO_4^{\bullet -}$ radicals to get into the excited state. Then, during the returning back to the ground state of the CDs, they emit light [116, 121]. In some other cases of ECL-based sensing systems, CDs have been used as ECL enhancers of some semiconductor quantum dots. For example, Zhang *et al*. [122] reported the amplification of ECL of CdS quantum dots by incorporating CDs with them, which further was used as a biosensor of oxidase substrate.

1.5.1.4. Photoelectrochemiluminescence-based (PECL-based) Sensors

The PECL-based sensors work based on a combined mechanism of the PL and ECL. The transfer of electrons in this sort of sensor occurs at electrodes in the presence of light [85]. For example, Gao et al. developed one PECL-based sensor by combining N-CQDs with TiO_2. They used this sensor to detect chlorpyrifos, in which the response showed 42% better result than the sensor used without CQDs [85].

1.5.2. Optoelectronics

Some of the unique yet important optoelectronics properties are tuneable bandgaps, robust, stable fluorescence, high mobility and ultrafast transfer of electrons, long lifetime of hot-electrons, etc. Due to the presence of high surface areas, CDs have shown great potential in optoelectronic applications such as light-emitting diodes (LEDs), solar cells, and photodetectors.

1.5.2.1. Light-emitting diodes (LEDs)

LEDs are now one of the booming research topics due to their energy-saving technology. Some rare earth materials or some other inorganic quantum dots have been used by researchers to prepare LEDs. However, the popularity of CDs, because of their low-cost production and low toxicity, has been observed as a potential replacement of inorganic quantum dots for the fabrication of LEDs. The LEDs, fabricated by using CDs, can be divided into two categories: PL-based LEDs, and EL based LEDs.

1.5.2.1.1. Photoluminescence-based (PL-based) LEDs

In PL-based LEDs, there consists of a combination of fluorescent CDs along with a UV or blue chip. Here, the CDs act as phosphors that get excited in the presence of intense UV light. However, one primary drawback of this system is that the aggregation induced quenching (AIQ) causes the feeble fluorescence of the CDs. There are several techniques that can help to overcome this issue. For example, embedding the CDs in solid matrices like starch, borax, resin, cellulose nanofiber, etc., can help ignore the AIQ effect by retaining the fluorescence of the CDs. Sun et al. embedded the CDs with a starch matrix to synthesize a CDs-based phosphor. The hydroxyl groups of starch got attached with the carboxyl and amide groups on the surface of the CDs to form this matrix. The authors then showed the potential applications of this matrix in LEDs, temperature sensors, and patterning [123]. Wang *et al*. [124] used boric acid as the matrix for embedding CDs in LEDs. The synthesized CDs matrix showed a QY of 80.1% and high thermal stability, which helped them to use it in LEDs applications with CIE coordinates at (0.33, 0.32). However, the first reported LED application by CDs shows that the synthesized CDs were emitting deep UV lights. The authors could convert blue light into white light by coating a blue LED with CDs [125]. This discovery expanded the opportunities for researchers to use CDs in the fields of optoelectronics (LEDs). Thereafter many works have been done by researchers to fabricate white LEDs using green, yellow, blue light-emissive CDs-based phosphors [123, 126-129]. However, most of the reported CDs-phosphors-based white LEDs have been facing criticism due to their poor stability, segregation of phases, aging of colors, and complicacy in the fabrication of devices. The dependency on the multi-components which emit different colors in the white light spectrum can be attributed to the above-mentioned criticism. Therefore, a single-component system that emits light in the range of 400-700 nm is highly desirable by scientists [130-132].

1.5.2.1.2. Electroluminescence-based (EL-based) LEDs

Apart from phosphor-based LEDs, CDs have been used for EL-based LEDs as well. Generally, CDs are sandwiched between a multi-layered device structure as emissive films. The first-ever EL-based LED using CDs (GQDs) has been articulated by Gupta et al. They fabricated an organic LED (OLED) using CDs where the power was generated electrically. The emissive layer was fabricated by a mixture of GQDs (functionalized with methylene blue; MB-GQD), which was doped in poly (2-methoxy-5-(2-ethylehexoloxy)-1,4-phenylenevenylene) (MEH-PPV) with several concentrations of GQDs. The result showed that the turn-on voltage got reduced from 6 V to 4 V when 1% of the MB-GQD was mixed with MEH-PPV [133]. However, further addition of GQDs to the mixture showed an adverse effect due to the aggregation of the CDs. Additionally, the extent of work on EL-based LEDs using CDs got expanded. In some cases, poly(3,4-ethylenedioxythiophene) : poly(styrenesulfonate) (PEDOT : PSS) has been used to increase the work function of ITO by using it as the buffer layer at the anode so that the roughness on the surface gets reduced. The other electrode was 1 nm thin LiF with 120 nm thin Al, whereas the electron transport layer was made with 1,3,5-tris(N-phenylbenzimidazol-2-yl) benzene (TPBI) [16, 134]. Having said so, the EL-based LEDs composed of CDs are still lagging in terms of efficiencies compared to the ones fabricated with semiconductor quantum dots [135, 136]. To overcome this drawback, there needs to be a proper approach to synthesize CDs with narrower bandwidth with even better QY.

1.5.2.2. Solar cells

Solar cells are the devices that depend on the carrier generation efficiencies due to photo-excitation. One of the crucial properties that can be handy to use the CDs in the solar cell application is the absorbance of light in the wide range of wavelength until the visible spectrum [9, 137, 138]. The solar cells have been subdivided into several categories, such as organic [139, 140], silicon-based [141, 142], dye-sensitized [143, 144], etc. The incorporation of CDs in solar cells can be done as sensitizers, absorbing agents, and transporting layers. Consequently, the as-prepared solar cells' efficiency also varies in a range from 0.1-9% [138]. One such example is the work reported by Bora *et al.* [145] The author solvothermally synthesized green light emitting CDs from citric acid using N, N-dimethylformamide as the solvent. The synthesized CDs were used as the co-sensitizers in dye-sensitized solar cells. The used dye in their work is N719. This overall system showed an efficiency for photo conversion of 6.9%. Shin *et al.* [140] reported the enhancement of power conversion efficiency (PCE) of a flexible organic solar cell from 3.56 to 4.23% after adding GQDs as an active layer. Diao *et al*. [146] presented the fabrication of CDs/n-silicon heterojunction for solar cell application. Using and adjusting the thickness of the CDs layer, they obtained a PCE value of up to 12.35%. This development in research regarding the use of CDs in solar cells application has shown a high potential of the CDs as the replacements of inorganic material based solar cells [147].

1.5.2.3. Photodetectors

The responsive nature of CDs under light illumination is proven to be a highly beneficial side of CDs to be utilized in photodetectors. The generation of electron-hole pairs under the light illumination further helps to separate them when applied to different potentials. This phenomenon ultimately helps to get a sufficient amount of photocurrent. However, CDs possess significantly less electrical conductivity due to less crystallinity. Hence, researchers have tried to make composites with other highly conductive materials to get better results in terms of photoresponsivity and detectivity. For example, the fabrication of a photodetector based on a silicon (Si) substrate with a heterojunction with CQDs is demonstrated by Hsiao *et al*. [148] The synthesized CQDs showed a dual-sized characteristic. In the heterojunction, the CQDs-containing bottom layer acted as a prominent photon harvester, whereas the top layer helped to extract the holes. The photoresponsivity of a Si-based photodetector was enhanced up to 203.8% by integrating a purple CD layer as a sensitizer as reported by Kalytchuk *et al*. [149] The CDs are capable of being utilized in deep UV photodetectors due to the presence of the absorbance peak at ~250 nm which is due to the $\pi - \pi^*$ transition [125, 150, 151]. A GQD decorated ZnO/PEDOT:PSS heterojunction was used as a Schottky diode to detect UV light by Dhar *et al*. [152] Their reported equivalent quantum efficiency (EQE), photoresponsivity, and photodetectivity are as high as 13,161%, 36 A/W, and 1.3 × 1012 Hz$^{1/2}$/W at -1V bias voltage, respectively. The hole-trapping phenomenon was increased due to the presence of GQDs at the surface of the ZnO nanorods, which eventually helped to get a higher photocurrent. In another work, Wang *et al*. [153] also fabricated a broadband photodetector by incorporating ZnO nanorod arrays with N-CQDs. The broadband as well as the faster response, high photoresponsivity, and sensitivity by the device can be ascribed to the presence of N-CQDs in the photodetector material. The authors used waste paper and urea as the precursor materials for the synthesis of the N-CQDs, which makes the fabrication cost of the overall device quite less. Apart from ZnO [154], CDs have been incorporated with other semiconductors as well such as, MoS_2 [155], silicon [156], perovskite [157], TiO_2 [158], WSe_2 [159], etc.

1.5.3. Energy storage

With the development of our society, the concern about the issues related to the environment is increasing with every passing day. The rapid diminution of non-renewable energy sources, high feeding of fossil fuels have made scientists strive for the search of renewable and clean energy sources. These constraints have made energy storage systems quite popular in recent years. Moreover, the expansion of electrical or hybrid vehicles has also led to the advancement of energy storage systems. Many materials like sulphides [160, 161], oxides [162, 163] have been used to develop several energy storage systems, such as supercapacitors, batteries, etc. However, incorporating CDs with the reported materials has shown terrific enhancement in the performances of the devices. Therefore, in this section, we have focused on discussing supercapacitors and batteries, where CDs have been used as fabricating materials.

1.5.3.1. Supercapacitors

The high power density of supercapacitors is one of the reasons for their exclusive demand in real-life applications. Based on the mechanism of charge storage, supercapacitors are generally categorized into two different types: electric double-layer capacitors (EDLC) and pseudocapacitors. The former one is based on the ion-adsorption mechanism, whereas the second one is based on the faradaic reaction method [138]. Kumar *et al*. [164] synthesized 4−7 nm CDs and used them in activated carbon (AC) based supercapacitor to improve the fast kinetics of the surface reaction of the EDLC electrode materials. They used Polyethylene glycol-400 (PEG400) as the precursor material for the CDs with sonication technique. The composite electrode was fabricated by sonicating CDs with ACs. Their result showed that the specific capacitance got increased three folds after adding CDs with ACs in 6 M KOH electrolyte. Another example of the composites containing carbon materials with CDs as electrode material for EDLC is presented by Hu *et al*. [165] The electrochemically synthesized CDs (2−5 nm) were adhered on the surface of horizontally associated carbon nanotubes (CNTs) arrays and were used as the electrodes. The incorporation of the CDs enhances the specific capacitance up to 200%. Another work where CDs have been used as one of the composite materials for the synthesis of the electrodes of a supercapacitor is reported by Zhao et al. In this work, they synthesized the CDs enhanced CuS/CNT electrode by in situ hydrothermal technique. The addition of CDs helped to get an enhanced performance in terms of specific capacitance and stability [166].

Moreover, CDs have been used in micro-supercapacitors as well. The first-ever micro-supercapacitor using CDs was reported by Liu *et al*. [167] They synthesized GQDs

(1−5.4 nm) by hydrothermal technique and GO by modified Hummer method. The GQDs were electrodeposited on interdigital Au electrodes. In order to fabricate an asymmetric micro- supercapacitor, GQDs were coated on one side and MnO_2 on the other side of the interdigital finger Au electrode. An aqueous solution of 0.5 M Na_2SO_4 was used as the electrolyte for the electrochemical analysis. They reported that the device retained ≈97.8% of its initial specific capacitance even after 5000 cycles. In another work, GQDs were used to prepare a micro-supercapacitor along with MnO_2 [168]. Ionic liquid gel was used as the electrolyte in this work. The GQDs were synthesized by hydrothermal technique from GO sheets [169]. The photoresponsive behavior of the CDs has also been utilized to fabricate light rechargeable supercapacitors. A group of scientists fabricated a fibrous supercapacitor (photo-assisted; NM_2P_1). They used N-CDs enhanced $Ti_3C_2T_x$ as the electrode material. The device showed a volumetric capacitance of 1,445 F/cm^3 at 10 A/cm^3 under photo-charging, which was 35.9% higher than the value in dark condition [170]. Apart from this, many other recent reports are there, where the scientists have used CDs for fabricating photo-rechargeable supercapacitors [171, 172].

1.5.3.2. Batteries

Another form of the energy storage device is a battery. There have been several works on the fabrication of Li-ion batteries for the last couple of decades. However, the first inclusion of CDs (GQDs) to synthesize electrode materials (positive electrode) was reported by Zhu et al. [151] The addition of GQDs with highly conductive CuO helped to increase the transport kinetics by decreasing the electrochemical impedance. The device showed an excellent power density of 157.3 mW/cm^2 [173]. In another work, the growth of Li on the anode of Li-ion battery was minimized by changing the morphology of the anode with the introduction of CDs in the Li plating. The synthesized CDs possessed several functional groups (−OH, −COOH) and negative surface charges. The functional groups and the negative charge at the surface helped to attract positive Li-ions, which made the transportation of Li ions uniform on the charge collector. This phenomenon helped to maintain the smoothness of the surface during the plating process. The device showed a capacity retention of 99% after 100 cycles [174]. Apart from the application of CDs in various Li-ion batteries [175, 176], there are several works, which report the application of CDs in sodium-ion batteries as well [177].

1.5.4. Catalysis

As discussed earlier, CDs are capable of multi-disciplinary applications. Also, is that the unique characteristics of consisting of several functional groups on the surfaces make the CDs quite handy in catalytic applications as well. More significantly, CDs act as both electron acceptors and electron donors. The catalytic application by CDs can be executed by attaching them with other nanomaterials or by using them individually as sole catalysts [42]. Based on the working methods of the CDs as catalysts, they have been sub-categorized into two distinct divisions; bare CDs –based catalysts, CDs-containing-composite-based catalysts. The catalytic activities of CDs have been explored to degrade several pollutants such as metal ions and organic dyes. Jusuf *et al.* [178] synthesized CDs from the ashes of the membranes of eggshell by microwave heating technique with an average particle size of 3.88 nm. They mixed these CDs with methylene blue to prepare the sample solutions at a concentration ratio of 4:1. The degradation was carried out under the irradiation of sunlight and characterized the degradation with UV-vis spectroscopy. The authors reported more than 50% degradation of methylene blue in this work. Arul *et* *al*. [179] also reported the methylene blue-reduction by using N-CDs. The addition of the CDs in the solution of $NaBH_4$ and methylene blue helped to reduce the absorbance intensity of the solution, indicating the reduction of methylene blue. The functional groups on the surface of the CDs attracted the methylene blue and $NaBH_4$, which resulted in the dye adsorption on the surface, and hence, the absorbance intensity got reduced. Considering the toxicity of Cr^{6+}, Bhati *et al*. [180] reduced it to Cr^{3+} using N-doped CDs. The reduction process was carried out in the presence of sunlight. The photons of sunlight excited the CDs to separate the electrons and holes. These photo-generated holes then interacted with the water molecules to generate H^+ ions. These H^+ ions and the photo-generated holes then helped to reduce the Cr^{6+} ions to less toxic Cr^{3+} ions. Further, these Cr^{3+} ions were separated by precipitation technique.

Furthermore, some composites have also been synthesized by attaching CDs with other nanomaterials and used in catalytic applications. For example, Ke *et al*. [181] synthesized a nano-composite by linking CDs with TiO_2 nanomaterial. The higher bandgap of TiO_2 (3.2 eV) limits the photocatalytic activity to the UV light region. However, attaching the CDs with TiO_2 by the authors helped to improve the photocatalytic activity even in the visible spectrum. They used this composite to degrade methylene blue, and the reported efficiency was almost 90%. The inclusion of CDs with the TiO_2 nanoparticles showed 3.25 times better degradation efficiency compared to pristine TiO_2 nanoparticles. In another work, Chai *et al*. [182] developed a photocatalyst by doping CDs/Zn^{2+} on CdS nanoparticles. They used this composite as the photocatalyst to reduce 4-nitroaniline (4-NA) under visible light. Similarly, Huo *et al*. [183] also developed a ternary composite system consisting of CDs, CdSe, and rGO. They synthesized this composite by hydrothermal technique. Further, they used this composite to degrade pollutants under the presence of light. There are many other example, where CDs have been used as photocatalysts [184-186].

1.5.5. Biological applications

The low toxicity of CDs is a vital characteristic to use in biological applications. Among the many in vitro cytotoxicity tests of CDs with the use of a series of cell lines, there have not been any morphological changes or acute toxicity has been reported till now [187, 188]. Moreover, similar results regarding toxicity were found for in vivo tests as well [189, 190]. These results instigated many bio-researchers to use CDs in different biological applications, such as bioimaging, biosensors, etc.

A great number of cell lines have been used to check the bioimaging capability of the CDs. Some of them are HeLa cells [9], HEK293 [191], Caco-2 cells [192], cell lines of the kidneys of pigs [193], B16F11 [191], BGC823 cells [194], Escherichia coli cells [195], etc. For example, Wang *et al.* [196] synthesized N, P-CDs by hydrothermal technique from L-arginine and phosphoric acid precursor materials. The high QY (18.39%) of the synthesized CDs and the low toxicity were further exploited to use them in cell imaging (HeLa) applications. In another work, the synthesis of dual emissive CDs has been reported by Hu *et al*. [197] They synthesized the CDs by hydrothermally treating a solution of dicyandiamide and *o*-phenylenediamine in dilute sulfuric acid. The CDs showed an excellent QY value of 30.2% in water. Owing to this higher fluorescence property of the CDs, the authors used it in cell (HeLa) imaging applications. Atchudan *et al*. [35] showed the in vivo bioimaging application of CQDs by staining the whole body of nematodes. The CQDs showed multicolour emission when excited at different wavelengths. The authors used the hydrothermal method to synthesize the CQDs from banana peel precursor material with a QY value of 20%. Not only in bioimaging, but the low toxicity of the CDs has also acted as an influence to use them in biosensing applications as well. Some biomaterials that have been targeted to detect by CDs are DNA [198, 199], cells and bacteria [200-202], proteins [203, 204], etc.

1.6. Knowledge gap

In the context of the earlier discussion, it is worth mentioning that the applications of CDs are not limited to a single field of research. Rather, these have been expanded to multiple directions. However, it is rarely observed that the CDs, which are obtained from a single source of precursor material, have been used in more than one application simultaneously. According to the literature, the CDs are either used in sensing applications or in bioimaging applications or in photocatalytic applications, etc. It is not common that the same CDs have been used in both sensing and bioimaging applications, or sensing and photodetector applications, and so forth.

Although the PL property of the CDs has been well utilized in the fields of PL-based sensing and bioimaging applications, it is found out from the literature that the light-responsive behavior of the CDs is very poorly explored in the fields of photodetection and energy storage applications. There are several examples in the literature where CDs have been used in the field of energy storage systems; however, the use of CDs in the fabrication of photo rechargeable energy storage devices is not yet reported to the best of our knowledge. Moreover, in most of the works, it is witnessed that the CDs are needed to be processed through some costly and time-consuming purification steps. Therefore, based on these literature gaps, the objectives of the thesis were decided, which are discussed in detail in the subsequent section.

1.7. Objective and outline of the thesis

In the previous sections, an extensive discussion about the synthesis of CDs and their applications have been made. The outcome of the discussion is such that the demand for CDs in the current scenario is growing exponentially owing to the low toxic environment-friendly characteristics of CDs, which is due to their natural resources. Their applications in several critical fields such as optoelectronics and energy storage systems have also played an essential role in developing CDs' popularity.

In the context of this, the current thesis explores several natural resources to synthesize CDs and used these CDs in applications such as sensing, bioimaging, optoelectronics, and energy storage systems. This thesis is divided into four different sections based on their applications. These are (A) Sensing, (B) Bioimaging, (C) Optoelectronics, and (D) Energy storage systems. Four different technical chapters have been prepared to discuss about these four sections along with the introduction as well as summary and future scope. An overall outline of the thesis in terms of different chapters is given below.

Chapter 1: This chapter starts with the introduction of the topic covering a detailed discussion of CDs, their synthesis, and applications in several fields. A rigorous review of the literature has been done. Based on the discussion of the literature, the objectives and approach of the thesis have been described.

Chapter 2: This technical chapter includes sections A and B (sensing and bioimaging). The synthesis of CDs by simple heating technique from potato has been shown and characterized in detail. The synthesized CDs show an average particle size of ~5.97 nm with a QY of ~6.08%. The presence of functional groups –OH and –COOH has been proven by Fourier transfer infrared spectroscopy (FTIR) analysis. The PL-based sensing of Cr^{6+} and Fe^{3+} metal ions by the synthesized CDs has also been reported in this chapter. Further, the same CDs have been used for in vitro cell imaging of HeLa cells.

Chapter 3: Sections A and C (sensing and optoelectronics) are elaborated in this technical chapter. Cigarette-tobacco is used to synthesize N-doped CDs by microwave assisted heating technique. The average particle size and the QY, in this case, are ~2.8 nm and ~9.98%, respectively. These synthesized CDs have also been used to detect picric acid (PA; explosive material) in the water sample. Further, the as-synthesized CDs are attached with MWCNT to prepare a nano-composite (CD-MWCNT) which has successfully acted as a UV-photodetector material.

Chapter 4: This technical chapter includes section C (optoelectronics). Here, we have not focused on the synthesis of CDs from some novel precursor materials. In this chapter, we have used the CDs that have been reported in **Chapter 3.** The focus of this chapter is to use the CDs in optoelectronic applications such as UV-photodetection. To obtain this goal, we have attached the CDs with ZnO nanorods, which have been grown on a graphite-coated paper substrate by hydrothermal technique. The as-prepared CD decorated ZnO nanorods grown on a graphite-coated paper substrate acts as a Schottky diode. This paper substrate-based Schottky diode is then used as a self-powered UV-photodetector.

Chapter 5: This technical chapter covers section D (energy storage system). In this chapter, we report the fabrication of a UV-photoresponsive supercapacitor, where the electrodes have been fabricated by attaching CDs on ZnO/MWCNT films. An ITO-coated PET sheet has been used as the substrate material. Here also, we have not focused on the synthesis of CDs from a novel precursor material. We have used citric acid and ethylenediamine (EDA) to synthesize the CDs by hydrothermal method. The primary focus of this chapter is to fabricate a photoresponsive supercapacitor using CDs and then exploring the working mechanism of the supercapacitor using electrochemical analysis, which we have successfully presented.

Chapter 6: This chapter summarizes the work reported in the thesis by drawing appropriate conclusions. Further, this chapter discusses the future scopes based on the work reported in the previous technical chapters.

References

[1] L.H. Madkour, Nanoelectronic Materials Fundamentals and Applications, Springer 2019.

[2] X. Liu, M. Wang, S. Zhang, B. Pan, Journal of Environmental Sciences, 25 (2013) 1263.

[3] G.D. Park, Y.C. Kang, Chemistry – A European Journal, 22 (2016) 4140.

[4] J.M. Schnorr, T.M. Swager, Chemistry of Materials, 23 (2011) 646.

[5] Y. Zhu, S. Murali, W. Cai, X. Li, J.W. Suk, J.R. Potts, R.S. Ruoff, Advanced Materials, 22 (2010) 3906.

[6] A. Dixit, S. Middya, S. Mitra, S. Maity, M. Bhattacharjee, D. Bandyopadhyay, The Journal of Physical Chemistry C, 123 (2019) 195.

[7] X. Xu, R. Ray, Y. Gu, H.J. Ploehn, L. Gearheart, K. Raker, W.A. Scrivens, Journal of the American Chemical Society, 126 (2004) 12736.

[8] J. Liu, R. Li, B. Yang, ACS Central Science, 6 (2020) 2179.

[9] R. Sinha, A.P. Bidkar, R. Rajasekhar, S.S. Ghosh, T.K. Mandal, The Canadian Journal of Chemical Engineering, 98 (2020) 194.

[10] R. Sinha, N. Roy, R. Rajasekhar, A. Karnawat, T.K. Mandal, Journal of Environmental Chemical Engineering, 9 (2021) 104971.

[11] K.A.S. Fernando, S. Sahu, Y. Liu, W.K. Lewis, E.A. Guliants, A. Jafariyan, P. Wang, C.E. Bunker, Y.-P. Sun, ACS Applied Materials & Interfaces, 7 (2015) 8363.

[12] M. Semeniuk, Z. Yi, V. Poursorkhabi, J. Tjong, S. Jaffer, Z.-H. Lu, M. Sain, ACS Nano, 13 (2019) 6224.

[13] S. Zhu, Y. Song, X. Zhao, J. Shao, J. Zhang, B. Yang, Nano Research, 8 (2015) 355.

[14] S. Zhu, J. Zhang, S. Tang, C. Qiao, L. Wang, H. Wang, X. Liu, B. Li, Y. Li, W. Yu, X. Wang, H. Sun, B. Yang, Advanced Functional Materials, 22 (2012) 4732.

[15] G.A.M. Hutton, B.C.M. Martindale, E. Reisner, Chemical Society Reviews, 46 (2017) 6111.

[16] F. Yuan, S. Li, Z. Fan, X. Meng, L. Fan, S. Yang, Nano Today, 11 (2016) 565.

[17] S. Zhu, Q. Meng, L. Wang, J. Zhang, Y. Song, H. Jin, K. Zhang, H. Sun, H. Wang, B. Yang, Angewandte Chemie International Edition, 52 (2013) 3953.

[18] Y. Wang, X. Chang, N. Jing, Y. Zhang, Analytical Methods, 10 (2018) 2775.

[19] F. Yuan, Z. Wang, X. Li, Y. Li, Z.a. Tan, L. Fan, S. Yang, Advanced Materials, 29 (2017) 1604436.

[20] Y. Zhuo, H. Miao, D. Zhong, S. Zhu, X. Yang, Materials Letters, 139 (2015) 197.

[21] Y. Xu, H. Li, B. Wang, H. Liu, L. Zhao, T. Zhou, M. Liu, N. Huang, Y. Li, L. Ding, Y. Chen, Microchimica Acta, 185 (2018) 252.

[22] H. Li, X. He, Y. Liu, H. Huang, S. Lian, S.-T. Lee, Z. Kang, Carbon, 49 (2011) 605.

[23] Q. Liu, J. Sun, K. Gao, N. Chen, X. Sun, D. Ti, C. Bai, R. Cui, L. Qu, Materials Chemistry Frontiers, 4 (2020) 421.

[24] H. Kalita, V.S. Palaparthy, M.S. Baghini, M. Aslam, Carbon, 165 (2020) 9.

[25] P.A.N.d. Yro, G.M.O. Quaichon, R.A.T. Cruz, C.S. Emolaga, M.C.O. Que, E.R. MagdaluyoJr, B.A. Basilia, AIP Conference Proceedings, 2083 (2019) 020007.

[26] W.S. Kuo, Y.T. Shao, K.S. Huang, T.M. Chou, C.H. Yang, ACS Appl Mater Interfaces, 10 (2018) 14438.

[27] Z. Li, L. Cao, P. Qin, X. Liu, Z. Chen, L. Wang, D. Pan, M. Wu, Carbon, 139 (2018) 67.

[28] J. Zhu, Y. Tang, G. Wang, J. Mao, Z. Liu, T. Sun, M. Wang, D. Chen, Y. Yang, J. Li, Y. Deng, S. Yang, ACS Applied Materials & Interfaces, 9 (2017) 14470.

[29] S.H. Lee, D.Y. Kim, J. Lee, S.B. Lee, H. Han, Y.Y. Kim, S.C. Mun, S.H. Im, T.-H. Kim, O.O. Park, Nano Letters, 19 (2019) 5437.

[30] M. Picard, S. Thakur, M. Misra, A.K. Mohanty, RSC Advances, 9 (2019) 8628.

[31] W. Wang, J. Chen, D. Wang, Y. Shen, L. Yang, T. Zhang, J. Ge, Analytical Methods, 13 (2021) 789.

[32] R. Qiang, S. Yang, K. Hou, J. Wang, New Journal of Chemistry, 43 (2019) 10826.

[33] S. Pramanik, S. Chatterjee, G. Suresh Kumar, P. Sujatha Devi, Physical Chemistry Chemical Physics, 20 (2018) 20476.

[34] D. Wang, L. Zhu, C. McCleese, C. Burda, J.-F. Chen, L. Dai, RSC Advances, 6 (2016) 41516.

[35] R. Atchudan, T.N. Jebakumar Immanuel Edison, M. Shanmugam, S. Perumal, T. Somanathan, Y.R. Lee, Physica E: Low-dimensional Systems and Nanostructures, 126 (2021) 114417.

[36] S.A.A. Vandarkuzhali, V. Jeyalakshmi, G. Sivaraman, S. Singaravadivel, K.R. Krishnamurthy, B. Viswanathan, Sensors and Actuators B: Chemical, 252 (2017) 894.

[37] M.Z. Fahmi, A. Haris, A.J. Permana, D.L. Nor Wibowo, B. Purwanto, Y.L. Nikmah, A. Idris, RSC Advances, 8 (2018) 38376.

[38] C. D'Angelis do E. S. Barbosa, J.R. Corrêa, G.A. Medeiros, G. Barreto, K.G. Magalhães, A.L. de Oliveira, J. Spencer, M.O. Rodrigues, B.A.D. Neto, Chemistry – A European Journal, 21 (2015) 5055.

[39] J. Wei, X. Zhang, Y. Sheng, J. Shen, P. Huang, S. Guo, J. Pan, B. Liu, B. Feng, New Journal of Chemistry, 38 (2014) 906.

[40] M. Jayanthi, S. Megarajan, S.B. Subramaniyan, R.K. Kamlekar, A. Veerappan, Journal of Molecular Liquids, 278 (2019) 175.

[41] A. Singh, E. Eftekhari, J. Scott, J. Kaur, S. Yambem, F. Leusch, R. Wellings, T. Gould, K. Ostrikov, P. Sonar, Q. Li, Sustainable Materials and Technologies, 25 (2020) e00159.

[42] N. Dhenadhayalan, K.-C. Lin, T.A. Saleh, Small, 16 (2020) 1905767.

[43] L. Bu, J. Peng, H. Peng, S. Liu, H. Xiao, D. Liu, Z. Pan, Y. Chen, F. Chen, Y. He, RSC Advances, 6 (2016) 95469.

[44] H. Wang, S. Liu, Y. Xie, J. Bi, Y. Li, Y. Song, S. Cheng, D. Li, M. Tan, New Journal of Chemistry, 42 (2018) 3729.

[45] M. Liu, T. Li, C. Zhang, Y. Zheng, C. Wu, J. Zhang, K. Zhang, Z. Zhang, Journal of hazardous materials, 415 (2021) 125699.

[46] C. Zhang, Z. Hu, L. Song, Y. Cui, X. Liu, New Journal of Chemistry, 39 (2015) 6201.

[47] X.-Y. Xu, B. Yan, Journal of Materials Chemistry C, 4 (2016) 1543.

[48] X. Qin, W. Lu, A.M. Asiri, A.O. Al-Youbi, X. Sun, Sensors and Actuators B: Chemical, 184 (2013) 156.

[49] Y. Guo, Carbon, 52 (2013) 583.

[50] Y. Hou, Q. Lu, J. Deng, H. Li, Y. Zhang, Analytica chimica acta, 866 (2015) 69.

[51] Z.-h. Gao, Z.-z. Lin, X.-m. Chen, H.-p. Zhong, Z.-y. Huang, Analytical Methods, 8 (2016) 2297.

[52] M.A. Issa, Z.Z. Abidin, S. Sobri, S.A. Rashid, M.A. Mahdi, N.A. Ibrahim, Scientific Reports, 10 (2020) 11710.

[53] P. Song, L. Zhang, H. Long, M. Meng, T. Liu, Y. Yin, R. Xi, RSC Advances, 7 (2017) 28637.

[54] H. Shah, Q. Xin, X. Jia, J.R. Gong, Arabian Journal of Chemistry, 12 (2019) 1083.

[55] Y. Li, Y. Liu, X. Shang, D. Chao, L. Zhou, H. Zhang, Chemical Physics Letters, 705 (2018) 1.

[56] S. Pawar, S. Kaja, A. Nag, ACS Omega, 5 (2020) 8362.

[57] V. Sharma, A.K. Saini, S.M. Mobin, Journal of Materials Chemistry B, 4 (2016) 2466.

[58] W. Gao, H. Song, X. Wang, X. Liu, X. Pang, Y. Zhou, B. Gao, X. Peng, ACS Applied Materials & Interfaces, 10 (2018) 1147.

[59] C. Zhao, X. Li, C. Cheng, Y. Yang, Microchemical Journal, 147 (2019) 183.

[60] C.-L. Li, C.-C. Huang, A.P. Periasamy, P. Roy, W.-C. Wu, C.-L. Hsu, H.-T. Chang, RSC Advances, 5 (2015) 2285.

[61] M. Tian, Y. Liu, Y. Wang, Y. Zhang, Analytical Methods, 11 (2019) 4077.

[62] N. Jing, M. Tian, Y. Wang, Y. Zhang, Journal of Luminescence, 206 (2019) 169.

[63] Z. Zhang, W. Sun, P. Wu, ACS Sustainable Chemistry & Engineering, 3 (2015) 1412.

[64] M. Yang, W. Kong, H. Li, J. Liu, H. Huang, Y. Liu, Z. Kang, Microchimica Acta, 182 (2015) 2443.

[65] A.H. da Silva Júnior, D. Lusitâneo Pier Macuvele, H. Gracher Riella, C. Soares, N. Padoin, Materials Letters, 283 (2021) 128813.

[66] Z. Zhang, Y. Shi, Y. Pan, X. Cheng, L. Zhang, J. Chen, M.-J. Li, C. Yi, Journal of Materials Chemistry B, 2 (2014) 5020.

[67] L. Yu, G. Ren, M. Tang, B. Zhu, F. Chai, G. Li, D. Xu, European Journal of Inorganic Chemistry, 2018 (2018) 3418.

[68] Y. Wang, C. Zhang, X. Chen, B. Yang, L. Yang, C. Jiang, Z. Zhang, Nanoscale, 8 (2016) 5977.

[69] J. Wang, R. Sheng Li, H. Zhi Zhang, N. Wang, Z. Zhang, C.Z. Huang, Biosensors and Bioelectronics, 97 (2017) 157.

[70] P. Das, S. Ganguly, M. Bose, S. Mondal, A.K. Das, S. Banerjee, N.C. Das, Materials Science and Engineering: C, 75 (2017) 1456.

[71] C. Wang, C. Pan, X. Wei, F. Yang, W. Wu, L. Mao, Talanta, 208 (2020) 120375.

[72] G. Gedda, C.-Y. Lee, Y.-C. Lin, H.-f. Wu, Sensors and Actuators B: Chemical, 224 (2016) 396.

[73] J. Chen, Y. Li, K. Lv, W. Zhong, H. Wang, Z. Wu, P. Yi, J. Jiang, Sensors and Actuators B: Chemical, 224 (2016) 298.

[74] W.J. Zhang, S.G. Liu, L. Han, H.Q. Luo, N.B. Li, Sensors and Actuators B: Chemical, 283 (2019).

[75] N.K.R. Bogireddy, V. Barba, V. Agarwal, ACS Omega, 4 (2019) 10702.

[76] J. Gu, D. Hu, W. Wang, Q. Zhang, Z. Meng, X. Jia, K. Xi, Biosensors and Bioelectronics, 68 (2015) 27.

[77] W.-J. Niu, D. Shan, R.-H. Zhu, S.-Y. Deng, S. Cosnier, X.-J. Zhang, Carbon, 96 (2016) 1034.

[78] M.Y. Pudza, Z.Z. Abidin, S. Abdul-Rashid, F.M. Yasin, A.S.M. Noor, J. Abdullah, Environmental science and pollution research international, 27 (2020) 13315.

[79] L. Li, D. Liu, A. Shi, T. You, Sensors and Actuators B: Chemical, 255 (2018) 1762.

[80] F. Qu, S. Wang, D. Liu, J. You, RSC Advances, 5 (2015) 82570.

[81] T. Alizadeh, N. Hamidi, M.R. Ganjali, P. Nourozi, Sensors and Actuators B: Chemical, 245 (2017) 605.

[82] X. Gao, C. Du, Z. Zhuang, W. Chen, Journal of Materials Chemistry C, 4 (2016) 6927.

[83] L. Feng, L. Tan, H. Li, Z. Xu, G. Shen, Y. Tang, Biosensors & bioelectronics, 69 (2015) 265.

[84] B. Wang, X. Liu, W. Duan, S. Dai, H. Lu, Microchemical Journal, 156 (2020) 104807.

[85] M. Li, T. Chen, J.J. Gooding, J. Liu, ACS Sensors, 4 (2019) 1732.

[86] L. Zhang, S. Chen, Q. Zhao, H. Huang, Analytica chimica acta, 880 (2015) 130.

[87] S.N.A. Mohd Yazid, S.F. Chin, S.C. Pang, S.M. Ng, Microchimica Acta, 180 (2013) 137.

[88] N. Gogoi, M. Barooah, G. Majumdar, D. Chowdhury, ACS Applied Materials & Interfaces, 7 (2015) 3058.

[89] W. Zhu, J. Zhang, Z. Jiang, W. Wang, X. Liu, RSC Advances, 4 (2014) 17387.

[90] X. Jiang, J. Huang, T. Chen, Q. Zhao, F. Xu, X. Zhang, International Journal of Biological Macromolecules, 153 (2020) 412.

[91] Y. Zhang, K. Zhou, Y. Qiu, L. Xia, Z. Xia, K. Zhang, Q. Fu, Sensors and Actuators B: Chemical, 339 (2021) 129922.

[92] S. Lu, Z. Li, X. Fu, Z. Xie, M. Zheng, Dyes and Pigments, 187 (2021) 109126.

[93] Z. Wang, L. Zhang, Y. Hao, W. Dong, Y. Liu, S. Song, S. Shuang, C. Dong, X. Gong, Analytica chimica acta, 1144 (2021) 1.

[94] S. Bian, C. Shen, Y. Qian, J. Liu, F. Xi, X. Dong, Sensors and Actuators B: Chemical, 242 (2017) 231.

[95] J. Li, L. Zhang, P. Li, Y. Zhang, C. Dong, Sensors and Actuators B: Chemical, 258 (2018) 580.

[96] G. Ren, M. Tang, F. Chai, H. Wu, European Journal of Inorganic Chemistry, 2018 (2018) 153.

[97] S. Venkatesan, A.J. Mariadoss, K. Arunkumar, A. Muthupandian, Sensors and Actuators B: Chemical, 282 (2019) 972.

[98] A. Chatzimarkou, T.G. Chatzimitakos, A. Kasouni, L. Sygellou, A. Avgeropoulos, C.D. Stalikas, Sensors and Actuators B: Chemical, 258 (2018) 1152.

[99] Y. Qu, G. Ren, L. Yu, B. Zhu, F. Chai, L. Chen, Journal of Luminescence, 207 (2019) 589.

[100] Z.M.S.H. Khan, S. Saifi, Shumaila, Z. Aslam, S.A. Khan, M. Zulfequar, Journal of Photochemistry and Photobiology A: Chemistry, 388 (2020) 112201.

[101] F. Cheng, X. An, C. Zheng, S. Cao, RSC Advances, 5 (2015) 93360.

[102] H. Zhang, Y. Chen, M. Liang, L. Xu, S. Qi, H. Chen, X. Chen, Analytical Chemistry, 86 (2014) 9846.

[103] S. Lan, X. Wang, Q. Liu, J. Bao, M. Yang, H. Fa, C. Hou, D. Huo, Talanta, 192 (2019) 368.

[104] M. Zheng, C. Wang, Y. Wang, W. Wei, S. Ma, X. Sun, J. He, Talanta, 185 (2018) 309.

[105] Y. Yang, D. Huo, H. Wu, X. Wang, J. Yang, M. Bian, Y. Ma, C. Hou, Sensors and Actuators B: Chemical, 274 (2018) 296.

[106] C. Wang, Y. Lan, F. Yuan, T.H. Fereja, B. Lou, S. Han, J. Li, G. Xu, Microchimica Acta, 187 (2019) 50.

[107] T. Hallaj, M. Amjadi, J.L. Manzoori, N. Azizi, Luminescence, 32 (2017) 1174.

[108] Y. Duan, Y. Huang, S. Chen, W. Zuo, B. Shi, ACS Omega, 4 (2019) 9911.

[109] X. Chen, J. Zhang, S. Han, H. Liu, Y. Du, Journal of the Chinese Chemical Society, 65 (2018) 883.

[110] L. Li, X. Lai, X. Xu, J. Li, P. Yuan, J. Feng, L. Wei, X. Cheng, Mikrochimica acta, 185 (2018) 136.

[111] Y. Liu, S. Han, Food Analytical Methods, 10 (2017) 3398.

[112] Y. Sun, C. Ding, Y. Lin, W. Sun, H. Liu, X. Zhu, Y. Dai, C. Luo, Talanta, 186 (2018) 238.

[113] J. Chen, J. Shu, J. Chen, Z. Cao, A. Xiao, Z. Yan, Luminescence, 32 (2017) 277.

[114] J. Zhang, X. Chen, Y. Li, S. Han, Y. Du, H. Liu, Analytical Methods, 10 (2018) 541.

[115] Z.-y. Yan, A. Xiao, H. Lu, Z. Liu, J.-q. Chen, New Carbon Materials, 29 (2014) 216.

[116] M.J. Molaei, Talanta, 196 (2019) 456.

[117] W. Miao, Chemical Reviews, 108 (2008) 2506.

[118] Y. Dong, N. Zhou, X. Lin, J. Lin, Y. Chi, G. Chen, Chemistry of Materials, 22 (2010) 5895.

[119] L. Zheng, Y. Chi, Y. Dong, J. Lin, B. Wang, J Am Chem Soc, 131 (2009) 4564.

[120] L.-L. Xu, W. Zhang, L. Shang, R.-N. Ma, L.-P. Jia, W.-L. Jia, H.-S. Wang, L. Niu, Biosensors & bioelectronics, 103 (2018) 6.

[121] Y. Dong, C. Chen, J. Lin, N. Zhou, Y. Chi, G. Chen, Carbon, 56 (2013) 12.

[122] Y. Zhang, S. Deng, J. Lei, Q. Xu, H. Ju, Talanta, 85 (2011) 2154.

[123] M. Sun, S. Qu, Z. Hao, W. Ji, P. Jing, H. Zhang, L. Zhang, J. Zhao, D. Shen, Nanoscale, 6 (2014) 13076.

[124] H. Wang, Z. Zhang, Q. Yan, C. Zhang, Y. Xing, Y. Xiong, F. Zhang, Z. Wang, ChemistrySelect, 5 (2020) 13969.

[125] L. Tang, R. Ji, X. Cao, J. Lin, H. Jiang, X. Li, K.S. Teng, C.M. Luk, S. Zeng, J. Hao, S.P. Lau, ACS Nano, 6 (2012) 5102.

[126] X. Li, Y. Liu, X. Song, H. Wang, H. Gu, H. Zeng, Angewandte Chemie International Edition, 54 (2015) 1759.

[127] H. Ding, S.-B. Yu, J.-S. Wei, H.-M. Xiong, ACS Nano, 10 (2016) 484.

[128] C. Sun, Y. Zhang, K. Sun, C. Reckmeier, T. Zhang, X. Zhang, J. Zhao, C. Wu, W.W. Yu, A.L. Rogach, Nanoscale, 7 (2015) 12045.

[129] Y. Wang, S. Kalytchuk, L. Wang, O. Zhovtiuk, K. Cepe, R. Zboril, A.L. Rogach, Chemical Communications, 51 (2015) 2950.

[130] X.T. Feng, F. Zhang, Y.L. Wang, Y. Zhang, Y.Z. Yang, X.G. Liu, Applied Physics Letters, 107 (2015) 213102.

[131] J. Luo, X. Wang, S. Li, J. Liu, Y. Guo, G. Niu, L. Yao, Y. Fu, L. Gao, Q. Dong, C. Zhao, M. Leng, F. Ma, W. Liang, L. Wang, S. Jin, J. Han, L. Zhang, J. Etheridge, J. Wang, Y. Yan, E.H. Sargent, J. Tang, Nature, 563 (2018) 541.

[132] T. Yuan, T. Meng, P. He, Y. Shi, Y. Li, X. Li, L. Fan, S. Yang, Journal of Materials Chemistry C, 7 (2019) 6820.

[133] V. Gupta, N. Chaudhary, R. Srivastava, G.D. Sharma, R. Bhardwaj, S. Chand, Journal of the American Chemical Society, 133 (2011) 9960.

[134] Q. Sun, Y.A. Wang, L.S. Li, D. Wang, T. Zhu, J. Xu, C. Yang, Y. Li, Nature Photonics, 1 (2007) 717.

[135] X. Li, Y.-B. Zhao, F. Fan, L. Levina, M. Liu, R. Quintero-Bermudez, X. Gong, L.N. Quan, J. Fan, Z. Yang, S. Hoogland, O. Voznyy, Z.-H. Lu, E.H. Sargent, Nature Photonics, 12 (2018) 159.

[136] Y. Cao, N. Wang, H. Tian, J. Guo, Y. Wei, H. Chen, Y. Miao, W. Zou, K. Pan, Y. He, H. Cao, Y. Ke, M. Xu, Y. Wang, M. Yang, K. Du, Z. Fu, D. Kong, D. Dai, Y. Jin, G. Li, H. Li, Q. Peng, J. Wang, W. Huang, Nature, 562 (2018) 249.

[137] R. Sekiya, Y. Uemura, H. Murakami, T. Haino, Angewandte Chemie International Edition, 53 (2014) 5619.

[138] X. Li, M. Rui, J. Song, Z. Shen, H. Zeng, Advanced Functional Materials, 25 (2015) 4929.

[139] T.T. Hoang, H.P. Pham, Q.T. Tran, Journal of Nanomaterials, 2020 (2020) 3207909.

[140] D.H. Shin, C.W. Jang, J.S. Ko, S.-H. Choi, Applied Surface Science, 538 (2021) 148155.

[141] C. Xie, B. Nie, L. Zeng, F.-X. Liang, M.-Z. Wang, L. Luo, M. Feng, Y. Yu, C.-Y. Wu, Y. Wu, S.-H. Yu, ACS Nano, 8 (2014) 4015.

[142] Z. Li, J. Guo, Z. Li, W. Han, G. Ren, C. Liu, L. Shen, W. Guo, Journal of Materials Chemistry A, 8 (2020) 5629.

[143] N. Gao, L. Huang, T. Li, J. Song, H. Hu, Y. Liu, S. Ramakrishna, Journal of Applied Polymer Science, 137 (2020) 48443.

[144] H. Safardoust-Hojaghan, O. Amiri, M. Salavati-Niasari, M. Hassanpour, H. Khojasteh, L.K. Foong, Journal of Molecular Liquids, 301 (2020) 112413.

[145] A. Bora, K. Mohan, S.K. Dolui, Industrial & Engineering Chemistry Research, 58 (2019) 22771.

[146] S. Diao, X. Zhang, Z. Shao, K. Ding, J. Jie, X. Zhang, Nano Energy, 31 (2017) 359.

[147] H. Tan, A. Jain, O. Voznyy, X. Lan, F.P. García de Arquer, J. Fan, R. Quintero-Bermudez, M. Yuan, B. Zhang, Z. Yicheng, F. Fan, P. Li, L. Quan, Y.-B. Zhao, Z.-H. Lu, Z. Yang, S. Hoogland, E. Sargent, Science, 355 (2017) 722.

[148] P.-H. Hsiao, Y.-C. Lai, C.-Y. Chen, Applied Surface Science, 542 (2021) 148705.

[149] S. Kalytchuk, L. Zdražil, M. Scheibe, R. Zbořil, Nanoscale, 12 (2020) 8379.

[150] Q. Zhang, J. Jie, S. Diao, Z. Shao, Q. Zhang, L. Wang, W. Deng, W. Hu, H. Xia, X. Yuan, S.-T. Lee, ACS Nano, 9 (2015) 1561.

[151] C. Zhu, D. Chao, J. Sun, I.M. Bacho, Z. Fan, C.F. Ng, X. Xia, H. Huang, H. Zhang, Z.X. Shen, G. Ding, H.J. Fan, Advanced Materials Interfaces, 2 (2015) 1400499.

[152] S. Dhar, T. Majumder, S.P. Mondal, ACS Applied Materials & Interfaces, 8 (2016) 31822.

[153] R.-C. Wang, J.-T. Lu, Y.-C. Lin, Journal of Alloys and Compounds, 813 (2020) 152201.

[154] R. Sinha, N. Roy, T.K. Mandal, ACS Applied Materials & Interfaces, 12 (2020) 33428.

[155] M. Min, S. Sakri, G.A. Saenz, A.B. Kaul, ACS Applied Materials & Interfaces, 13 (2021) 5379.

[156] T. Dey, S. Mukherjee, A. Ghorai, S. Das, S.K. Ray, The Journal of Physical Chemistry C, 124 (2020) 12161.

[157] A. Subramanian, J. Akram, S. Hussain, J. Chen, K. Qasim, W. Zhang, W. Lei, ACS Applied Electronic Materials, 2 (2020) 230.

[158] S. Kunwar, S. Pandit, R. Kulkarni, R. Mandavkar, S. Lin, M.-Y. Li, J. Lee, ACS Applied Materials & Interfaces, 13 (2021) 3408.

[159] D.A. Nguyen, H.M. Oh, N.T. Duong, S. Bang, S.J. Yoon, M.S. Jeong, ACS Applied Materials & Interfaces, 10 (2018) 10322.

[160] H. Li, X. Chen, E. Zalnezhad, K.N. Hui, K.S. Hui, M.J. Ko, Journal of Industrial and Engineering Chemistry, 82 (2020) 309.

[161] G.-L. Zhu, C.-Z. Zhao, H. Yuan, B.-C. Zhao, L.-P. Hou, X.-B. Cheng, H.-X. Nan, Y. Lu, J. Zhang, J.-Q. Huang, Q.-B. Liu, C.-X. He, Q. Zhang, Energy Storage Materials, 31 (2020) 267.

[162] X. Zhang, X. Liu, Y. Zeng, Y. Tong, X. Lu, Small Methods, 4 (2020) 1900823.

[163] X. Zhang, X. Zhang, G. Qu, Z. Wang, Y. Wei, J. Yin, G. Xiang, X. Xu, Applied Surface Science, 512 (2020) 145621.

[164] V.B. Kumar, A. Borenstein, B. Markovsky, D. Aurbach, A. Gedanken, M. Talianker, Z. Porat, The Journal of Physical Chemistry C, 120 (2016) 13406.

[165] Y. Hu, Y. Zhao, G. Lu, N. Chen, Z. Zhang, H. Li, H. Shao, L. Qu, Nanotechnology, 24 (2013) 195401.

[166] T. Zhao, X. Peng, X. Zhao, J. Hu, T. Jiang, X. Lu, H. Zhang, T. Li, I. Ahmad, Journal of Alloys and Compounds, 817 (2020) 153057.

[167] W.-W. Liu, Y.-Q. Feng, X.-B. Yan, J.-T. Chen, Q.-J. Xue, Advanced Functional Materials, 23 (2013) 4111.

[168] B. Shen, J. Lang, R. Guo, X. Zhang, X. Yan, ACS Applied Materials & Interfaces, 7 (2015) 25378.

[169] M. Shaker, R. Riahifar, Y. Li, FlatChem, 22 (2020) 100171.

[170] H. Wang, J. Cao, Y. Zhou, X. Wang, H. Huang, Y. Liu, M. Shao, Z. Kang, Nano Research, (2021).

[171] H. Wang, J. Cao, Y. Zhou, Z. Wang, Y. Zhao, Y. Liu, H. Huang, M. Shao, Y. Liu, Z. Kang, Nanoscale, 12 (2020) 17925.

[172] L. Wang, L. Wen, Y. Tong, S. Wang, X. Hou, X. An, S.X. Dou, J. Liang, Carbon Energy, n/a (2021) 1.

[173] M. Wang, Y. Li, J. Fang, C.J. Villa, Y. Xu, S. Hao, J. Li, Y. Liu, C. Wolverton, X. Chen, V.P. Dravid, Y. Lai, Advanced Energy Materials, 10 (2020) 1902736.

[174] D. Hong, Y. Choi, J. Ryu, J. Mun, W. Choi, M. Park, Y. Lee, N.-S. Choi, G. Lee, B.-S. Kim, S. Park, Journal of Materials Chemistry A, 7 (2019) 20325.

[175] Y. Jin, C. Hu, Q. Dai, Y. Xiao, Y. Lin, J.W. Connell, F. Chen, L. Dai, Advanced Functional Materials, 28 (2018) 1804630.

[176] V.C. Hoang, K. Dave, V.G. Gomes, Nano Energy, 66 (2019) 104093.

[177] D. Chao, C. Zhu, X. Xia, J. Liu, X. Zhang, J. Wang, P. Liang, J. Lin, H. Zhang, Z.X. Shen, H.J. Fan, Nano Letters, 15 (2015) 565.

[178] B.N. Jusuf, N.S. Sambudi, Isnaeni, S. Samsuri, Journal of Environmental Chemical Engineering, 6 (2018) 7426.

[179] V. Arul, T.N.J.I. Edison, Y.R. Lee, M.G. Sethuraman, J Photochem Photobiol B, 168 (2017) 142.

[180] A. Bhati, S.R. Anand, D. Saini, Gunture, S.K. Sonkar, npj Clean Water, 2 (2019).

[181] J. Ke, X. Li, Q. Zhao, B. Liu, S. Liu, S. Wang, Journal of colloid and interface science, 496 (2017) 425.

[182] Y.-Y. Chai, D.-P. Qu, D.-K. Ma, W. Chen, S. Huang, Applied Surface Science, 450 (2018) 1.

[183] P. Huo, J. Guan, M. Zhou, C. Ma, X. Liu, Y. Yan, S. Yuan, Journal of Industrial and Engineering Chemistry, 50 (2017) 147.

[184] N. Li, Z. Liu, M. Liu, C. Xue, Q. Chang, H. Wang, 58 (2019) 5746.

[185] A. Bhati, S.R. Anand, Gunture, A.K. Garg, P. Khare, S.K. Sonkar, ACS Sustainable Chemistry & Engineering, 6 (2018) 9246.

[186] W. Li, C. Zhao, Q. Zhang, Catalysis Communications, 107 (2018) 74.

[187] Y. Zhao, Q. Liu, S. Shakoor, J.R. Gong, D. Wang, Toxicology Research, 4 (2015) 270.

[188] M. Havrdova, K. Hola, J. Skopalik, K. Tomankova, M. Petr, K. Cepe, K. Polakova, J. Tucek, A.B. Bourlinos, R. Zboril, Carbon, 99 (2016) 238.

[189] M. Nurunnabi, Z. Khatun, K.M. Huh, S.Y. Park, D.Y. Lee, K.J. Cho, Y.-k. Lee, ACS Nano, 7 (2013) 6858.

[190] N. Parvin, T.K. Mandal, RSC Advances, 6 (2016) 18134.

[191] E.J. Goh, K.S. Kim, Y.R. Kim, H.S. Jung, S. Beack, W.H. Kong, G. Scarcelli, S.H. Yun, S.K. Hahn, Biomacromolecules, 13 (2012) 2554.

[192] P.G. Luo, S. Sahu, S.-T. Yang, S.K. Sonkar, J. Wang, H. Wang, G.E. LeCroy, L. Cao, Y.-P. Sun, Journal of Materials Chemistry B, 1 (2013) 2116.

[193] P.-C. Hsu, Z.-Y. Shih, C.-H. Lee, H.-T. Chang, Green Chemistry, 14 (2012) 917.

[194] F. Wang, Z. Xie, H. Zhang, C.-y. Liu, Y.-g. Zhang, Advanced Functional Materials, 21 (2011) 1027.

[195] J.R. Bhamore, S. Jha, T.J. Park, S.K. Kailasa, Journal of Photochemistry and Photobiology B: Biology, 191 (2019) 150.

[196] D. Wang, X. Mei, S. Wang, J. Li, C. Dong, New Journal of Chemistry, 45 (2021) 3508.

[197] Y. Hu, Z. Yang, X. Lu, J. Guo, R. Cheng, L. Zhu, C.-F. Wang, S. Chen, Nanoscale, 12 (2020) 5494.

[198] K.P. Divya, R. Karthikeyan, B. Sinduja, A. Anancia Grace, S.A. John, J.H. Hahn, V. Dharuman, Biosensors and Bioelectronics, 133 (2019) 48.

[199] R. Guo, B. Chen, F. Li, S. Weng, Z. Zheng, M. Chen, W. Wu, X. Lin, C. Yang, Sensors and Actuators B: Chemical, 264 (2018) 193.

[200] X. Sun, Y. Lei, TrAC Trends in Analytical Chemistry, 89 (2017) 163.

[201] A.I. Robby, S.G. Kim, U.H. Lee, I. In, G. Lee, S.Y. Park, Chemical Engineering Journal, 403 (2021) 126351.

[202] M. Kumari, S. Chaudhary, Colloids and Surfaces B: Biointerfaces, 196 (2020) 111333.

[203] H.O. Othman, F. Salehnia, M. Hosseini, R. Hassan, A. Faizullah, M.R. Ganjali, Microchemical Journal, 157 (2020) 104966.

[204] X. Wang, S. Yu, J. Wang, J. Yu, M. Arabi, L. Fu, B. Li, J. Li, L. Chen, Talanta, 211 (2020) 120727.

Chapter 2

Synthesis of non-toxic Carbon dots from potato for the detection of Cr^{6+} and Fe^{3+} in water samples and bioimaging applications

Sensing and bioimaging

Contents

Graphical abstract

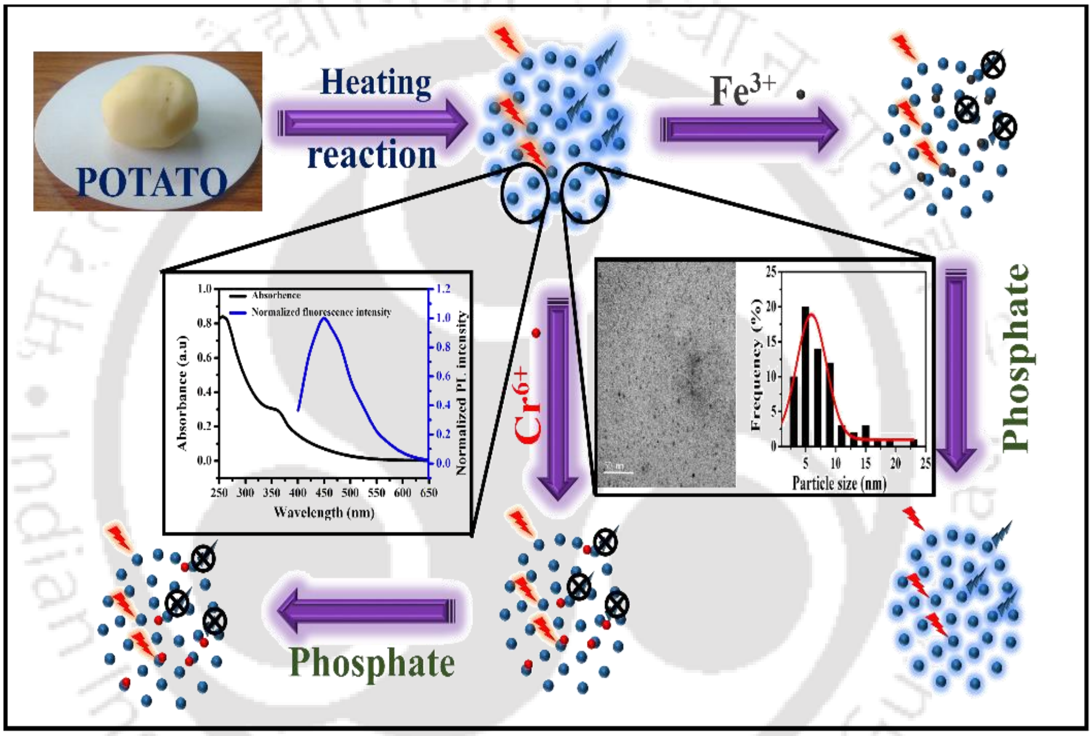

The contents in this chapter have been published as "A Facile Synthesis of Nontoxic Luminescent Carbon Dots for Detection of Chromium and Iron in Real Water Sample and Bio-imaging." **Rupam Sinha**, Anil P. Bidkar, Ravula Rajasekhar, Siddhartha S. Ghosh and Tapas K. Mandal, *Can. J. Chem. Eng.*, 98, 194, 2020. DOI: **10.1002/cjce.23630**

Abstract

In this study, we have reported the synthesis of luminescent carbon dots (CDs) from indigenous potato sources by simple heating reactions. The as-synthesized CDs exhibited an average size of ~ 5.97 nm with a quantum yield (QY) of 6.08%. Furthermore, the CDs possessed high water-solubility, possibly due to the presence of ─COOH and ─OH groups on their surfaces. The quenching of luminescence of the CDs, specifically by Cr^{6+} and Fe^{3+} ions, was used to detect chromium and iron in the water sample. The minimum limit of detection (LOD) for Cr^{6+} and Fe^{3+} ions was found to be 0.012 μM and 0.000549 μM, respectively, in a linear range of 0.5 μM-100 μM and 0.5 μM-5 μM for Cr^{6+} and Fe^{3+}, respectively, which was well below the concentration specified by WHO. We used our sensing system to detect the metal ions in water from the Brahmaputra River as well as in tannery water. In addition, the MTT-based cell viability experiments showed that the CDs were non-toxic within 200 μg/mL. High quantum yield and the easy uptake of CDs enabled the quick labeling of the cytoplasm of the HeLa cells, which can be further attributed to bioimaging applications.

2.1. Introduction

The carbon dot (CD) has been an essential member of the carbon family since the day of its incidental discovery in 2004 [1]. CDs are nanoparticles with an average size of <10 nm. They consist of sp^2 hybridized carbon with a crystalline or amorphous core [2]. The CDs have an oxidized carbon surface with a large number of carboxyl (─COOH) [3] and hydroxyl (─OH) [4] groups along with sp^3 hydrocarbons (─CH_3) [5]. CDs also possess special mellifluous traits such as photoluminescence (PL) [1], low toxicity, water-solubility, high chemical stability, easy functionalization [6], and impressive biocompatibility [7]. These properties have been used extensively in various fields such as electrochemistry, wastewater treatment [8, 9], photocatalysis [10], bioimaging [11-13], light-emitting devices [14], sensing [2, 15, 16], etc.

There are different methods to synthesize CDs, as mentioned in the previous chapter, such as the electrochemical method [17], the hydrothermal method [15], microwave synthesis technique [18-20], simple heating technique [21], etc. The hydrothermal method and the simple heating technique are advantageous and better than other techniques due to the simple preparation process and low energy consumption. These processes enable easy control over chemical reactions. There are several bioresources full of carbohydrates such as starch, polysaccharide, and sugar that can be considered as adequate bio-precursor for CD synthesis. Some bioresources that can be considered for producing low-cost non-toxic CDs are orange juice [3], garlic [22], grape juice [23], and banana juice [4]. Elements like O and H present in the carbohydrate (apart from C element) help to synthesize CDs with −OH and −COOH functional groups. These functional groups are responsible for the extraordinary water-solubility of CDs. There have been several reports about the synthesis of CDs from carbohydrate-rich bioresources. For example, Sk *et al.* [24] showed the presence of CDs in food caramels in their work in 2012. In this work, the authors used, jaggery, a type of locally available bread, and sugar as the precursors for the synthesis of CDs with QY of 1.2%, 0.55%, and 0.63%, respectively. In addition, Zhao *et al*. [22] used a hydrothermal technique to synthesize bi-functional fluorescent CD from garlic and showed its application in bioimaging and free radical scavenging. The synthesized CDs showed a QY of 17. 5%. Mondal *et al*. [25] used lemon juice as the precursor for the synthesis of N doped CDs, which they used as a sensing probe to detect Fe^{3+} in water, and their work reports a detection limit of 140 ppb (2.5 μM). Although a considerable amount of research on the synthesis of CDs from bioresources has been conducted successfully, there are many more bioresources to be discovered for synthesizing CDs with substantial properties.

Apart from bioimaging, CDs have recently been widely used to detect heavy metal ions in water bodies. For example, CDs respectively synthesized from grass [15], bamboo leaves [26], and prawn shells have a greater tendency to detect Cu^{2+} [27]. For Hg^{2+} assaying, CDs from pomelo peel and cucumber have been used [2, 28]. It is also reported that CDs from sweet potatoes and banana peels can be used for Fe^{3+} sensing [11, 29]. CDs can sense Fe^{3+}, Cu^{2+}, and Hg^{2+} due to the presence of hydroxyl groups, amino groups, and carboxyl groups, respectively [30]. The application of CDs as sensing probes is not limited to metal ion assaying. A significant amount of research has been done on detecting molecules, including methylene blue [31], glucose [32], etc., using CDs from bioresources.

Although the detection of different metal ions by CDs has been successfully performed by numerous researchers, a limited number of reports discuss the simultaneous sensitive and selective detection of two different metals using the same CDs. Therefore, in this chapter, we report the simultaneous detection of chromium in the form of Cr^{6+} and iron in the form of Fe^{3+} by using CDs as sensing nanoprobes. We show the selective and sensitive detection of these two ions in the presence of other cations as well as anions. In addition, we synthesized the CDs by a simple heating technique from a potato bioresource. The CDs were also used to detect these two metal ions in a real water system. The chemical composition, cytotoxicity, fluorescence properties, and stability of these CDs were analyzed in detail. The as-synthesized hydroxyl and carboxyl functional group rich CDs with an average size of ~ 5.97 nm manifested adequate stability with storage time and detected a chromium and iron concentration well below the World Health Organization (WHO) recommendation. Further, we used these non-cytotoxic CDs as a bioimaging agent as well.

2.2. Experimental section

2.2.1. Materials

$Al(NO_3)_3 \cdot 9H_2O$, $Zn(NO_3) \cdot 6H_2O$, $CdCl_2 \cdot H_2O$, $Na(NO_3)$, KCl, $K_2Cr_2O_7$, $CaCl_2$, KH_2PO_4, ethanol, and H_2O_2 were purchased from Merck, India. $Co(NO_3)_2 \cdot 6H_2O$, $MnCl_2 \cdot 4H_2O$, $Pb(NO_3)_2$, $NiCl_2$, and $FeCl_2 \cdot xH_2O$ were obtained from Lobachemie, India. $Cu(NO_3)_2 \cdot 3H_2O$, $MgCl_2$, $FeCl_3$, $NaASO_2$, $HClO_4$, $KMnO_4$, and AgCl were procured from SRL Pvt. Ltd., India. Human cervical cancer cells (HeLa) were purchased from the National Centre for Cells Science (NCCS), Pune, India. All of the chemicals were used without further purification. The potatoes were purchased from the local market in Amingaon, Guwahati, India, and were washed with water for further usage.

2.2.2. Synthesis of fluorescent CDs

The fluorescent CDs were synthesized by a simple heating technique similar to that reported by Sk and Chattopadhyay [21]. As in the typical method, 50 g of washed potato was blended with 125 mL of deionized water using a mixer grinder (Samsung, MG 2573) and the mixture was heated at 150°C for 90 minutes with constant magnetic stirring. Then, the potato pulp was removed by simple filtration, and 20 mL of the liquid mixture was mixed with 20 mL ethanol. This mixture was heated at 200°C for 2.5 hours. The remaining material after heating was then dissolved in 20 mL of de-ionized water. Afterward, the solution was filtered again using Whatman filter paper (pore size: 11 µm) to remove the larger particles, and the brownish filtrate was then dissolved in 30 mL of ethanol. This brown CD solution was then centrifuged for 10 minutes at 12 000 rpm to remove the remaining larger particles.

2.2.3. Characterizations

UV-vis spectra of the synthesized CDs were obtained by a UV-vis spectrophotometer (PerkinElmer, Lambda 35). Fluorescent spectra were obtained by a photoluminescent spectrometer (PerkinElmer, LS 45). Field emission transmission electron microscopy (FETEM) images were obtained using a field emission transmission electron microscope (FETEM; JEM, 2100F). For the FETEM analysis, the sample was prepared by putting a dilute CD solution on a carbon coated copper grid and allowing it to dry at room temperature (300 K). The FETEM image was used to calculate the CD particle size distribution by using ImageJ software (version: 1.45 seconds). The Fourier transform infrared (FTIR) spectrum was obtained using an FTIR spectrophotometer (Shimadzu, IRAffinity-1) in the range of 1000-4000 cm^{-1}. The analysis for the different elements was performed using energy dispersive x-ray spectroscopy (Zeiss, sigma; EDX). The fluorescence decay and average fluorescence lifetime were analyzed using a picosecond time-resolved cum steady state luminescence spectrometer (Eddinburg Instruments, FSP920). The cell images were taken using a confocal microscope (Zeiss, LSM 880).

2.2.4. Quantum yield calculation

The quantum yield (QY) of the prepared CDs was calculated by the method used by Goswami *et al*. [33] As in the typical method, the QY of the CDs was determined with a reference fluorescent sample quinine sulphate. The quinine sulphate reference was prepared by dissolving it in a 0.1 M H_2SO_4 solution. The following formula was used to calculate the QY of CDs. Both the reference material and sample material were excited at the same wavelength:

$$QY_S = QY_R \times \frac{A_S}{A_R} \times \frac{Abs_R}{Abs_S} \times \frac{\eta_S^2}{\eta_R^2} \tag{2.1}$$

where QY_R and QY_S denote the quantum yield of reference and sample, respectively; A_S and A_R refer to the area under the emission peak of the sample and reference, respectively at an excitation wavelength of 345 nm at a slit width of 2 nm; Abs_R and Abs_S are the absorbance reading of the reference and sample, respectively; and η refers to the refractive index of the solvent (1.33 for both the sample and reference). The quantum yield (QY_R) of reference (quinine sulphate) was 54%.

2.2.5. Stability of the CDs

The stability of the CDs was examined with respect to the pH of the solvent, the ionic strength of the salt, and the storage time. The PL intensities of the CD solutions were verified at different solvent-pH values, where the pH was adjusted by an H_2SO_4 and NaOH solution. The effect of ionic strength on the emission of the CDs was examined by using different concentrations of NaCl solution (0.1 M-2 M), whereas the effect of storage time was verified by measuring the PL intensity of a 0.5 mg/ml CD solution prepared on day one at different time intervals up to four months.

2.2.6. Cell culture

The HeLa cells were maintained in a CO_2 incubator (5% CO_2) with humidified air. The cells were maintained in a DMEM (Dulbecco's Modified Eagle's Medium) with 10% (v/v) fetal bovine serum and 1% penicillin and streptomycin.

2.2.7. Cytotoxicity test

To study the cytotoxicity of the prepared CDs, an MTT (3-[4,5-Dimethyl-2-thiazolyl]-2,5-diphenyl-2H-tetrazolium bromide) assay was carried out on HeLa (human cervical cancer) cells. Briefly, the HeLa cells were seeded in the 96-well plate (5000 cells/well) and incubated for 24 hours in a CO_2 incubator. After incubation, the cells were treated with a range of CDs concentrations (0 µg/ml–200 µg/ml) for 24 hours. The supernatant containing CDs was discarded and the MTT solution (0.3 mg/ml PBS) was slowly added to each well. After 3 hours of incubation, the MTT was aspirated and 150 µl DMSO was added. The absorbance was measured at 570 nm by a Tecan plate reader.

2.2.8. Bioimaging

HeLa cells at a density of 2×10^5 were grown on a coverslip placed in a 6-well plate. Cells were treated with the prepared CDs at a concentration of 200 µg/ml and were incubated for 4 hours in the CO_2 incubator. After incubation, the cells were washed with PBS to remove the free CDs, fixed with 4% formaldehyde, and observed under the confocal microscope using an excitation laser of 355 nm.

2.2.9. Detection of chromium and iron

As in the typical method, a stock solution of CDs was prepared with a concentration of 0.25 mg/ml. Then, 40 µl of a particular concentration of chromium in the form of Cr^{6+} was added to 5 ml of the CD solution. The final concentration of Cr^{6+} ranged from 0 µM−100 µM. The fluorescence spectra were recorded at an excitation wavelength of 345 nm after 20 min of reaction time at room temperature (300 K). To verify the selectivity towards Cr^{6+}, different metal ions were added to the CD solution with a concentration of 100 µM. Exactly the same procedure was followed for the detection of iron in the form of Fe^{3+} ions. All of the sensitivity and selectivity measurements were performed in triplicate.

2.3. Results and discussion

2.3.1. Optical property of CDs

The optical properties of the CDs were analyzed using UV-vis spectroscopy and fluorescence spectroscopy. Figure 2.1 shows the UV-vis spectra and fluorescence spectra of the CD aqueous solution. In the UV-vis spectra (black line), a continuous increase in absorbance from 600 nm-230 nm and a broad peak at 275 nm are observed. This peak refers to the $\pi-\pi^*$ and $n-\pi^*$ transition of conjugated C═C and C═O bonds. Moreover, this particular peak at 275 nm and the long tail to 600 nm suggest the occurrence of CDs, and they are in accordance with the information provided in previous articles [34-36]. This CD solution also shows a strong PL spectra (blue line) at 450 nm when excited at 345 nm. This peak confirms the fluorescence property of the prepared CDs. Figure 2.2a shows the dependency of the PL intensities of the CD solution on the excitation wavelength. It is observed from the figure that the increase in excitation wavelength from 305 nm-345 nm shows an increase in the emission PL intensity, while the PL intensity begins to decrease along with a further increase in the excitation wavelength, i.e., 365 nm and onwards. In addition, a plot is also shown in figure 2.2b where the redshift of the emission maxima is depicted when the CD solution was excited at different wavelengths ranging from 305 nm−505 nm. The CD solution is exposed to higher energy when it is excited at a lower wavelength, compared to the case when it is excited at a higher wavelength. Therefore, when it gives emission spectra corresponding to its excitation wavelength, we can observe a maxima at a lower emission wavelength for a lower excitation wavelength, and vice versa. This is the probable reason behind the redshift of

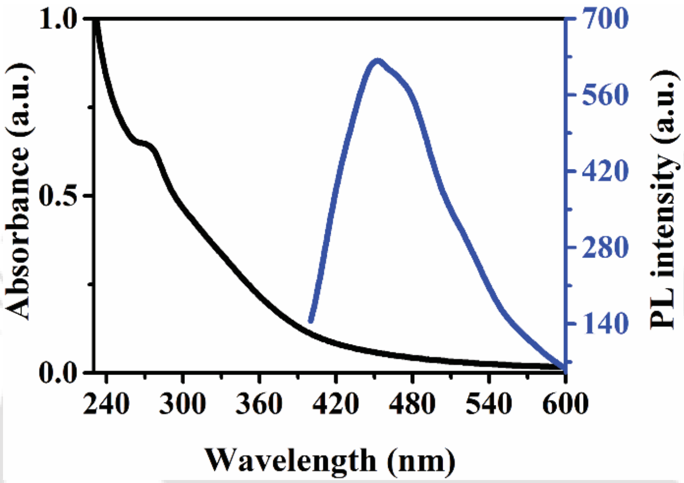

Figure 2.1. UV spectra (black line) and PL spectra (blue line) of CDs in aqueous solution.

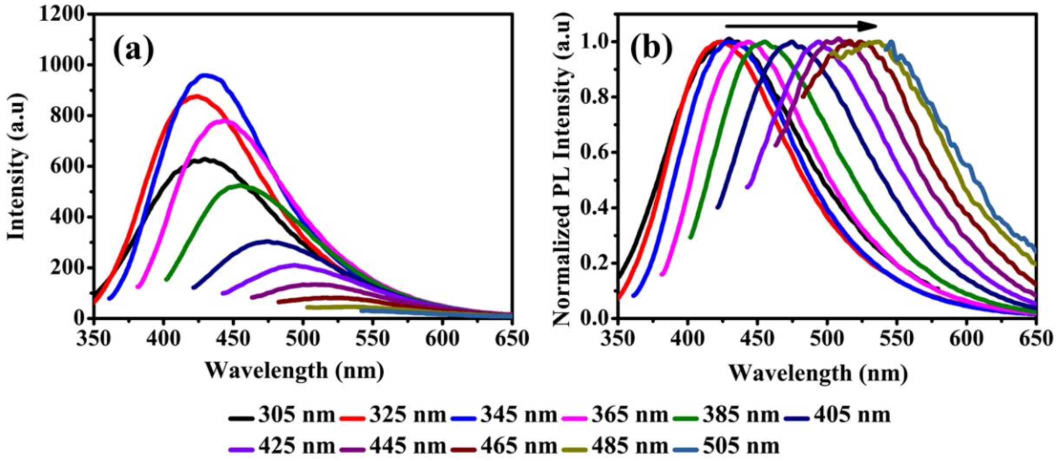

Figure 2.2. (a) Emission spectra of CDs at different excitation wavelengths. (b) Normalized PL spectra.

the emission maxima, although the correct explanation for this redshift is still unknown. The average fluorescence lifetime was calculated, and for our sample, the average lifetime value is 14.22 ns, which is adequate. The fluorescence decay plot is shown in figure 2.3.

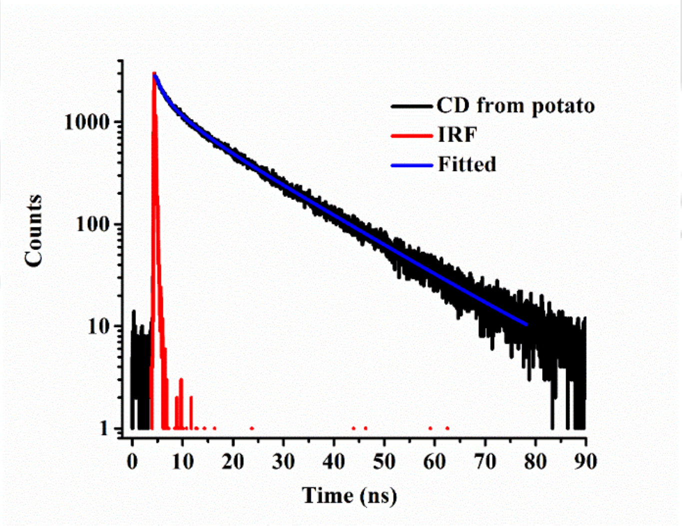

Figure 2.3. Fluorescence decay curve of CD particles.

The fitting equation for the plot of figure 2.3 is as follows,

$$f(t) = A_1 e^{\left(-\frac{t}{\tau_1}\right)} + A_2 e^{\left(-\frac{t}{\tau_2}\right)} + A_3 e^{\left(-\frac{t}{\tau_3}\right)} \tag{2.2}$$

where $f(t)$ denotes the PL intensity at time t, A_1, A_2, and A_3 denote the amplitudes, whereas τ_1, τ_2, and τ_3 represent the PL decay times of each component [37, 38].

In addition, in this study the QY of the prepared CDs have been calculated to be 6.08% using quinine sulphate (QY = 54%) as the reference. In the case of the PL mechanism, Zhu *et al*. [39] postulated two possible theories; one is the defect state emission; and the other is intrinsic state emission.

2.3.2. Characteristics, particle size, and stability of the CDs

Along with the fluorescence characterization, the characterization of the surface functional groups of the CDs was also conducted. For this, an FTIR analysis was

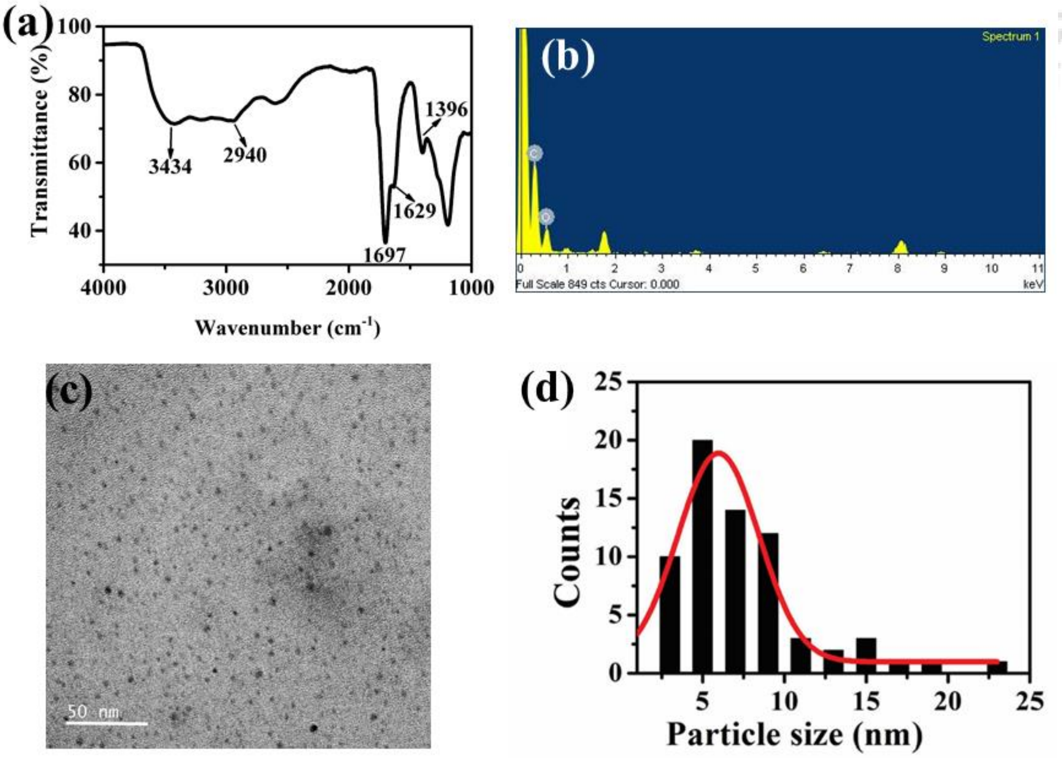

Figure 2.4. (a) FTIR spectrum of CDs. (b) EDX spectra of the prepared CDs. (c) TEM image of CDs, and (d) corresponding particle size distribution.

performed and is shown in figure 2.4a. This figure shows that there are two broad bands at ~3434 cm^{-1} and 2940 cm^{-1}. These two broad bands correspond to the stretching vibration of −OH (due to the presence of −COOH group) and C−H groups. The presenceof peaks at 1697 cm^{-1} and 1629 cm^{-1} are due to the existence of C=O and C=C, respectively. The peak at 1396 cm^{-1} signifies the bending vibration of C−H. All of these results related to the FTIR peaks are in agreement with previous works [11, 35]. An elemental analysis was also conducted on the prepared CD samples. Figure 2.4b shows the EDX spectrum of the CD sample. From this characterization, the presence of element O is confirmed along with element C. The presence of element O is the reason behind the existence of the −OH group and the −COOH group on the surface of the CDs, and because of these two functional groups, the prepared CDs have adequate water solubility. The crystallinity, shape, and size distribution of the particles was studied using an FETEM image of the synthesized CD particles. Figure 2.4c and d show the FETEM image and particle size distribution histogram, respectively. From the FETEM image (figure 2.4c) it is clear that the synthesized CD particles are well separated from each other. This image was further used to obtain the average particle size of the CDs. For this, the FETEM image was imported into ImageJ software to calculate the size of the individual particle as discussed in section 2.2.3, and the overall particle size distribution was plotted. Figure 2.4d shows the size distribution diagram, and it was observed that the CD particles had an average particle size of 5.97 ± 2.47 nm. In this present work, the stability of the synthesized CDs was explored without further purification by stabilizing with additional chemicals. Figure 2.5a shows the PL dependency of the CDs on the pH of the solution. The plot reveals that the PL intensity decreases in either very high (pH 13) or very low (pH 1) pH values of the solution. However, the PL does not change from pH

3–pH 11. The PL emission, controlled by either the surface or the molecular core, is dependent on the pH value of the solution. At a very high or very low pH, the molecular groups are significantly affected [40].

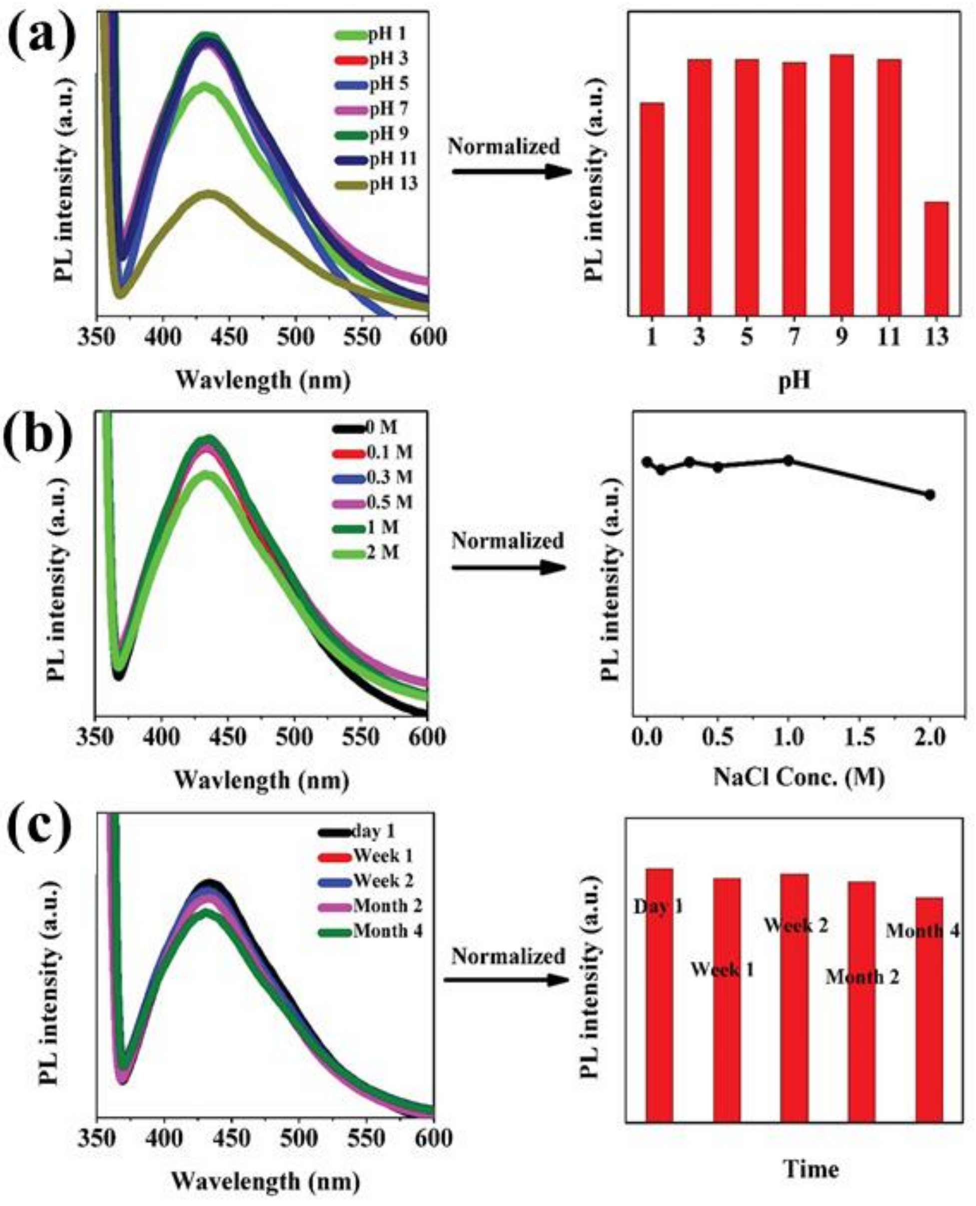

Figure 2.5. Stability plots of CDs: (a) pH dependency of PL intensity of CDs. (b) PL dependency of CDs on the ionic strength (ionic strength was verified at different concentrations of NaCl solution). (c) Effect of storage time of CDs on their PL. For (a) and (b), the error bars represent the SD value considering three different measurements.

Figure 2.5b shows that the PL intensity is not significantly affected by a substantial increase in the ionic strength of the solution. The indication of the non-interference of Cl^- and Na^+ ions is a favourable and desired situation in the present study because the CDs are meant for the detection of iron and chromium in a real water sample, in which the generation of the actual results is important among the many factors that can interfere with the accuracy of the sensing system. The stability of the CDs is shown in figure 2.5c. The PL of the as-synthesized CDs retained their intensity of ~ 89% up to a period of 4 months of storage.

2.3.3. Detection of chromium and iron in water sample

We used the PL property of the CDs to detect chromium in the form of Cr^{6+} and iron in the form of Fe^{3+} ions. Figure 2.6 shows the PL spectra of the blank CD solution and the solution with these two metal ions. From the two plots of figure 2.6, it can be observed that the PL intensity of the CD solution noticeably decreases when the metal ions are added to the solution. From this observation related to the decrease in the PL intensity, it

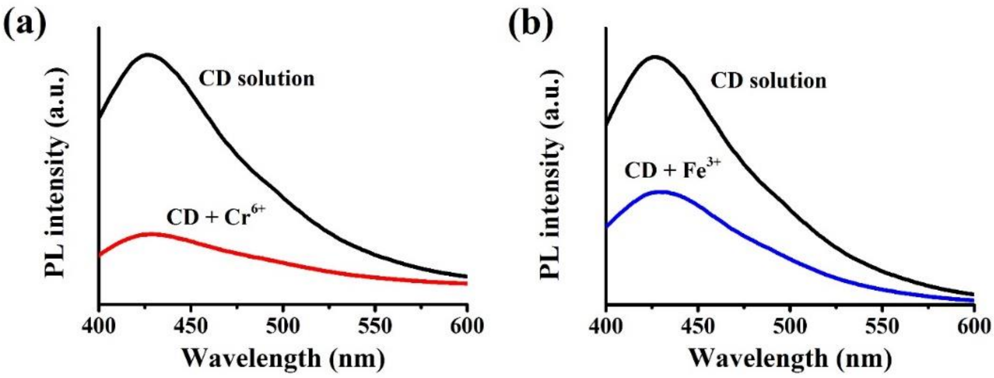

Figure 2.6. (a) PL spectra of CD solution and CD+200 μM Cr^{6+} solution. (b) PL spectra of CD solution and CD+ 200 μM Fe^{3+} solution.

can be inferred that these two metal ions (Cr^{6+} and Fe^{3+}) are capable of effectively quenching the fluorescence of the CDs. This quenching is attained by electron transfer or energy transfer [30, 34]. The sensitivity of the CDs towards these metal ions have also been studied in this work. For chromium, the fluorescence of the CDs with different known concentrations of Cr^{6+} ion ranging from 0 μM−100 μM was investigated. Figure 2.7a shows the PL spectra of the CD solution with different Cr^{6+} concentrations. This figure shows that the PL intensity is decreased with the increase in Cr^{6+} ions at 427 nm. This trend solidifies the fact that the sensing system is sensitive to Cr^{6+} ion concentration. The PL quenching data trails the Stern−Volmer equation. The mechanism

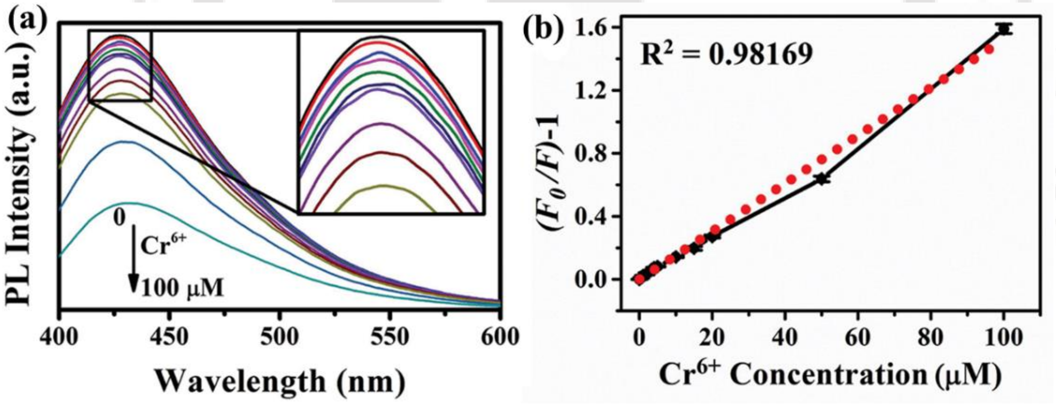

Figure 2.7. (a) PL spectra of the CD solution in the presence of different Cr^{6+} concentrations (from top to bottom: 0, 0.5, 1, 2, 3, 4, 5, 10, 15, 20, 50, and 100 μM). (b) Linearly fitted Stern−Volmer plot for the quenching of PL of CD with Cr^{6+} (excitation wavelength: 345 nm; F and F_0 are the PL intensities of the CD solution at 427 nm in the presence and absence of Cr^{6+}, respectively; the error bars represent the SD value considering three different measurements).

is either static or dynamic, and the equation can be written is as follows:

$$\frac{F_0}{F} - 1 = K_{SV}(M) \quad (2.3)$$

where (M) denotes the metal ion concentration (here, Cr^{6+}); F_0 and F denote the PL intensities of CDs at 427 nm in the absence and presence of chromium in the form of Cr^{6+} ions; and K_{SV} is the Stern−Volmer quenching coefficient. Figure 2.7b shows the Stern−Volmer plot for the Cr^{6+} ions, and it is observed that it shows an adequate linear fit with a correlation coefficient (R^2) of 0.982. In addition, this sensing system detected chromium up to a concentration of 0.012 µM. According to WHO, the acceptable chromium ion (Cr^{6+}) concentration in drinking water should be below 900 nM (0.9 µM) [34], which is easily achievable with the present detection technique. In fact, the present detection limit is quite lower than the acceptance limit specified by WHO. Moreover, the

Table 2.1. Comparison of works for Cr^{6+} detection.

Methods	Linear range (µM)	LOD (µM)	Ref.
g-C_3N_4 fluorescence probe	0.6−300	0.15	[41]
CDs fluorescence sensor	2−180	2.10	[42]
GQD-modified membranes	1−500	0.19	[43]
N,S-CDs fluorescence sensor	0.5−125	0.02	[44]
N-CDs fluorescence sensor	0.01−250	0.005	[45]
P,N-CDs fluorescence sensor	1.5−30	0.023	[46]
wsCQDs	-	0.073	[34]
GQDs fluorescence sensor	0.05−500	0.0037	[47]
CDs sensor from potato	0.5−100	0.012	**Current work**

comparison of LOD for Cr^{6+} reported in the literature, as shown in table 2.1, highlights the superior detection efficiency of the present detection system, besides the work done by Zhang *et al*. [45] and Huang *et al*. [47] Most importantly, the CDs have been used without further purification and stabilization in the proposed technique of the present study.

Different studies have been carried out regarding the quenching mechanism [48]. The quenching of PL due to the presence of Cr^{6+} can be explained as a non-radiative recombination of the electron-hole pair by energy or electron transfer process. This is due to the presence of vacant d orbital and low-lying d-d transition states [49], which ultimately aids the fluorescence quenching of the CDs. A similar procedure was followed to verify the sensitivity of the Fe^{3+} ion. Figure 2.8a shows the PL intensity change of the CD solution at different Fe^{3+} ion concentrations (from 0 μM-100 μM). Figure 2.8b shows

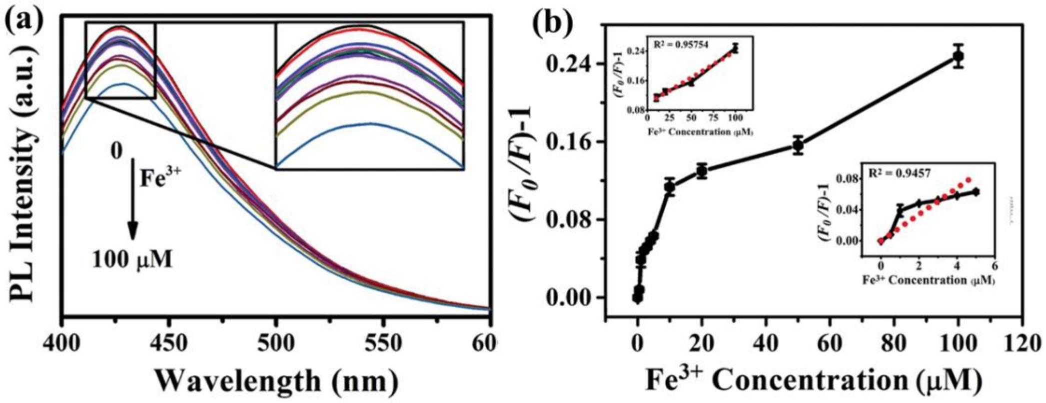

Figure 2.8. (a) PL spectra of the CD solution in the presence of different Fe^{3+} concentrations (from top to bottom: 0, 0.5, 1, 2, 3, 4, 5, 10, 20, 50, and 100 μM). (b) Stern−Volmer plot for the quenching of PL of CD with Fe^{3+}. The top inset shows the fitted curve for data from 10 μM to 100 μM and the inset below shows the fitted curve for data from 0 to 5 μM (excitation wavelength: 345 nm; F and F_0 are the PL intensities of the CD solution at 427 nm in the presence and absence of Fe^{3+}, respectively; the error bars represent the SD value considering three different measurements).

the Stern−Volmer plot for Fe^{3+} to show the quenching of this metal ion, referring to equation 2.3. In this case, (M) represents the concentration of Fe^{3+}, and F_0 and F denote the PL intensities of CDs at 427 nm in the absence and presence of Fe^{3+} ions. This figure shows that the Stern−Volmer plot does not fit linearly over the whole concentration range. Two linear fits are there for two different concentration ranges and these two fits are shown in the insets of figure 2.8b (lower inset: 0 µM−5 µM of Fe^{3+}; upper inset: 10 µM−100 µM of Fe^{3+}). The correlation coefficients (R^2) are 0.95 and 0.96 for concentration ranges 0 µM−5 µM and 10 µM−100 µM, respectively. This indicates that in this sensing system, both dynamic and static quenching may occur. Fe^{3+} has an outer electronic configuration of $4s^23d^5$, which means that it has five half-filled d orbitals in the outer shell. Therefore, when they are added to the CD solution, the excited electrons from the conduction band of CD are transferred to the half-filled 3d orbital of Fe^{3+} and hence a PL quenching takes place [25]. However, when KH_2PO_4 is added to the CD-Fe^{3+} solution, then the PL property of the CD particles returns. This is due to the strong

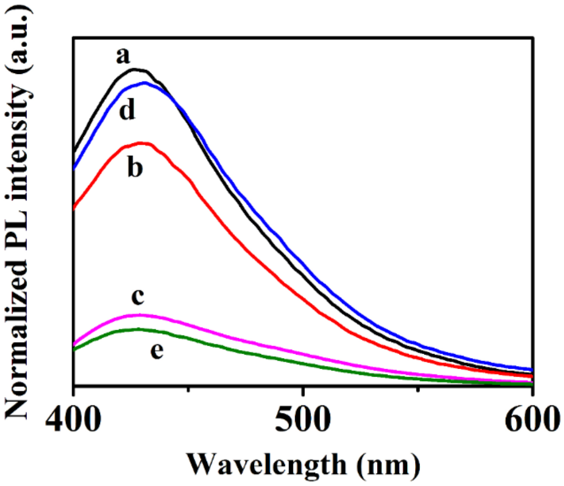

Figure 2.9. Normalized PL spectra of solutions containing only CDs (curve a), CDs-Fe^{3+}mixture (curve b), CDs-Cr^{6+}mixture (curve c), CDs-Fe^{3+}-KH_2PO_4 mixture (curve d), and CDs-Cr^{6+}-KH_2PO_4 mixture (curve e).

affinity of Fe^{3+} towards the phosphate group, which helps the Fe^{3+} to form a complex with the phosphate group by Fe─O─P bonds [50]. The regaining of the PL property of the CD is shown in figure 2.9. The lower limit for Fe^{3+} detection by our sensing system is 0.000549 µM, which is significantly below the limit provided by WHO for Fe^{3+} which is 5.36 µM [11]. A comparative study of LOD of Fe^{3+} with the available methods is shown in table 2.2. The table signals the significant contribution of the present work since it possesses the lowest detection limit among the existing methods. Moreover, we calculated the recovery percentage of the two metal ions by using our sensing system. We used a known concentration (5 µM) of the metal ions in the experiments and then measured the concentrations using our sensing system. The calculated recovery percentages for Cr^{6+} and Fe^{3+} were therefore determined as 104.53% and 89.52%, respectively.

Table 2.2. Comparison of works for Fe^{3+} detection.

Methods	Linear range (µM)	LOD (µM)	Ref.
Chemiluminescent CDs	5−80	0.7	[7]
CDs from sweet potato	1−100	0.32	[11]
CQDs from graphite electrode	10−200	1.8	[17]
CDs fluorescence sensor	1−40	0.87	[42]
C-dots from banana peel	2−16	0.211	[29]
N-doped C-Dots sensor	0.01−500	0.0025	[51]
CDs sensor from potato	0.5−5	0.000 549	**Current work**

2.3.4. Selectivity of the detection method for chromium and iron

To verify the selectivity of the sensing system towards a specific ion, the experiments were repeated with different metal ions, namely Co^{3+}, Mn^{2+}, Cu^{2+}, Mg^{2+}, K^{+}, Ca^{2+}, Ni^{2+}, Cd^{2+}, Al^{3+}, Pb^{2+}, Na^{+}, As^{2+}, Zn^{2+}, and Fe^{2+} under the same conditions. The change in PL intensities in the presence of different metal ions is shown in figure 2.10a. From this figure it can be concluded that a significant PL intensity decay was observed in the cases of Cr^{6+} and Fe^{3+} ions, compared to the other metal ions. Similarly, the PL intensity of the CDs remained unaltered under the influence of other oxidants such as Ag^{+}, MnO_4^- , ClO_4^- , and H_2O_2, as shown in figure 2.10b . This indicates the selectivity of the CDs towards these two ions. Although Fe^{3+} ions are an interference for Cr^{6+} detection and vice versa, this interference can be circumvented by using KH_2PO_4 as a complex forming agent for Fe^{3+}, as discussed in section 2.3.3 and shown in figure 2.9. This phenomenon is helpful to confirm the presence of Fe^{3+} ion in water bodies. For instance, if the synthesized CDs indicate the presence of a metal ion in the water sample, it can either be Fe^{3+} or Cr^{6+} ions. However, with the help of KH_2PO_4 we could determine whether the metal is Fe^{3+} or Cr^{6+}. If the sample shows a PL regain after adding KH_2PO_4, then the presence of Fe^{3+} can be confirmed, and if it does not regain its PL, then the present metal can be confirmed as Cr^{6+}.

This confirmatory test gives an extra edge to this CDs-based sensor over some other reported solid state sensing systems as it makes our sensor able to be used for the selective detection of both Fe^{3+} or Cr^{6+} ions. There are several previously reported articles, which show the selective detection of these two ions by some solid state sensors. For example, Tan *et al.* [52] has fabricated an rGO based chemiresistive sensor for the detection of

Cr^{6+}. Sanchez-Moreno *et al.* [53], and Jin *et al.* [54] also reported the selective detection of Cr^{6+} with a potentiometric and CV-based sensors, respectively. Similarly, sevral reports are there on the solid state sensors based selective detection of Fe^{3+} [55, 56]. However, these reported articles do not account the selective detection of both these ions by the same sensor as we have shown in this work.

2.3.5. Feasibility with real samples

We have verified the feasibility of the prepared CDs for detecting Cr^{6+} and Fe^{3+} in real water samples from the Brahmaputra River, Guwahati, India. With regard to the Brahmaputra water, the collected water sample was first filtered through a 0.2 μm syringe filter to remove the suspended solids. The resultant water samples were used to detect the presence of Cr^{6+}, and the results showed that there was no Cr^{6+} in the Brahmaputra water. Then, the water was used to verify the performance regarding selectivity as well as sensitivity towards the chromium ions in the form of Cr^{6+} of CDs in this complex

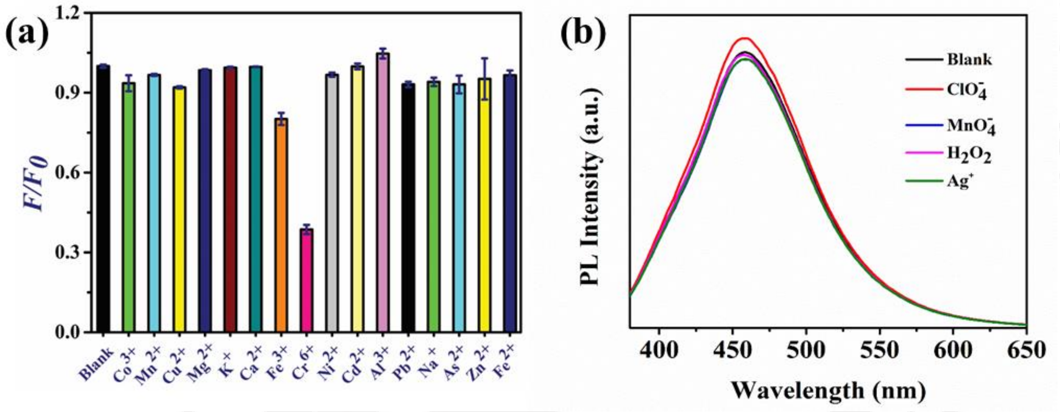

Figure 2.10. (a) The difference in PL intensity of the CD solution with different metal ions (excitation: 345 nm; Metal ion concentration = 100 μM; F and F_0 are fluorescence intensities of CD solution at 427 nm in the presence and absence of ions, respectively; the error bars represent the SD value considering three different measurements). (b) Interaction of the CDs with Ag^+, MnO_4^- , ClO_4^- and H_2O_2.

situation, since the Brahmaputra water carries a significant amount of organic and inorganic matter. For this, the filtered river water was spiked with a standard metal ion solution containing different concentrations of metal ions. Experiments were conducted separately for the Cr^{6+} and Fe^{3+} ions. It was observed that the PL intensity decreased with an increased Cr^{6+} concentration from 0.05 μM−2 μM, shown in figure 2.11a. To determine the concentration of Cr^{6+} in the river water, a calibration curve is also prepared by plotting $(\frac{F_0}{F} - 1)$ vs the concentration of Cr^{6+} in figure 2.11b. A similar procedure was

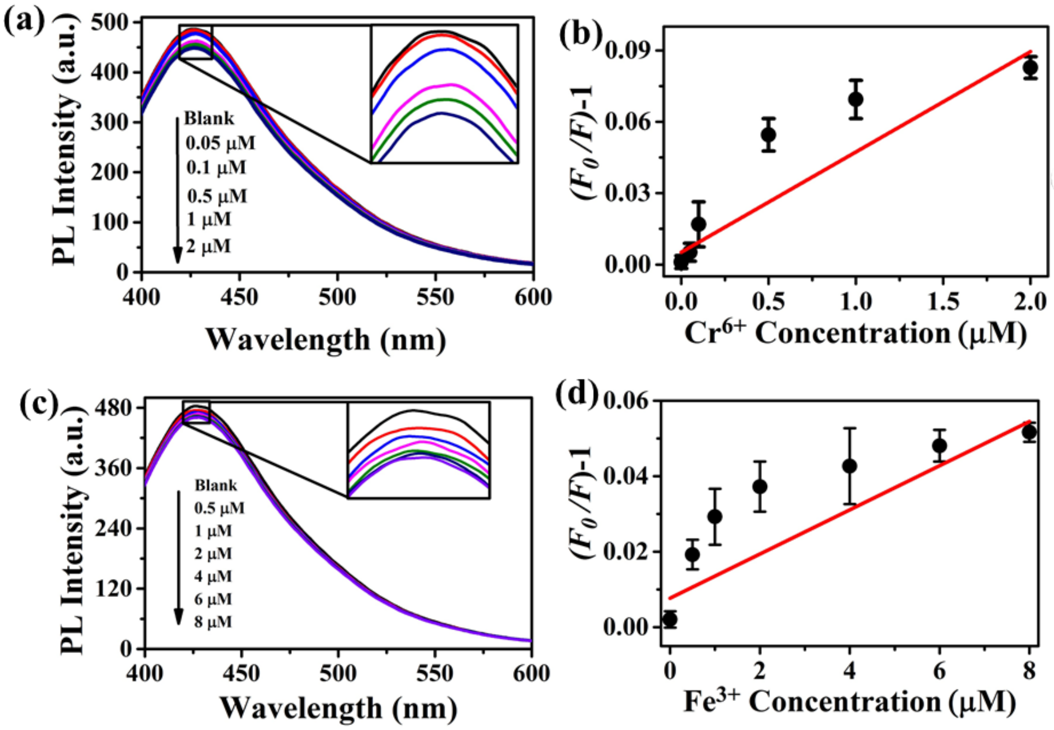

Figure 2.11. (a) PL spectra of CD solution in the presence of different Cr^{6+} concentrations (from top to bottom: 0, 0.05, 0.1, 0.5, 1 and 2 μM) in Brahmaputra river water. (b) Linearly fitted Stern–Volmer plot for the quenching of CD solution PL with Cr^{6+} within the range of 0 to 2 μM. (c) PL spectra of CD solution in the presence of different Fe^{3+} concentrations (from top to bottom: 0.5, 1, 2, 4, 6, and 8 μM) in Brahmaputra river water. (d) Linearly fitted Stern–Volmer plot for the quenching of CD solution PL with Fe^{3+} within the range of 0 to 8 μM (The error bars represent the standard deviation value considering three different measurements).

applied for Fe^{3+}. For the Fe^{3+} ion, the concentration range was from 0.5 μM−8 μM, which is shown in figures 2.11c and d. Although there was interference from different organics and minerals present in the river water, our sensing system could detect the difference between the fresh river water and the water spiked with 0.05 μM of Cr^{6+} and 0.5 μM of Fe^{3+}.

The ability of the sensing probe was further tested to detect chromium ions in tannery water. The tannery water carried Cr^{3+} and its total chromium concentration was measured

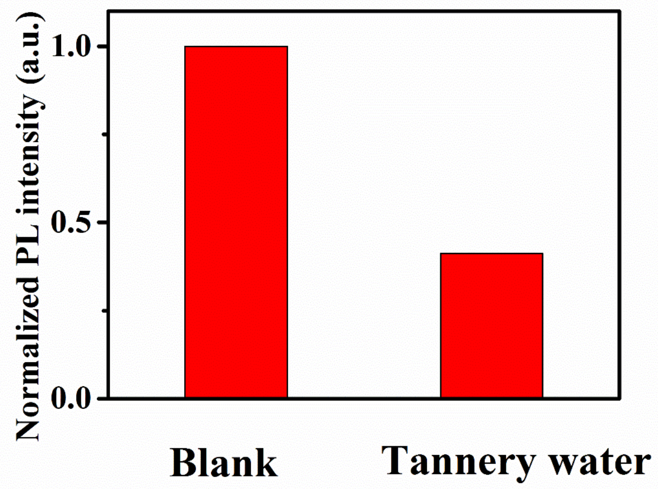

Figure 2.12. Normalized PL intensity plot of blank CD solution and CD solution with oxidized tannery water.

by UV-vis spectroscopy. At first, Cr^{3+} was converted to Cr^{6+} following the standard H_2O_2-UV technique [57], and then our synthesized CD solution was used to detect the oxidized chromium (as Cr^{6+}) ions. The plot in figure 2.12 confirms the detection of Cr^{6+} in the sample by showing a fluorescence decay of ~ 60% after adding the tannery water and also confirms the feasibility of the present technique.

2.3.6. Cytotoxicity and bioimaging

We also verified the toxicity of the as-synthesized CDs and it is shown in figure 2.13. This figure shows the viability of the HeLa cells treated with CDs. From the data it can be observed that CDs are non-toxic and suitable for bio-imaging. Even at a higher concentration of 200 µg/ml the prepared CDs caused the death of only 10% of the cells. This indicates that these CDs are not toxic to HeLa cells and the CDs' characteristics have been used for bioimaging. The non-toxic nature of the synthesized CDs implies that further purification during the synthesis of the CDs is not required at all. Herein, we have studied the imaging-related applications of the CDs on cervical cancer cells (HeLa). Accordingly, the HeLa cells were incubated with the CDs at a concentration of 200 ug/ml for 4 hours in a CO_2 incubator. Thereafter, the fluorescence of the CDs that entered inside the cells was recorded in the confocal laser scanning microscope. The fluorescence image

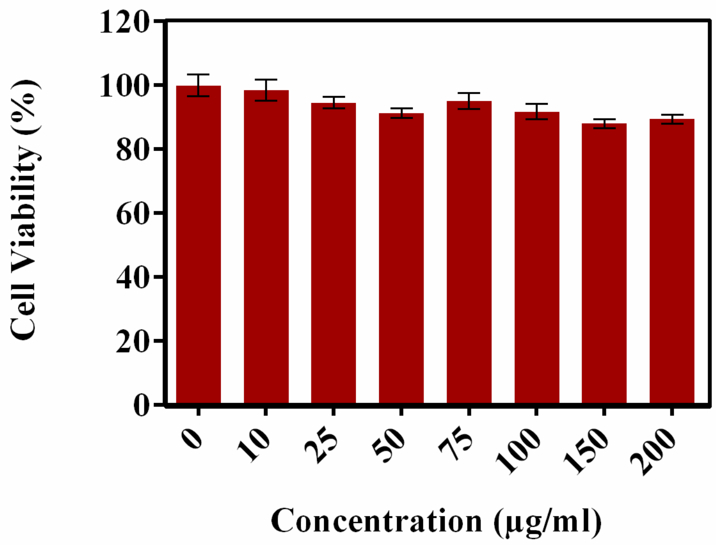

Figure 2.13. MTT-based cytotoxicity test (the error bars represent the SD value considering three different measurements).

(fiigure 2.14) shows that the CDs have been successfully internalized in the cells. The blue fluorescence coming from the cytoplasm of the cells demonstrates that the CDs are localized in the cytoplasm, whereas no fluorescence was seen in the nucleus. It is to be noted that nanodots of sizes <10 nm are easily diffused in the cells [58]. In our study, the entry of the CDs inside the cells is attributed to their small size, which makes it easier to pass through the cell membrane. However, the CDs were not able to pass through the nuclear pores, which is an advantage of this system since it can also be used in live cell imaging without interfering with the nuclear processes. The cytoplasm localization of the CDs confirms their potential use as a cell imaging agent.

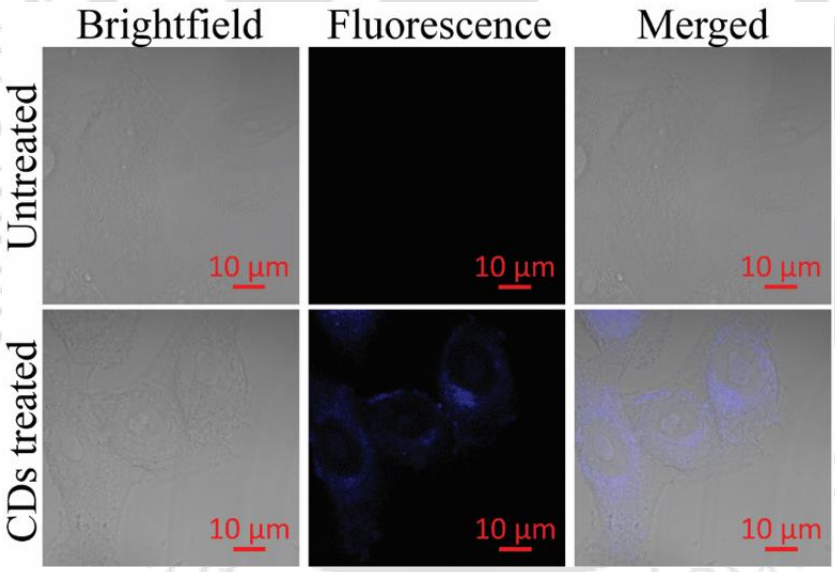

Figure 2.14. Confocal images of HeLa cells. The fluorescence image was obtained at 355 nm wavelength.

2.4. Conclusions

In a nutshell, a facile synthesis of CDs from potato was developed in this work. The synthesized CD particles without further refining and stabilizing showed adequate optical properties with an average diameter of ~5.97 nm. In addition, it was found out that these CDs were water soluble, which may be due to the presence of the functional groups −OH and −COOH that were detected in the FTIR analysis. Thus, the synthesized CDs showed a noticeable fluorescence property with a QY of ~6.08% at 345 nm. The luminescent property of the synthesized CDs was used to detect heavy metals in the water sample and the CDs showed a good selectivity and sensitivity towards Cr^{6+} and Fe^{3+} ions with a detection limit of 0.012 μM and 0.000 549 μM for Cr^{6+} and Fe^{3+}, respectively. To verify the superiority of the technique, the metal detection experiments were carried out in a real water sample from the Brahmaputra River, Guwahati, India, where the above-mentioned two metal ions were detected. A sample of tannery water was also taken to verify the feasibility of our sensing system in the detection of Cr^{6+} and it showed positive results. In addition, MTT-based cell viability experiments revealed CDs as non-toxic within the limit of 200 μg/ml. This non-toxic nature, easy uptake, and the high QY of the synthesized CDs were used for the bioimaging of cells. The success of the present work exists in achieving the high stability, PL tunability, LOD for Cr^{6+} and Fe^{3+}, and non-toxicity and bio-imaging for the HeLa cells from the as-synthesized CDs.

References

[1] X. Xu, R. Ray, Y. Gu, H.J. Ploehn, L. Gearheart, K. Raker, W.A. Scrivens, Journal of the American Chemical Society, 126 (2004) 12736.

[2] W. Lu, X. Qin, S. Liu, G. Chang, Y. Zhang, Y. Luo, A.M. Asiri, A.O. Al-Youbi, X. Sun, Analytical Chemistry, 84 (2012) 5351.

[3] S. Sahu, B. Behera, T.K. Maiti, S. Mohapatra, Chemical Communications, 48 (2012) 8835.

[4] B. De, N. Karak, RSC Advances, 3 (2013) 8286.

[5] H. Guo, B. You, S. Zhao, Y. Wang, G. Sun, Y. Bai, L. Shi, RSC Advances, 8 (2018) 24002.

[6] K. Hola, A.B. Bourlinos, O. Kozak, K. Berka, K.M. Siskova, M. Havrdova, J. Tucek, K. Safarova, M. Otyepka, E.P. Giannelis, R. Zboril, Carbon, 70 (2014) 279.

[7] P. Zhang, Z. Xue, D. Luo, W. Yu, Z. Guo, T. Wang, Analytical Chemistry, 86 (2014) 5620.

[8] C.S. Lim, K. Hola, A. Ambrosi, R. Zboril, M. Pumera, Electrochemistry Communications, 52 (2015) 75.

[9] P.S. Saud, B. Pant, A.-M. Alam, Z.K. Ghouri, M. Park, H.-Y. Kim, Ceramics International, 41 (2015) 11953.

[10] J. Pan, Y. Sheng, J. Zhang, J. Wei, P. Huang, X. Zhang, B. Feng, Journal of Materials Chemistry A, 2 (2014) 18082.

[11] J. Shen, S. Shang, X. Chen, D. Wang, Y. Cai, Materials Science and Engineering: C, 76 (2017) 856.

[12] S.A.A. Vandarkuzhali, V. Jeyalakshmi, G. Sivaraman, S. Singaravadivel, K.R. Krishnamurthy, B. Viswanathan, Sensors and Actuators B: Chemical, 252 (2017) 894.

[13] Y. Song, S. Zhu, B. Yang, RSC Advances, 4 (2014) 27184.

[14] L.-H. Mao, W.-Q. Tang, Z.-Y. Deng, S.-S. Liu, C.-F. Wang, S. Chen, Industrial & Engineering Chemistry Research, 53 (2014) 6417.

[15] S. Liu, J. Tian, L. Wang, Y. Zhang, X. Qin, Y. Luo, A.M. Asiri, A.O. Al-Youbi, X. Sun, Advanced Materials, 24 (2012) 2037.

[16] L. Zhou, Y. Lin, Z. Huang, J. Ren, X. Qu, Chemical Communications, 48 (2012) 1147.

[17] M. Liu, Y. Xu, F. Niu, J.J. Gooding, J. Liu, Analyst, 141 (2016) 2657.

[18] A. Jaiswal, S.S. Ghosh, A. Chattopadhyay, Chemical Communications, 48 (2012) 407.

[19] L. Bu, J. Peng, H. Peng, S. Liu, H. Xiao, D. Liu, Z. Pan, Y. Chen, F. Chen, Y. He, RSC Advances, 6 (2016) 95469.

[20] C. López, M. Zougagh, M. Algarra, E. Rodríguez-Castellón, B.B. Campos, J.C.G. Esteves da Silva, J. Jiménez-Jiménez, A. Ríos, Talanta, 132 (2015) 845.

[21] M.P. Sk, A. Chattopadhyay, RSC Advances, 4 (2014) 31994.

[22] S. Zhao, M. Lan, X. Zhu, H. Xue, T.-W. Ng, X. Meng, C.-S. Lee, P. Wang, W. Zhang, ACS Applied Materials & Interfaces, 7 (2015) 17054.

[23] H. Huang, Y. Xu, C.-J. Tang, J.-R. Chen, A.-J. Wang, J.-J. Feng, New Journal of Chemistry, 38 (2014) 784.

[24] M.P. Sk, A. Jaiswal, A. Paul, S.S. Ghosh, A. Chattopadhyay, Scientific Reports, 2 (2012) 383.

[25] T.K. Mondal, A. Gupta, B.K. Shaw, S. Mondal, U.K. Ghorai, S.K. Saha, RSC Advances, 6 (2016) 59927.

[26] Y. Liu, Y. Zhao, Y. Zhang, Sensors and Actuators B: Chemical, 196 (2014) 647.

[27] G. Gedda, C.-Y. Lee, Y.-C. Lin, H.-f. Wu, Sensors and Actuators B: Chemical, 224 (2016) 396.

[28] C. Wang, D. Sun, K. Zhuo, H. Zhang, J. Wang, RSC Advances, 4 (2014) 54060.

[29] R. Vikneswaran, S. Ramesh, R. Yahya, Materials Letters, 136 (2014) 179.

[30] Y. Guo, L. Zhang, S. Zhang, Y. Yang, X. Chen, M. Zhang, Biosensors and Bioelectronics, 63 (2015) 61.

[31] M. Xue, M. Zou, J. Zhao, Z. Zhan, S. Zhao, Journal of Materials Chemistry B, 3 (2015).

[32] D. Wu, X. Deng, X. Huang, K. Wang, Q. Liu, J Nanosci Nanotechnol, 13 (2013) 6611.

[33] U. Goswami, A. Dutta, A. Raza, R. Kandimalla, S. Kalita, S.S. Ghosh, A. Chattopadhyay, ACS Applied Materials & Interfaces, 10 (2018) 3282.

[34] A. Tyagi, K.M. Tripathi, N. Singh, S. Choudhary, R.K. Gupta, RSC Advances, 6 (2016) 72423.

[35] P. Dubey, S.K. Sonkar, S. Majumder, K.M. Tripathi, S. Sarkar, RSC Advances, 3 (2013) 7306.

[36] S.N. Baker, G.A. Baker, Angewandte Chemie International Edition, 49 (2010) 6726.

[37] R. Sato, Y. Iso, T. Isobe, Langmuir, 35 (2019) 15257.

[38] Y. Li, S. Natakorn, Y. Chen, M. Safar, M. Cunningham, J. Tian, D. Li, Frontiers in Physics, 8 (2020) 576862.

[39] S. Zhu, J. Zhang, S. Tang, C. Qiao, L. Wang, H. Wang, X. Liu, B. Li, Y. Li, W. Yu, X. Wang, H. Sun, B. Yang, Advanced Functional Materials, 22 (2012) 4732.

[40] S. Zhu, Q. Meng, L. Wang, J. Zhang, Y. Song, H. Jin, K. Zhang, H. Sun, H. Wang, B. Yang, Angewandte Chemie International Edition, 52 (2013) 3953.

[41] M. Rong, L. Lin, X. Song, Y. Wang, Y. Zhong, J. Yan, Y. Feng, X. Zeng, X. Chen, Biosensors and Bioelectronics, 68 (2015) 210.

[42] C. Li, W. Liu, X. Sun, W. Pan, J. Wang, Sensors and Actuators B: Chemical, 252 (2017) 544.

[43] P.M. Carrasco, I. García, L. Yate, R. Tena Zaera, G. Cabañero, H.J. Grande, V. Ruiz, Carbon, 109 (2016) 658.

[44] Y. Liu, X. Gong, Y. Gao, S. Song, X. Wu, S. Shuang, C. Dong, RSC Advances, 6 (2016) 28477.

[45] Y. Zhang, X. Fang, H. Zhao, Z. Li, Talanta, 181 (2018) 318.

[46] X. Gong, Y. Liu, Z. Yang, S. Shuang, Z. Zhang, C. Dong, Analytica chimica acta, 968 (2017) 85.

[47] S. Huang, H. Qiu, F. Zhu, S. Lu, Q. Xiao, Microchimica Acta, 182 (2015) 1723.

[48] Q. Wang, X. Liu, L. Zhang, Y. Lv, Analyst, 137 (2012) 5392.

[49] Y. Han, Y. You, Y.-M. Lee, W. Nam, Advanced Materials, 24 (2012) 2748.

[50] J. Xu, Y. Zhou, G. Cheng, M. Dong, S. Liu, C. Huang, Luminescence, 30 (2015) 411.

[51] H. Zhang, Y. Chen, M. Liang, L. Xu, S. Qi, H. Chen, X. Chen, Analytical Chemistry, 86 (2014) 9846.

[52] F. Tan, L. Cong, X. Jiang, Y. Wang, X. Quan, J. Chen, A. Mulchandani, Sensors and Actuators B: Chemical, 247 (2017) 265.

[53] R.A. Sánchez-Moreno, M.J. Gismera, M.T. Sevilla, J.R. Procopio, Sensors and Actuators B: Chemical, 143 (2010) 716.

[54] W. Jin, G. Wu, A. Chen, Analyst, 139 (2014) 235.

[55] Q. Fan, J. Li, J. Wang, Z. Yang, T. Shen, Y. Guo, L. Wang, M.S. Irshad, T. Mei, X. Wang, Journal of Materials Chemistry C, 8 (2020) 4685.

[56] C. Liu, Z. Ye, X. Wei, S. Mao, Electrochemical Science Advances, n/a e2100137.

[57] D.L. Rodman, N.A. Carrington, Z.-L. Xue, Talanta, 70 (2006) 668.

[58] W. Shi, X. Li, H. Ma, Angewandte Chemie International Edition, 51 (2012) 6432.

Chapter 3

N-doped carbon dots from cigarette-tobacco: Picric acid sensing in real water sample and synthesis of CD-MWCNT nanocomposite for UV-photodetection

Sensing and optoelectronics

Contents

Graphical abstract

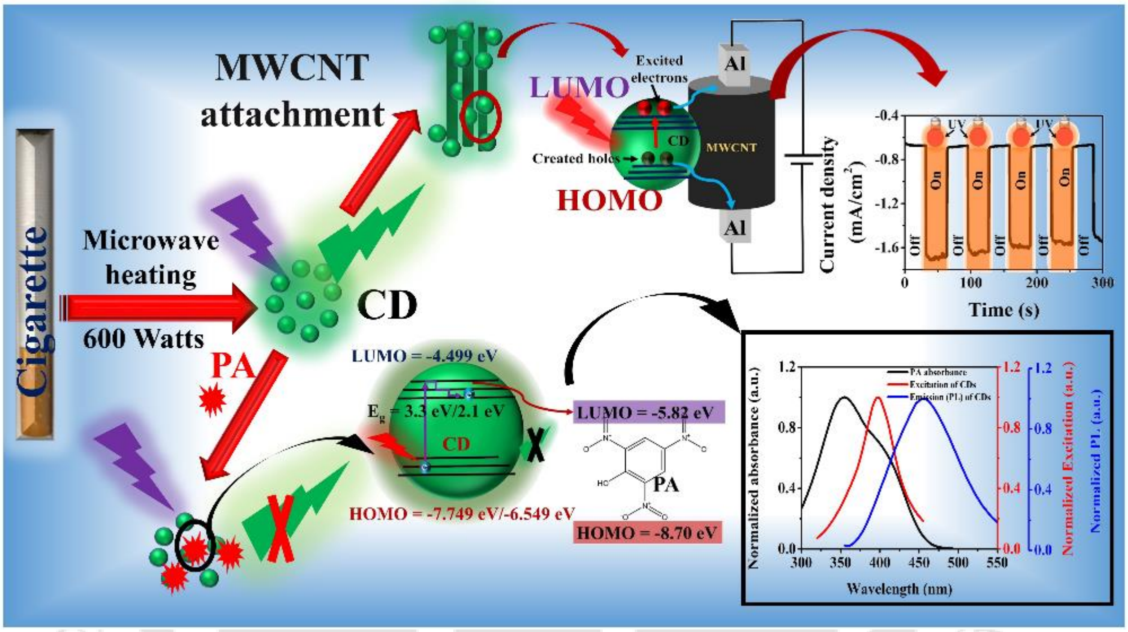

The contents in this chapter have been published as "N-doped Carbon Dot from Cigarette-Tobacco: Picric Acid Sensing in Real Water Sample and Synthesis of CD-MWCNT Nano-Composite for UV-Photodetection." **Rupam Sinha**, Nirmal Roy, Ravula Rajasekhar, Aabhas Karnawat and Tapas K. Mandal, *J. Environ. Chem. Eng.*, 9, 104971, 2021. DOI: **10.1016/j.jece.2020.104971**

Abstract

Carbon dots (CDs) are one of the most valuable nanomaterials in the recent world because of their diversity in applications. This chapter reports the applications of N-doped CDs in photoluminescence (PL) based picric acid (PA) sensing and the synthesis of CD- multi-walled carbon nanotubes (MWCNT) nanocomposite for UV-photodetection. The CDs were synthesized from cigarette-tobacco by a single-step microwave-assisted heating technique. The detailed characterizations of the synthesized CDs have been performed as well. These synthesized CDs showed an average particle size of 2.8 ± 1.04 nm with a quantum yield (QY) up to ~9.98%. The calculated detection limit (LOD) for PA-sensing was 32.1 ppb, which is relatively low compared to the reported literature considering a wider linear range of concentration (0.1–50 µM). The sensing mechanism is also discussed in detail. This sensing ability was then successfully tested to detect PA acid in real water samples, which showed a good recovery percentage with a minimal deviation of ± 10%. For the second application, the CDs were attached with (MWCNTs) to synthesize a novel UV-photoresponsive CD-MWCNT nanocomposite. The photocurrent-generation and the mechanism of electron transfer through the nanocomposite have been discussed with detailed explanations. The transient photo-response of the nanocomposite has also been presented. This transient response was used to calculate the rise and decay time of the system, and the observed values are of 0.38 and 0.42 s, respectively. Therefore, the ability of the CDs to be used in different areas of applications has opened up a vast range of scopes for the researchers.

3.1. Introduction

The photoluminescence-based (PL-based) sensing of heavy metals (Cr^{6+}, Fe^{3+}) by carbon dots (CDs) is reported in detail in the previous chapter. However, the PL-based sensing application of CDs is not limited to detect heavy metals in water samples. The quenching of PL of the CDs in the presence of several quenchers is further explored by scientists to detect numerous explosive materials such as trinitrophenol (TNP), nitrobenzene (NB), trinitrotoluene (TNT), 2,4,6-trinitrophenol (TNP), etc. These materials are considered as some of the significant components of industrially prepared explosive materials. These compounds create environmental hazards by contaminating the water bodies and soil. Amongst these nitroaromatic compounds, 2,4,6-trinitrophenol (TNP), also known as Picric Acid (PA), is most explicitly used in glass, fireworks, dyes, and leather industries [1]. Therefore, the detection of PA has become a vital task among the research fraternity for environmental wellness. Although several other materials have also been tested to detect PA [2, 3], scientists have always favored CDs because of their low toxicity and easy synthesis techniques.

There are numerous methods to synthesize CDs, such as hydrothermal method [4], microwave assisted synthesis technique [5], electrochemical process [6], laser ablation [7], ultrasonic [8], solvothermal process [9], etc. as mentioned in the previous chapters. Among these techniques, the hydrothermal method is most widely used, and it produces high quantum yield (QY) CDs. However, the microwave assisted synthesis technique also has some advantages over the hydrothermal technique. It helps to synthesize CDs in a single step, making this the most time-efficient method. Jaiswal *et al.* [5] used this technique to get CDs from PEG and utilized them in bioimaging applications. Liu *et al.* [10] prepared wavelength-tunable photoluminescent CDs following microwave assisted synthesis technique and used the CDs as PL-based Co^{2+} sensors. Moreover, apart from the applications of CDs in bioimaging and PL-based sensing, they have been used in photodetection as well. For example, Subramanian *et al.* [11] made a photoresponsive hybrid by attaching graphene quantum dots with perovskite, which showed a high detectivity and responsivity of 6.5×10^{11} Jones and 12 A/W, respectively. On the other hand, Chen *et al.* [12] reported the synthesis of CD-coupled graphene/silicon heterojunction, which showed an enhancement in photoresponsivity by 4.3%.

Another noteworthy nanomaterial that has already gained popularity in the research fraternity is carbon nanotubes (CNTs). These CNTs have been used extensively in supercapacitors and actuators [13], electronics devices as field emission sources [14], sensors [15, 16], etc. Not only this, CNTs have also been used as fillers as well to make different nanocomposites. The objective of incorporating CNTs with other materials is to improve their electrical, mechanical, and thermal properties. There are some reports where CNTs have been integrated with some inorganic quantum dots. For example, Juarez *et al.* [17] reported on the non-covalent attachment of CNT with CdSe nanoparticles to show the change in the morphology of CdSe nanoparticles in the presence of the CNTs. Kim and Park [18] also reported the synthesis of a nanocomposite by attaching CNTs with CdS nanoparticles, and they used this composite as a photocatalyst to synthesize H_2 from water. There have been very few reports on the attachment of CNTs with CDs, although the composite of CNTs with inorganic quantum dots has been reported numerously. Yu *et al.* [19] reported on the electron transfer mechanism in CDs-graphene oxide nanocomposite in their work without exploring the potential applications of the nanocomposite. They showed the attachment of CDs with CNTs also in this work. They also did not report the potential side of photodetection by the composite material in their work.

The aforementioned discussion shows that a very limited amount of work is there, which has reported the utilization of CDs, synthesized from the same precursor material in the fields of photodetection as well as PL-based sensing. In this chapter, we have reported the applications of N-doped CDs, synthesized from cigarette-tobacco, in two different fields simultaneously. One of them is the PL-based sensing of PA in water bodies, and the other is to use the CDs to synthesize UV-responsive CD-multi walled carbon nanotube (MWCNT) nanocomposite. For the study of PL-based sensing of PA, the quenching mechanism has also been presented with appropriate shreds of evidence. This PA sensing ability of the CDs in water bodies has further been explored to detect PA in real water samples (tap water and Brahmaputra water). On the other hand, in the case of the synthesis of the UV-responsive nanocomposite, the CDs were attached with MWCNTs. The photocurrent generation through this nanocomposite has been presented along with a detailed mechanism. The electronic transfer through the nanocomposite has also been reported with a comprehensive explanation.

3.2. Experimental section

3.2.1. Materials

$Al(NO_3)_3{\bullet}9H_2O$, $CdCl_2{\bullet}H_2O$, $Na(NO_3)$, KCl, $CaCl_2$, ethanol, methanol, acetone, acetonitrile, iso-propanol, o-nitrotoluene (O-NT), 4-nitrophenol (4-NP), 2,4-dinitrophenol (DNP), Ethylenediamine (EDA; 98%), and carboxyl group functionalized

MWCNT (>8% carboxylic acid-functionalized, avg. dia × L: 9.5 nm × 1.5 µm) were purchased from Merck, India. $Co(NO_3)_2 \cdot 6H_2O$, $Pb(NO_3)_2$, $FeCl_2 \cdot xH_2O$, $NiCl_2$, PA were obtained from Loba Chemie, India. $Cu(NO_3)_2 \cdot 3H_2O$, $MgCl_2$, $FeCl_3$, AgCl, and $NaAsO_2$ were procured from SRL Pvt. Ltd. India. The silicon wafer was procured from University Wafer, USA. All the chemicals used were of reagent grade and were used without additional purification. The experiments were carried out using DI water unless and until mentioned otherwise.

3.2.2. Synthesis of fluorescent CDs

A simple one-step microwave assisted heating technique was used to synthesize the photoluminescent N-doped CDs from the cigarette [20]. The schematic representation of the synthesis steps is shown in scheme 3.1. In a typical method, the nicotine-containing tobacco material of the cigarette was grounded using a mortar, then 1.14 g of the grounded material was added to 22 ml of DI water. Then this mixture was heated with the help of a microwave at 600 watts for 1 min. A dark blackish-brown colored solution was produced. After that, 10 ml of water was further added to the mixture solution. Then the mixture was filtered through a 0.2 µm syringe filter. This solution was lyophilized for 16 h to get the CDs in powder form. The picture of the CD solution under visible and UV light is shown in the inset of scheme 3.1. For obtaining CDs with higher QY, we used ethylene diamine (EDA) during the synthesis process. The same procedure was followed in this case as well. The only additional part was the addition of a different amount of EDA (0, 50, 150, and 300 µl) to the water-tobacco mixture before heating in the microwave.

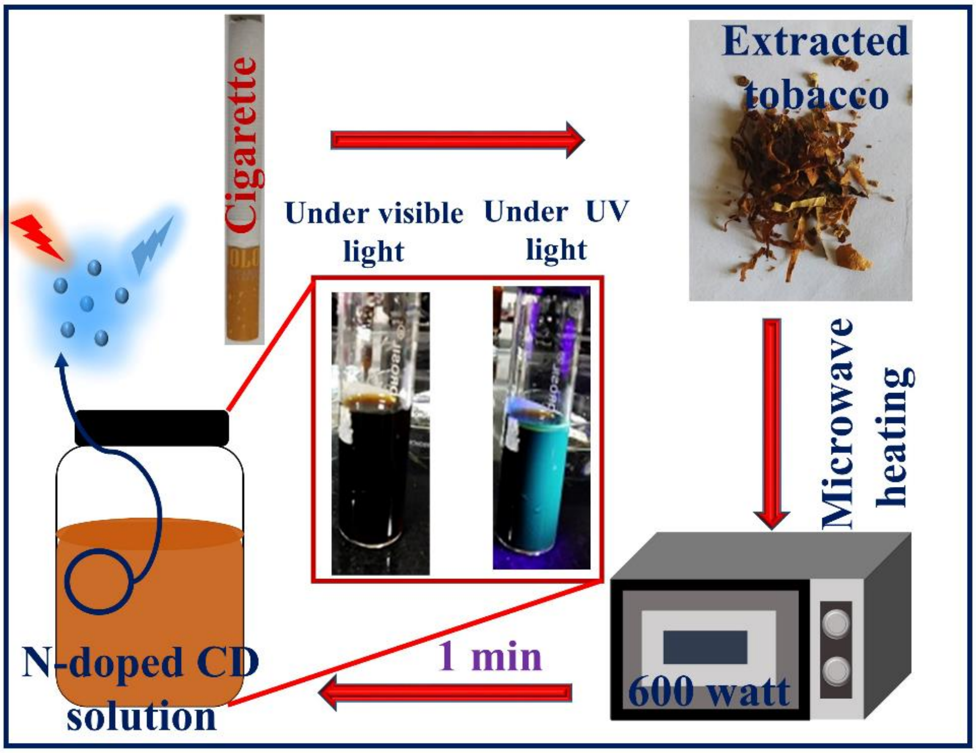

Scheme 3.1. Schematic representation of the synthesis steps of the CDs. The photographs of the CD solution in the presence and absence of UV light are shown in the inset.

3.2.3. Synthesis of CD-MWCNT nanocomposite

Oxidized MWCNT was used to synthesize the CD-MWCNT nanocomposite. In a typical process, 0.5 mg of oxidized MWCNT was dispersed in 1 ml of 30 mg/ml CD solution, in which a 100 µl of Nafion solution (5%) was added further. This mixture solution was then ultrasonicated for 45 min, followed by a rigorous mixing of 10 min. This mixture solution was kept for 16 h at room temperature before separating the nanocomposite by using centrifugation.

3.2.4. Device fabrication and photoresponse measurement

To show the photoresponsive properties of the nanocomposites, we have developed a conductive device. In a typical process, a silicon wafer with a thermally grown oxide layer (300 nm) was used as a substrate. The fabrication of the device was done by a simple two-step process. The steps are schematically shown in figure 3.1a. Firstly, the aluminium (Al) electrodes were deposited on the substrate by the thermal evaporation technique. Secondly, the composite material (CD-MWCNT) was drop-casted on the channel area (between the two electrodes, as shown in the figure) of the device and let dry. A photograph of the device is also shown in figure 3.1b. The device was then connected to a probe station. The photoresponse of the device was measured using a semiconductor characterization system (Keithley 4200-SCS) in the presence and absence of different UV light source.

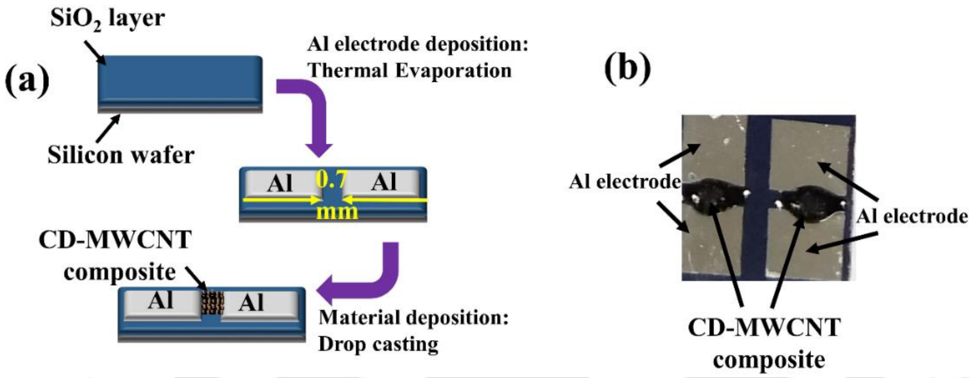

Figure 3.1. (a) Schematic representation of the fabrication of the conductive device. (b) Photograph of the device.

3.2.5. Characterization of the CDs and the CD-MWCNT nanocomposite

UV-vis spectrophotometer (PerkinElmer, Lambda 35) was used to obtain the UV-vis spectra of the synthesized CDs. PL spectra were attained using a photoluminescent spectrometer (PerkinElmer, LS 45). X-ray photoelectron spectroscopy (XPS) analysis was done to get the composition near the surface of the CDs using X-ray photoelectron spectroscopy. PHI 5000 Versa Probe II, FEI Inc. spectrometer was used to get the XPS data. The binding energies of all the elements were calibrated by fixing the C1s peak at 284.6 eV, and the peaks were resolved using XPSPEAK Version 4.1 software. A field emission transmission electron microscope (FETEM; JEM, 2100F) was used to get the FETEM images of the synthesized CDs and the nanocomposites. The selected area electron diffraction (SAED) pattern of the CDs was also obtained by using this instrument. To get the FETEM images, the samples were drop-casted on a carbon-coated copper grid and allowed to dry at room temperature for 24 h. The average particle size of the CDs was calculated by using Image J (version: 1.45s) software from the FETEM image of the CDs. The PL decay curve and average PL lifetime of the synthesized CDs and the nanocomposites were obtained by using Picosecond time-resolved cum steady-state luminescence (TRPL) spectrometer (Eddinburg Instruments, FSP920). Raman spectrophotometer (Horiba LabRam HR Evolution) was used to characterize the attachment of the CDs on the surface of MWCNTs.

3.2.6. Calculation of Quantum yield (QY)

The quantum yield (QY) was calculated using equation 2.1, as given in chapter 2.

3.2.7. Detection method of PA

In a typical method, a CDs solution of a concentration of 0.5 mg/ml was prepared as a stock solution. 5 ml of the CD solution from the stock was collected separately in different culture tubes where 40 μl of varying concentrations of PA were added. The overall concentrations of PA were in the range of 0 to 100 μM. The excitation wavelength used to get the PL spectra was 365 nm. The reaction between PA and the CDs was carried out for 20 min at room temperature. The sensing system's selectivity was also examined by checking the impact of other different quenching materials (different heavy metals and other organic compounds like methanol, acetonitrile, etc.) on the PL intensity of the CD solution. In this case also, the samples were prepared in a similar method, and the overall concentration of the interfering material in the CD solution was kept at 200 μM. All the sensitivity and selectivity measurements were performed in triplicates.

3.2.8. Stability tests of the CDs

The stability tests of the synthesized CDs were also performed. The effect of solvent pH, the CDs' storage time, and the solvent’s ionic strength were the tested parameters to check the stability of the synthesized CDs. The pH of the solvent was adjusted using NaOH and H_2SO_4 solution, whereas the ionic strength was examined by using different concentrations of NaCl solution (0.05 M to 1 M). The stability of the CDs with storage time was checked by taking the PL reading of a CD solution (0.5 mg/mL) at different times up to 18 weeks.

3.3. Results and discussion

3.3.1. Optical properties of CDs

UV–Vis and PL spectroscopy have been carried out to understand the optical properties of the synthesized CDs. The UV–vis spectrum and PL spectra have been shown in figure 3.2. In figure 3.2a, the black line corresponds to the UV–vis spectrum of the CDs ranging from 220 nm to 600 nm, whereas the blue line depicts the PL spectrum of the CDs at an excitation wavelength of 360 nm. A little hump-like peak at 260 nm in the UV–vis spectrum is observed. This peak at 260 nm can be ascribed as the overlapping of spectra caused due to the n$-\pi^*$ and $\pi-\pi^*$ electronic transitions of conjugated C=O and C=C bonds [21-23]. Moreover, the broadening of the peak can be due to the presence of π-π^* transition of C=C along with the n-π^* transition of C=O . In this plot, it is also observed that the UV–vis spectrum is extended till 600 nm as a long tail, which also confirms the formation of CDs, and this accords with some of the previous reports [24]. The PL property of the CDs was also examined. The blue line in figure 3.2a shows the emission maxima of the CDs at 457 nm wavelength when excited at 360 nm. Thus, it confirms the presence of the PL property in the synthesized CDs. The PL property of the CDs has been further tested to obtain the optimum excitation wavelength. For that, the CD solution was excited at different wavelengths ranging from 280 nm to 440 nm. The plots are shown in figure 3.2b, and it is observed from the figure that the maximum PL intensity was obtained at an excitation wavelength of 360 nm. In the case of PL spectra, the emission wavelength remained almost the same at 457 nm when excited with a wavelength in the range of 280–380 nm, and also, the emission maxima were observed at an excitation wavelength in the UV spectral region. This indicates that the PL property of the CDs was dominating in the UV domain. However, the PL intensity got decreased and red-shifted when the excitation wavelength was varying from 400 nm to 440 nm. Various sorts of double bond conjugation of different degrees in the CDs can be the probable reason behind this PL behavior [25]. The PL intensity can be modified using a surface passivator like EDA. The change in the PL maxima of the N-doped CDs in the presence of different dosage amounts of EDA during the synthesis is shown in a plot between normalized PL intensity and emission wavelength in figure 3.2c. It is observed in this figure that the emission maxima get redshifted with the addition of EDA. This can be ascribed as the existence of multi emission centres [26] due to the influence of the additional doping agents. To get a clearer picture, we have deconvoluted the normalized PL spectra and represented in figure 3.3. The peaks present in the range of ~410 nm can be attributed to the presence of a zigzag edge state in the synthesized CDs [27]. The peaks in the range of ~440–460 nm are observed due to the N-doping in the CDs [26]. Interestingly, the zigzag edge state gets a little prominent when EDA is added to the precursor material, as observed in figure 3.3b and c. However, this zigzag effect gets minimized when further EDA is added (figure

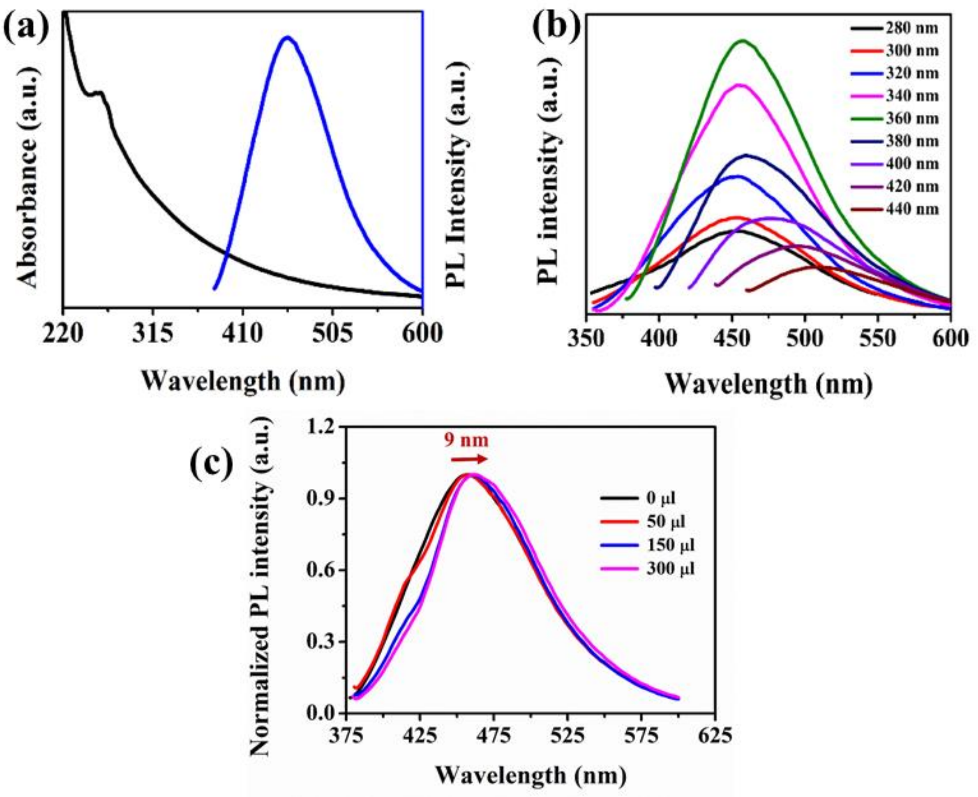

Figure 3.2. (a) UV–vis absorption peak (black line) and PL emission spectrum (blue line) of aqueous CDs solution. (b) Various excitation wavelength-based PL spectra of the CDs. (c) Normalized peaks of PL intensities of the CDs with different EDA dosage ($\lambda_{ex} = 360$ nm).

3.3d). Moreover, based on our XPS investigation (discussed later), the presence of peaks in the range of ~450 nm and ~460 nm are due to the recombination of the electron and hole at C−N [26] and the peaks at ~490 nm can be attributed to the presence of C−OH [27]. Therefore, the increment in the QY with the increase in the dosage of EDA can also be attributed to the addition of functional groups. The gap energy and highest occupied molecular orbital-lowest unoccupied molecular orbital (HOMO-LUMO) energy

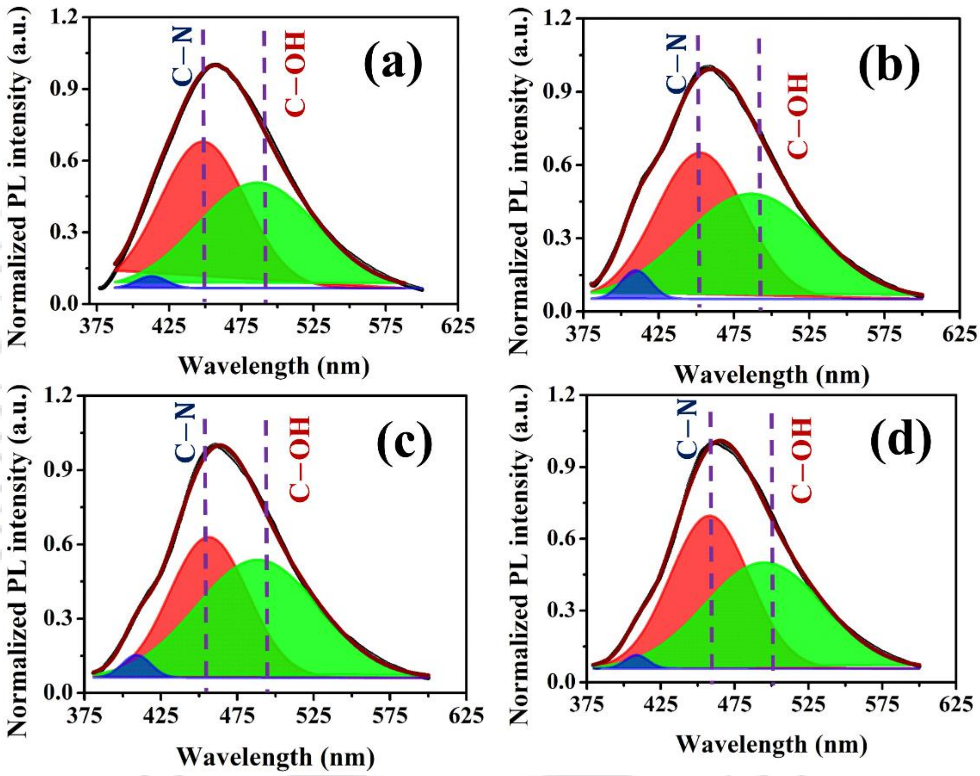

Figure 3.3. Deconvoluted peaks of normalized PL intensities of the CDs with different dosages of EDA ((a) 0 µl, (b) 50 µl, (c) 150 µl, and (d) 300 µl).

levels of the synthesized CDs were also calculated. UV–vis spectrum (figure 3.2a) was used to get the Tauc’s plot (figure 3.4a,b) for gap energy calculation, whereas the HOMO-LUMO energy levels were estimated using cyclic voltammetry (CV) measurement (figure

3.4c). In the CV curve, one reduction peak is observed at -0.241 V. For calculations of the HOMO-LUMO levels, the following equations have been utilized [28, 29]:

$$E_{LUMO} = -(E_{red} + 4.4 + 0.34)\ \text{eV} \tag{3.1}$$

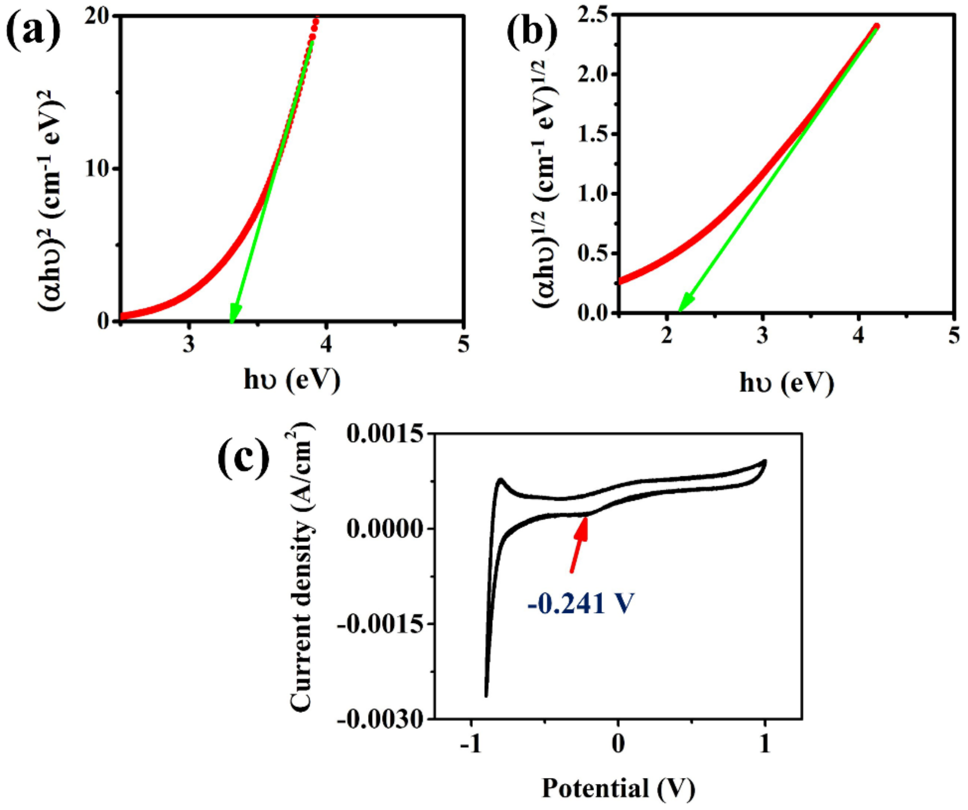

Figure 3.4. (a) $(\alpha h\vartheta)^2$ vs. $h\vartheta$ and (b) $(\alpha h\vartheta)^{1/2}$ vs $h\vartheta$ plot of the synthesized CDs, (c) CV curve of 0.5 mg/mL CD solution in 0.1 M KCl solution (vs. Ag/AgCl).

$$E_{HOMO} = \left(E_{LUMO} - E_g\right)\ \text{eV} \tag{3.2}$$

where, E_{LUMO} and E_{HOMO} denote the energy levels of LUMO and HOMO, respectively. E_{red} implies reduction potential obtained against a saturated calomel electrode (SCE) and E_g corresponds to the energy gap of the CDs, which was calculated by using Tauc's equation as given below [30],

$$(\alpha h\vartheta)^{1/n} = A(h\vartheta - E_g) \tag{3.3}$$

where, α is the absorption coefficient, $h\vartheta$ is the incident photon energy, whereas A is a constant that depends on the transition probability. n is dependent on the type of electronic transition. When the value of n is ½, the transition is a direct allowed transition, and for the case of indirect allowed transition, the value of n becomes 2. Figure 3.4a,b represent the plots of $(\alpha h\vartheta)^{1/n}$ vs $h\vartheta$ for n = 1/2 and n = 2 respectively. In these plots, the linear regions were extrapolated to the x-axis to get the gap energy values. From the figure, the obtained gap energy values were 3.3 eV and 2.1 eV for direct and indirect bandgap, respectively; the HOMO and LUMO levels were also calculated with the help of equations 3.1 and 3.2. The calculated LUMO energy level is -4.499 eV, whereas the HOMO energy level is calculated to be -7.749 eV for the direct gap and -6.549 eV for the indirect gap.

3.3.2. Surface characteristics and stability of the CDs

The surface characteristics of the CDs were identified by XPS experiments, and the XPS spectra are shown in figure 3.5. The full scan spectrum (figure 3.5a) specifies the existence of C1s, N1s, and O1s in the synthesized CD. The peaks at 284.6 eV, 398.2 eV, and 532.8 eV in this overall spectrum can be interpreted as the peaks for C1s, N1s, and O1s, respectively. The deconvolution of the C1s spectrum in figure 3.5b shows three peaks at 284.4, 285.5, and 288.8 eV, which are assigned to C−C, C−N/ C−O, and C=O, respectively [4, 31]. The fitted two peaks in figure 3.5c at 530.5 eV and 531.9 eV correspond to the C=O and C−OH groups, respectively [31]. The three peaks at 401.92 eV, 400.36 eV, and 399.58 eV in N1s spectra (figure 3.5d) are attributed to the

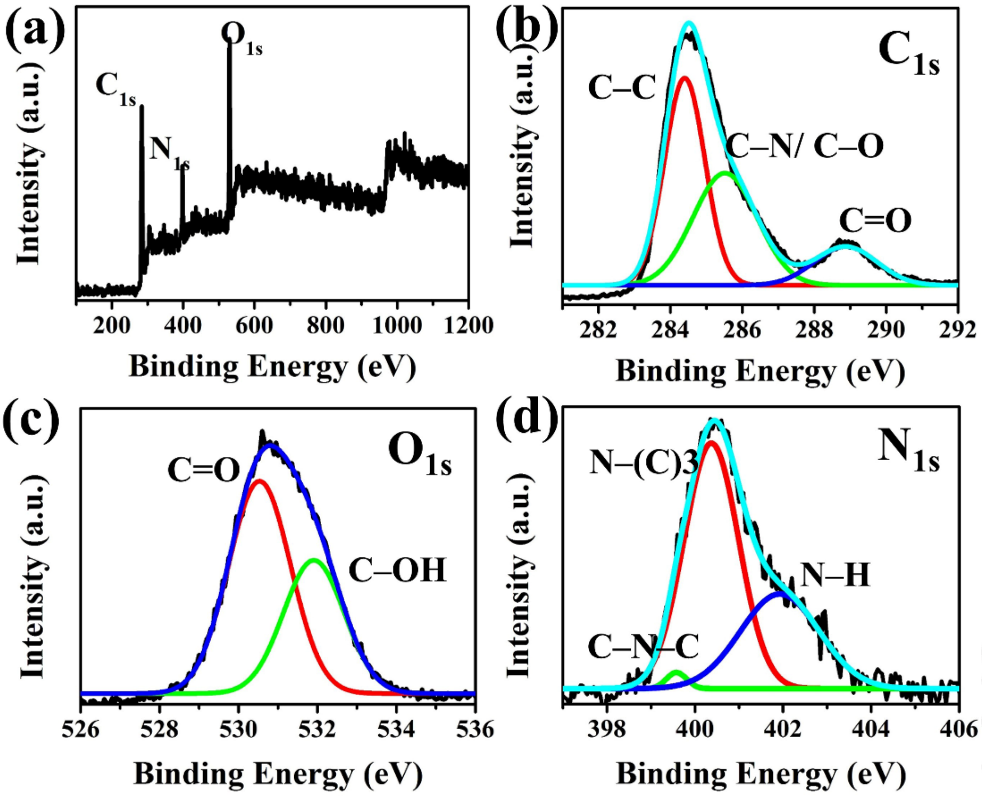

Figure 3.5. (a) XPS, (b) C1s, (c) O1s, and (d) N1s spectra of the synthesized CDs.

N−H of the amino group, N−(C)3 and C−N−C groups, respectively [4]. The XPS spectra were also used to calculate the relative contents of N, O, and C. These values are 11.10, 22.20, and 66.70% for N, O, and C, respectively.

The stability of the PL intensity of the synthesized CDs was also examined. The parameters considered in this case were the storage time, pH of the solvent, and the solvent's ionic concentration (NaCl concentration). In figure 3,6a, it is observed that the PL intensity of the CD solution remains almost unchanged even after 18 weeks of its storage time. The PL dependency of the CDs on the solvent's pH was also measured, and this relation is shown in figure 3,6b. This plot expresses that the PL intensity remains almost constant at pH values ranging from 3 to 11, whereas it decreases in either very low (pH 1) or very high (pH 13) pH values of the solvent. The PL emission of the CDs is controlled either by the core molecular group or by the surface of the CDs. Moreover, the molecular groups get sturdily affected at higher or lower pH values [32]. Figure 3,6c tells about the un-impactful effect of the solvent's ionic strength on the PL intensity of the CD. This indicates that the Na^+ and cl^- ions do not interfere in the PL phenomenon of the CDs.

The average particle size of the synthesized CDs was calculated using the FETEM image shown in figure 3.7a. This FETEM image shows that the CD particles are well separated from one another. The corresponding particle size distribution plot tells that the average particle size of the synthesized CDs is 2.8±1.04 nm. An SAED plot is also shown in figure 3.7b, which suggests the amorphous nature of the synthesized CDs.

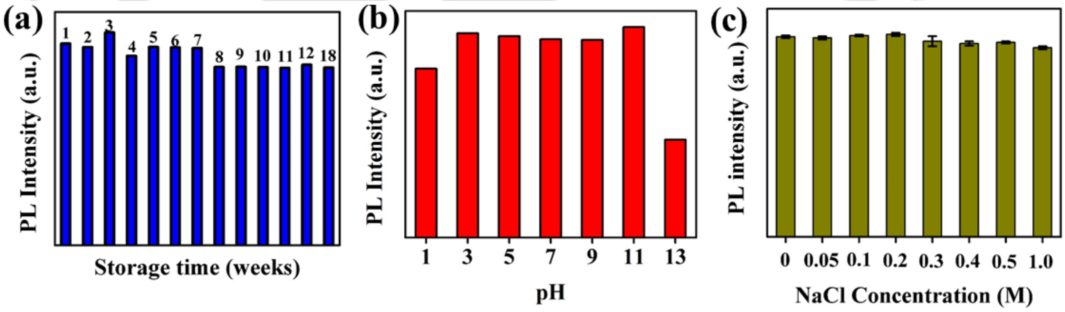

Figure. 3.6. Stability analysis of the synthesized CDs with (a) storage time, (b) pH of the solvent, and (c) ionic strength of the solvent (different concentration of NaCl was used to check the ionic strength). The error bars in (c) represent the standard deviation values taken from three different measurements.

3.3.3. Sensing of PA

We have used the PL property of the synthesized CDs to detect PA in water samples. For this, the sensitivity of the CDs towards the detection of PA has been tested and shown in figure 3.8a. In this figure, a plot between the PL intensity of the CDs and various

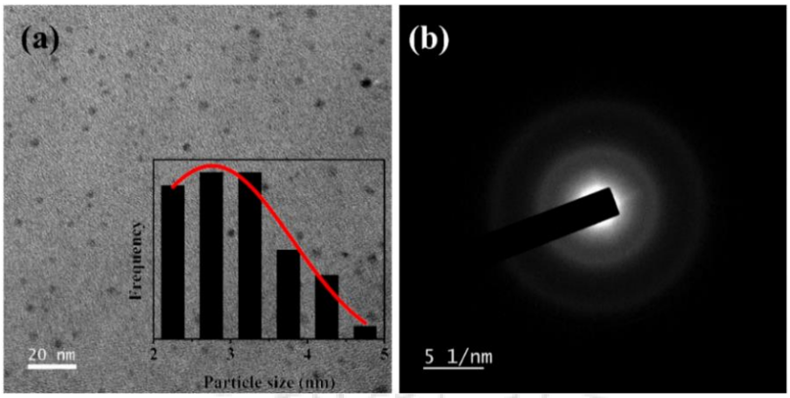

Figure. 3.7. (a) FETEM image of the synthesized CDs with a particle size distribution plot in the inset, (b) SAED pattern of the CDs.

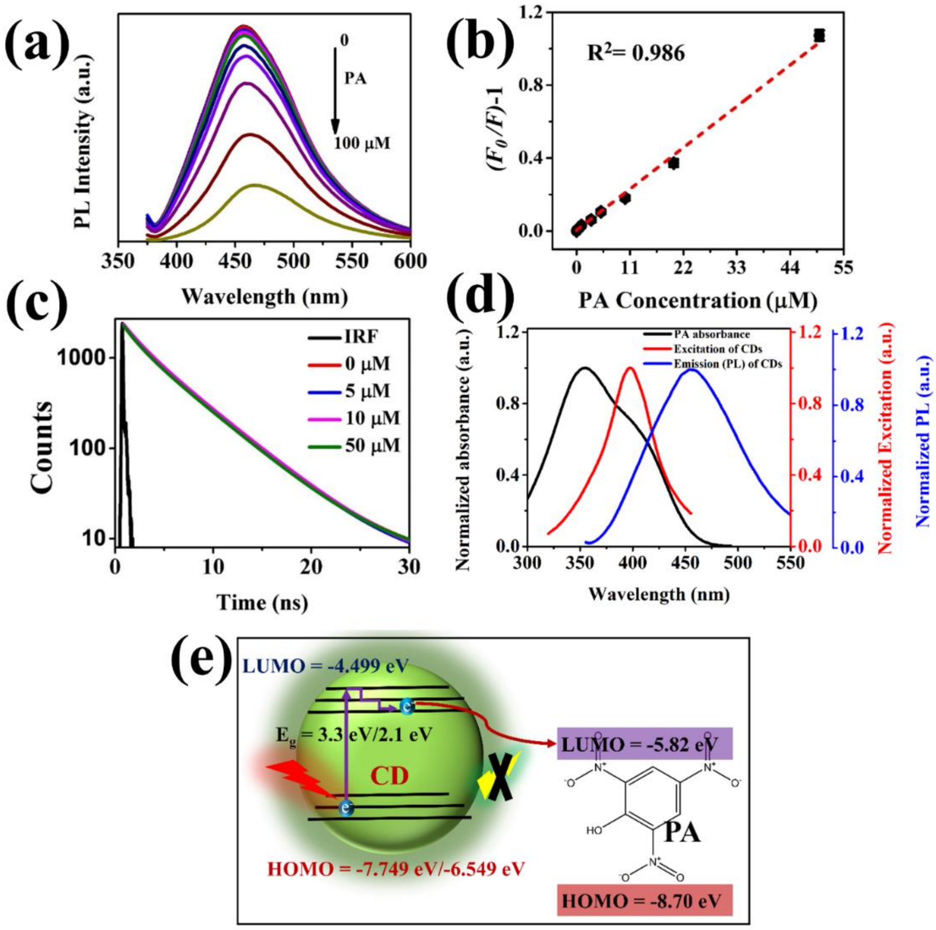

Figure 3.8. (a) Emission peaks of CDs at an excitation wavelength of 360 nm in the presence of different concentrations of PA. (b) Linearly fitted S−V plot of the CD solutions with varying concentrations of PA. (c) TRPL spectra of the different CD solutions in the presence of a various concentration of PA. (d) The overlapping of the

absorbance of PA with the excitation and the emission peaks of the CD solution. (e) Schematic diagram of PL quenching mechanism of the CDs in the presence of PA. The error bars in (b) represent the standard deviation values taken from three different measurements.

concentrations of PA ranging from 0 to 100 μM is presented. This figure conveys that the PL intensity of the CDs decreases with the increasing concentration of PA, which can be attributed to the quenching of the PL of the CDs in the presence of PA. The quenching efficiency was also plotted using the Stern–Volmer (S−V) equation against the PA concentration and is shown in figure 3.8b. The S−V equation is given below [4];

$$\frac{F_0}{F} - 1 = K_{SV}[Q] \tag{3.4}$$

where, K_{SV} is the quenching coefficient of the S−V plot, and [Q] denotes the concentration of PA. F and F_0 correspond to the maximum PL intensities of the synthesized CDs in the presence and absence of PA, respectively. This figure confirms that the S−V data follow a straight-line path with a regression coefficient (R^2) of 0.986, which ensures a very good fit. The extracted quenching coefficient value from the figure was 0.021 $\mu M^{-1,}$ which is relatively high. This sensing system was able to sense PA up to

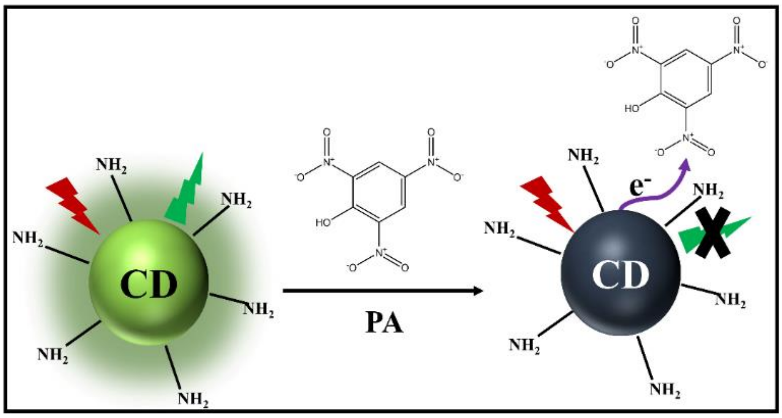

Figure 3.9. Schematic representation of the PL quenching based detection of PA.

to a detection limit (LOD) of 140 nM (32.1 ppb) in a linear range of 0.1–50 μM. Figure 3.9 is presented to explain the reason behind the quenching of PL property of the CDs in the presence of PA. PA contains the electron-withdrawing nitro group, whereas the CDs contain the electron-donating amino group, as mentioned in an earlier section (section 3.3.2). This helps in transferring electrons from the CDs to the PA, resulting in quenching of the PL intensity as described by Niu *et al*. [33] However, the lower impact on the quenching by the other nitro group containing explosive materials (O−NT, 4−NP, DNP) suggests that the explained mechanism may not be the sole reason for the detection of PA. Therefore, to further understand the PL quenching mechanism, we performed TRPL analysis of the samples, and it is shown in figure 3.8c. From this figure, it is evident that there is no significant change in the fluorescence decay curves before (0 μM in the figure) and after the addition of PA. This suggests that the quenching phenomenon is not dynamic, rather static. This is in accordance with the previously reported literature [34]. However, in static quenching, the fluorophore (CDs) and the quenching element (PA) do not form any non-photoluminescent complex in the ground state. To justify this statement,

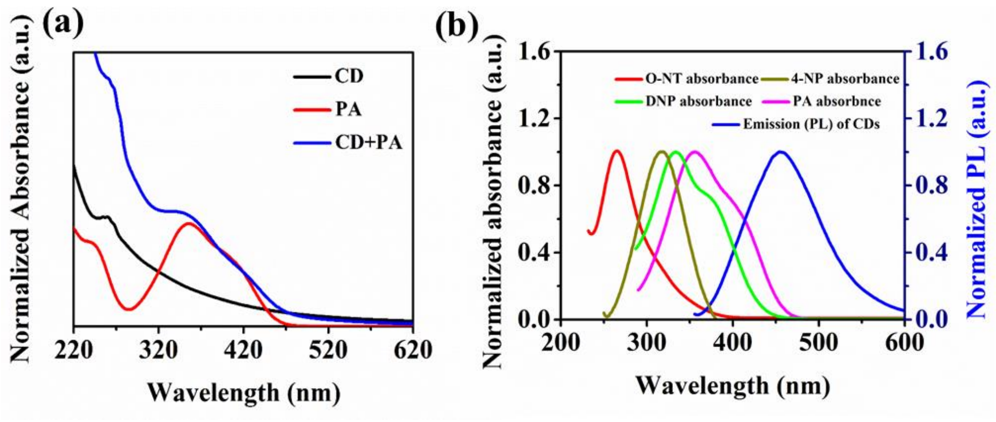

Figure 3.10. (a) Normalized UV-vis spectra of CDs, PA, and CDs in the presence of PA. (b) Comparison of overlapping between the emission peak of CD and the absorbance peaks of O-NT, 4-NP, DNP, and PA.

we are showing the UV–vis peaks of CD solution in the presence and absence of PA along with the UV–vis peak of PA separately in figure 3.10a. This figure suggests the non-formation of any non-photoluminescent complex in the ground state. It is observed in the figure that there is no new absorption peak after the addition of PA in the CD solution, which justifies the previous statement. This phenomenon supports the above statement, i.e., the CDs do not form any non-photoluminescent complex in the ground state. Moreover, to understand furtherabout the exact reason behind the quenching phenomenon in the presence of PA, we investigated further and checked whether the quenching mechanism is based on Forster resonance energy transfer (FRET) or inner filter effect (IFE). For IFE or FRET to be the reason, the emission peak of the fluorophore (CDs) and the absorbance peak of the quencher (PA) should be overlapping [35]. Figure 3.8d shows an apparent overlapping between the absorbance peak of PA with the excitation and emission peak of the CD solution. Therefore, the quenching mechanism can either be influenced by IFE or FRET. However, figure 3.8c shows no change in the TRPL plots of the CDs at different PA concentrations. Hence the possibility of FRET is ruled out. Furthermore, to check the influence of the IFE mechanism on the quenching of CDs with other nitro groups containing explosive materials, the overlapping of the absorbance peaks of these compounds (O-NT, 4-NP, DNP) and the emission peak of the CDs are shown in figure 3.10b. It is evident from the figure that the extent of overlapping is maximum for PA as compared to the others. Although the IFE influences the process of quenching of the PL of CDs in the presence of PA, the lower value of LOD (32.1 ppb) suggests that there is a high possibility of the involvement of some other sensing

Table 3.1. Comparison between the different PA sensing systems (Abbreviations: CA: citric acid. HCL: hydrochloric acid. EDA: ethylenediamine.ET: electron transfer. FRET: Forster resonance energy transfer. DET: dual electron transfer. EI: electron interaction. CTC: charge transfer complex, IFE: inner filter effect. PET: photoinduced electron transfer).

Precursor	**Method**	**LOD (nM)**	**Linear range (µM)**	**Mechanism**	**Ref.**
Mandelic acid and EDA	Hydrothermal	41	0.5-30	FRET	[36]
CA and tris hydroxymethyl)amino methane	Pyrolysis	300	1-60	ET/EI	[37]
Ammonium citrate dibasic	Microwave	250	0-100	PET/FRET	[38]
Dextrose and HCL	Ultrasonication	200	0.5-200	-	[39]
CA and ammonia	Hydrothermal	5	0.009-0.87	Dynamic quenching	[40]
CA and Urea	Microwave	1000	-	EI	[33]
Chloroform and o-phenylenediamine	Solvothermal	2000	-	DET	[41]
Ascorbic acid and hexadecylamine	Ultrasonication	1800	0-110	IFE/CTC	[42]
L-Lysine and thiourea	Hydrothermal	240	1-10	FRET	[43]
Sucrose phosphate	Hydrothermal	16.9	0.2-17	FRET	[44]
Grape skin	Hydrothermal	10	0.6-79.4	IFE/ charge transfer	[45]
Adenosine derrivatives	Hydrothermal	30	0-100	IFE/Static quenching	[46]
Cigarette-tobacco	Microwave	140	0.1-50	CTC/IFE	**Current work**

mechanism as well. There is a high possibility of the fluorophore to form exciplex, i.e., excited state charge transfer complex (CTC) with the quencher as the ability of excited state molecules to participate in an active reaction process is more compared to the ground-state molecules. This process occurs through the transfer of electrons, and it does not indulge in creating any new absorption peak of the fluorophore material [34]. A schematic is shown in figure 3.8e to get further insight into the quenching mechanism. The LUMO and HOMO energy levels of the CDs were calculated as − 4.499 eV and − 7.749 eV, respectively, for direct transition and − 4.499 eV and − 6.549 eV in the case of indirect transition. The HOMO and LUMO energy levels of PA are − 8.70 eV and − 5.82 eV, respectively. The excited electron in the LUMO state of the CDs gets transferred to the LUMO state of PA, as shown in figure 3.8e, resulting in a significant quenching of PL intensity of the CDs [34, 47]. That means the sensing mechanism of PA by the synthesized CDs is a combination of CTC formation and IFE mechanism. A comparison in different parameters (LOD, mechanism, precursors, linear range, and synthesis technique) is shown in table 3.1. It is observed from the table that, even for such a large linear range of concentration, the LOD of our sensing system is comparatively low.

3.3.3.1. Selectivity test

The selectivity towards PA was examined by checking the PL quenching of the CDs in the presence of other various quenchers. These quenchers include different heavy metals as well as various organic compounds. The selectivity plot is shown in figure 3.11. The PL intensity under the influence of various quenchers except for nitrophenols was measured at their concentrations of 200 μM, whereas all the nitrophenols (PA, DNP, and

4−NP) were maintained at 100 µM. Figure 3.11 shows no significant interference from other quenching material towards the selectivity of PA.

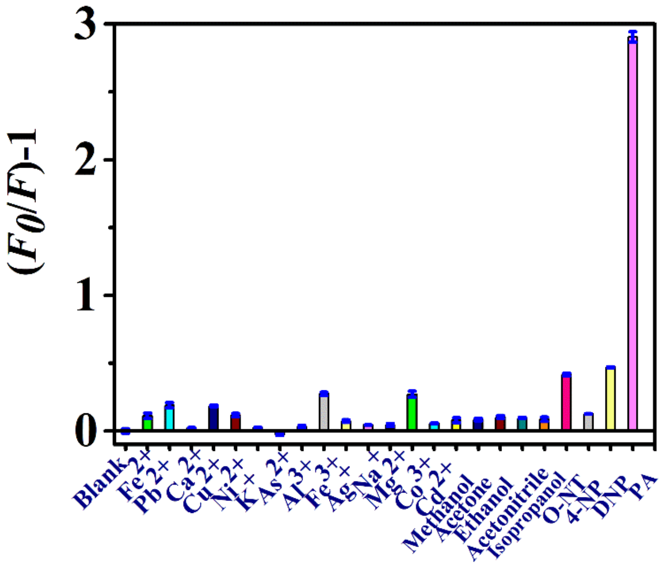

Figure 3.11. PL quenching efficiency of CD solution in the presence of different quenching materials (excitation wavelength: 360 nm; concentration of PA, 4−NP, and DNP = 100 µM and the concentration of other quenchers = 200 µM; F_0 and F are PL intensities of CD solutions in the absence and presence of quenching materials respectively (The error bars correspond to the standard deviation values taken from three different measurements).

3.3.3.2. Tests in real water samples

The feasibility of the detection of PA by the synthesized CDs was further examined by testing the detection ability of the CDs in real water samples. The water used for these experiments was collected from the Brahmaputra River, Guwahati, India, and tap water from the Indian Institute of Technology Guwahati, India. The water samples were first filtered through a 0.2 µm syringe filter to eliminate the suspended larger particles. The blank water samples did not show any PL quenching phenomenon confirming the absence of any quenching material (specifically PA) in them. Further, the sensitivity in these water samples was studied by spiking with five different PA concentrations in the water samples. The change in PL intensities is shown in figure 3.12, along with the corresponding S-V plots. Figures 3.12a and b represent the spiked tap water results and figure 3.12c and d denote the result of spiked Brahmaputra water. We checked the accuracy of our sensing system by measuring the known concentration of PA in the real water samples, and it was found out that our sensing system was showing quite a good recovery percentage with a little deviation of ± 10%. These test results are shown in table

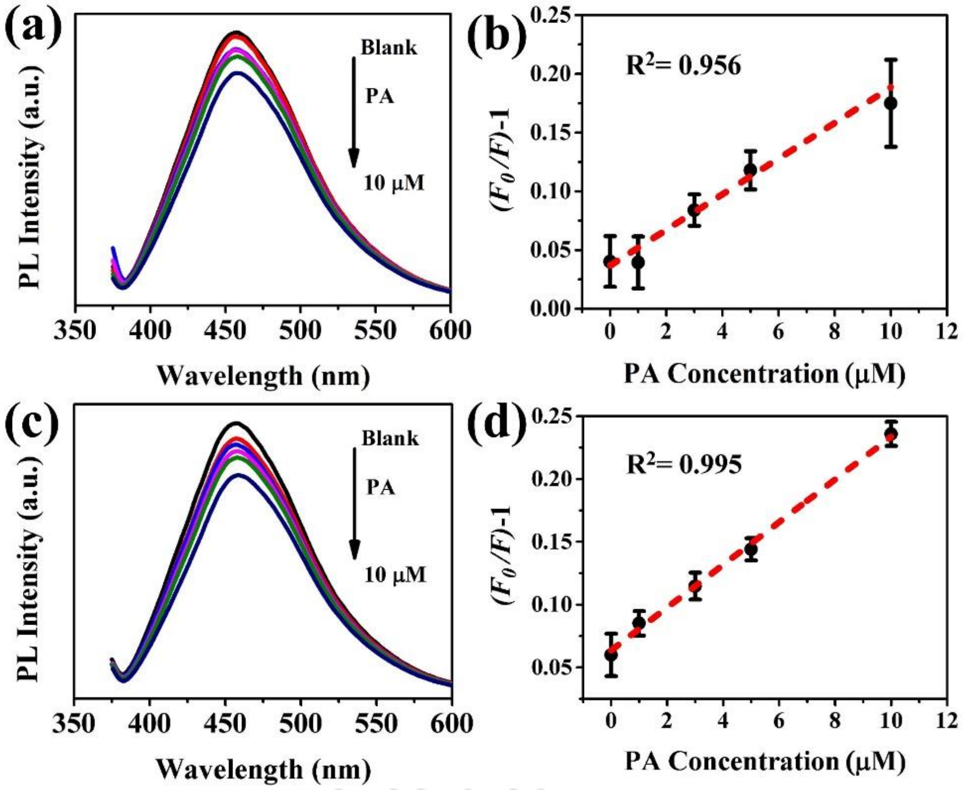

Figure 3.12. (a,c) The PL intensities of CD solutions in the presence of different concentrations of PA using tap water and Brahmaputra water, respectively, and (b,d) the corresponding S-V plot. The error bars in (b) and (d) represent the standard deviation values taken from three measurements.

3.2. Along with these results, the validation of our sensing system has also been checked. For that, a set of analyses with tap water spiked with PA has been done by using UV spectroscopy. The change in absorbance maxima with PA concentration and the calibration curve is shown in figure 3.13a and b, respectively. With this calibration curve, we have calculated the recovery percentage of samples of the concentrations of 2 and 4 µM. The observed recovery percentages were 99.25 ± 10.6% and 96.63 ± 5.9%, respectively, which are relatively close to our reported values.

Table 3.2. Test results with real water samples (*RSD: Relative Standard Deviation).

Sample	Spiked amount (µM)		Detected amount (µM)		Recovery (%)		RSD* (%)	
	River	**Tap**	**River**	**Tap**	**River**	**Tap**	**River**	**Tap**
1	0	0	0	0				
2	2	2	2.05 ± 0.04	1.82 ± 0.07	102.5	90.91	0.81	3.34
3	4	4	3.8 ± 0.15	3.98 ± 0.03	94.31	99.34	3.41	0.74

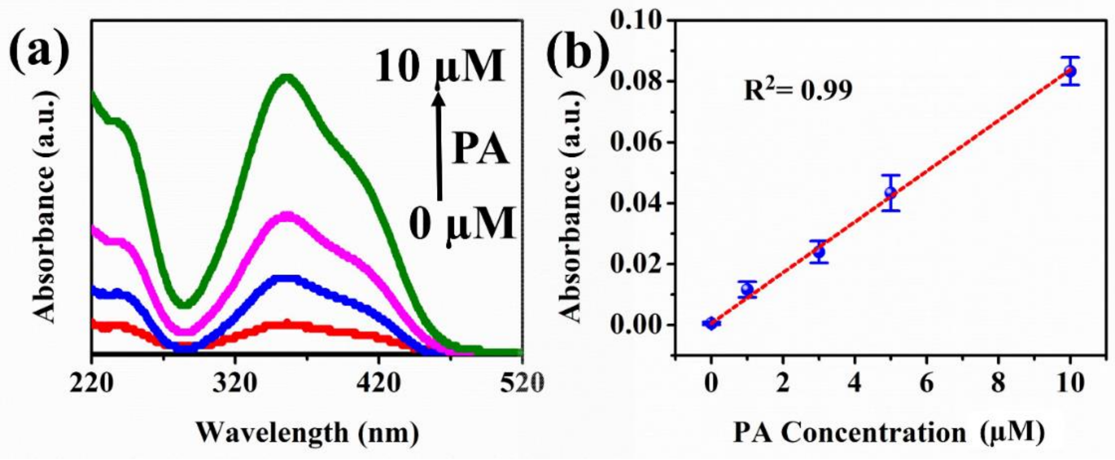

Figure 3.13. (a) UV-vis spectra of PA at different concentrations (tap water), (b) calibration curve.

3.3.4. Characteristics of CD-MWCNT nanocomposite

Another potential application of the synthesized CDs reported in this article is the UV-photodetection. For this, the CDs were attached with MWCNT to synthesize CD-MWCNT nanocomposite. The attachment of the CDs with MWCNT was confirmed by performing FETEM characterization, Raman spectroscopy, and also with PL spectroscopy. Figure 3.14 shows the FETEM images of the MWCNT before and after the

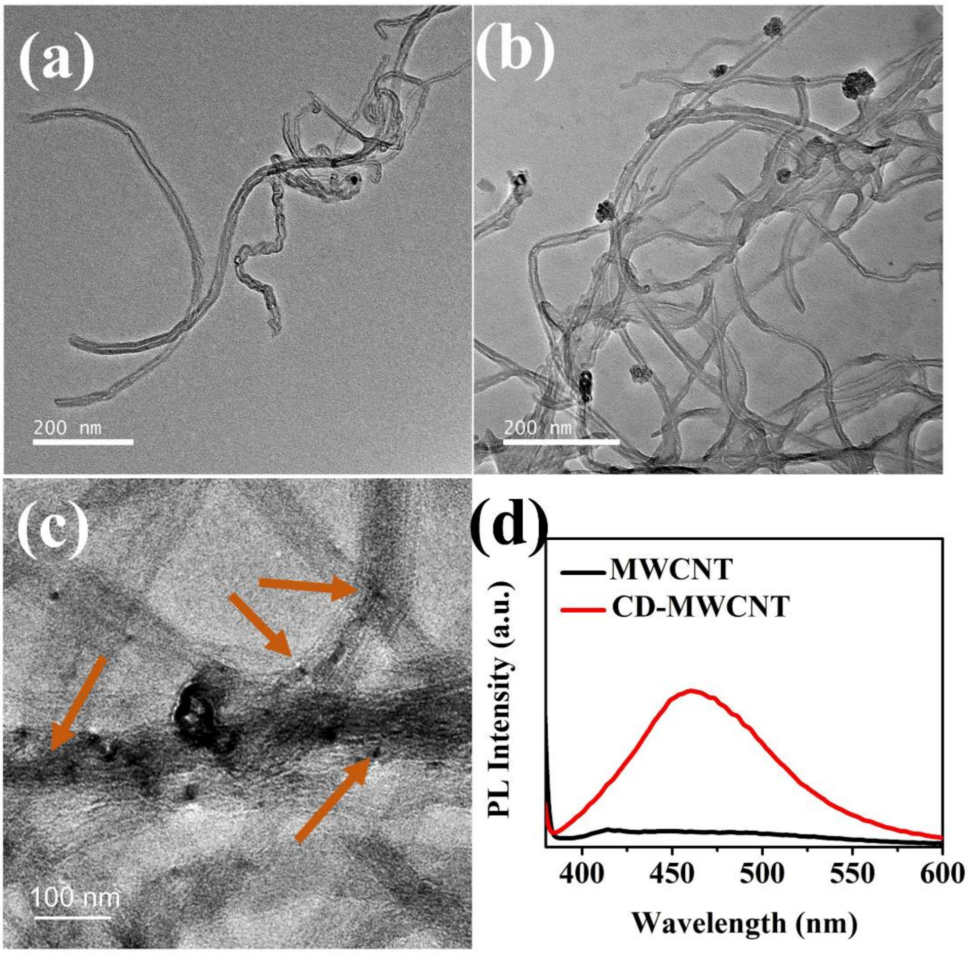

Figure 3.14. FETEM image of (a) MWCNT at 200 nm length scale, (b) CD-MWCNT at 200 nm length, (c) CD-MWCNT at 100 nm length, and (d) PL spectra of MWCNT and CD-MWCNT nanocomposite.

attachment with CDs (figure 3.14a-c) along with the PL spectra of MWCNT before and after the attachment with CDs (figure 3.14d). Figure 3.14a represents the FETEM image

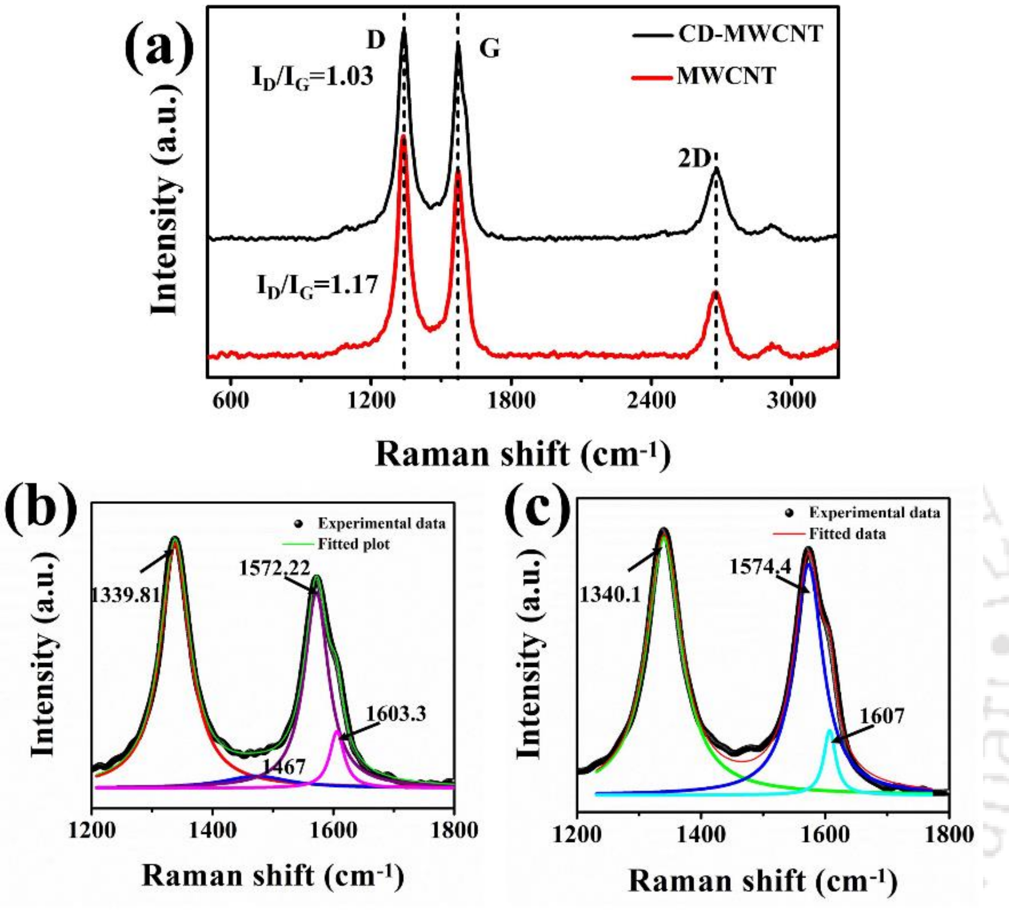

Figure 3.15. (a) Raman spectra of MWCNT and CD-MWCNT nanocomposite, (b) deconvoluted Raman peaks of MWCNT, and (c) deconvoluted Raman peaks of CD-MWCNT nanocomposite.

of MWCNT when CDs were not attached with them, whereas figure 3.14b shows the attachment of CDs with the MWCNT surface. The dark cluster-like spots on the image are evidence of the CD attachment. In figure 3.14c, another image is shown where the CDs are attached to the MWCNT in an entirely segregated manner. The CDs on the MWCNT are indicated with arrows in this figure. Attachment of the CDs on the MWCNT has introduced PL property to the nanocomposite, which is shown in figure 3.14d. From this figure, it is clear that MWCNT does not have any PL property itself (the black line). However, when the CDs get attached with the MWCNT, the composite shows the presence of PL property in it, and this is shown in figure 3.14d (red line). The presence of PL property in the nanocomposite can be ascribed as the presence of CDs in the nanocomposite.

Raman spectra, shown in figure 3.15a, give a clearer idea about the attachment of the CDs with MWCNT. The Raman spectra of oxidized MWCNT and the CD-MWCNT nanocomposite show the presence of three bands at 1340, 1573, and 2680 cm^{-1}, called the D−band, G−band, and the 2D−band, respectively. In the case of MWCNT, D−band specifies the existence of the defected carbon structure of the nanotubes, which is associated with the sp^2 sites existing in carbon tubes in ring form [48]. These defects can be either because of defects in the sp^2 carbon or distortion of the lattice due to bending or can be due to the oxidization of the nanotubes [48]. Whereas the stretching vibrations of the sp^2 carbons are specified by the G−band [48], and the 2D band corresponds to the 'D band' overtone of the MWCNTs [49]. The ratio between the intensities of the D−band and the G−band (I_D/I_G) gives information about the degree of defects present in the nanotubes [50]. The inherent properties of the MWCNT have been retained in the nanocomposite as the characteristic Raman peaks of the nanotubes can be observed in the Raman spectra of the synthesized nanocomposite. The calculated value of the I_D/I_G ratio for the synthesized CD-MWCNT nanocomposite is 1.03, whereas this value for oxidized MWCNT is 1.17. This indicates that the attachment of the CDs on MWCNT has reduced the degree of defects of MWCNT by blocking the honeycomb structure of the surface of MWCNT [50]. We have deconvoluted the D and G peaks to obtain more detailed information about the MWCNT and the CD-MWCNT nanocomposite. These deconvoluted peaks are shown in figure 3.15b and c, respectively. The peak at 1339.81 cm^{-1} in figure 3.15b is considered the characteristic peak of the D−band. The asymmetry of the G−band leads to get deconvoluted into two different peaks. One is at 1572.22 cm^{-1}, which suggests its semiconducting nature (G^{-} band), whereas the other is at 1603.3 cm^{-1}, which can be assigned to the (G^{+} band [51-53]. All the deconvoluted peaks of the nanocomposite, shown in figure 3.15c, especially the deconvoluted G−band peaks have been redshifted, although the semiconducting behavior has remained intact.

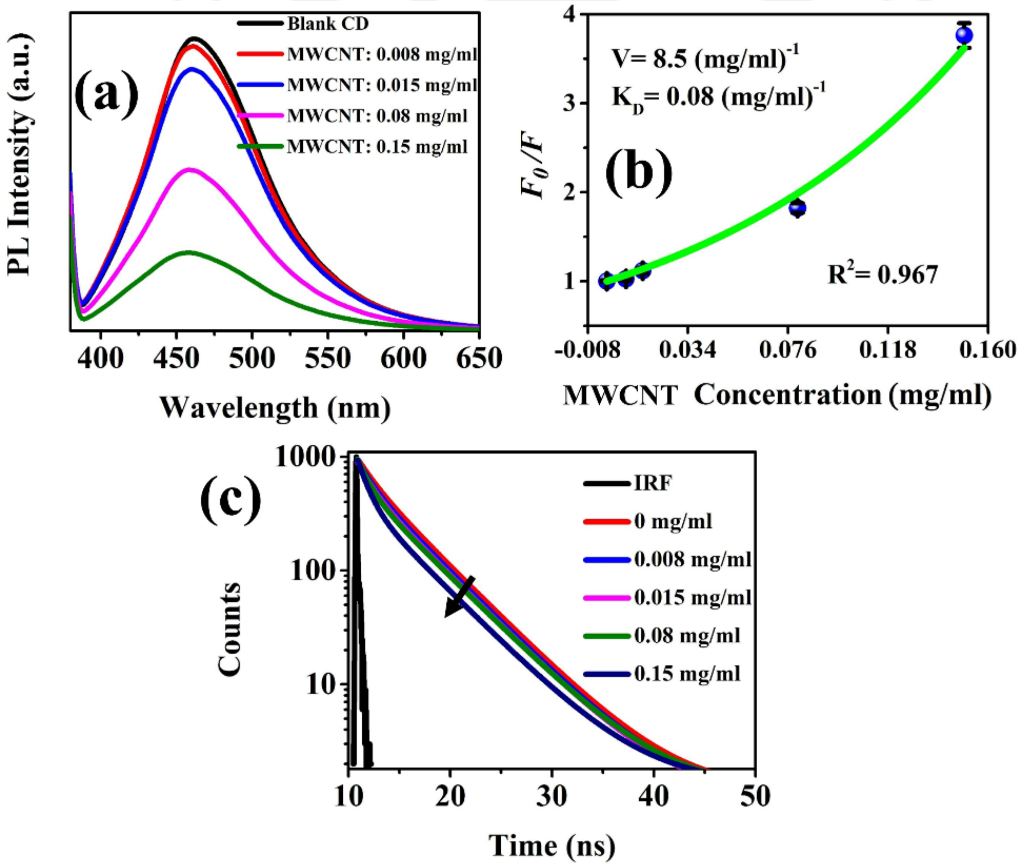

Figure 3.16. (a) Emission peaks of CDs at an excitation wavelength of 360 nm in the presence of different concentrations of MWCNT. (b) Modified S-V plot of the CD-MWCNT solution. (c) TRPL spectra of the different CD-MWCNT solutions. The error bars in (b) represent the standard deviation values taken from three different measurements.

This little shift also confirms the attachment of CDs with the MWCNT. Moreover, it is noted that the G−band gets narrower after the attachment of the CDs with the MWCNT owing to the good dispersion of the CDs [54]. The change in PL intensity of the synthesized CDs in the presence of different concentrations of MWCNT was also observed. The PL intensity decreased with the increasing concentration of MWCNT, as shown in figure 3.16a. This figure shows no shift in the emission wavelength after attaching MWCNT to the CDs. To get more insight of the PL quenching mechanism of CDs, we have demonstrated the S−V plot in figure 3.16b. The plot shows an exponential rise curve. This rise of the curve in the S−V plot can be ascribed to either static quenching or a combination of static and dynamic quenching. Amongst which, the former was usually understood as a "sphere of action" which is basically defined by the modified S−V equation [19];

$$\frac{F_0}{F} = (1 + K_D[Q])e^{([Q]V)} \tag{3.5}$$

where $[Q]$ represents MWCNT-concentration; V and K_D are static and dynamic quenching constants, respectively. The quencher material comes adjacent to the fluorophore during excitation, which is the reason behind the static quenching according to the sphere of action phenomenon. So, during excitation, the quencher-fluorophore pair helps to quench the PL emission immediately [19]. This pair is generally termed as dark complex. The quenching mechanism was further studied by performing TRPL analysis. The TRPL plot is shown in figure 3.16c. In this figure, it is observed that there is a very minute but noticeable change in the PL decay curves with MWCNT concentrations. This tells us that a certain percentage of dynamic quenching is also responsible, along with the static quenching of PL of the CDs. So, the S−V characteristics follow double exponential growth and accordingly, the static and dynamic quenching constants (V, K_D respectively) were calculated and their calculated values were found to be 8.5 (mg/ml)$^{-1}$ and 0.08 (mg/ml)$^{-1}$ respectively.

3.3.5. Photoresponse characteristics of the nanocomposite

As mentioned previously (section 3.2.4), a photoconductive device system was fabricated to perform the experiments for checking the photoresponse characteristics of the synthesized nanocomposite. A schematic representation of the fabricated device system has been shown in figure 3.17a. We recorded the photoresponse of the device under UV excitation. The current density vs. voltage (*J*–*V*) plot of the device under dark and illuminated conditions is shown in figure 3.17b. The characteristics of this plot suggest that the *J*–*V* properties of this device system deviate from the ideal ohmic current curve. This plot somewhat resembles the characteristics of a near ohmic current curve. It is previously known that MWCNTs generally act as p-type semiconductors [55, 56]. So, there is a high possibility of the formation of a Schottky junction when MWCNT comes in contact with Al. The present results accord with the outcomes obtained by Grottrup *et al.* [57], where they reported the formation of Schottky junction when ZnO and Al were in contact at both ends of the electrodes. For this, when the two metal (Al) ends are connected to the source meter, one of the two junctions gets forward bias. In contrast, the other gets reverse bias, and the *J*–*V* plot suggests that the device responds significantly (generates photocurrent) at negative applied voltages. The transient photocurrent of the nanocomposite was tested under the exposure of a UV light spectra with an illumination intensity of 20 mW/cm^2. As the UV source is turned on and off, the device system shows a significant rise and decay of the photocurrent. This transient response of the composite was recorded at a bias voltage of − 2 V, and it is shown in figure 3.17c. One cycle of figure 3.17c has been enlarged to show the time constants of photocurrent rise and photocurrent decay in figure 3.17d and e, respectively. The calculated values of time constants of photocurrent rise and photocurrent decay were 0.38 s and 0.42 s, respectively. In this work, the time constant of photocurrent rise and decay has been considered as the highest value from 10% to 90% of the photocurrent as defined by Li *et al*. in 2015 [58].

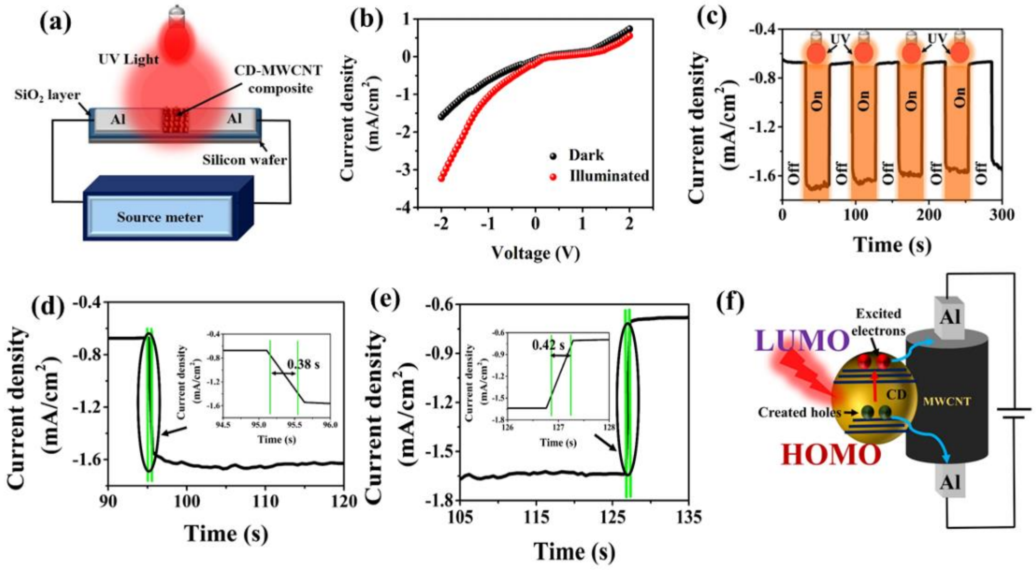

Figure 3.17. (a) Schematic representation of the device system used to check the photoresponsive behavior of the nanocomposite. (b) Current density vs. voltage curve of the CD-MWCNT nanocomposite in dark and illuminated conditions. (c) Transient photoresponse of the nanocomposite under the illumination of a UV light spectra. (d) Rise time, (e) decay time of the photoresponsive device. (f) Schematic representation of the mechanism of generation of photocurrent.

A mechanism has been proposed to explain the reason behind the photocurrent generation and is shown in figure 3.17f. As light incidents on the CDs, the electrons of the HOMO state of the CDs get excited and get transferred to the LUMO region by creating holes in the HOMO region, as shown in the figure [20]. The electrons participating in this transition are generally the electrons present as the electron clouds in the CDs. These electrons then get transferred to the MWCNT, enabling themselves to move freely through the nanocomposite. This is why the quenching of PL (dynamic) of the CDs occurs when they are attached with the MWCNT. The phenomenon of dynamic quenching of PL of the CDs, when attached with the MWCNT, has already been discussed in the previous section (section 3.3.4; figure 3.16c). Further, an applied bias on the system helps the electrons to move towards the positive end whereas the created holes travel towards the negative end, i.e., the electrons and the holes get drifted away because of the applied bias, which ultimately helps to get an increment in the magnitude of the current value, i.e., a certain amount of photocurrent gets generated in the nanocomposite. The difference in current values of CDs and CD-MWCNT is shown in figure 3.18a in the current density vs. voltage curve. It is seen in this figure that the current density value of CDs is almost zero, whereas the current density value rises up to the order of mA/cm^2 range as soon as it gets attached with the MWCNTs. The light dependency of the current value of the

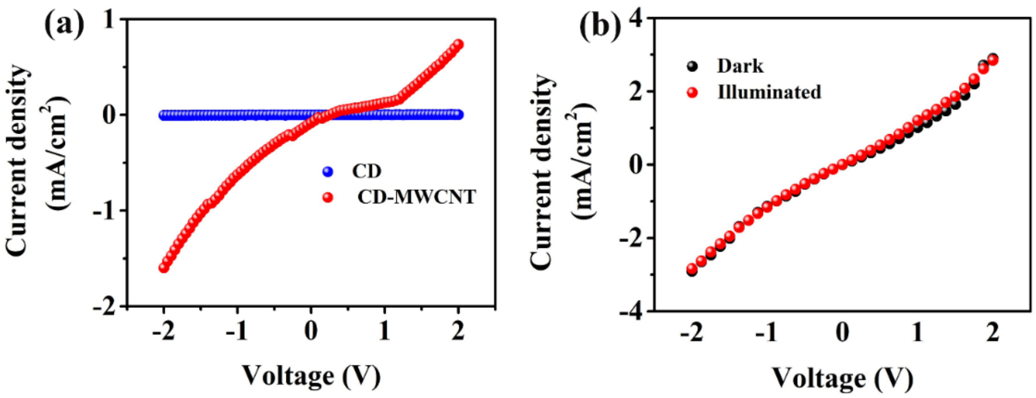

Figure 3.18. (a) Comparison of current density between CD-MWCNT nanocomposite and blank CDs. (b) Current density vs. voltage plot of MWCNTs in dark and illuminated conditions.

MWCNTs is also shown in figure 3.18b, and it is clear from the figure that light does not have any significant impact on the current density value of MWCNT.

3.4. Conclusions

In this chapter, we have reported the applications of N-doped CDs, synthesized from cigarette-tobacco, in two different fields simultaneously. One of them is the PL-based sensing of PA in water bodies, and the other is to use the CDs to synthesize UV-responsive CD-MWCNT nanocomposite. The CDs were synthesized by a one-step microwave assisted synthesis technique, which showed an average particle size of 2.8±1.04 nm and a QY of ~1.02%±0.09. The QY increased with surface passivation by EDA, and the maximum observed QY was ~9.98%±0.50 when 300 μl EDA was added with the precursor material. A detailed characterization of the synthesized CDs was also performed. The PL property of the CDs was utilized to selectively detect PA in water bodies with a detection limit as low as 140 nM (32.1 ppb) in a relatively wider linear range of concentration (0.1–50 μM). The sensitivity was checked for real water systems as well, in which it showed a good recovery percentage with a minimal deviation of ± 10%. A complete mechanism of PL quenching due to the presence of PA has also been deliberated with a detailed explanation, which suggests that the quenching of the PL of CDs in the presence of PA is due to the combination of CTC formation and IFE. For the second application to be accomplished, the CDs were attached with MWCNTs to synthesize UV-photoresponsive novel CD-MWCNT nanocomposite. The detailed mechanism of electron transfer in the nanocomposite was studied. This nanocomposite showed a near ohmic characteristic when connected to an electric field. Further, the detailed mechanism of the photocurrent generation has also been provided with appropriate evidence. The transient response of the UV responsive nanocomposite has been shown with the calculated rise time and decay time of 0.38 s and 0.42 s, respectively. This photoresponsive property of the nanocomposite can be explored in the field of photocatalysis as well. Also, the ability of the nanocomposite to detect UV light can further be used to fabricate carbon material-based portable devices for UV detection. Moreover, the possibility of increasing the QY of the CDs can be used as a scope for future work in the fields of LEDs and bioimaging. Therefore, the ability of the CDs to be used in different areas of applications has opened up a vast range of scopes for researchers.

References

[1] S. Mukherjee, S. Ganguly, A. Chakraborty, A. Mandal, D. Das, ACS Sustainable Chemistry & Engineering, 7 (2019) 819.

[2] S. Senapati, K.K. Nanda, ACS Sustainable Chemistry & Engineering, 6 (2018) 13719.

[3] S. Senthilkumar, R. Goswami, N.L. Obasi, S. Neogi, ACS Sustainable Chemistry & Engineering, 5 (2017) 11307.

[4] W. Lu, X. Qin, S. Liu, G. Chang, Y. Zhang, Y. Luo, A.M. Asiri, A.O. Al-Youbi, X. Sun, Analytical Chemistry, 84 (2012) 5351.

[5] A. Jaiswal, S.S. Ghosh, A. Chattopadhyay, Chemical Communications, 48 (2012) 407.

[6] M. Liu, Y. Xu, F. Niu, J.J. Gooding, J. Liu, Analyst, 141 (2016) 2657.

[7] S.Y. Lim, W. Shen, Z. Gao, Chemical Society Reviews, 44 (2015) 362.

[8] Z. Ma, H. Ming, H. Huang, Y. Liu, Z. Kang, New Journal of Chemistry, 36 (2012) 861.

[9] P. Zhao, X. Li, G. Baryshnikov, B. Wu, H. Ågren, J. Zhang, L. Zhu, Chemical Science, 9 (2018) 1323.

[10] H. Liu, Z. He, L.-P. Jiang, J.-J. Zhu, ACS Applied Materials & Interfaces, 7 (2015) 4913.

[11] A. Subramanian, J. Akram, S. Hussain, J. Chen, K. Qasim, W. Zhang, W. Lei, ACS Applied Electronic Materials, 2 (2020) 230.

[12] X. Chen, C. Yang, H. Sun, S. Ning, H. Zhou, H. Zhang, S. Wang, G. Feng, S. Zhou, Laser Physics Letters, 16 (2019) 076201.

[13] K. Saeed, I. Khan, Carbon letters, 14 (2013) 131.

[14] A.G. Rinzler, J.H. Hafner, P. Nikolaev, L. Lou, S.G. Kim, D. Tománek, P. Nordlander, D.T. Colbert, R.E. Smalley, Science, 269 (1995) 1550.

[15] N. Roy, R. Sinha, T.T. Daniel, H.B. Nemade, T.K. Mandal, IEEE Sensors Journal, 20 (2020) 13245.

[16] N. Roy, S. Mitra, N.M. Das, N. Mandal, D. Bandyopadhyay, H.B. Nemade, T.K. Mandal, IEEE Sensors Journal, 20 (2020) 2278.

[17] B.H. Juárez, C. Klinke, A. Kornowski, H. Weller, Nano Letters, 7 (2007) 3564.

[18] Y.K. Kim, H. Park, Energy and Environmental Science, 4 (2011) 685.

[19] P. Yu, X. Wen, Y.-R. Toh, Y.-C. Lee, K.-Y. Huang, S. Huang, S. Shrestha, G. Conibeer, J. Tang, Journal of Materials Chemistry C, 2 (2014) 2894.

[20] R. Sinha, N. Roy, T.K. Mandal, ACS Applied Materials & Interfaces, 12 (2020) 33428.

[21] A. Tyagi, K.M. Tripathi, N. Singh, S. Choudhary, R.K. Gupta, RSC Advances, 6 (2016) 72423.

[22] P. Dubey, S.K. Sonkar, S. Majumder, K.M. Tripathi, S. Sarkar, RSC Advances, 3 (2013) 7306.

[23] S.N. Baker, G.A. Baker, Angewandte Chemie International Edition, 49 (2010) 6726.

[24] M.P. Sk, A. Jaiswal, A. Paul, S.S. Ghosh, A. Chattopadhyay, Scientific Reports, 2 (2012) 383.

[25] A.B. Bourlinos, R. Zbořil, J. Petr, A. Bakandritsos, M. Krysmann, E.P. Giannelis, Chemistry of Materials, 24 (2012) 6.

[26] R. Das, S. Parveen, A. Bora, P. Giri, Carbon, 160 (2020) 273.

[27] G. Rajender, P.K. Giri, Journal of Materials Chemistry C, 4 (2016) 10852.

[28] H.-X. Wang, J. Xiao, Z. Yang, H. Tang, Z.-T. Zhu, M. Zhao, Y. Liu, C. Zhang, H.-L. Zhang, Journal of Materials Chemistry A, 3 (2015) 11287.

[29] T. Majumder, K. Debnath, S. Dhar, J.J.L. Hmar, S.P. Mondal, Energy Technology, 4 (2016) 950.

[30] S. Dhar, P. Chakraborty, T. Majumder, S.P. Mondal, ACS Applied Materials & Interfaces, 10 (2018) 41618.

[31] J. Pan, Y. Sheng, J. Zhang, J. Wei, P. Huang, X. Zhang, B. Feng, Journal of Materials Chemistry A, 2 (2014) 18082.

[32] S. Zhu, Q. Meng, L. Wang, J. Zhang, Y. Song, H. Jin, K. Zhang, H. Sun, H. Wang, B. Yang, Angewandte Chemie International Edition, 52 (2013) 3953.

[33] Q. Niu, K. Gao, Z. Lin, W. Wu, Analytical Methods, 5 (2013) 6228.

[34] Y.Z. Fan, Y. Zhang, N. Li, S.G. Liu, T. Liu, N.B. Li, H.Q. Luo, Sensors and Actuators, B: Chemical, 240 (2017) 949.

[35] A.S. Tanwar, S. Hussain, A.H. Malik, M.A. Afroz, P.K. Iyer, ACS Sensors, 1 (2016) 1070.

[36] Y. Wang, X. Chang, N. Jing, Y. Zhang, Analytical Methods, 10 (2018) 2775.

[37] L. Lin, M. Rong, S. Lu, X. Song, Y. Zhong, J. Yan, Y. Wang, X. Chen, Nanoscale, 7 (2015).

[38] X. Sun, J. He, Y. Meng, L. Zhang, S. Zhang, X. Ma, S. Dey, J. Zhao, Y. Lei, Journal of Materials Chemistry A, 4 (2016) 4161.

[39] A.B. Siddique, A.K. Pramanick, S. Chatterjee, M. Ray, Sci. Rep., 8 (2018).

[40] S. Chen, Y. Song, F. Shi, Y. Liu, Q. Ma, Sens. Actuators, B, 231 (2016).

[41] B. Ju, Y. Wang, Y.-M. Zhang, T. Zhang, Z. Liu, M. Li, S. Xiao-An Zhang, ACS Applied Materials & Interfaces, 10 (2018) 13040.

[42] F. Cheng, X. An, C. Zheng, S. Cao, RSC Advances, 5 (2015) 93360.

[43] Z.M.S.H. Khan, S. Saifi, Shumaila, Z. Aslam, S.A. Khan, M. Zulfequar, Journal of Photochemistry and Photobiology A: Chemistry, 388 (2020) 112201.

[44] D. Shi, F. Yan, T. Zheng, Y. Wang, X. Zhou, L. Chen, RSC Adv., 5 (2015) 98492.

[45] J. Li, L. Zhang, P. Li, Y. Zhang, C. Dong, Sensors and Actuators B: Chemical, 258 (2018) 580.

[46] N. Li, S.G. Liu, Y.Z. Fan, Y.J. Ju, N. Xiao, H.Q. Luo, N.B. Li, Analytica Chimica Acta, 1013 (2018) 63.

[47] B.B. Chen, Z.X. Liu, H.Y. Zou, C.Z. Huang, Analyst, 141 (2016) 2676.

[48] M. Baro, P. Nayak, T.T. Baby, S. Ramaprabhu, Journal of Materials Chemistry A, 1 (2013) 482.

[49] L. Bokobza, J. Zhang, Express Polymer Letters, 6 (2012) 601.

[50] S. Dhall, N. Jaggi, Bulletin of Materials Science, 37 (2014) 1427.

[51] Z.K. Tang, J.P. Zhai, Y.Y. Tong, X.J. Hu, R. Saito, Y.J. Feng, P. Sheng, Physical Review Letters, 101 (2008) 047402.

[52] S.D.M. Brown, A. Jorio, P. Corio, M.S. Dresselhaus, G. Dresselhaus, R. Saito, K. Kneipp, Physical Review B, 63 (2001) 155414.

[53] D.K. Singh, P.K. Iyer, P.K. Giri, Diamond and Related Materials, 19 (2010) 1281.

[54] R. Das, G. Rajender, P.K. Giri, Physical Chemistry Chemical Physics, 20 (2018) 4527.

[55] Q.T.M. Nguyet, N.V. Duy, C.M. Hung, N.D. Hoa, N.V. Hieu, Applied Physics Letters, 112 (2018) 153110.

[56] O.K. Varghese, P.D. Kichambre, D. Gong, K.G. Ong, E.C. Dickey, C.A. Grimes, Sensors and Actuators, B: Chemical, 81 (2001) 32.

[57] J. Gröttrup, V. Postica, D. Smazna, M. Hoppe, V. Kaidas, Y.K. Mishra, O. Lupan, R. Adelung, Vacuum, 146 (2017) 492.

[58] L. Li, Z. Lou, G. Shen, ACS Applied Materials & Interfaces, 7 (2015) 23507.

Chapter 4

Carbon dots and ZnO based flexible and self-powered Schottky diode for UV-photodetection

Optoelectronics

Contents

Graphical abstract

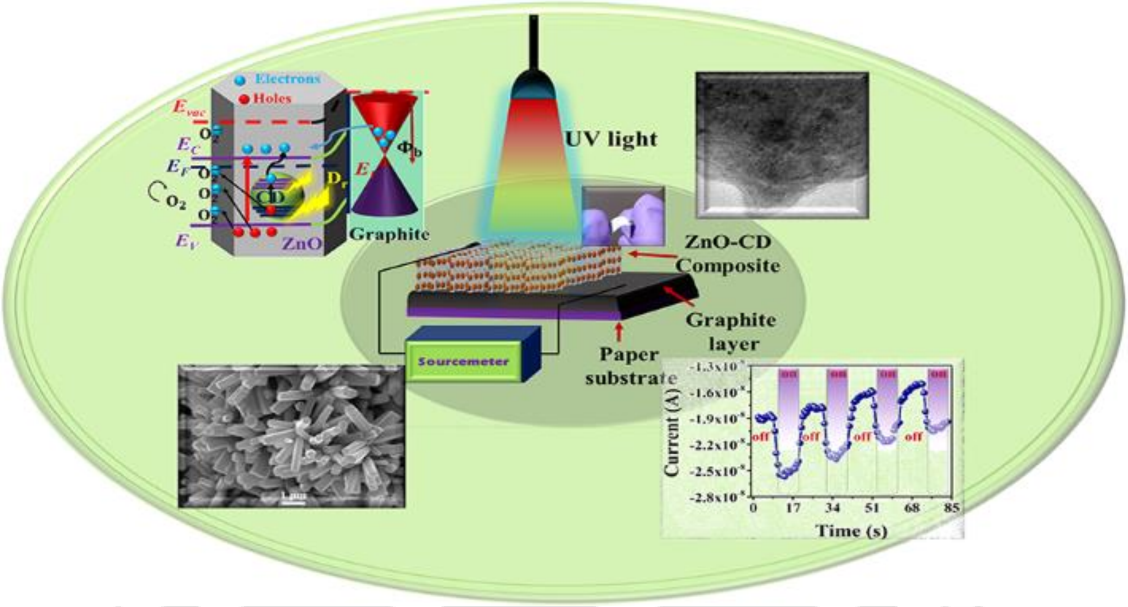

The contents in this chapter have been published as "Growth of Carbon Dot-Decorated ZnO Nanorods on a Graphite-Coated Paper Substrate to Fabricate a Flexible and Self-Powered Schottky Diode for UV Detection." **Rupam Sinha**, Nirmal Roy and Tapas K. Mandal, *ACS Appl. Mater. Interfaces*, 12, 33428, 2020. DOI: **10.1021/acsami.0c10484**

Abstract

The fabrication of flexible as well as self-powered optoelectronic devices is a growing and challenging area of research. Some scientists have reported the fabrication of either flexible or self-powered photodetectors recently. However, most of the literature studies fail to report the fabrication of self-powered as well as flexible photodetectors. This chapter reports the fabrication of a self-powered, carbon dot (CD)-enhanced, flexible ZnO/graphite heterojunction-based UV detector where cellulose paper has been used as the substrate. A detailed study on the crystallinity and the defects of the ZnO nanorods has been done with appropriate characterizations. The CD-enhanced ZnO/graphite heterojunction showed Schottky characteristics. The Schottky parameters such as the barrier height, ideality factor, and the series resistance have also been calculated using the Cheung–Cheung method. The observed values of barrier height, ideality factor, and the series resistance are 0.74 eV, 3.74, and 503 kΩ, respectively. The transient response at self-powered condition has been demonstrated. The response time and the recovery time at self-powered condition have also been calculated with the help of the transient response, and those values are ~2 and ~3.2 s, respectively. The responsivity and the specific detectivity of the fabricated UV detector have been calculated as 9.57 mA/W and 4.27×10^8 Jones, respectively, at 330 nm wavelength, which is quite comparable with literature-reported values, considering a self-powered photodetector.

4.1. Introduction

The photoluminescence (PL) property of carbon dots (CDs) has been proven to be an excellent probe in the applications of bioimaging, sensing heavy metal ions (Cr^{6+}, Fe^{3+}), and explosive materials (picric acid; PA), as discussed in the previous chapters (chapter 2 and 3). Moreover, the photoresponsive nature of CDs has also been tested by fabricating a UV-responsive nano-composite (CD_MWCNT). However, a multi-walled carbon nanotube (MWCNT) is not a photoresponsive material individually. Therefore, it can be hypothesized that the photoresponsive efficiencies can be enhanced if the MWCNT could be replaced with another photoresponsive semiconductor material, such as TiO_2, ZnO, MoS_2, etc. and such research has been done by several scientists in this current era. For example, Dhar *et al.* [1] showed the fabrication of a GQD-sensitized ZnO/PEDOT:PSS Schottky diode for detecting UV light with high responsivity and detectivity. The authors reported the detectivity and responsivity of the UV detector as high as 1.3×10^{12} $Hz^{1/2}/W$ and 36 A/W, respectively. Fazio *et al.* [2] reported the enhancement of the photoresponsivity and the photoconductive gains of the GQD based photodetectors, where they attached these GQDs with TiO_2 semiconductors. Not only this, the attachment of inorganic quantum dots (QDs) also enhances the photoconductivity of the semiconductor material consisting nano-composites [3]. However, the toxicity becomes a genuine concern for the use of such inorganic QDs on a daily basis. In recent years, CDs have been perceived as a potential replacement for the inorganic QDs, owing to their low toxicity and high water solubility [4]. The CDs have been considered as noble photosensitizers due to their high optical properties along with the other advantages such as low cost and easy synthesis technique. The CDs help to enhance the photosensitivity and detectivity of the semiconductor materials as they help to generate more charge carriers in the presence of light with favourable wavelengths.

One such widely used semiconductor material is ZnO nanomaterials, which have gathered much attention in recent years because of their ability to be utilized in photoresponsive applications. For example, Wang *et al*. [5] reported the tuning of the band structure of the electron transport layer to suppress the trap-state density of $CsPbIBr_2$ films by the addition of NH_4Cl to the ZnO precursor. Their reported power conversion efficiency (PCE) of the solar cell is 10.16%, which is considered to be the best among all the pure $CsPbIBr_2$ perovskite solar cells at a quite low manufacturing temperature (160 °C). Li *et al*. [6] showed the usefulness of ZnO nanoparticles in enhancing the crystallinity and the lifetime of $CsPbBr_3$ when added in an optimized proportion. This optimized addition of ZnO with $CsPbBr_3$ also helped to improve the lasing threshold as well as the emission efficiency of the $CsPbBr_3$:ZnO films as compared to the pristine $CsPbBr_3$ films. On the other hand, another photoresponsive characteristic of the ZnO nanoparticle is the PL property. Zang and Tang [7] reported about the PL property of ZnO nanoparticles in their work and used it in the bioimaging application. In a different work, Zang [8] experimentally proved the enhancement of PCE of ZnO/Cu_2O solar cells with micrometer-sized and properly oriented Cu_2O, and their reported PCE value is 3.18%. ZnO is also one of the favorite materials for photodiodes to detect UV light, owing to its high energy gap (3.2–3.4 eV), easy and cost-effective synthesis technique [9-13], behavior similar to n-type semiconductors, a comparatively larger excitonic binding energy (60 meV) at normal temperature (i.e. room temperature) etc. [14] Especially UV photodetectors based on ZnO/polymer junction have gathered high faith of the scientists because of their suitability for applications in flexible photodetectors, high sensitivity, and easy synthesis techniques [15-17]. Typically, it is reported for a heterojunction of ZnO NRs/PEDOT:PSS that the values of sensitivity and responsivity are 37.65 and 5.046 AW^{-1}, respectively, under UV exposure (130 μW, $\lambda = 256$ nm) and the photocurrent of 6.74×10^{-4} A [1]. Metal sulfide (e.g., PbS, CdS, etc.) decorated ZnO has shown high photosensing ability by generating more electron–hole pairs, which help to overcome the charge recombination problems [18-20]. As mentioned in the previous paragraph, that the low toxicity of CDs instigated the researchers to replace inorganic QDs (metal sulfides) with CDs although the inorganic QDs help to enhance the photoconductivity of the semiconductor nanomaterials such as ZnO nanorods. As examples, we have already mentioned the works reported by Dhar *et al*. [1] and Fazio *et al*. [2]. However, these two works also lack in describing the fabrication of flexible photodetectors.

In the current era of science and technology, lightweight and flexible photodetectors have emerged as highly demanding photodiodes because of their possible applications in wearable and portable optronic devices [21]. The recent development of hybrid inorganic–organic perovskite halide is one of the biggest examples where the material is perceived as a potential lightweight and flexible photodetector due to its flexibility and capabilities to harvest light. The inorganic–organic perovskite halide hybrid obtains these two characteristics because of its crystallinity in a lower temperature, proper energy gap (~1.5 eV), binding energies at the low excitation wavelength, etc. [21] However, there still remain some limitations for most of these composites despite having the advantages in the form of flexibility. For example, most of these composites involve external power sources to operate as photodiodes. This increases the size and weight of the devices, which limit the scopes of the material in a wide range of applications [22]. The development of self-powered photodiodes has been observed as an ideal solution to this problem. Xiong *et al*. [23] reported the fabrication of photodetector arrays based on ZnO/Cu_2O heterojunction, which was operable at zero bias voltage. The authors used the photodetector arrays in transmitting ASCII encoded information for its excellent performance in optical communication. Gao *et al*. [24] developed a self-powered high-performance TiO_2/NiO heterojunction UV detector. The reported photodetector showed a response speed of less than 0.1 s. However, these articles do not report the fabrication of the flexible photodetectors, although they conveniently show the development of self-powered photodiodes. Thus, the fabrication of flexible as well as self-powered photodetectors has caught the attention of the researchers, and it has become a challenging task also. Scientists from all across the globe have already started working in this area. They have approached to fulfill the goal by fabricating photodiodes following some complex methods like the construction of Schottky or *p–i–n* junctions [25, 26]. Not only this, but also the researchers have tried to fabricate the photodetectors by using simpler techniques as well. For example, Leung *et al*. [27] and Lu *et al*. [28] have demonstrated the fabrication of self-powered flexible photodetectors by simply integrating the photodiode with an energy-harvesting unit. However, the integrated methods to fabricate self-powered photodiodes possess some deficiencies such as less adaptability of the substrate, larger size of the device, etc. To counter these deficiencies, another fabrication method has been introduced by Saraf and Maheshwari [29]. The authors fabricated a self-powered photodetector using Au/$MAPbI_3$/Au heterojunction. The reported photodetector was working based on the principle of the electric field-induced effect in which the built-in electric field helped the carriers to get separated. Therefore, it is noticed from the discussion till now that there is a huge gap in the field of UV-photodetection, when the concern of fabrication of a flexible as well as a self-powered UV photodetector comes into the scenario.

In this chapter, we have demonstrated the growth of CD-decorated ZnO nanorods on a graphite-coated paper substrate, and we have used the CD-decorated ZnO/graphite heterojunction-based diode as a flexible and self-powered UV photodetector. Here, the growth of the ZnO nanorods on the graphite-coated paper substrate is the novel contribution. The UV-sensing mechanism has also been deliberated in detail with probable explanations. A comprehensive discussion about the characteristics of the ZnO nanorods has been reported as well.

4.2. Experimental section

4.2.1. Materials

Zinc acetate dihydrate, isopropanol, diethanolamine, zinc nitrate hexahydrate, ethylenediamine (EDA), and hexamethylenetetramine (HMTA) were all bought from Sigma Aldrich, India Ltd. 6B apsara pencil, A4 paper, and cigarettes were procured from the local market, IIT Guwahati, India.

4.2.2. ZnO nanorod fabrication

The growth of ZnO nanorods on a graphite-coated paper substrate was done by using a simple hydrothermal method [1]. In a typical process, a paper substrate was coated with graphite by sketching with a 6B apsara pencil. This graphite-deposited paper substrate was dip-coated into a ZnO solution to deposit a ZnO seed layer on the graphite coating, which was then heated at 100 °C for 15 min, and this step was repeated four times. To prepare the ZnO solution, 50 ml of isopropyl alcohol was used as a solvent in which 0.01

M of zinc acetate dihydrate was dissolved. This dissolving process was carried out by stirring and heating the system at 65 °C for 1 h. This process was followed by the addition of 0.02 M diethanolamine in the solution to obtain a transparent ZnO solution. The ZnO seed-deposited graphite-coated paper substrate was then treated in a hydrothermal reaction at 90 °C for 6 h to grow the ZnO nanorods. The solution for the hydrothermal reaction was prepared by mixing two equimolar solutions of HMTA (0.05 M) and zinc nitrate hexahydrate (0.05 M). Afterward, the ZnO grown substrate was kept at 50 °C overnight to improve the crystallinity of the nanorods. The whole process was repeated for four times to get the proper growth of crystalline ZnO on the paper substrate.

4.2.3. CD synthesis and attachment with ZnO

The CDs were synthesized by the method reported in the previous chapter (chapter 3). The CDs were attached with the ZnO nanorods by dipping the nanorods in a CD solution for 2 h.

4.2.4. Electrical measurement

A probe station (Keithley 4200-SCS) was used to carry out the electrical characterizations. A 150 W Collimated Industrial Grade Arc Lamp Source (Model: 101-9153) was used as a broadband light source to measure the photoresponse of the device. Two tungsten probes were connected with the graphite end and the ZnO end of the device for the measurement of electrical response.

4.2.5. Characterizations

Field emission scanning electron micrographs (FESEM) were taken by a field emission scanning electron microscope (Zeiss, Sigma). Energy dispersive X-ray (EDX) spectra were obtained from an energy dispersive X-ray spectroscope (Zeiss, Sigma). A field emission transmission electron microscope (FETEM; JEM, 2100F) was used to record the field emission transmission electron micrograph and the selected area electron diffraction (SAED) pattern. The crystallinity of the sample was checked with an X-ray diffractometer (XRD; Burker, D8 Advance), photoluminescence (PL) measurement was taken by a photoluminescence spectrometer (PerkinElmer, LS 45). For the preparation of samples for FETEM and PL characterizations, the ZnO grown paper was dipped into 5 ml of DI water inside a cultured tube and ultrasonicated for 10 min. Now, for FETEM, this newly prepared dispersion was drop-casted on a carbon-coated copper grid and dried overnight before the analysis, whereas for PL analysis, the dispersion was poured in a cuvette, and the measurement was taken.

4.3. Results and discussion

4.3.1. ZnO characteristics

Figure 4.1a represents the FESEM image of the ZnO nanorods. The hexagonal shape of the ZnO nanorod is quite evident in this figure. Figure 4.1b shows the proof of the growth of ZnO on the graphite layer, which is coated on a paper substrate. The paper substrate and the graphite layer are indicated separately in this figure to show them in a distinguishable manner. The marked portion in figure 4.1c was selected for EDX analysis and elemental mapping of the synthesized nanorods. The peaks in figure 4.1d are confirming the presence of elements Zn and O. The inset shows the weight percentages of these two elements, whereas figure 4.1e,f shows the uniform scattering of Zn and O elements in the area of scanning. Figure 4.2a represents a typical FETEM image of the CD-decorated ZnO nanorods. In figure 4.2b, an enlarged section of figure 4.2a is shown.

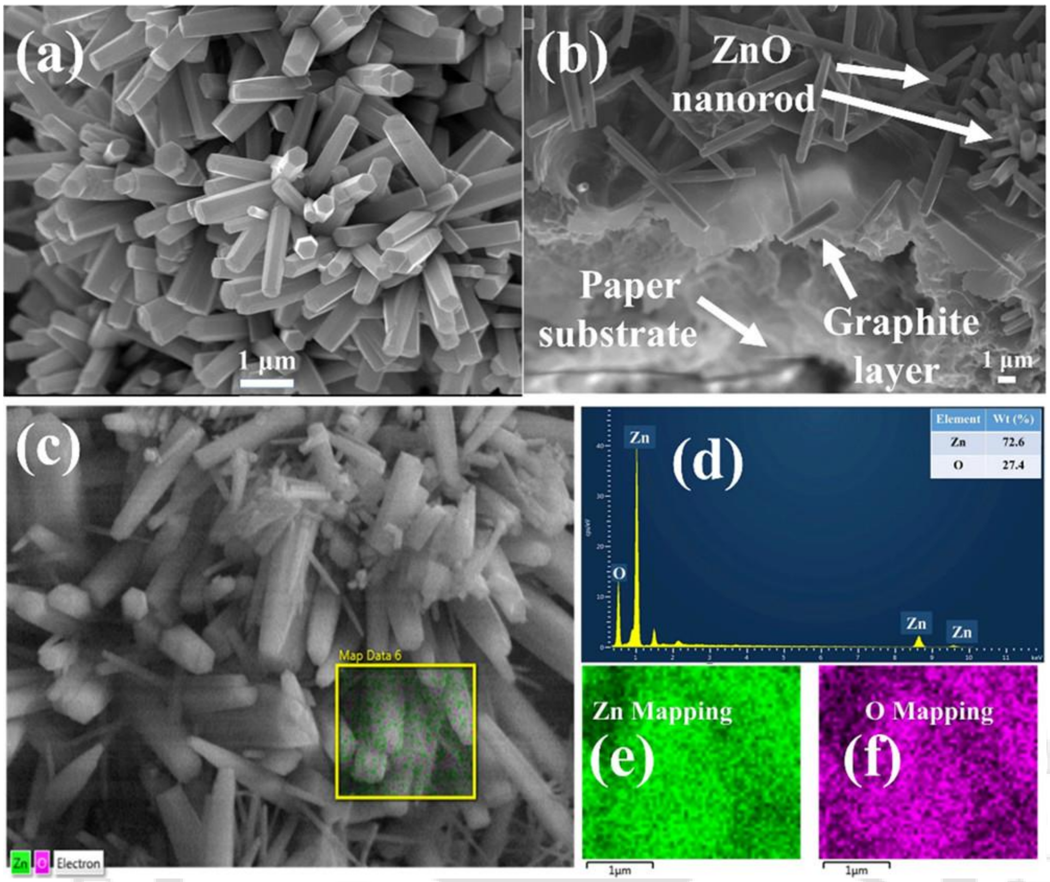

Figure 4.1. (a) FESEM image to show the synthesized ZnO nanorods. (b) FESEM image to show the growth of ZnO nanorods on graphite-coated paper substrate. (c) Scanning area for EDX analysis. (d) EDX spectrum of the synthesized ZnO nanorods. (e) Zn and (f) O mapping images.

The image unveils several tiny spots on the surface of the nanorod as pointed with the arrows, which can be ascribed as the attachment of CDs onto the surface of the ZnO nanorod. The HRTEM image of a section of the nanorod is represented in figure 4.2c. Although the lattice spacing of mono crystallinity is shown in this figure, the polycrystallinity of the synthesized ZnO nanorods can be confirmed by the SAED pattern shown in figure 4.2d. The presence of multiple circular orbits of the bright dots is the evidence of the polycrystallinity of the nanorods. This statement can be confirmed from the XRD pattern of the synthesized nanorods, which is shown in figure 4.3a. In the figure,

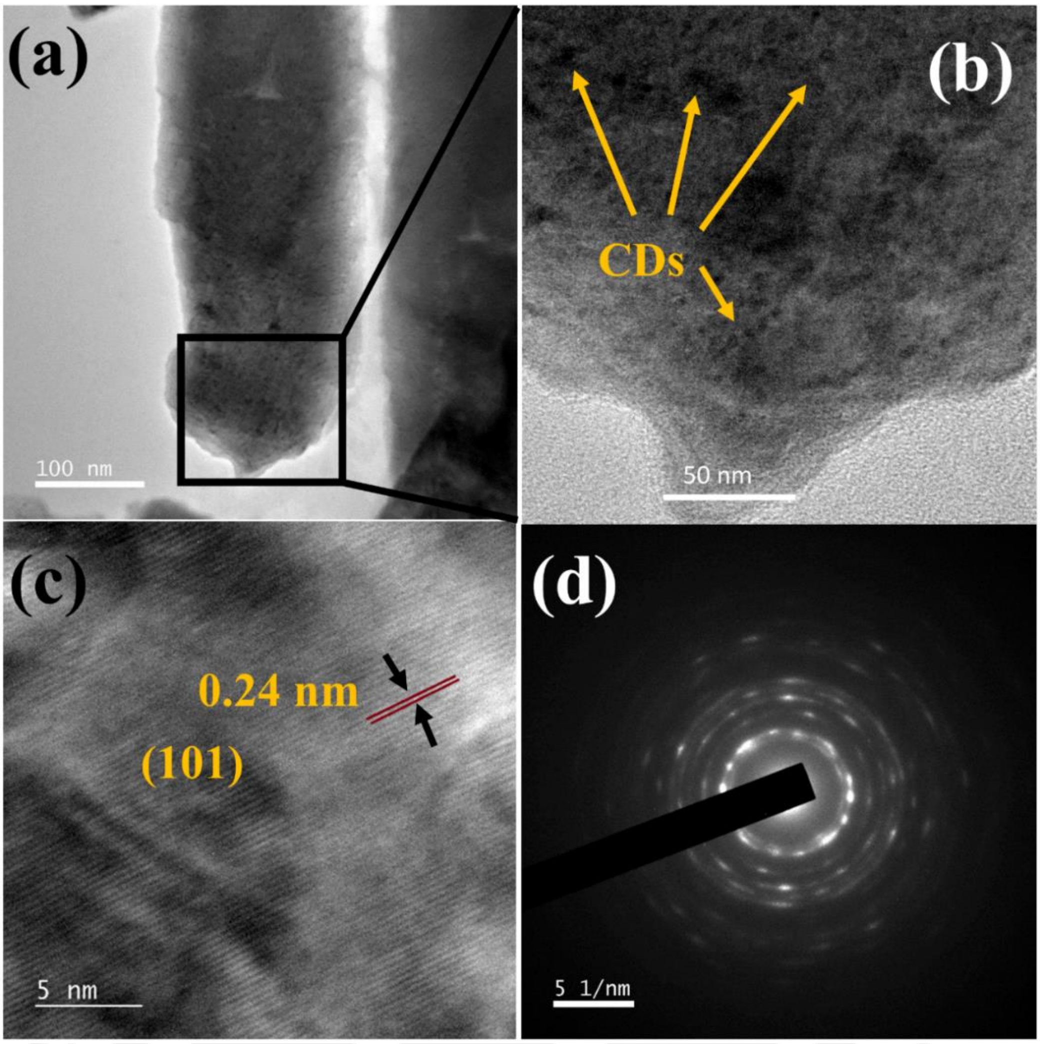

Figure 4.2. FETEM image of the CD decorated ZnO nanorods at 100 nm (a), and 50 nm (b) scales, the HRTEM image (c), and the SAED pattern (d) of the ZnO nanorod.

the formation of polycrystalline ZnO nanorods can be verified by comparing the crystal planes (100), (002), (101), (102), (110), (103), (112), and (201) at 2θ values of 31.86, 34.54, 36.36, 47.64, 56.68, 62.98,68.06, and 69.17° respectively. Notably, these values are in good agreement with previously reported XRD data of ZnO nanorods [30]. The presence of the planes (100), (002), and (101) suggests the formation of hexagonal wurtzite ZnO nanorods [31], and these peaks are sharp, narrow, and of quite high intensity, which tells us about the better crystallinity of the sample. However, the lower intensities of the other diffraction peaks correspond to some defects present in the crystalline structure of the nanorods. The defect in the crystalline structure creates a strain in the nanorods, which ultimately causes a change in the overall crystallite size. The Williamson–Hall (W-H) technique [32] has been implemented to calculate the average crystallite size (L) and strain (ε) of the nanorods. The equation is given below,

$$\frac{\beta cos\theta}{\lambda} = \frac{1}{L} + \frac{\varepsilon sin\theta}{\lambda} \tag{4.1}$$

where β stands for full width at half-maxima (FWHM), θ is the Bragg angle, and λ corresponds to the wavelength used in XRD (λ = 0.15418 nm). The intercept and the slope of the plot between $\frac{\beta cos\theta}{\lambda}$ and $\frac{sin\theta}{\lambda}$ shown in figure 4.3b, helps to get the average crystallite size (L) and the strain (ε), respectively. The obtained values of average crystallite size and the strain are 135.13 nm and 0.0067, respectively. The information about the amount of defect present in the crystal structure can be calculated from the parameter termed as dislocation density (δ). The dislocation density was calculated using the following equation [33].

$$\delta = \frac{1}{L^2} \tag{4.2}$$

The calculated value of dislocation density is 5.476×10^{-5} nm^{-2}. Considering the high intensities of the peaks present at 31.86, 34.54, and 36.36°, we have calculated the lattice constants of the synthesized ZnO nanorods for the crystalline planes (100), (002), and (101), respectively. The following equations [34] were used to calculate the constants.

$$c = \frac{\lambda}{sin\theta} \tag{4.3}$$

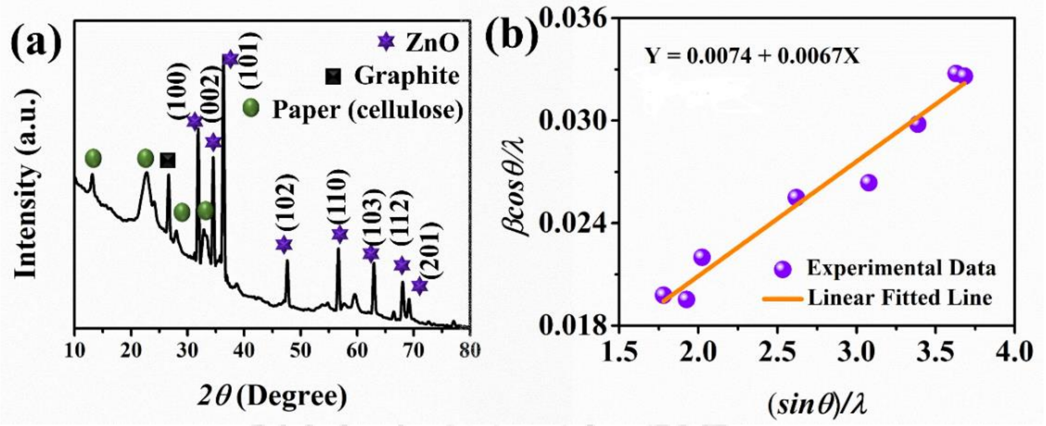

Figure 4.3. (a) XRD pattern of the sample, (b) $\frac{\beta cos\theta}{\lambda}$ vs. $\frac{sin\theta}{\lambda}$ plot.

$$a = \sqrt{\frac{1}{3}} \frac{\lambda}{sin\theta} \tag{4.4}$$

The calculated values are reported in table 4.1. A little deviation in the values of these lattice constants from the standard values can be attributed to the thermal as well as the lattice mismatch between the ZnO nanorods and the substrate on which the rods were grown. Apart from the peaks corresponding to ZnO, the peaks for the paper substrate (cellulose) can also be observed in the XRD plot shown in figure 4.3a. The broad diffraction peaks from 13 to 15 and 21 to 25° suggest the presence of cellulose, which is in good agreement with the previous reports [35, 36]. The peak at 26.5° confirms the existence of graphitic carbon in the substrate material [37].

Table 4.1. Lattice constants for different crystalline planes.

Crystalline plane	2θ	c(nm)	a(nm)
100	31.86°	5.061	3.239
002	34.54°	5.187	2.994
101	36.36°	4.936	2.849

The information about the defects in the synthesized ZnO was obtained from the PL spectra of the ZnO nanorods. Figure 4.4a shows the PL peaks of the nanorods at two different excitation wavelengths (340 and 380 nm). The peaks in this figure convey that the ZnO nanorods emit at a wide range of wavelengths. The presence of UV emission (370–385 nm) in the PL can be attributed to the recombination of the excitons, which were created near the bandgap region of the ZnO nanorods. The emissions at zones of green (485–525 nm), blue (455–485 nm), and violet (385–455) correspond to the deep level emissions (DLE) [38, 39]. The DLEs occur because of the presence of structural defects in ZnO nanorod crystals. These structural defects can be of several types, such as zinc vacancies, Zn interstitials intrinsic defects, oxygen antisites, oxygen vacancies, etc. [38] The presence of green emission gets prominent when the excitation wavelength gets increased, as shown in figure 4.4a. This phenomenon can well be explained with the term “red-edge-effect” (REE), where the emission maxima get red-shifted with the increase in excitation wavelength [40]. This red shift of the peak with the increase in excitation

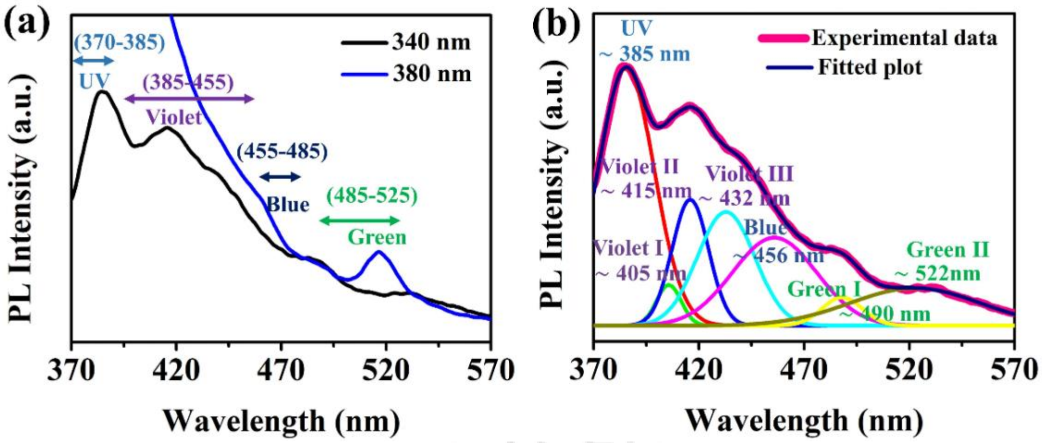

Figure 4.4. (a) PL peaks of ZnO at excitation wavelengths of 340 nm and 380 nm. (b) Deconvoluted PL peak of 340 nm excitation wavelength.

wavelength can be explained as follows. The ZnO sample gets exposed to higher energy when it is excited at a lower wavelength, compared to the case when it is excited at a higher wavelength. Therefore, when it gives the emission spectra corresponding to its excitation wavelength, we can observe the peak at a lower emission wavelength for a lower excitation wavelength and vice versa. That is why, when the excitation wavelength gets increased, the presence of the green emission also gets prominent, whereas, in the case of a lower excitation wavelength, the other peaks (such as violet, blue, etc.) were more prominent. A similar sort of characteristic was generally recorded for ionic liquid (IL) with a dipolar probe molecule [41, 42]. In our system also, the ZnO nanorods were dispersed in water (polar solvent) to obtain the PL spectra, which emphasized getting a prominent green emission as the excitation light gets increased (from 340 to 380 nm). The emission peak (excitation: 340 nm) has been deconvoluted in figure 4.4b to show the presence of individual components separately. The emission at ~385 nm in this figure is corresponding to the exciton-based emission. In this case, the electron-hole recombination can occur at the valance band or at the traps present nearer to the valance band. The peak at ~405 nm is due to the electronic transition to the single ionized oxygen vacancy (V_O^+)from the conduction band. The peaks at ~415, ~432, and ~456 nm can be attributed to the presence of defects such as interstitial Zn (Zn_i), ionized interstitial Zn (Zn_i^-), and doubly ionized interstitial Zn (Zn_i^{2-}) defects, respectively. The oxygen antisite (O_{Zn}), and the deep level oxygen vacancy (V_O) can be the reason behind the emission peaks in the green zone [38, 39]. The PL of the ZnO attached with CD is also shown in figure 4.5. In this figure, it is observed that the V_O, Zn_i, and Zn_i^{2-} defects have remained intact into the composite as there are peaks in the green and violet zones.

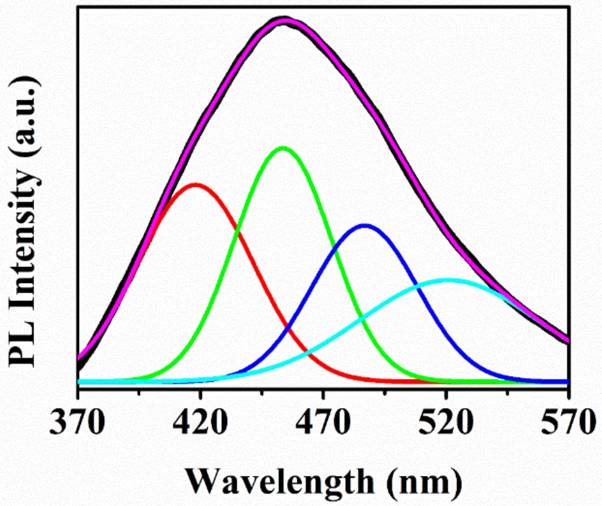

Figure 4.5. Deconvolute PL peak of CD enhanced ZnO nanorods at an excitation wavelength of 340 nm.

.

4.3.2. Schottky diode analysis

Figure 4.6a represents a schematic diagram of the experimental setup. The image of the CD-attached ZnO nanorod grown on the graphite-coated paper substrate is also shown in the inset of this figure. The current versus voltage (*I*–*V*) plot in the absence of light is shown in figure 4.6b, along with its semilogarithmic plot (inset). It is evident from this figure that the *I*–*V* characteristic follows rectifying behavior. The diode shows rectifying nature even when the ZnO rods are not enhanced with CDs. The *I*–*V* plot of the diode (without CD decoration) is shown in figure 4.6c. The attachment of the CDs on the ZnO nanorods has helped the diode to intensify the rectification ratio from 3.13 to 17.33 at ±1.2 V. The graphite/ZnO interface can be deemed responsible for this rectifying behavior. Owing to the unavoidable gap between the work function of graphite (5.0 eV) and the electron affinity of ZnO (4.35 eV), the heterojunction of graphite/ZnO nanorod behaves as a typical metal–semiconductor heterojunction Schottky diode [43]. The parameters of the Schottky diode, like ideality factor (η), series resistance (R_s), and the

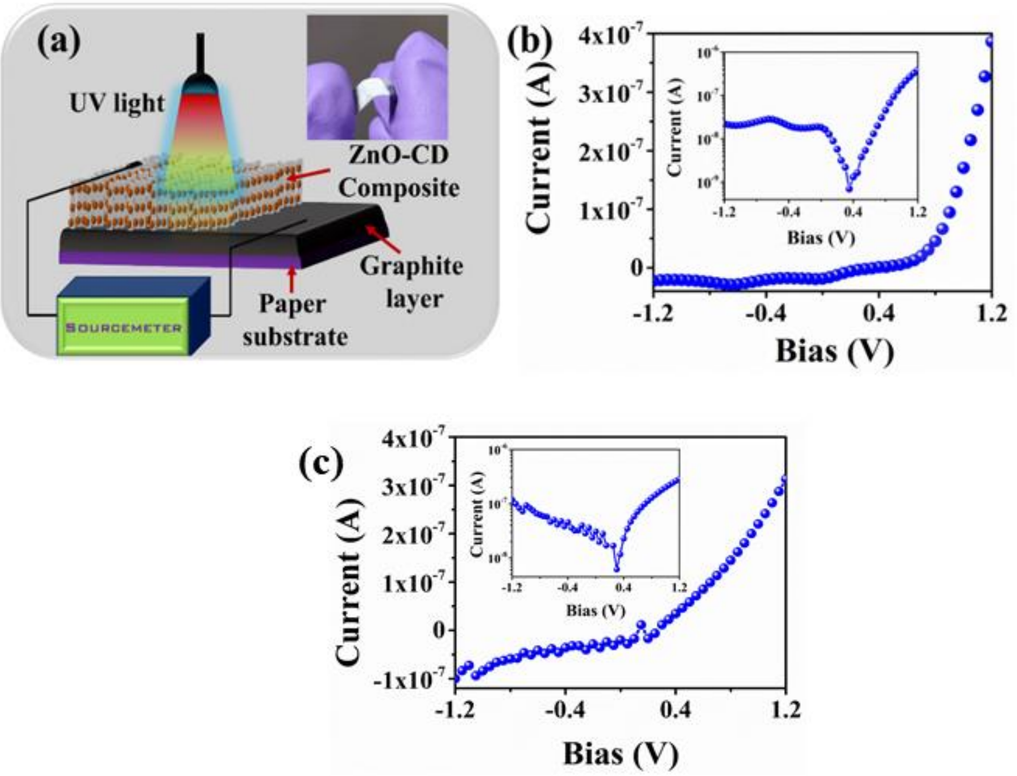

Figure 4.6. (a) Schematic representation of the experimental setup and a photograph of the Schottky diode (inset). (b) $I\!-\!V$ plot of the CD enhanced ZnO/graphite Schottky diode in linear and semilogarithmic scale (inset) in dark. (c) $I\!-\!V$ plot of the ZnO/graphite Schottky diode in linear and semilogarithmic scale (inset) in dark.

barrier height (ϕ_B) were obtained from the method, as shown by Cheung–Cheung [44]. The equations used in this method are as follows.

$$\frac{dV}{d(lnI)} = IR_s + \eta\frac{K_BT}{q} \tag{4.5}$$

$$H(I) = V - \eta(\frac{K_BT}{q})\ln(\frac{I}{AA^*T^2}) \tag{4.6}$$

$$H(I) = IR_s + \eta\phi_B \tag{4.7}$$

In these equations, the terms V, K_B, T, q, A, and A^* correspond to the applied bias, Boltzman constant, temperature (300 K), electronic charge, exposed device area, and Richardson constant (36 A cm^{-2} K^{-2}) [1], respectively. The plots $\frac{dV}{d(lnI)}$ vs. I and $H(I)$ vs. I obtained from equations 4.5 and 4.7, respectively, give straight lines. The y-axis intercept and the slope of the plot $\frac{dV}{d(lnI)}$ vs. I presented in figure 4.7a gives the values of the ideality factor and series resistance, respectively. In the case of figure 4.7b, i.e., the plot $H(I)$ vs. I, the intercept to the y-axis gives the value of $\eta\phi_B$.

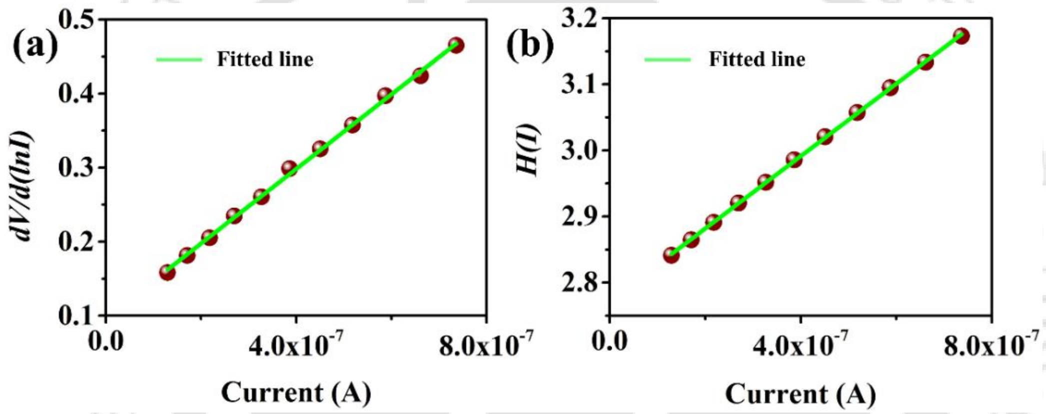

Figure 4.7. (a) $\frac{dV}{d(lnI)}$ vs. I plot, (b) $H(I)$ vs. I plot of the CD enhanced ZnO/graphite Schottky diode in dark condition.

The calculated values of the ideality factor, series resistance, and the barrier height are 3.74, 503 kΩ, and 0.74 eV, respectively. The presence of trapped electrons on the surface of the ZnO nanorods can be the reason behind the deviation of the ideality factor from the ideal Schottky diode ($\eta \approx 1$). One unavoidable characteristic of the diode is that the I–V curve does not pass through the origin of the plot (figure 4.6b). The curve, not passing through the origin, suggests the presence of voltage source characteristics as well in the Schottky diode [45]. The probable reason behind this particular characteristic is the defects that are present in the ZnO crystals. The presence of the defects can trap charges in the nanorods, for which there can be an accumulation of charges in the defects of the nanorod crystals [46]. The accumulation of the carrier charges ultimately leads to giving a non-zero current at a 0 V bias voltage. This current, generated in the device, is dependent on the trap levels present in the semiconductor materials [47]. The distribution of energy of the trapping levels is associated with the imperfections present in the structure of the crystal [46]. Mark and Helfrich reported the trap-effect on the charge (electron) transport, the energy of which is distributed exponentially [48]. The relation between the free carriers and the trapped carrier density and the trap-limited current are as follows [46, 48, 49],

$$\frac{n}{N} = \left(\frac{n_t}{N_t e^{E_{tc}/K_B T_t}}\right)^r \tag{4.8}$$

$$I = A N_c q \mu_e \left(\frac{\varepsilon_0 \varepsilon_r}{q N_t e^{E_{tc}/K_B T_t}}\right)^r \left[\left(\frac{2r+1}{r+1}\right)^{r+1} \left(\frac{r}{r+1}\right)^r\right] \frac{V^{r+1}}{L^{2r+1}} \tag{4.9}$$

where n denotes the free carrier density, N is the transport sites' density, n_t corresponds to the trapped carrier density, the trap density is represented by N_t, $E_{tc}$is trap-energy, which is measured either from the underneath of the CB (conduction band; electron trap) or from the top side of the VB (valance band; holes trap), $r = T_t/T$, with T being the temperature, whereas T_t is the trap-temperature, and K_B represents Boltzman constant. I, A, N_c, q, μ_e correspond to the current (trap-limited), exposed device area, effective density of states (DOS), electronic charge, and the free electron mobility, respectively. ε_0, ε_r are the permittivity in vacuum and the relative permittivity, respectively, whereas, V corresponds to the applied voltage and L is the thickness of the device. According to equation 4.9, the r-value can be obtained directly from the slope of the plot between log(I) and log(V), which is shown in figure 4.8. In this figure, the two parameters (log(I) and log(V)) have been plotted in the forward bias condition. The slope of the best fit line is 5.48. This slope value (>2) indicates the trap-limited space-charge-limited-current (SCLC) through the diode in the forward bias condition [50]. In another way, there occurs a phenomenon of charging and discharging of current in the semiconductor junction [51]. This additional current is completely dependent on the direction of the sweep. Based on the sweep direction, the overall carrier transportation through the junction either increases or decreases. A similar phenomenon has been witnessed for Schottky diodes, which are fabricated using ZnO [51].

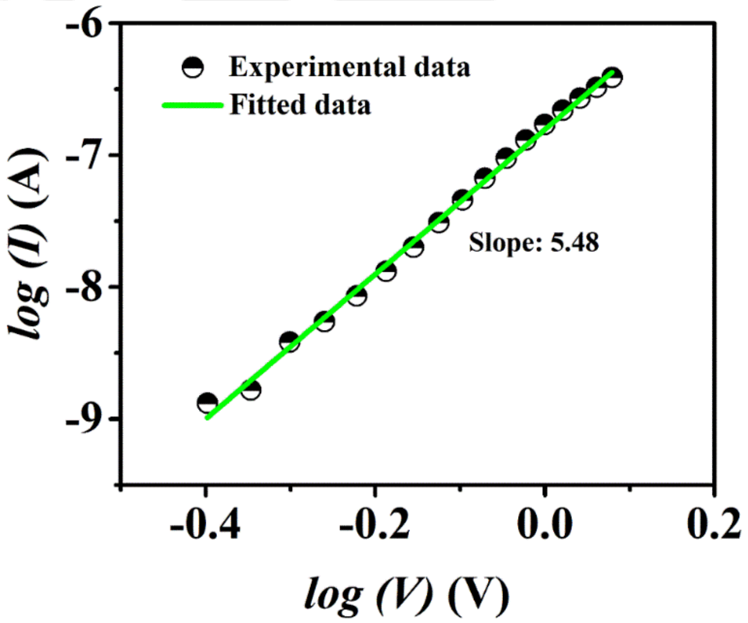

Figure 4.8. log(I) vs. log(V) plot of the CD enhanced ZnO/graphite Schottky diode (in the forward bias condition).

4.3.3. Photoresponsive behavior of the diode

We have studied the photodetector properties of the diode. Figure 4.9a represents the I–V curve of the device in dark and illuminated conditions. For illumination, full spectra of

UV light with a power density of 20 mW/cm^2 were used. A semilogarithmic *I–V* plot of the same is also shown in the inset. The generation of photocurrent in the presence of light is quite evident in this figure. However, more interestingly, it is observed that the diode possesses a photovoltaic effect as well. The photovoltaic property of the diode is shown in figure 4.9b. The encircled section of figure 4.9a is magnified in figure 4.9b. The photocurrent generated was 19 nA. The photovoltaic effect of the diode, i.e., the generation of the photocurrent, can be attributed to the operation of the photodiode at the self-biased condition. Figure 4.10a shows the transient response (*I–t*) of the diode at zero bias voltage to show its ability to be operated at the self-biased condition. This plot shows a good ON/OFF current of the diode at zero bias voltage. The characteristics of the transient response at zero bias voltage are represented in the plot shown in figure 4.10b. The response time and recovery time of the diode are obtained to be 2 and 3.2 s, respectively. The comparatively slower response time and recovery time can be explained based on the mechanism of the photocurrent generation of the ZnO photodiode. The photoresponsive behavior of the ZnO nanorods is basically based on the

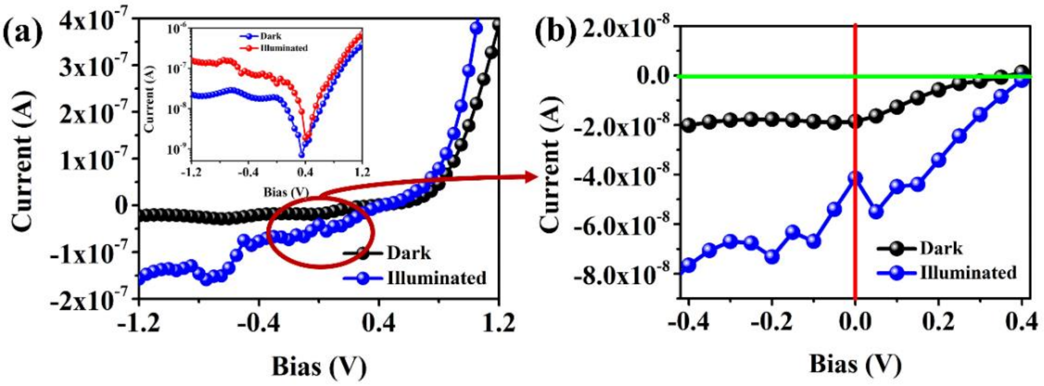

Figure 4.9. (a) *I*−*V* plot of the CD enhanced ZnO/graphite Schottky diode in linear and semilogarithmic scale (inset) in dark and illuminated conditions. (b) Zoomed in image of the encircled section of (a).

adsorption/desorption process of the atmospheric oxygen on the ZnO surface (the detailed mechanism is discussed in the later section; section 4.3.5). When the diode is excited with UV light, the photodesorption of the adsorbed oxygen from the ZnO surface starts occurring, whereas the re-adsorption of the oxygen molecules on the ZnO surface starts

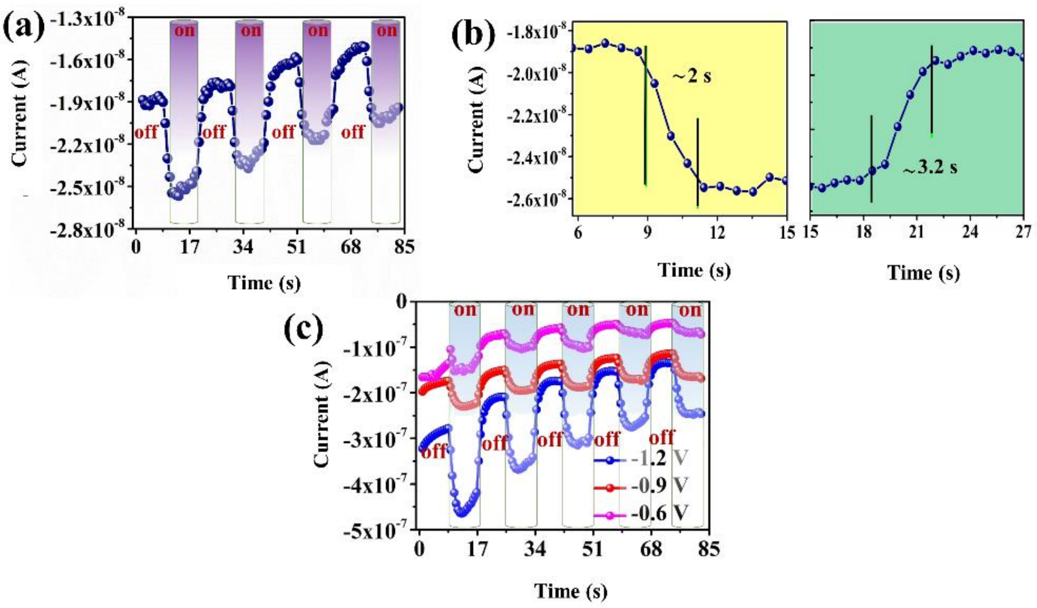

Figure 4.10. (a) Transient response of the Schottky diode at self-powered condition. (b) Response and recovery time extraction from the transient response. (c) Transient response at different reverse bias conditions. The power density of the used UV light for illumination is 20 mW/cm^2.

when the UV light is switched off [1]. This adsorption and desorption of the atmospheric oxygen molecules is a time consuming process, which has already been reported by several researchers [44, 52]. Hence, we can assume that the slower response and recovery time of the photodiode is due to the adsorption/desorption process of oxygen molecules on the ZnO surface. However, the slow response of the ZnO based photodiodes can be overruled by encapsulating the ZnO nanorods with suitable encapsulating materials (for example SiO_2) as reported by Özdoğan *et al*. [52] The transient response of the diode at different reverse bias is also shown in figure 4.10c. In this figure, it is observed that the diode maintained its transient characteristics at different bias voltages as well. To make this statement clearer, one cycle of the transient response of the diode at bias voltages −0.6, −0.9, and – 1.2 V are shown in figure 4.11 to represent the response and recovery times at these bias voltages, respectively. The response times of the diode at bias voltages −0.6, −0.9, and – 1.2 V are calculated to be 2.15, 2.3, and 2.37 s, respectively, whereas the recovery times are 2.35, 2.32, and 2.14 s respectively. It is noteworthy that the response time has decreased, whereas the recovery time has increased along with the decrement of the reverse bias voltage.

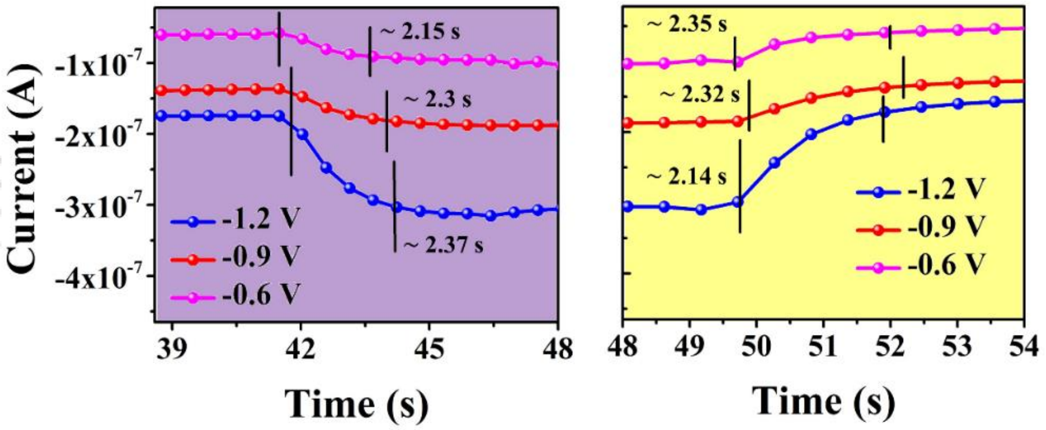

Figure 4.11. The response time and the recovery time of the CD enhanced ZnO/graphite Schottky diode at different reverse bias voltages.

4.3.4. Band diagram

To explain the Schottky diode characteristics, the band diagrams of the graphite/ZnO nanorod (n-type) heterojunction at different bias conditions are shown in figure 4.12. Figure 4.12a represents the schematic of the basic band structures of graphite and ZnO nanorods before contact. The terms E_{vac}, E_C, E_F, and E_V correspond to the energy of the vacuum, conduction band, Fermi level, and valance band, respectively. The work functions of graphite (Φ_{graphite}) and ZnO (Φ_{ZnO}) were taken as 5 and 4.5 eV, respectively, whereas the electron affinity and gap energy (E_g) of ZnO were considered to be 4.35 and 3.37 eV, respectively. These values were extracted from previous literature studies [43, 53]. The moment a contact between the graphite and ZnO nanorod occurs, the diode junction attains thermal equilibrium by making both the Fermi layers flat. As a result, a band-bending phenomenon takes place, as shown in figure 4.12b. Generally, the transportation of electrons from graphite to ZnO starts occurring due to the contact between them. This transfer of electrons continues till the Fermi levels of graphite and ZnO become flat. This flattening of fermi levels is responsible for the bending of the energy band, as represented in figure 4.12b. Owing to this phenomenon, a depletion region gets formed in the junction of the Schottky diode, and it is represented as D_r.

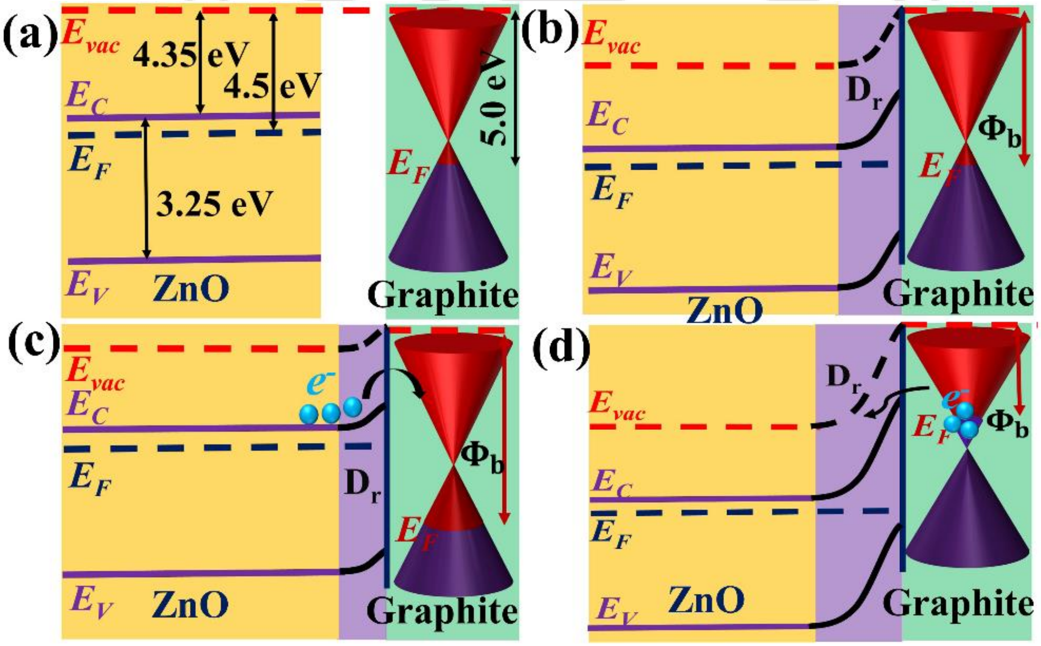

Figure 4.12. Schematic representation of the band diagram of ZnO/graphite interface, (a) before contact, (b) at zero bias, (c) at forward bias, (d) at reverse bias.

Before moving to the band diagrams at different bias conditions, it is worthwhile to mention that, at reverse bias condition of the diode, the current does not attain any particular saturation point. In figure 4.13, the *I*–*V* curve at the reverse bias voltage is shown and it is obvious from the figure that the reverse current does not attain saturation point. The oscillatory nature of the curve can be associated with the tunnelling of current. Moreover, the reason behind the non-saturation current can be known through tuning the Fermi energy level of graphite by applying a single cathode–anode bias [54]. For example, the application of a forward bias to the graphite deepens the Fermi energy level and hence raises the work function, as shown in figure 4.12c. On the other hand, in the reverse bias condition, the work function gets reduced due to the rise in the Fermi energy level as portrayed in figure 4.12d. This reduction of the work function of the graphite becomes more dominant as the bias voltage gets increased in the reverse direction and causes a variation in Schottky barrier height (SBH). This phenomenon ultimately leads

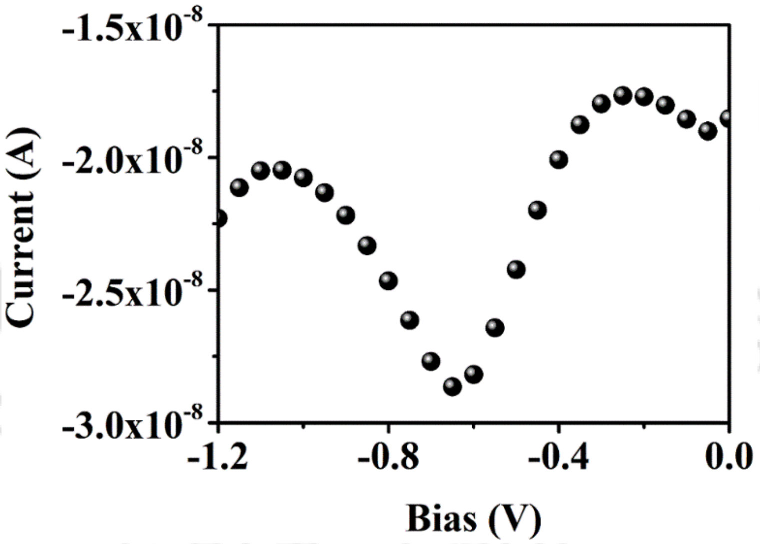

Figure 4.13. Non-saturation characteristic of reverse current of the CD enhanced ZnO/graphite Schottky diode in dark.

to obtain an unsaturated reverse current. The upward bending of the band helps the diode to transport electrons from the conduction band of the ZnO nanorod to graphite, as shown in figure 4.12c. However, the reverse bias at the junction enforces the transportation of electrons from graphite to the conduction band of the ZnO nanorods, as shown in figure 4.12d.

4.3.5. Self-powered (zero biased) photodetection and flexibility of the diode

The self-powered UV detection can be explained with the help of figure 4.14. First of all, the formation of the heterojunction between the CD-attached ZnO nanorods and graphite enforces the band bending phenomenon, as shown in figure 4.14a. Furthermore, in the literature, it is reported that there are trapped electrons on the oxide surface of n-type ZnO nanorods [1, 55]. Therefore, in dark conditions, the ambient atmospheric oxygen (O_2) molecules get adsorbed on electron-trapped ZnO surface $[O_2(g) + e^- \rightarrow O_2^-(ad)]$. This leads to develop a depletion layer on the surface, which ultimately endorses a built-in

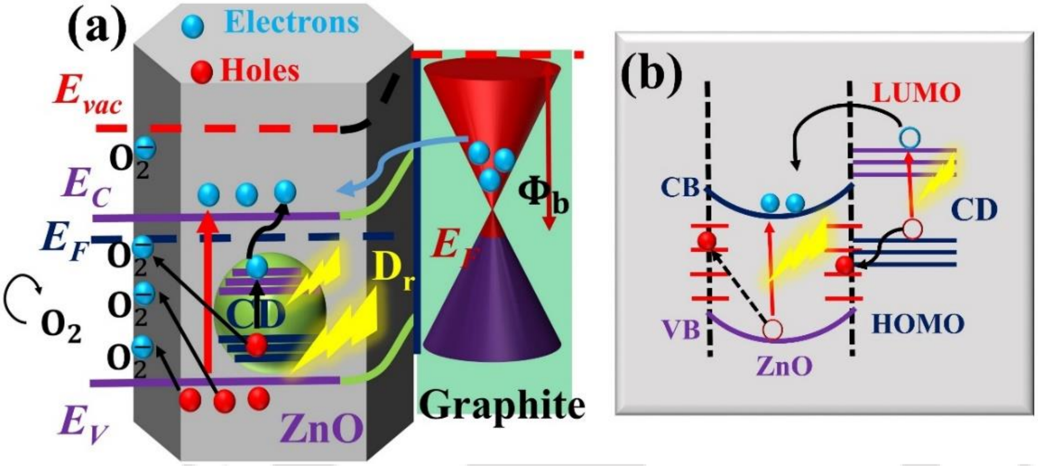

Figure 4.14. (a) The photocurrent generation mechanism of the CD enhanced ZnO/graphite Schottky diode in self-powered condition. (b) Participation of the CD in hole trapping mechanism on ZnO surface.

potential at the graphite/ZnO heterojunction, as shown in the figure. The moment photon energy (UV light) is falling on the surface, the generation of electron-hole pairs get started $[h\vartheta \rightarrow e^- + h^+]$. Afterward, these generated holes (h^+) travel toward the surface of the nanorods owing to the band bending, which ultimately leads to release the adsorbed $O_2^-(ad)$ ions $[h^+ + O_2^-(ad) \rightarrow O_2(g)]$. As a consequence, the oxygen molecules get photodesorbed [55]. The remaining unpaired electrons move toward the electrodes, which enrich the photocurrent in the diode. Considering all these characteristics of ZnO for generating photocurrent, our fabricated Schottky diode showed even more advantages by being able to be operated at zero bias condition. A meticulous investigation of our results indicates that the ability of the graphite/ZnO heterojunction to be operated in the self-powered condition is because of its working mechanism, which follows the photovoltaic effect. In the device, the photovoltaic effect exploits the built-in potential produced by the Schottky barrier in the junction, to drift away the generated electron-hole pairs. Hence, it induces a rise in the photocurrent. Moreover, the attachment of CD on the ZnO enhances more generation of photocurrent in the device. As the CD is also UV responsive, the illumination causes a generation of electron-hole pairs in the CD as well, as represented in figure 4.14a. These generated holes have a fair share of possibilities to be transported to the ZnO surface and participated in the oxygen photodesorption mechanism. Meanwhile, the electrons join the other remaining electrons of ZnO, which move to the connected electrodes, which ultimately helps in enhancing photocurrent. To make this statement clearer, we have shown a pictorial representation of the probable mechanism in figure 4.14b. As the CD is also UV responsive, the electron gets excited in the presence of UV and transferred to the LUMO, leaving behind a generated hole in the HOMO, as shown in this figure. This generated electron in the LUMO of the CD then travels toward the CB, whereas the hole moves toward the trapping sites of the ZnO nanorods, as shown in the figure. The trapping of holes of the CDs (along with the holes trapping of ZnO) ultimately reduces the possibility of electron–hole recombination, resulting in the generation of a higher photocurrent compared to the pristine ZnO. This hole trapping phenomenon because of the presence of CD is also reported by Dhar *et al.* [1] in their work. Another probability is that the left holes in the HOMO of the CDs then take part in electrostatic interaction with the negatively charged oxygen-containing species at the surface of the ZnO nanorods. Therefore, the desorption of the oxygen molecule (neutral) in the atmosphere gets enhanced, leaving the CD in its charge-neutral condition [56].

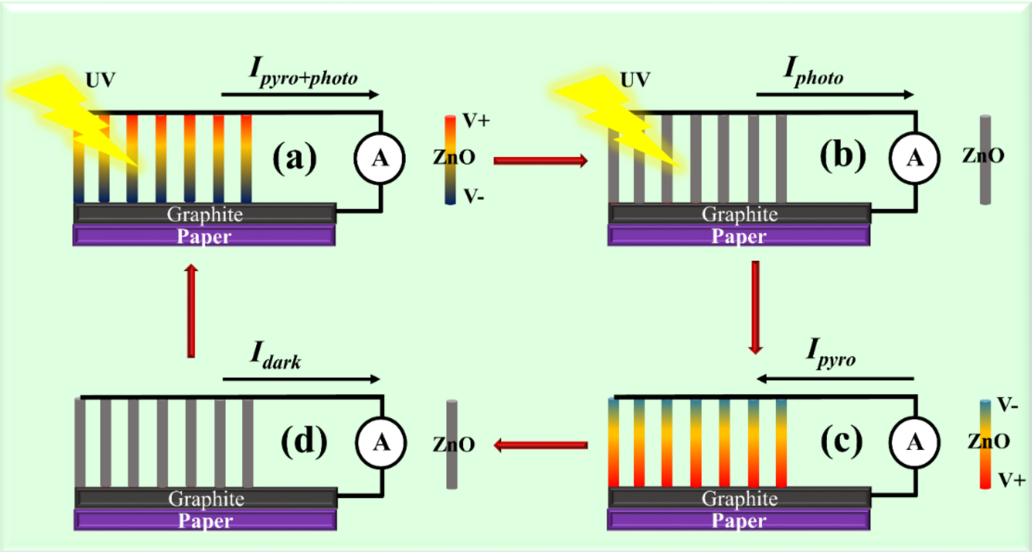

Figure 4.15. Mechanism of pyro-phototronic current generation. (a) Generation of photocurrent and pyro-current. (b) Flow of photocurrent. (c) Flow of pyrocurrent under dark condition. (d) Flow of dark current.

The ability of the photodiode to be operated at self-biased condition can also be explained in terms of the pyro-phototronic effect.[57, 58]. A complete four-stage dynamics is shown in figure 4.15. At first, during UV illumination, the photodiode absorbs the light and generates electron-hole pairs. Besides this, the transient temperature of the ZnO nanorods gets also increased, which leads to the generation of pyroelectric potentials (pyro-potentials) in the ZnO nanorods because of its pyroelectric effect. This pyro-potential helps to obtain I_{pyro} (pyro-current) along with I_{photo} (photocurrent). That is why the generated current in the first stage of UV-illumination is contributed by both I_{photo} and I_{pyro} This current is denoted as $I_{\text{pyro + photo}}$ as shown in figure 4.15a. In the next stage, the current is mainly contributed by I_{photo} because the variation in the temperature of the ZnO nanorods attains a halt, and it is represented in figure 4.15b. Similarly, when the UV is turned off, initially due to the decrease in transient temperature I_{pyro} comes into the play, followed by the dark current (I_{dark}) when the temperature gets stagnant in the ZnO nanorods as shown in figure 4.15c,d, respectively. In the transient response, shown in figure 4.10a, it is observable that the current does not attain a saturated value instantly when it is exposed under UV. Initially, the current value gets spiked and then slowly gets decreased under the illuminated condition, which proves the presence of the pyro-phototronic effect in our device. However, the sudden spikes in current during the illuminated condition are not sharp. The peak is rather broadened. This can be due to the direct connection of the tungsten probe with the ZnO end of the device. The performance of the fabricated self-powered flexible photodetector has been evaluated by calculating the responsivity (R_λ), the external quantum efficiency (EQE), and the specific detectivity (D^*) at zero bias condition. All the values (i.e., R_λ, EQE, and D^*) are attained considering the presence of both photocurrent and pyrocurrent. The responsivity of a photodiode can be defined as the amount of photocurrent generated per unit power density, whereas the EQE can be denoted as the number of charge carriers produced in the form of electrons per unit incident photon energy. On the other hand, D^* gives the idea about the ability of the photodiode to detect weak optical signals. The formulae for the calculation of EQE and responsivity are as follows [21, 44].

$$\mathrm{EQE}\ (\%) = \frac{1240 I_\lambda}{A\lambda P_\lambda} \times 100 \qquad (4.10)$$

$$R_\lambda = \frac{I_\lambda}{A P_\lambda} \qquad (4.11)$$

$$D^* = \frac{R_\lambda}{\left(\frac{2qI_{OFF}}{A}\right)^{\frac{1}{2}}} \qquad (4.12)$$

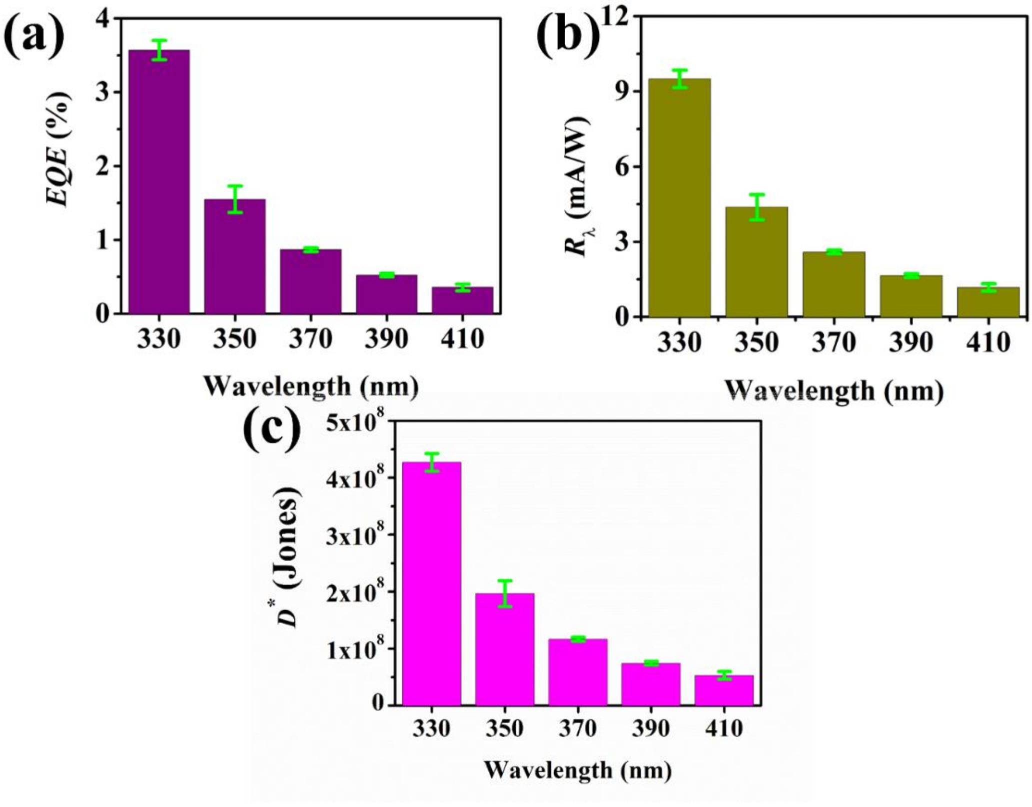

Figure 4.16. (a) External quantum efficincy (EQE) vs. wavelength plot, (b) responsivity vs. wavelength plot, and (c) specific detectivity vs. wavelength.

In these equations, I_λ denotes the combination of photocurrent and pyrocurrent, A is the active area, λ is the wavelength, and P_λ denotes the power density of the incident light (mW/cm^2). The plots between EQE and wavelength, R_λ and wavelength, and D^* and wavelength are portrayed in figure 4.16a−c, respectively. The maximum value is obtained at the 330 nm wavelength as shown in the figures. The obtained maximum values of EQE, R_λ, and D^* at zero applied voltage are 3.57%, 9.5 mA/W, 4.27×10^8 Jones,

Table 4.2. Comparison of the photodiode parameters.

Material	**Flexible**	**Self-powered**	**Response time**	**Recovery time**	**Responsivity**	**Ref.**
Graphene/ZnO	Yes	No	8.76 s	18.13 s	6.27 mA/W	[59]
ZnO/GaN	No	Yes	1023.5 ms	40.1 ms	225 mA/W	[60]
CuO/ZnO	No	Yes	27 s	5 s	0.272 mA/W	[61]
ZnO/Al_2O_3	No	Yes	<100 s	<100 s	1.78 μA/W	[17]
ZnO/CuSCN	No	Yes	4 ns	6.7 μs	-	[62]
$CsPbBr_3$:ZnO	No	Yes	0.409 s	0.0178 s	11.5 mA/W	[63]
Cl-ZnO NRs/DMSO-PEDOT:PSS	No	Yes	30 ms	32 ms	0.80 mA/W	[64]
Cl:ZnO NRs/PEDOT:PSS	No	Yes	28 ms	23 ms	2.33 mA/W	[57]
n-ZnO/p-NiO	No	Yes	0.23 s	0.21 s	0.44 mA/W	[65]
p-ZnO(Li,N)/ n-ZnO	No	Yes	-	-	0.018 mA/W	[66]
ZnO NWs/CuSCN	No	Yes	-	-	0.02 A/W	[67]
Graphene/ZnO :Al NRs	No	Yes	37 μs	330 μs	-	[68]

Table 4.2. Comparison of the photodiode parameters.

Material	Flexible	Self-powered	Response time	Recovery time	Responsivity	Ref.
Polyaniline/ MgZnO	No	Yes	0.3 s	0.3 s	0.16 mA/W	[69]
p-GaN/n-ZnO	No	Yes	-	-	0.68 mA/W	[70]
ZnO NRs & Pt/FTO PECC	No	Yes	0.09 s	0.31 s	2.33 A/W	[71]
Graphene/ZnO NWs	No	No	11.9 s	240 s	32000 A/W	[72]
Graphite/ZnO	**Yes**	**Yes**	**2 s**	**3.2 s**	**9.5 mA/W**	**Current work**

respectively. A comparison between different diode parameters with previously reported articles are shown in table 4.2 (ZnO photodiodes). It is observed from the table that our

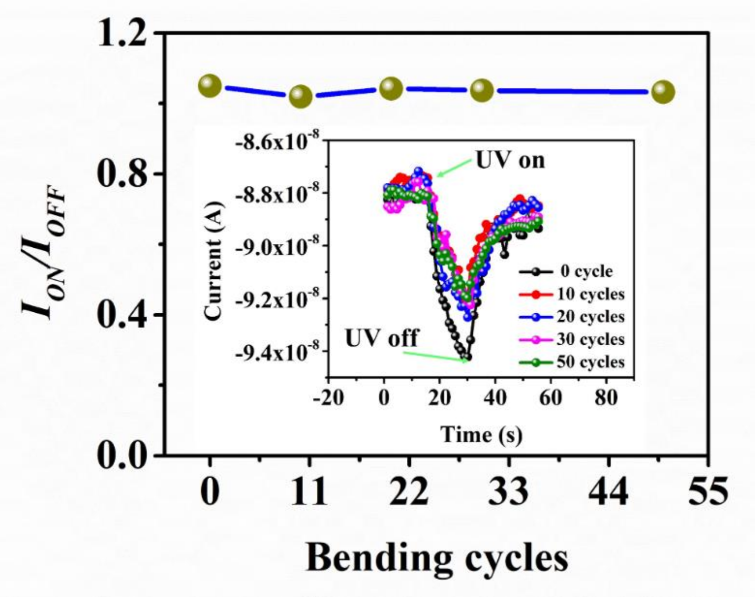

Figure 4.17. ON/OFF current ratio of the flexible UV-detector at different bending cycles. The inset shows the corresponding transient responses at the same bending cycles.

system is giving better results in terms of response and recovery time as well as the responsivity considering the possession of two important properties such as its flexibility and ability to be operated at the self-powered conditions.

The flexibility of the fabricated Schottky diode has also been tested, and the result is shown in figure 4.17. The ON/OFF current ratio at different bending cycles is shown in this figure, and the corresponding transient response of the device is also presented in the inset. It is evident from the figure that after 50 bending cycles, the photodiode retains its ON/OFF current ratio more than 90% of the first bending cycle. This observation proves that our device can be used as a flexible photodetector.

4.4. Conclusions

In summary, we have successfully grown ZnO nanorods on a graphite-coated paper substrate. The detailed characteristics of the as-grown ZnO nanorods, such as the crystallinity and presence of different defects, have been discussed in detail. The ZnO nanorods were then decorated with CDs. The graphite and the CD-decorated ZnO heterojunction on a paper substrate has been characterized and proven as a Schottky diode by providing its Schottky diode parameters. These Schottky diode parameters, such as the ideality factor, series resistance, and the Schottky barrier height, have been obtained from the I–V characteristics with the help of the Cheung–Cheung method. The photoresponsive behavior of the diode has also been studied using a broadband UV light source. A noteworthy observation from the photoresponsive behavior of the Schottky diode is its ability to be operated at self-powered condition, owing to the presence of the photovoltaic effect in the heterojunction. The transient response at self-powered condition has also been represented which has helped us in obtaining the response time and recovery time of the diode as ~2 and ~3.2 s, respectively. A probable explanation behind the self-powered photosensing mechanism has been provided. The responsivity and the specific detectivity of the fabricated UV detector have been calculated as 9.57 mA/W and 4.27×10^{8} Jones, respectively, at a 330 nm wavelength. So, in a nutshell, we have successfully fabricated a self-powered flexible CD-enhanced ZnO/graphite heterojunction-based Schottky diode, which was used to detect UV light.

References

[1] S. Dhar, T. Majumder, S.P. Mondal, ACS Applied Materials & Interfaces, 8 (2016) 31822.

[2] D. De Fazio, B. Uzlu, I. Torre, C. Monasterio-Balcells, S. Gupta, T. Khodkov, Y. Bi, Z. Wang, M. Otto, M.C. Lemme, S. Goossens, D. Neumaier, F.H.L. Koppens, ACS Nano, 14 (2020) 11897.

[3] N.A. Putri, V. Fauzia, I. Isnaeni, I. Lewa, C. Imawan, IOP Conference Series: Materials Science and Engineering, 1098 (2021) 062071.

[4] R. Sinha, A.P. Bidkar, R. Rajasekhar, S.S. Ghosh, T.K. Mandal, The Canadian Journal of Chemical Engineering, 98 (2020) 194.

[5] H. Wang, S. Cao, B. Yang, H. Li, M. Wang, X. Hu, K. Sun, Z. Zang, Solar RRL, 4 (2020) 1900363.

[6] C. Li, Z. Zang, C. Han, Z. Hu, X. Tang, J. Du, Y. Leng, K. Sun, Nano Energy, 40 (2017) 195.

[7] Z. Zang, X. Tang, Journal of Alloys and Compounds, 619 (2015) 98.

[8] Z. Zang, Applied Physics Letters, 112 (2018) 042106.

[9] Y. Jin, J. Wang, B. Sun, J.C. Blakesley, N.C. Greenham, Nano Letters, 8 (2008) 1649.

[10] N. Gogurla, A.K. Sinha, S. Santra, S. Manna, S.K. Ray, Scientific Reports, 4 (2014) 6483.

[11] C. Tian, D. Jiang, B. Li, J. Lin, Y. Zhao, W. Yuan, J. Zhao, Q. Liang, S. Gao, J. Hou, J. Qin, ACS Applied Materials & Interfaces, 6 (2014) 2162.

[12] F. Zhang, S. Niu, W. Guo, G. Zhu, Y. Liu, X. Zhang, Z.L. Wang, ACS Nano, 7 (2013) 4537.

[13] H. Zhang, A.V. Babichev, G. Jacopin, P. Lavenus, F.H. Julien, A.Y. Egorov, J. Zhang, T. Pauporté, M. Tchernycheva, Journal of Applied Physics, 114 (2013) 234505.

[14] B. Deka Boruah, Nanoscale Advances, 1 (2019) 2059.

[15] F. Guo, B. Yang, Y. Yuan, Z. Xiao, Q. Dong, Y. Bi, J. Huang, Nature Nanotechnology, 7 (2012) 798.

[16] P. Lin, X. Yan, Z. Zhang, Y. Shen, Y. Zhao, Z. Bai, Y. Zhang, ACS Applied Materials & Interfaces, 5 (2013) 3671.

[17] Z. Zhang, Q. Liao, Y. Yu, X. Wang, Y. Zhang, Nano Energy, 9 (2014) 237.

[18] S. Sarkar, D. Basak, ACS Applied Materials & Interfaces, 7 (2015) 16322.

[19] R. Dong, C. Bi, Q. Dong, F. Guo, Y. Yuan, Y. Fang, Z. Xiao, J. Huang, Advanced Optical Materials, 2 (2014) 549.

[20] Z. Zou, C. Xie, S. Zhang, C. Yang, G. Zhang, L. Yang, Sensors and Actuators B: Chemical, 188 (2013) 1158.

[21] F. Cao, W. Tian, L. Meng, M. Wang, L. Li, Advanced Functional Materials, 29 (2019) 1808415.

[22] S. Chen, C. Teng, M. Zhang, Y. Li, D. Xie, G. Shi, Advanced Materials, 28 (2016) 5969.

[23] D. Xiong, W. Deng, G. Tian, Y. Gao, X. Chu, C. Yan, L. Jin, Y. Su, W. Yan, W. Yang, Nanoscale, 11 (2019) 3021.

[24] Y. Gao, J. Xu, S. Shi, H. Dong, Y. Cheng, C. Wei, X. Zhang, S. Yin, L. Li, ACS Applied Materials & Interfaces, 10 (2018) 11269.

[25] C. Bao, W. Zhu, J. Yang, F. Li, S. Gu, Y. Wang, T. Yu, J. Zhu, Y. Zhou, Z. Zou, ACS Applied Materials & Interfaces, 8 (2016) 23868.

[26] H. Sun, W. Tian, F. Cao, J. Xiong, L. Li, Advanced Materials, 30 (2018) 1706986.

[27] S.-F. Leung, K.-T. Ho, P.-K. Kung, V.K.S. Hsiao, H.N. Alshareef, Z.L. Wang, J.-H. He, Advanced Materials, 30 (2018) 1704611.

[28] H. Lu, W. Tian, F. Cao, Y. Ma, B. Gu, L. Li, Advanced Functional Materials, 26 (2016) 1296.

[29] R. Saraf, V. Maheshwari, ACS Applied Materials & Interfaces, 10 (2018) 21066.

[30] V.D. Mote, Y. Purushotham, B.N. Dole, Journal of Theoretical and Applied Physics, 6 (2012) 6.

[31] Y. Du, F. Zhao, L. Liu, Y. Gao, L. Xing, Q. Li, C. Fu, Z. Zhong, X. Zhang, CrystEngComm, 19 (2017) 868.

[32] B. Saha, K. Sarkar, A. Bera, K. Deb, R. Thapa, Applied Surface Science, 418 (2017) 328.

[33] A. Kurda, Y. Hassan, N. Alrawi, World Journal of Nano Science and Engineering, 05 (2015) 34.

[34] M. Kashif, U. Hashim, M. Ali, S.M. Usman Ali, M. Rusop, Z. Ibupoto, M. Willander, Journal of Nanomaterials, 2012 (2012) 1.

[35] A.A. Oun, J.-W. Rhim, Carbohydrate Polymers, 127 (2015) 101.

[36] M. Fathy, T. Abdel Moghny, M.A. Mousa, A.-H.A.A. El-Bellihi, A.E. Awadallah, Applied Nanoscience, 6 (2016) 1105.

[37] M.A. Saiful Badri, M.M. Salleh, N.F.a. Md Noor, M.Y.A. Rahman, A.A. Umar, Materials Chemistry and Physics, 193 (2017) 212.

[38] D. Das, P. Mondal, RSC Advances, 4 (2014) 35735.

[39] J. Ghosh, R. Ghosh, P.K. Giri, Sensors and Actuators B: Chemical, 254 (2018) 681.

[40] L. Irimpan, B. Krishnan, A. Deepthy, V.P.N. Nampoori, P. Radhakrishnan, Journal of Physics D: Applied Physics, 40 (2007) 5670.

[41] B. Murali, S.B. Krupanidhi, Journal of Applied Physics, 114 (2013) 144312.

[42] S. Saha, P.K. Mandal, A. Samanta, Physical Chemistry Chemical Physics, 6 (2004) 3106.

[43] G.-H. Nam, S.-H. Baek, I.-K. Park, Journal of Alloys and Compounds, 613 (2014) 37.

[44] S. Dhar, P. Chakraborty, T. Majumder, S.P. Mondal, ACS Applied Materials & Interfaces, 10 (2018) 41618.

[45] A.B. Swain, M. Rath, P.P. Biswas, M.S.R. Rao, P. Murugavel, APL Materials, 7 (2019) 011106.

[46] D. Abbaszadeh, A. Kunz, G.A.H. Wetzelaer, J.J. Michels, N.I. Crăciun, K. Koynov, I. Lieberwirth, P.W.M. Blom, Nature Materials, 15 (2016) 628.

[47] M.A. Lampert, Physical Review, 103 (1956) 1648.

[48] P. Mark, W. Helfrich, Journal of Applied Physics, 33 (1962) 205.

[49] D. Abbaszadeh, A. Kunz, N.B. Kotadiya, A. Mondal, D. Andrienko, J.J. Michels, G.-J.A.H. Wetzelaer, P.W.M. Blom, Chemistry of Materials, 31 (2019) 6380.

[50] D.D. Sang, H.D. Li, S.H. Cheng, Q.L. Wang, Q. Yu, Y.Z. Yang, Journal of Applied Physics, 112 (2012) 036101.

[51] J. Kaczmarski, M.A. Borysiewicz, K. Piskorski, M. Wzorek, M. Kozubal, E. Kamińska, Semiconductor Science and Technology, 33 (2017) 015010.

[52] M. Özdoğan, C. Çelebi, G. Utlu, Materials Science in Semiconductor Processing, 107 (2020) 104863.

[53] Y. Zhou, C. Gao, Y. Guo, Journal of Materials Chemistry A, 6 (2018) 10286.

[54] D. Periyanagounder, P. Gnanasekar, P. Varadhan, J.-H. He, J. Kulandaivel, Journal of Materials Chemistry C, 6 (2018) 9545.

[55] C. Soci, A. Zhang, B. Xiang, S.A. Dayeh, D.P.R. Aplin, J. Park, X.Y. Bao, Y.H. Lo, D. Wang, Nano Letters, 7 (2007) 1003.

[56] D. Cammi, K. Zimmermann, R. Gorny, A. Vogt, F. Dissinger, A. Gad, N. Markiewcz, A. Waag, J.D. Prades, C. Ronning, S.R. Waldvogel, T. Voss, The Journal of Physical Chemistry C, 122 (2018) 1852.

[57] B. Deka Boruah, S. Naidu Majji, S. Nandi, A. Misra, Nanoscale, 10 (2018) 3451.

[58] W. Peng, X. Wang, R. Yu, Y. Dai, H. Zou, A.C. Wang, Y. He, Z.L. Wang, Advanced Materials, 29 (2017) 1606698.

[59] R.S. Veerla, P. Sahatiya, S. Badhulika, Journal of Materials Chemistry C, 5 (2017) 10231.

[60] M. Mishra, A. Gundimeda, T. Garg, A. Dash, S. Das, Vandana, G. Gupta, Applied Surface Science, 478 (2019) 1081.

[61] Q.-M. Fu, D.-C. He, Z.-C. Yao, J.-L. Peng, H.-Y. Zhao, H. Tao, Z. Chen, Y.-F. Tu, Y. Tian, D. Zhou, G. Zheng, Z.-B. Ma, Materials Letters, 222 (2018) 74.

[62] S.M. Hatch, J. Briscoe, S. Dunn, Advanced Materials, 25 (2013) 867.

[63] C. Li, C. Han, Y. Zhang, Z. Zang, M. Wang, X. Tang, J. Du, Solar Energy Materials and Solar Cells, 172 (2017) 341.

[64] B.D. Boruah, S.N. Majji, A. Misra, Nanoscale, 9 (2017) 4536.

[65] Y. Shen, X. Yan, Z. Bai, X. Zheng, Y. Sun, Y. Liu, P. Lin, X. Chen, Y. Zhang, RSC Advances, 5 (2015) 5976.

[66] H. Shen, C.X. Shan, B.H. Li, B. Xuan, D.Z. Shen, Applied Physics Letters, 103 (2013) 232112.

[67] J. Garnier, R. Parize, E. Appert, O. Chaix-Pluchery, A. Kaminski-Cachopo, V. Consonni, ACS Applied Materials & Interfaces, 7 (2015) 5820.

[68] L. Duan, F. He, Y. Tian, B. Sun, J. Fan, X. Yu, L. Ni, Y. Zhang, Y. Chen, W. Zhang, ACS Applied Materials & Interfaces, 9 (2017) 8161.

[69] H. Chen, P. Yu, Z. Zhang, F. Teng, L. Zheng, K. Hu, X. Fang, Small, 12 (2016) 5809.

[70] L. Su, Q. Zhang, T. Wu, M. Chen, Y. Su, Y. Zhu, R. Xiang, X. Gui, Z. Tang, Applied Physics Letters, 105 (2014) 072106.

[71] X. Peng, Y. Zeng, X. Pan, W. Wang, Y. Zhou, F. Wang, Q. Lu, Z. Ye, RSC Advances, 7 (2017) 29440.

[72] B.D. Boruah, D.B. Ferry, A. Mukherjee, A. Misra, Nanotechnology, 26 (2015) 235703.

Chapter 5

Carbon dots decorated SWCNT/ZnO based hybrid electrode for optically responsive supercapacitor

Energy storage system

Contents

Graphical abstract

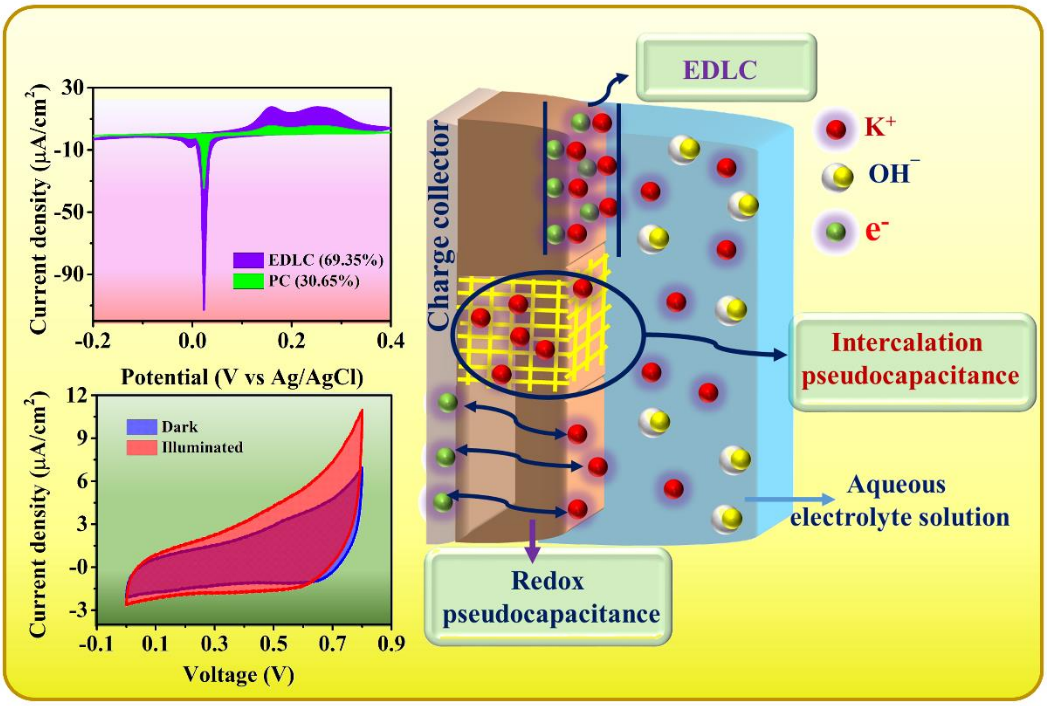

The contents in this chapter have been submitted as “SWCNT/ZnO nanocomposite decorated with carbon dots for photoresponsive supercapacitor applications.” **Rupam Sinha**, Nirmal Roy and Tapas K. Mandal, *Chem. Engg. J.* 431, 133915, 2022. DOI: [10.1016/j.cej.2021.133915](https://doi.org/10.1016/j.cej.2021.133915)

Abstract

The optical properties of ZnO and carbon dots (CDs) are well utilized in optoelectronics. However, these properties can be explored in the areas of energy storage systems as well. In this chapter, we report the fabrication of an optically responsive hybrid supercapacitor. The hybrid electrode material for the supercapacitor was synthesized by attaching CDs on the SWCNT/ZnO nanocomposites, and the formation of the composite was verified by X-ray diffraction (XRD), Field effect transmission electron microscopy (FETEM), and Raman analysis. The optical properties of CDs and ZnO have been explored by operating the supercapacitor under illuminated conditions (UV light). It was observed that the areal capacitance of the fabricated supercapacitor got enhanced by ~41.38% at 50 mV/s scan rate. The working mechanism of the supercapacitive system has also been explored. It is observed that the overall capacitance of the hybrid electrode is a combination of both electric double layer capacitance (EDLC) and pseudocapacitance. The EDLC and pseudocapacitance contributions were confirmed by using the Dunn method, and the values of the individual capacitance contributions are 69.35 and 30.65% for EDLC and pseudocapacitance, respectively. Moreover, the reaction mechanism of the system has also been explored, and the occurrence of intercalation of K^+ ions in the defects of ZnO has been confirmed with justified explanations.

5.1. Introduction

The heavy usage of fossil fuels results in their steady depletion along with the augmentation of CO_2 emissions, which is a primary reason behind global warming [1]. Hence, renewable energy sources like wind, biomass, ocean, and solar energy are gaining incredible demand in the current era. High energy storage devices are generally able to use such renewable energy sources, and also they cause a minimal effect on global warming. Electrochemical energy storage devices, such as supercapacitors, are considered high power/energy storage devices [2]. Therefore, several researchers from all across the globe have been focusing their research on the study of high energy storage systems, i.e., supercapacitive systems since the last decade [3-5]. The qualities such as high power density, easy and safe operation, longer life cycle, etc., have been positively attracted the researchers to focus their works on supercapacitors [6]. Supercapacitors have been categorized in two different types, such as electrochemical double-layer capacitors (EDLCs) and pseudocapacitors [7]. In the former category, the electrodes adsorb the ions (oppositely charged) from the electrolyte and form a layer at the electrode/electrolyte interface. In contrast, the working principle of the latter category of supercapacitors is based on redox /intercalation reactions, which occur largely at the electrode surfaces (mostly oxide-based electrode materials) [7, 8].

Several materials have been tested till now as electrode materials for supercapacitive devices over the last decade. Amongst them, carbon materials have garnered much praise from the scientific fraternity for their better performances [9, 10]. For example, Mitra *et al.*[11] reported different unexplored paths of energy storage in parallel as well as curved-plate-supercapacitors. They used rGO as the active electrode material for their system.

Besides rGOs, carbon nanotubes (CNTs) have also been used as electrode materials for supercapacitors, as reported by Koo *et al.* [12] in their article. They have described the fabrication of thin CNT sheets from thick CNT sheets. Moreover, they have used these sheets as electrodes and reported a maximum specific capacitance value of 51.37 F/g. On the other hand, bimetallic transition metal phosphide [13], transition metal oxides, and conducting polymers have also got massive attention as electrode materials for pseudocapacitors [9]. For instance, Yang *et al.* [14] fabricated an asymmetric supercapacitor by growing α-MnO_2 nanowires and amorphous Fe_2O_3 nanotubes on a flexible carbon fabric. In this work, they have reported the enhancement of capacitance value as well as the energy density based on the pseudocapacitive characteristics of the material. In another work, Wang *et al.* [15] synthesized an electrode material for an energy storage system by encapsulating rGO with polybromopyrroles. This material showed a high specific capacitance of 256 F/g. Most importantly, the presence of pseudocapacitive behavior was reported in this article. This pseudocapacitive property of the material helped to get such a high specific capacitance value.

Apart from the simple supercapacitors, researchers have recently started working on the fabrication of photo-rechargeable supercapacitors as well. This helps the society to advance towards the utilization of renewable light energy sources. Photoresponsive materials such as ZnO, V_2O_5, organohalide perovskite, etc. [16-18] are some of the superior materials for the fabrication of photo-rechargeable supercapacitors. Some reports have shown the combination of a solar cell with a supercapacitor, where the solar cell helps to charge the supercapacitor by providing energy from its harnessed energy source. For example, the work reported by Xu *et al.* [19] shows the combination of perovskite-based solar cell with a polypyrrole-based supercapacitor. This power pack combination achieved an efficiency of 10%. This value is much higher than many other combined systems. However, combining a solar cell with a supercapacitor is considered quite a space-occupying arrangement. Therefore, to overcome this difficulty, self-rechargeable supercapacitors have started gaining more attention and popularity. For example, Boruah and Mishra [17] reported an optically responsive solid-state supercapacitor. In this reported work, they used a heterostructure made by a combination of zinc cobalt oxide and zinc oxide nanorods as electrodes for the supercapacitor. They reported an enhancement of 174% in the charge storage capacity by the supercapacitor in the presence of UV light. Moreover, their reported photogenerated areal capacitance was 150 μF/cm^{2,} whereas the energy density under illuminated condition (UV light) was 11.8×10^{-3} μWh/cm^2. The photoconductivity of the photoresponsive metal oxides (such as, ZnO, Cu_2O, CuO, etc.) can be increased by attaching quantum dots on the surfaces [20]. However, inorganic metal-based quantum dots are considered to be highly toxic in nature. Therefore, researchers are trying to replace these quantum dots with carbon dots (CDs) due to their low toxic nature [21]. Therefore, the use of CDs seems to be more favorable as compared to other inorganic metal-based quantum dots. The attachment of CDs to other materials helps to improve the photoresponsive behavior of the composite, as shown in our previous works [22, 23]. Not only this, CDs even help to improve the performances of supercapacitors as well. For example, Sahoo *et al.* [24] showed the enhancement in the performance of the supercapacitor when the electrode material (NiS) was decorated with CDs. Their reported specific capacitance is 880 F/g at a current density of 2 A/g.

Although the above-mentioned literature describes the fabrication of several hybrid electrodes for supercapacitors, it is very rare that the researchers have used hybrid electrodes composed of three or more different materials. Moreover, despite all the recent progress in the fabrication of high-performing as well as photorechargeable supercapacitors, very few works are there till date which actually discuss the working mechanism of the supercapacitors. Therefore, in this work, we are reporting for the first time to our knowledge about the fabrication of CD decorated SWCNT/ZnO hybrid electrodes for the application in optically responsive supercapacitors. Moreover, we have also reported the detailed working mechanism of the supercapacitor, which showed the presence of EDL-based capacitance as well as pseudocapacitance.

5.2. Experimental section

5.2.1. Materials

Citric acid, Ethylenediamine (EDA), single-walled carbon nanotube (SWCNT), Zinc acetate dihydrate, ethanol, glacial acetic acid, Whatman filter paper, and potassium hydroxide (KOH) were purchased from Sigma Aldrich, India. Polyvinyl alcohol (PVA) was procured from Lobachemie, India. Whereas ITO coated PET sheets (ITOP15X1; 100 mm × 100 mm) were purchased from Shilpa Enterprises, India. All the chemicals were used without further purifications.

5.2.2. Synthesis of CDs

The CDs were synthesized using the hydrothermal method as reported by Zhu *et al.* [25] with a little modification. In a typical process, 1.051 g citric acid was dissolved in 10 ml of DI water. In that solution, 335 μl of EDA was added, and this solution was hydrothermally treated in a Teflon-lined autoclave at 150 °C for 7 h. After that, the solution was allowed to cool down at room temperature, and then it was filtered through a 0.2 µm syringe filter.

5.2.3. Fabrication of hybrid electrode and the supercapacitor device

For preparing the electrode, ITO coated PET sheets were first cut with the dimensions of 25 mm × 25 mm. Then this sheet was washed thoroughly with DI water and acetone and dried under nitrogen flow. After washing, the ITO coated sheets were treated in UV-ozone for 1 h. Subsequently, a film of CD decorated SWCNT/ZnO hybrid material was formed on the ITO coated sheets. To prepare this film, we followed the method used by Teng *et al*. [26] with a little modification. In a typical process, a 7.5 ml solution was made in which 2.2 g of zinc acetate dihydrate, 1 g of PVA, 2 mg of SWCNT, and 1 ml of the synthesized CD solution was added as shown in scheme 1a(I). Then this as-synthesized mixture was stirred for 45 min on a hot plate with setting the hot plate temperature at 100 °C. As a result, the mixture was transformed into gel form. Further, this gel was allowed to come to room temperature with continuous stirring. Then, 1 ml of ethanol and 0.5 ml of glacial acetic acid was added to this gel and stirred for 15 more minutes to get the gel solution of the hybrid electrode material, and these steps are shown in schemes 1a(II) and (III). 1ml of this gel solution was then drop-casted on the ITO coated PET sheet, and it was spin coated for 15 seconds at 3000 rpm as represented in schemes 1b(I) and (II). These two steps were repeated 5 times, and then this film was allowed to dry on the hot plate (100 °C) for 5 min (scheme 1b(III)). This whole process was repeated 3 times, and then the PET sheet was kept in a hot air oven at 105 °C for 42 h.

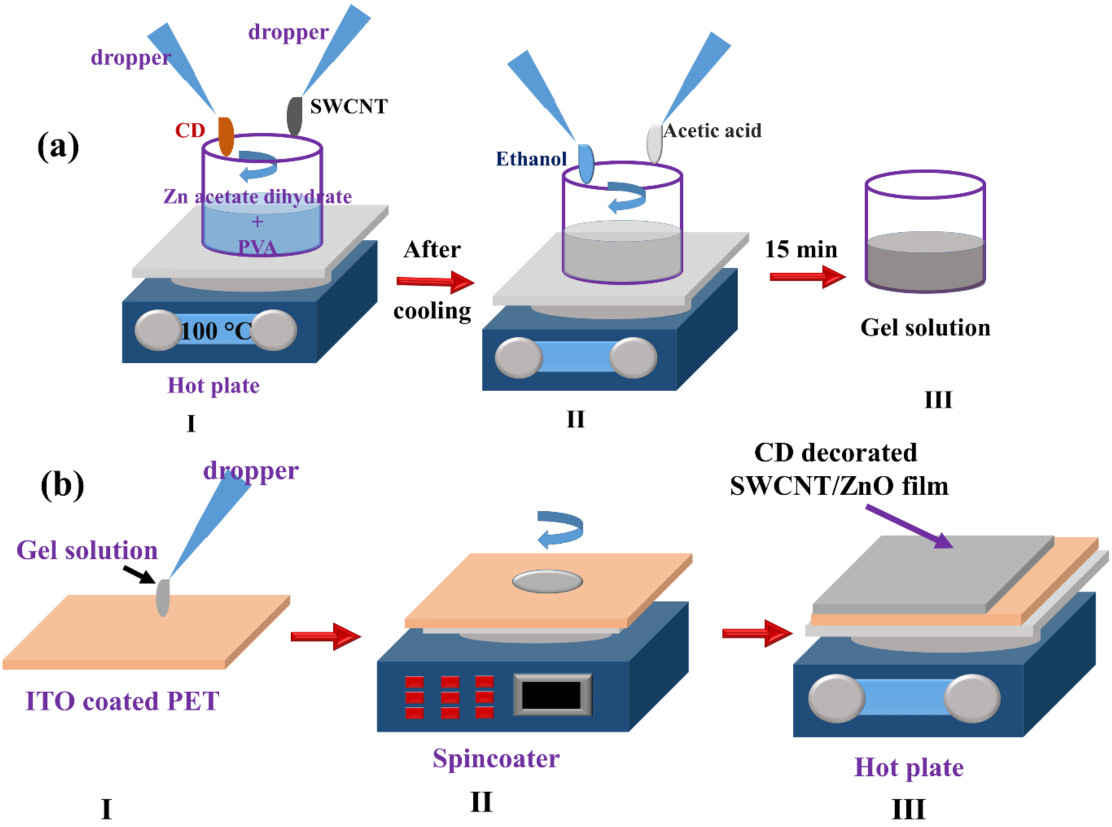

Scheme 5.1. (a) Steps for synthesizing the gel solution of the hybrid electrode material. (b) Fabrication of the electrode.

For preparing the supercapacitor device, two of the electrodes were first cut into desired dimensions and then assembled in a sandwich-type pattern with a separator placed in between them. A Whatman filter paper was used as a separator, and 20 µl of 4 M KOH solution was used as the electrolyte solution, which was drop-casted on the separator before assembling. Afterward, this assembled device was clipped from both sides. For the analysis of the photoresponsive behaviour of the material, we prepared a photodetector as well. For this, Al electrodes were deposited on the CD decorated SWCNT/ZnO film by thermal evaporation technique. The gap between the two electrodes was 200 µm.

5.2.4. Characterizations

A field emission scanning microscope (Zeis, Sigma) was used to get the field emission scanning micrograph (FESEM) and the energy dispersive X-ray (EDX) spectra of the samples. The field emission transmission electron micrograph (FETEM) and the selected area electron diffraction (SAED) pattern were recorded using the field emission transmission electron microscope (JEM, 2100F). The crystallinity of the material was examined by an X-ray diffractometer (XRD; Burker, D8 Advance), whereas the Raman spectra was obtained from a Raman spectroscope (Horiba LabRam HR Evolution). A photoluminescent spectrometer (PerkinElmer, LS 45) was used to obtain the PL spectra. X-ray photoelectron spectroscopy (XPS) analysis was done to get the composition near the surface of the composite material by using an X-ray photoelectron spectroscope (Thermo Fisher Scientific Pvt. Ltd., ESCALAB Xi$^+$). For getting the fluorescence lifetime and fluorescent decay curve, we used Picosecond time-resolved cum steady-state luminescence (TRPL) spectrometer (Eddinburg Instruments, FSP920).

5.2.5. Electrochemical and electrical analysis

All the electrochemical analyses (CV analysis, GCD analysis, EIS analysis) were done with the help of a potentiostat (PGSTATM204; Autolab Metrohm). For the analysis in three-electrode systems, a Pt wire and an Ag/AgCl electrode were used as a counter electrode and reference electrode. For the analysis of the electrical characterizations, a Keithley 4200- SCS probe station was used, and for the measurement of the photoresposponse of the device, a 75 W UV bulb was used as the light source.

5.3. Results and discussion

5.3.1. Characteristics of electrode material

The characteristics of the synthesized CD decorated SWCNT/ZnO hybrid electrode were examined, and the results are shown in figure 5.1. The top view of the electrode surface is shown in figure 5.1a. The cross-sectional image is also presented in figure 5.1b, where, the clearly distinguished film layer, ITO layer, and PET layer can be observed. These different layers are marked and shown separately in the image. The thickness of the film layer is calculated from the image, and this value is ~596 nm. Figure 5.1c represents the FETEM image of the electrode material at a scale of 100 nm. The ZnO particles, covered with CD, are enclosed with a web created by the SWCNT. Another image at a scale of 50 nm is presented in figure 5.1d to show the presence of CDs and the ZnO particles in a clearer way. The dark spots on the larger particles in this figure are the CDs, which assures the attachment of the CDs on the ZnO particles. We have encircled the ZnO nanoparticles and marked the CDs with arrows in this figure for a better understanding. The HRTEM image is also shown in figure 5.1e, where three different crystal planes can be observed, and these different planes are marked in the image along with the calculated lattice spacing values. A hint about the polycrystallinity can be extracted from this image, and therefore an SAED pattern is also presented in figure 5.1f. The existence of amorphous characteristics in the material can be ascribed to the presence of CDs as well as the SWCNTs in the hybrid material. A detailed crystallinity study has also been done, and an elaborated discussion is presented later with XRD analysis. The elemental analysis of the hybrid material was done by EDX spectroscopy, and the corresponding spectrum is given in figure 5.1g. The presence of Zn, O, C, and N is visible in this spectrum. The appearance of the peak for N is due to the presence of N in the synthesized CDs (N-doped CDs). The

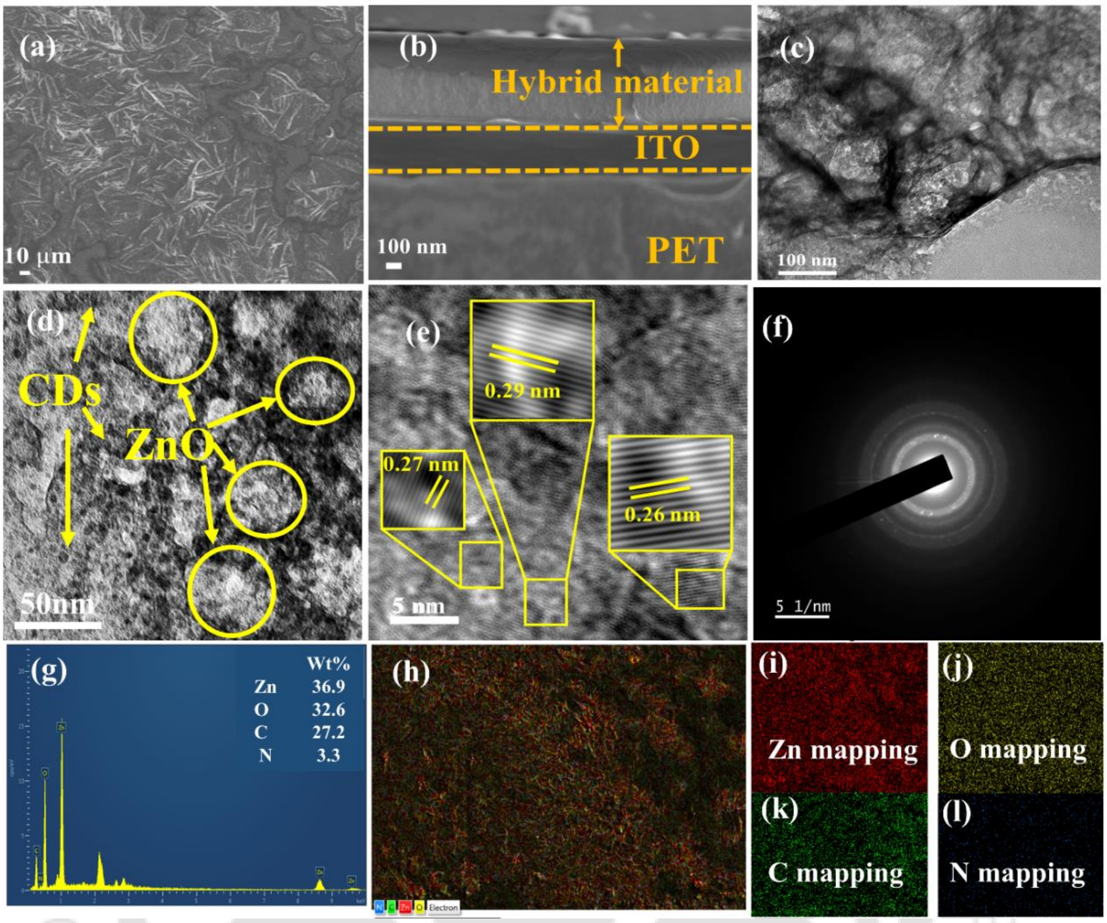

Figure 5.1. FESEM images to show the (a) top view, and the (b) side view of the electrode. FETEM images of the electrode material at the scales of (c) 100, and (d) 50 nm. (e) HRTEM image, and (f) the SAED pattern of the electrode material. (g) Energy dispersive X-ray (EDX) spectrum, and (h) scanning area for EDX analysis of the material. (i-l) Mapping images of Zn, O, C, and N.

wt% of these elements are 36.9, 32.6, 27.2, and 3.3% respectively. The overall scanning area for elemental mapping is shown in figure 5.1h. The uniform scattering of the elements are clearly observed in figures 5.1i-l.

The XRD spectrum of the synthesized hybrid electrode material (CD-SWCNT/ZnO) is presented in figure 5.2a. The peaks at 2θ values of 32.28, 34.98, 36.75, 47.98, 57.02, 63.24, 68.27, and 69.35° correspond to the lattice planes (100), (002), (101), (102), (110), (103), (112), and (201) respectively. These values are in agreement with the previously reported [23] data. However, the little deviations of these values can be ascribed to the outcome of the microstrain in the crystals during their synthesis. Apart from this, the presence of SWCNT and CDs is also observable in the XRD spectrum of the composite.

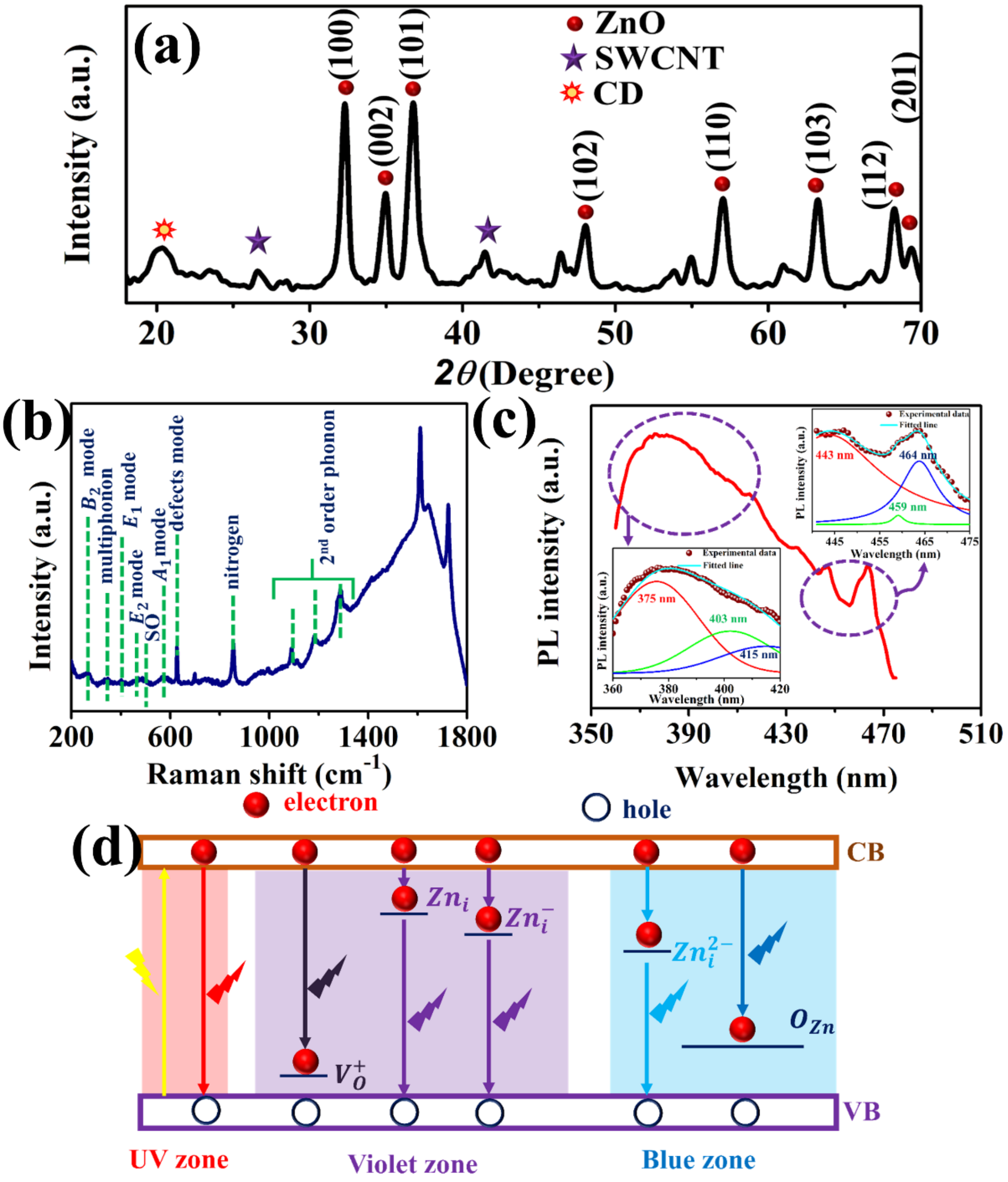

Figure 5.2. (a) XRD peaks of the hybrid electrode material. (b) Raman spectrum. (c) Photoluminescence (PL) spectrum at an excitation wavelength of 340 nm with deconvoluted sections in the insets. (d) Schematic representation of the transfer of electrons.

The peaks at 26.2 and 41.5° are the evidences of the presence of the SWCNT [27], whereas the broad peak at 20.31° confirms the presence of CDs in the composite (figure 5.2a) [28]. We have performed Raman spectroscopy as well to obtain more information about the crystallinity and phase of the hybrid electrode material in a detailed manner. The Raman spectrum of the same is shown in figure 5.2b. The peaks at ~270 and ~857 cm^{-1} can either be assigned to the standard B_2 mode of ZnO or can be ascribed to the incorporation of nitrogen into the ZnO via the addition of the CDs (N-doped) [29, 30]. The peaks at ~334 and ~1170 cm^{-1} are due to the multiphonon process [31, 32]. The peak at ~407 cm^{-1} can be referred to the E_1(TO) mode [33]. The doubly degenerate mode E_2(high) is represented by the peak at ~458 cm^{-1}, whereas the peak at ~490 cm^{-1} can be due to the surface optical (SO) phonons [29, 34]. The peak at ~579 cm^{-1} can be referred to the A_1(high) mode [29], whereas the peak at ~630 cm^{-1} can well be assigned to the defect-associated mode. A second-order phonon mode can be assigned to the peaks at ~1080, ~1170, and ~1287 cm^{-1} [35, 36]. The presence of CDs and SWCNTs in this

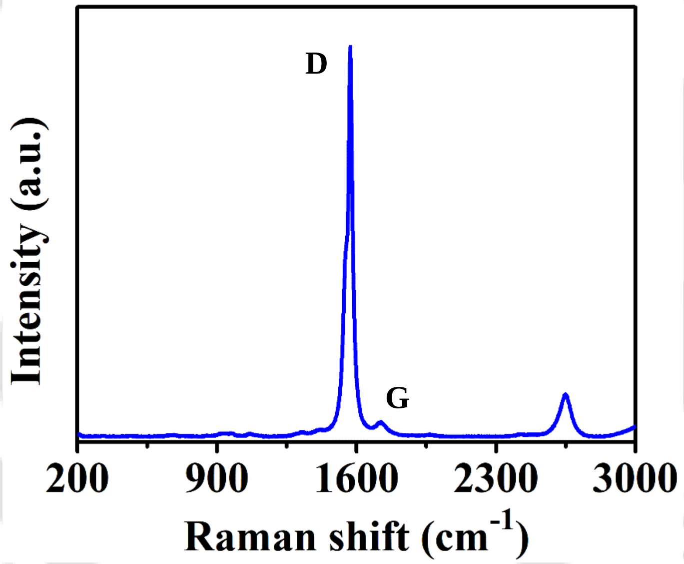

Figure 5.3. Raman spectrum of pristine SWCNT.

hybrid material can also be confirmed from the peaks ranging from 1340-1800 cm^{-1}. The broadening of the peak in this region can affirm the presence of CDs as it is found in the literature that the CDs have Raman peaks at the wavelengths around ~1367 and ~1611 cm^{-1} [37], whereas the peaks at ~1597 and ~1730 cm^{-1} can confirm the presence of SWCNTs. The Raman peak of the pristine SWCNT is shown in figure 5.3.

The photoluminescence (PL) characteristics of the hybrid electrode material were also studied to get a clearer idea about the defects present in it. A PL spectrum of the hybrid electrode material at an excitation wavelength of 340 nm is shown in figure 5.2c. Three different regions can be observed from the overall PL spectrum (red line), which are the UV region (360-385nm), the violet region (385-455 nm), and the blue region (455-475 nm). The emissions at the blue and violet zones can be ascribed to the deep level emissions (DLE) [23, 38]. In the ZnO nanoparticles, the presence of defects, such as vacancies of Zn and O, intrinsic defects of Zn interstitials, etc., triggers the DLE [23]. The deconvolution of the spectrum gives information about the defects in a distinguished manner, as represented in the insets of figure 5.2c. The peak at ~ 375 nm (~ 3.30 eV) corresponds to the near-band-edge emission (NBE) [38, 39]. Here, the recombination of the electron-hole pair can occur at or near the valance band. The peak at ~ 403 nm (~ 3.07 eV) corresponds to the electronic transition from the conduction band to the defect corresponding to the single ionized oxygen vacancy (V_O^+), whereas the interstitial Zn (Zn_i) can be responsible for the peak at ~ 415 nm (~ 2.98 eV) [23]. The peaks at ~ 443 nm, ~ 459 nm, and ~ 464 nm (~ 2.79, ~2.70, and ~2.67 eV) can be assigned to the ionized interstitial Zn (Zn_i^-), doubly ionized interstitial Zn (Zn_i^{2-}), and oxygen antisite respectively [23, 38]. However, a little shift of these peaks can be attributed to the formation of the composite between CD, ZnO and SWCNT. A schematic is shown in figure 5.2d to pictorially represent the transfer of electrons from the conduction band to the several defect regions corresponding to the PL spectrum.

5.3.2. Electrochemical analysis of the electrode material

The energy storage process is not as simple at all. A better fundamental understanding of the energy storage process is essential as a hybrid electrode material (CD-SWCNT/ZnO) may show the contribution from two parts, namely (i) double-layer capacitance and (ii) pseudocapacitance. Therefore, it is important to get insight into the supercapacitor's charge storage mechanism, i.e., whether it is capacitive-controlled or diffusion-controlled. The information about the capacitance contribution can be obtained by using Dunn method [40]. The dependence of the current on the scan rate needs to be examined to obtain this information. The cyclic voltammetry (CV) responses of the hybrid electrode material at different scan rates ranging from 0.1 – 2 mV/s are shown in figure 5.4a. Two oxidation (O_1, O_2) and their corresponding reduction peaks (R_1, R_2) are observed in this figure. The presence of the oxidation and reduction peaks are the evidence of the redox reactions in the system, which can contribute to redox psedocapacitance [41]. In principle, the dependence of the current on the scan rate is as follows [42];

$$i = a\nu^{b} \tag{5.1}$$

or,

$$\log(i) = \log(a) + b\log(\nu) \tag{5.2}$$

where, a and b correspond to two variable parameters whereas, i and ν correspond to the current and scan rate values. Different b values are obtained from the redox peaks. These values can be obtained from the slopes of the plots between $\log(\nu)$ and $\log(i)$ as shown in figure 5.4b and these values generally range from 0 to1. For the capacitive-controlled process, the b value becomes ~1, whereas, for a diffusion-controlled electrochemical process, this value becomes ~0.5 [42, 43]. From figure 5.4b, the calculated values of b for the peaks O_1, O_2, R_1, and R_2 are 0.42, 0.54, 1.01, and 1.04, respectively. This indicates the contribution from both capacitive process as well as from diffusive process as the b values for oxidation and reduction process are ranging from 0.5 to 1. A similar observation is also reported by Boruah *et al.* [42] in their article in which their b values were also ranging from 0.5 to 1. Hence they concluded the presence of contributions from both capacitive and diffusive processes. Although these values are giving information about the contribution from both the processes (capacitive and diffusive process), a quantitative value of the contribution of the individual process is not determinable from the b-values. However, these values can be calculated from the following equation [42, 44] by expressing the current response with respect to the scan rate values.

$$i(V) = k_1\nu + k_2\nu^{1/2} \tag{5.3}$$

Dividing both sides of the equation by $\nu^{1/2}$, we get,

$$i(V)/\nu^{1/2} = k_1\nu^{1/2} + k_2 \tag{5.4}$$

where, $i(V)$ is denoted as the current at a constant voltage, k_1 and k_2 are constants. The term $k_1\nu$ refers to the current contribution in the capacitive form (EDLC) whereas, $k_2\nu^{1/2}$corresponds to the contributions from the diffusion-controlled process (pseudocapacitance). We have shown a plot between $i(V)/\nu^{1/2}$ vs. $\nu^{1/2}$ in figure 5.4c to get the values of k_1 and k_2 and hence the values of capacitive contribution and the pseudocapacitive (diffusion-controlled) contribution. A CV plot is also shown in figure 5.4d at 2 mV/s to represent the individual contribution in the charge storage process of the hybrid electrode material. It is observed from the figure that the capacitive contribution is 69.35%, whereas the pseudocapacitive percentage is 30.65%. A schematic

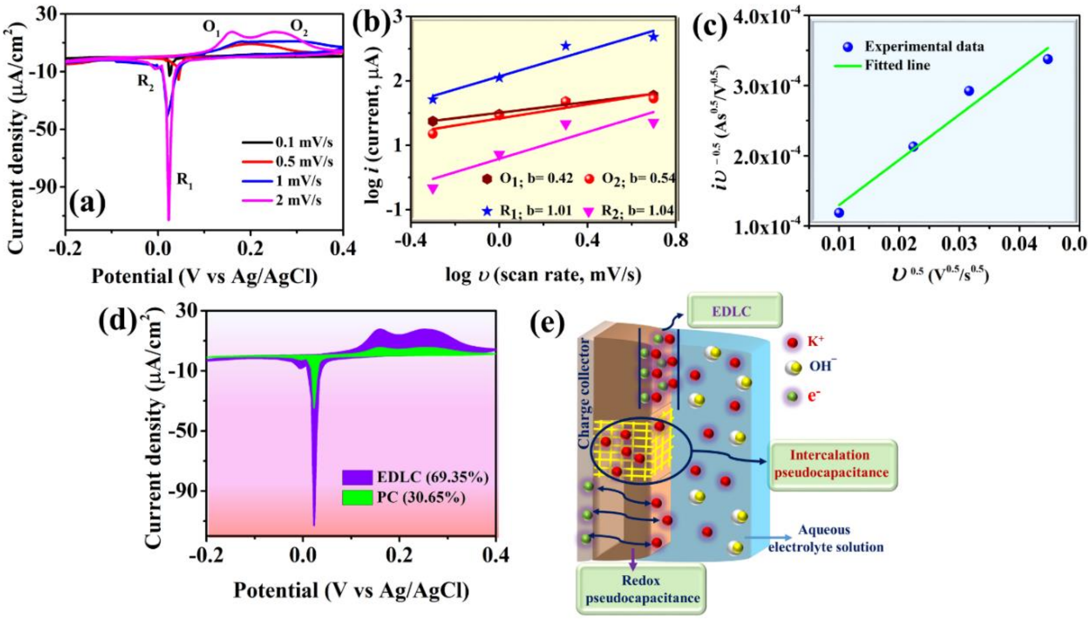

Figure 5.4. (a-d) Dunn method analysis; (a) CV plots of electrode material at different scan rates (0.1-2 mV/s). (b) Estimation of b values for the oxidation and reduction peaks (O_1, O_2, R_1, and R_2). (c) $i\ \nu^{-0.5}\ vs\ \nu^{0.5}$ Plot at a potential of 0.26 V vs. Ag/AgCl. (d) CV plot at 2 mV/s to show the capacitance percentage contributed by EDLC and PC. (e) Schematic representation of electrode-electrolyte interaction to represent the capacitance mechanism.

is shown in figure 5.4e to represent all the possible charge storage mechanism pathways. At the electrode-electrolyte interface (at the top of the figure), the EDLC layer is shown. At the bottom section of the electrode material, the possible pathway of pseudocapacitance is shown. In case of pseudocapacitance, the possibilities of the presence of both intercalation as well as redox pseudocapacitance are there. Therefore, both of these two phenomena are shown in the figure. However, it is essential to have an idea about the diffusivity for the case of intercalation pseudocapacitance, and it can be obtained from the following equation [42, 45];

$$i_p = 0.4463F(F/RT)^{1/2}\, C^{*}\nu^{1/2}AD^{1/2} \tag{5.5}$$

or,

$$i_p = K\nu^{1/2}AD^{1/2} \tag{5.6}$$

where, i_p corresponds to the current value at the peaks in the CV plot, $C^{*}$is the concentration (mol/cm^3), ν is the scan rate (V/s), whereas, F refers to the Faraday constant, A is the working area of the electrode (cm^2), and K is a constant (= $0.4463F(F/RT)^{1/2}\, C^{*}$). A plot between i_p/K vs $\nu^{1/2}$ is shown in figure 5.5. The diffusion constant values for the oxidation peaks (O_1, O_2) are 0.13 and 0.14 mm^2/s, respectively, whereas the same for the reduction peaks (R_1, R_2) are 1 and 0.07 mm^2/s, respectively. Moreover, the occurrence of the redox process at the electrode-electrolyte

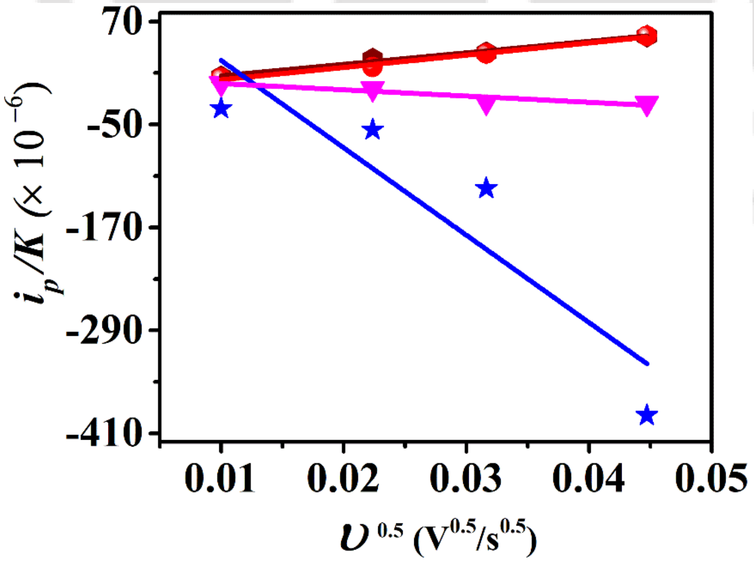

Figure 5.5. Plot to calculate diffusion constant.

interface can enhance the contribution from pseudocapacitance, and as mentioned earlier, the presence of the redox peaks in the CV plots are confirming the presence of the redox pseudocapacitance. In this case, the expected reaction at the surface of the electrode material (interaction between ZnO and potassium ion) can be as follows [46],

$$\text{ZnO (surface)} + \text{K}^+ + e^- \rightarrow (\text{ZnO}^+\text{K}^-)\text{surface}. \qquad (5.7)$$

Apart from this surface phenomenon, the possibility of the involvement of K^+ ions in the intercalation mechanism is also there, which is discussed in detail in the later section (**Reaction mechanism**).

5.3.3. Device performance

We checked the overall device performance after examining the electrochemical properties of the electrode material. The device fabrication has been discussed in the experimental section. Owing to the photoresponsive behavior of the electrode material (both CD and ZnO), we have tested the electrochemical performances of the device in the

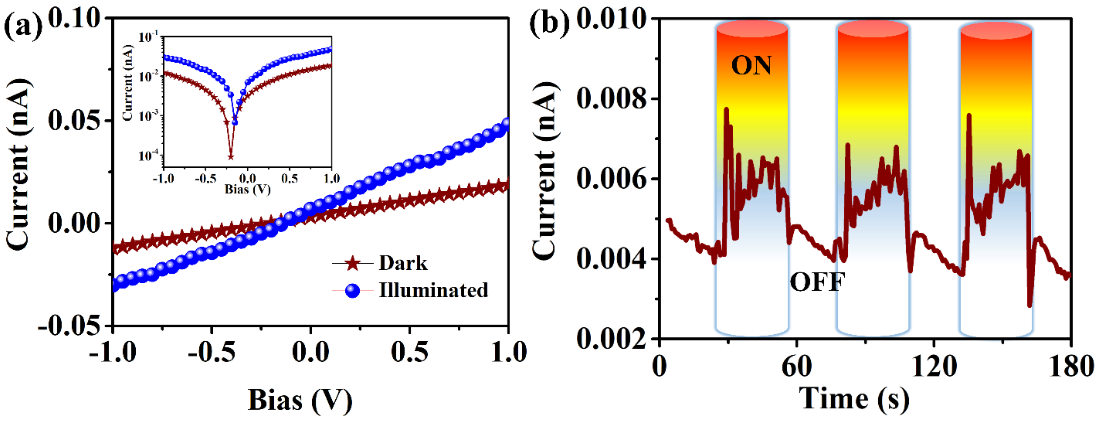

Figure 5.6. (a) *I-V* plot of the photodetector (the hybrid electrode material) in absence and presence of light in linear and semi-logarithmic scale (inset). (b) Transient response of the device using a UV bulb (100 mW/cm^2).

absence as well as in the presence of UV light. The photoresponsive behavior of the electrode material is shown in figure 5.6. In this figure, the I-V curve in the absence and presence of UV light and the transient response (at 0V bias) are shown. The explanation behind the generation of photocurrent at 0V bias has already been discussed in our previous chapter [23]. A schematic representation of the device in the presence of light source is shown in figure 5.7a. Figure 5.7b represents the supercapacitor device before charging it, whereas the charge storage processes in the absence and presence of light are also represented in figure 5.7c and figure 5.7d, respectively. Figure 5.7c shows the accumulation of the cations on the negative electrode and the anions on the positive electrode. These accumulated ions help to participate in both EDL capacitance as well as pseudocapacitance. The interaction between the negative electrode and K^+ on the surface of the electrode is already mentioned in equation 5.7. However, the interaction between the positive electrode and the anions (OH^-) can be represented by the following equation [17].

$$ZnO + OH^- \rightarrow ZnO - OH^- \tag{5.8}$$

There are obvious evidence of the formation of electrical double layers on the electrodes (as discussed in the previous section). Yet, we have only represented the redox/intercalation reactions on the electrodes by equations 5.7 and 5.8. We have performed XPS analysis of the electrode material of the device before and after performing the electrochemical analysis to understand the exact reaction mechanism, which is discussed in the later section (**Reaction mechanism**). The mechanism of charging in the presence of light can be elaborated from figure 5.7d. We assume that the photon energy helps to generate electron-hole pairs, which then get separated due to the built-in electric field. Further, the separated holes and electrons contribute to the separation of the ions in the electrolyte for charge storage in the presence of UV light.

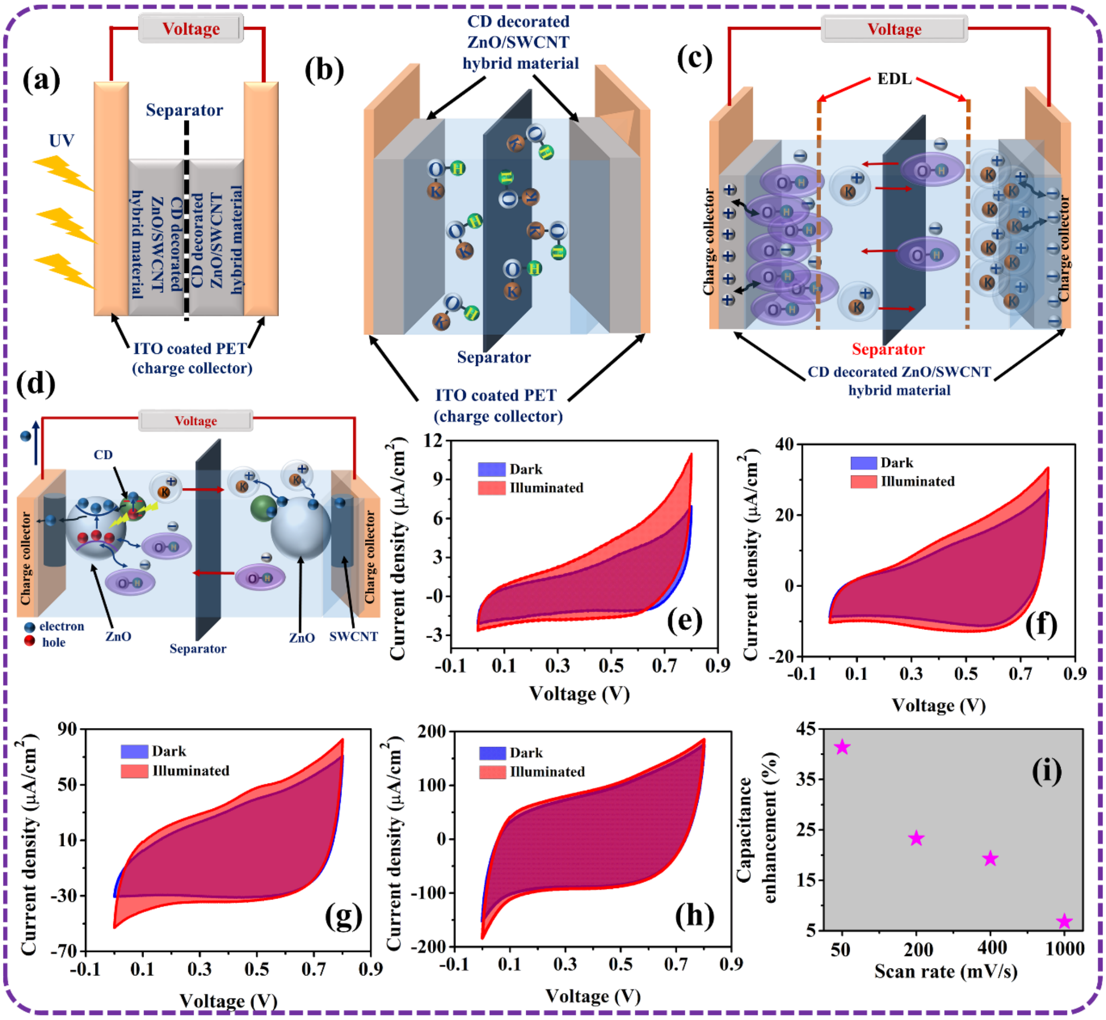

Figure 5.7. (a) Schematic of the supercapacitor device. (b) Schematic of the device before charging. Schematic of the device during charging (c) in the absence of light and (d) in the presence of light. (e-h) CVs of the supercapacitor device at scan rates of 50, 200, 400, and 1000 mV/s in the absence and presence of light (UV light; 100 mW/cm^2), respectively. (i) Plot between areal capacitance enhancements with scan rate.

For the electrochemical analysis of the device, the CV plots are shown in figures 5.7e-h at different scan rates (50, 200, 400, and 1000 mV/s). The asymmetry in the CV plots can be assumed due to the presence of surface reactions as well as the double layer formation on the electrodes in an irregular manner [17]. A little hump in the CV plot on the positive-scan side can be observed for 50, 200, and 400 mV/s, implying the redox reactions, whereas this hump is missing for 1000 mV/s. The slower rate of electronic transition compared to the higher scan rate can be the reason behind this, i.e., at a higher scan rate, the potential goes forward to the direction of the scan rate before the electronic transition fully generates the current. Due to this reason, the hump in the CV curve is missing in figure 5.7h. The CV curves followed a similar trend in the presence of UV light (100 mW/cm^2) as well. An obvious enhancement in the area surrounded by the CV curves in the presence of light compared to the ones in the absence of light is observed. From this enhancement of the area, we calculated the enhancement in the areal capacitance ($\frac{C_l - C_d}{C_d} \times 100\%$; where, C_l is the areal capacitance in presence of light and C_d is the area capacitance in the absence of light). The calculated enhancements for the scans of 50, 200, 400, and 1000 mV/s are 41.38, 23.23, 19.28, and 6.79%, respectively, and this change in areal capacitance enhancement in the presence of light is shown in figure 5.7i. All the CV plots at different scan rates for both the illuminated and dark conditions are

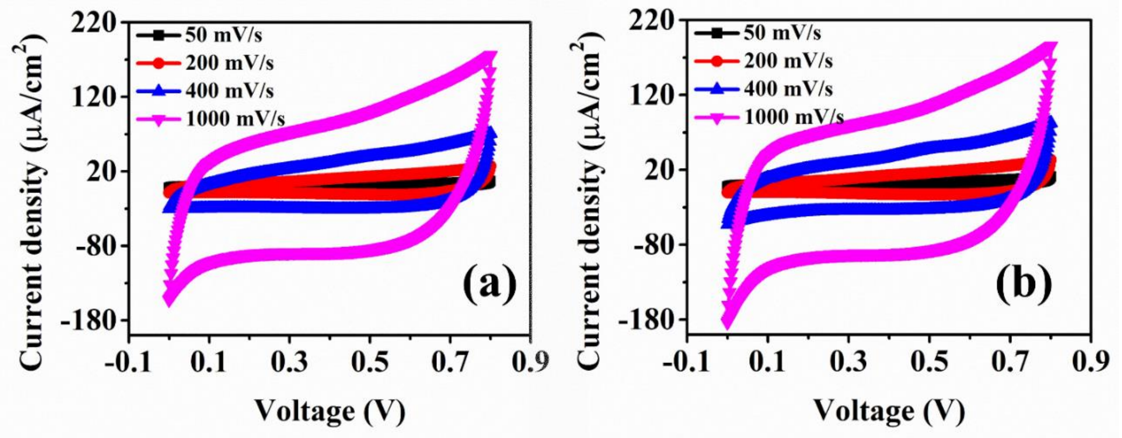

Figure 5.8. CV plots of the supercapacitor device at different scan rates in (a) dark and (b) illuminated condition.

shown in figure 5.8. The change in the area inside the CV curves at different scan rates is observable for both cases (dark and illuminated).

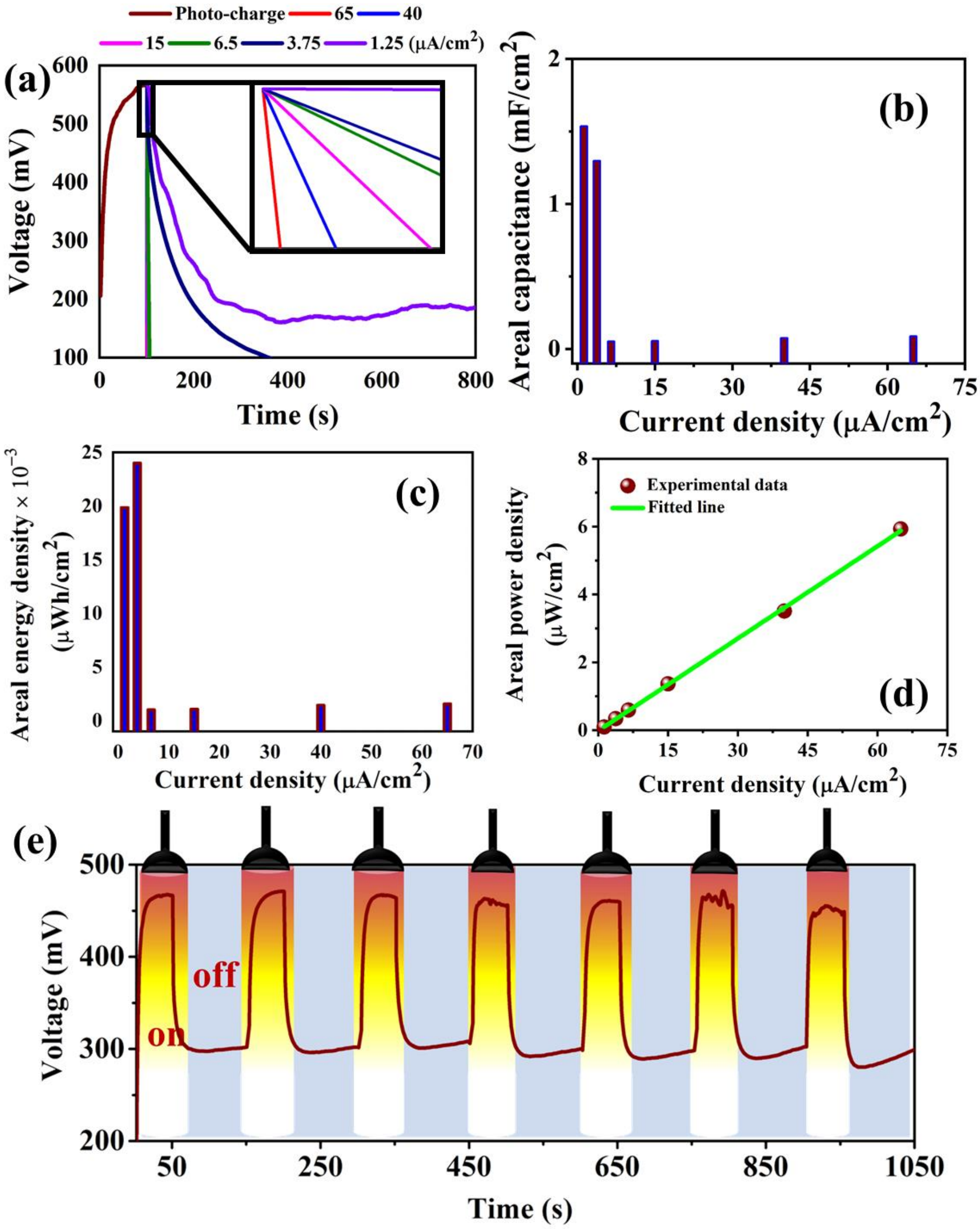

Figure 5.9. (a) UV photo-charge (100 mW/cm^2) and galvanostatic discharge at different current density values. Plots between (b) areal capacitance, (c) areal energy density, and (d) areal power density against current density values from the data obtained from (a). Cyclic photo-charge (UV bulb; 100 mW/cm^2) and galvanostatic discharge (0.5 μA/cm^2) plot.

Due to the UV responsive behavior of the electrode material, we further analyzed the supercapacitor device by photo-charging and galvanostatically discharging at different current density values. In figure 5.9a, the plots of photo-charging (UV light, 100 mW/cm^2) and galvanostatic discharging at current density values of 1.25, 3.75, 6.5, 15, 40, and 65 μA/cm^2 are shown. We calculated the areal capacitance, areal energy density, and areal power density values using the data obtained from figure 5.9a. The change in the areal capacitance, areal energy density, and areal power density values with respect to current density values is plotted and shown in figure 5.9b,c & d, respectively. An important observation from figure 5.9d is that, unlike the areal capacitance and the areal energy density, the areal power density is linearly dependent on the current density values. Therefore, we fitted the data with a straight line, which gives the value of slope about 0.091. The photo-charged areal capacitance values at 1.25 and 65 μA/cm^2 are 1.53 and

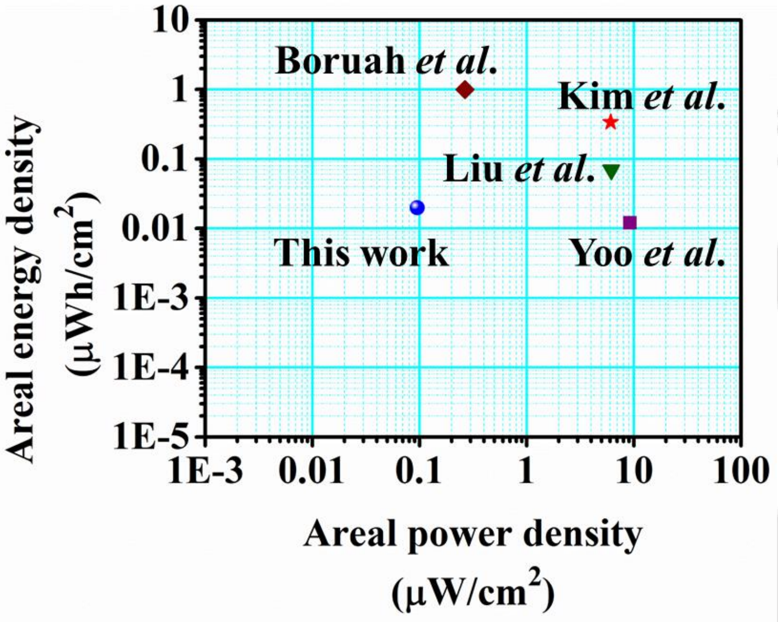

Figure 5.10. Ragone plot of the device to compare the performance with the work reported by Boruah *et al*. [47], Kim *et al*. [48], Liu *et al*. [49], and Yoo *et al*.[50]

0.09 mF/cm^2, whereas the values of areal energy density and areal power density at these two current density values are 19.85$\times 10^{-3}$ and 1.56$\times 10^{-3}$µWh/cm^2, and 0.0953 and 5.93 µW/cm^2 respectively. A Ragone plot is also shown to compare the data with the previously reported work, and it is shown in figure 5.10.

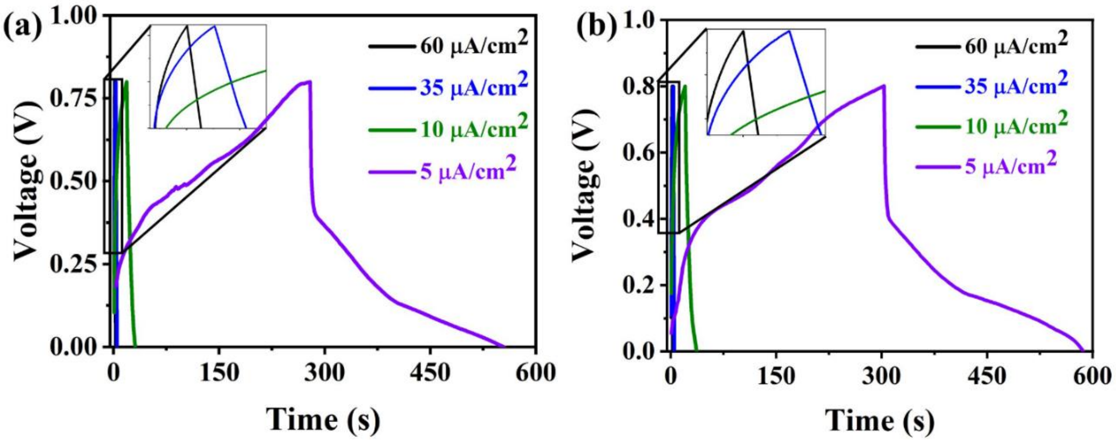

Figure 5.11. Galvanostatic charging and discharging at different current density values in (a) dark and (b) illuminated conditions.

We then checked the repeatability of the device by photo-charging for 50 s (UV light; 100 mW/cm^2) and galvanostatically discharging at 0.5 µA/cm^2. We tested the repeatability for 7 cycles, and it was observed that there was a very negligible change in the areal capacitance value after 7 cycles of the photo-charge and galvanostatic discharge process and it is shown in figure 5.9e. Along with the photo-charging and galvanostatic discharging, we examined the galvanostatic charging and discharging (GCD) phenomena of the device in absence and presence of UV light, and these observations are shown in figure 5.11. Furthermore, we checked the sustainability of the device by obtaining the GCD cycles at a current density of 15 µA/cm^2. This observation is presented in figure 5.12 and it is observed from the figure that the device retains its stability up to 800 cycles under the exposure of light. For a better visualization of the individual cycles, we have shown a zoomed in image of figure 5.12a in figure 5.12b.

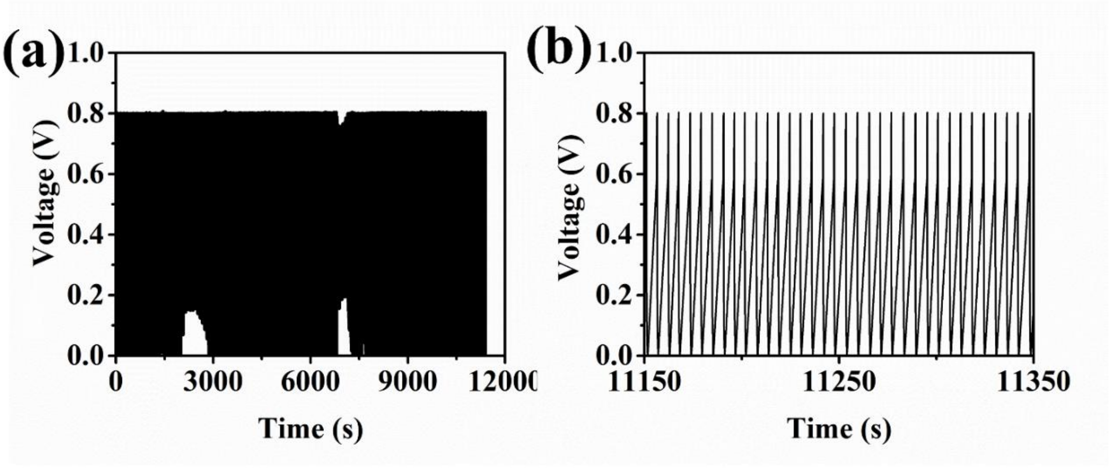

Figure 5.12. (a) Galvanostatic charging and discharging cycles. (b) Zoomed in image of a section of (a).

The electrochemical impedance spectroscopy (EIS) was also performed. The measurements of the EIS spectra were taken in the frequency range of 100 kHz to 10 mHz. The considered voltage amplitude value was 10 mV. The obtained EIS spectra in the absence and presence of light are represented in figure 5.13a. These data were further fitted using Randell's model, and the equivalent circuit for both (dark and illuminated) the plots are shown in figure 5.13b. The resistance represented by R_s is considered as the equivalent series resistance (ESR). This resistance is basically a combination of the electrolyte resistance as well as the electrode's internal resistance [51]. Whereas CPE stands for constant phase element, and R_{CT} is the charge transfer resistance. Because of the low diffusion process, the Warburg impedance (Z_W) also comes into consideration and is connected in series with the charge transfer resistance. The ESR value got decreased from 1.06 to 0.075 kΩ, and the charge transfer resistance got decreased from 46 to 8.8 kΩ when exposed to UV light. The decrease in the value of R_{CT} in the presence of UV light can be attributed to the enhancement of charge carrier density which ultimately helps to get a better conductivity (electrical conductivity). This observation is in accordance with some previously reported articles [16].

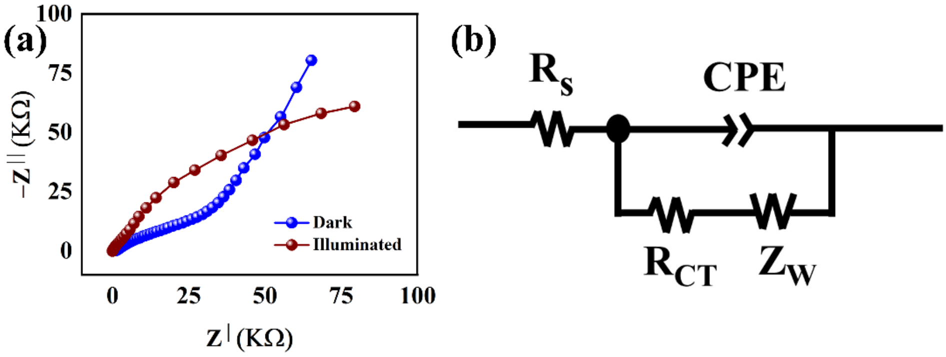

Figure 5.13. (a) EIS plots of the sample at dark and illuminated conditions. (b) Equivalent circuit.

5.3.4. Reaction mechanism

The statement regarding the occurrence of intercalation pseudocapacitance can be assured with figure 5.14. In this figure, a PL spectrum of the hybrid electrode material (figure 5.14a) after electrochemical reactions and a time-resolved photoluminescence (TRPL) plot (figure 5.14b) of the material before and after electrochemical reactions are presented. It appears in figure 5.14a that the overall PL spectrum has been shifted towards its right (compared to the one shown in figure 5.2c). After deconvoluting the spectrum, it is found that the electronic transition from the conduction band to the defect corresponding to the single ionized oxygen vacancy at ~ 3.07 eV and the electronic transition at oxygen antisites (~2.67 eV) are missing in the PL spectrum. This might suggest that the defects related to oxygen vacancies could well be participating in the intercalation process during the charging and discharging of the supercapacitive hybrid electrode material. This argument can be verified with previously reported literature where, Kim *et al.* [52] reported the influence of oxygen vacancies in the enhancement of charge storage capacity of MoO_{3-x}. The PL decay curves of the hybrid electrode material is also shown in figure 5.14b. It is obvious from the figure that the slope of the curve got steeper for the sample after the electrochemical reaction, giving a hint about the decay in its overall average lifetime. Hence, we calculated the average PL lifetime (τ_{avg}) for both the samples, and the calculated values for these two samples are 7.87 and 3.91 ns, respectively. However, it is observed that three components were taking part in PL emission in case of the sample before reaction whereas, these participating components in case of the sample after reaction got reduced to two. These individual components along with their lifetimes are given in table 5.1. The reduction in the number of components can also be ascribed as the utilization of the available defects in the ZnO material, as mentioned earlier, for participating in the intercalation process. A schematic representation of the intercalation process of K^+ ions in the defect regions is shown in figure 5.14c. It is understood from the figure that after the electrochemical process, some

Table 5.1. PL lifetime of individual components before and after the electrochemical reaction.

Sample	$\boldsymbol{\tau_1}$ **(ns)**	$\boldsymbol{\tau_2}$ **(ns)**	$\boldsymbol{\tau_3}$ **(ns)**
Before reaction	0.81	3.13	8.95
After reaction	1.069	5.512	-

of the defects in the ZnO get blocked by the K^+ ions (intercalation of K^+ ions). The authentication of this statement is further verified by XPS analysis of the electrode material before and after the electrochemical reaction. Figure 5.14d shows the high resolution core level spectra of Zn2p before and after the reaction. In this figure, the plot at the top section is representing the Zn2p spectrum before the electrode material went through the electrochemical reaction. This figure depicts that the binding energy difference (ΔBE) between the peaks Zn2p$_{1/2}$ and Zn2p$_{3/2}$ is ~23.35 eV. This value is in well agreement with the previously reported values with a minute deviation [53]. The deviation of the value of energy difference between the two Zn2p core peaks can be assumed due to the interactions of the ZnO with other components such as CDs and SWCNTs. However, this ΔBE value gets reduced to ~22.94 eV after the electrode material was processed through a number of charging-discharging cycles (electrochemical reaction), as shown in the bottom section of figure 5.14d. An electrochemical interaction with the electrolyte (4 M KOH) can be one plausible reason behind the change in the ΔBE value. After the deconvolution of the core spectrum of Zn2p$_{3/2}$, it is noticed that the component peaks appear at 1021.59 and 1023.78 eV. The former peak can be ascribed to the elemental Zn in the hybrid electrode material [54]. More precisely, this peak can be related to the Zn^{2+} in the wurtzite ZnO structure as reported by Bai *et al*. [55] On the other hand, the peak at 1023. 78 eV can be assigned to the Zn^{2+}, which is associated with the hydroxide group [56]. However, this peak gets blue-shifted to 1022.14 eV after the charging-discharging cycles of the electrode material. The shift of this peak can also be associated with the electrochemical interaction of ZnO with the hydroxide groups of the electrolyte material, as mentioned in equation 5.8.The deconvolution of the Zn2p$_{1/2}$ peak resulted in obtaining two different components as well.

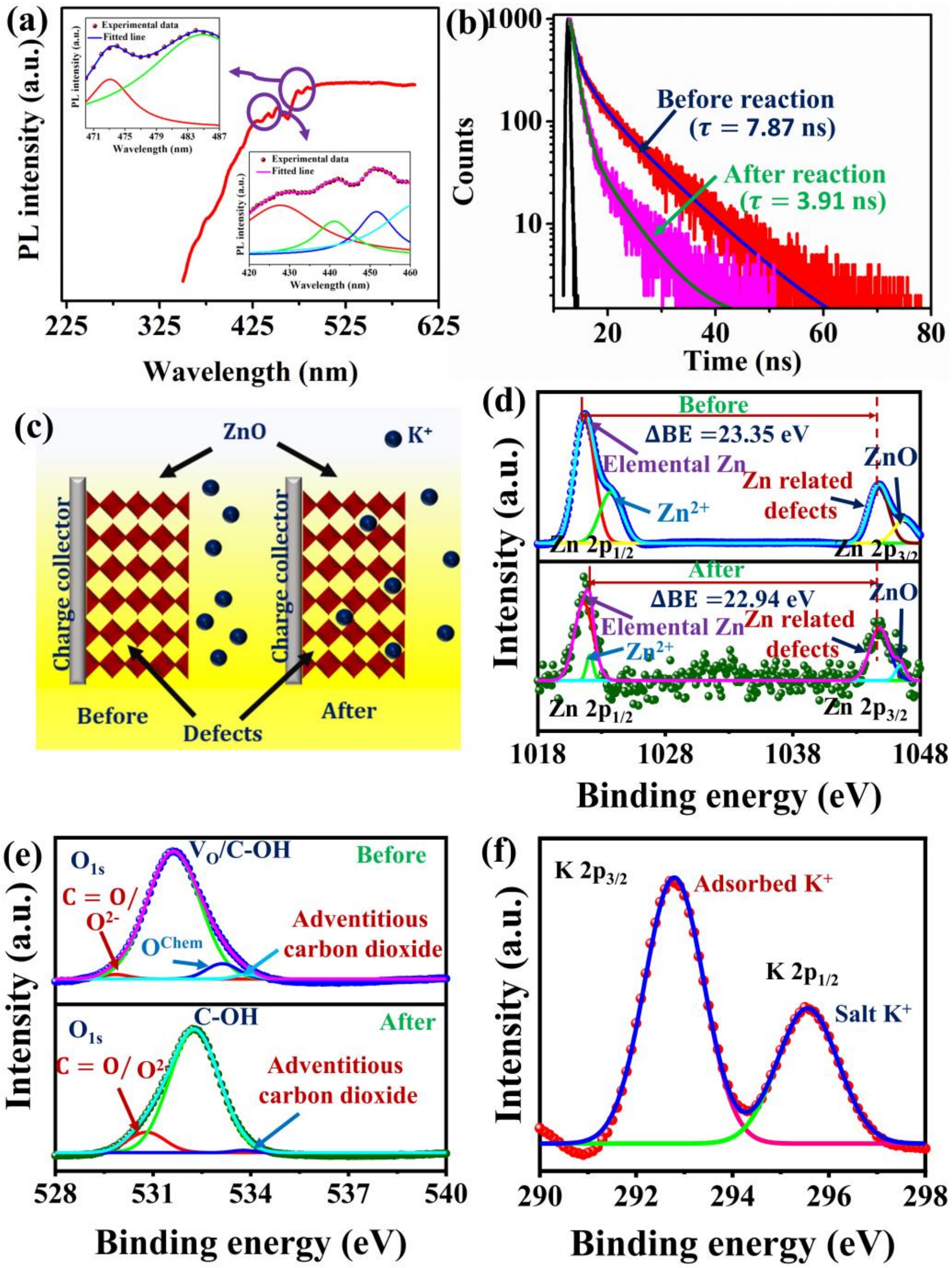

Figure 5.14. (a) Deconvoluted PL spectra of the hybrid material after the electrochemical reaction. (b) PL decay curves for the hybrid material before and after the electrochemical reaction. (c) Schematic representation of the intercalation of K^+ ions into the defects of ZnO. (d) High resolution XPS spectra of (d) Zn2p and (e) O1s before and after the electrochemical reaction. (f) High resolution XPS spectra of K2p after the electrochemical process.

One is at 1044.94 eV, which refers to the ZnO matrix in the hybrid electrode material and the other is at 1046.92 eV, which conveys the presence of different Zn-related defects such as oxygen vacancy, Zn interstitial, etc. [54] Here also, a shift in the two components is observed after the electrode material is processed through the charging-discharging cycles. This shift is assumed to be due to the electrochemical interaction of the electrode material with the electrolyte. We have compared the O1s spectra of the electrode material before and after the reaction and the spectra are shown in figure 5.14e. The deconvolution of the peak gives four different components at 529.8, 531.5, 533.0, and 533.9 eV. The peak at 529.8 is assigned to either the O^{2-} ion that is associated with the wurtzite ZnO [53, 57] or the $\mathrm{C=O}$ group [22], which is associated with the CDs. In another way, it can be conveying the presence of both O^{2-} ion and $\mathrm{C=O}$ simultaneously. This assumption justifies the little shift of the peak position from the standard peak position as well. The broad peak at 531.5 eV can be attributed to the presence of oxygen vacancy in the ZnO nanomaterial [53, 57] and $\mathrm{C-OH}$ group, which is present due to the presence of CDs in the composite [22]. Chemically adsorbed oxygen can be assigned to the peak at 533.0 eV [58], and the peak at 533.9 eV can be related to the adventitious carbon dioxide ($\mathrm{O-C=O}$), which is assumed to be present on the surface of the ZnO [59]. Interestingly, after the electrochemical process, it is observed that all the O1s peaks are still intact except for the peak of oxygen vacancy, as shown in the lower section of figure 5.14e. It can be interpreted from this observation that the oxygen vacancy was participating in the intercalation process during the electrochemical reaction. Apart from that, the minute shift in the other peaks can also be an indication of the active electrochemical participation of the electrode material during the charging-discharging cycles. As is mentioned earlier that the electrochemical process in this system is carried out by the intercalation of K^+ ions into the defects of ZnO, therefore we have shown the high resolution core spectra of K2p of the electrode material after the chagrining-discharging cycles and the spectrum is represented in figure 5.14f. The two prominent peaks of $K2p_{1/2}$ and $K2p_{3/2}$ at 295.6 and 292.7 eV, respectively are representing the presence of electro adsorbed K^+ ions and K^+ ions present as salts, respectively [60]. Hence, the occurrence of intercalation process can be confirmed from the results shown in figure 5.14, which confirms the presence of intercalation pseudocapacitance in the fabricated supercapacitor device. Moreover, the high resolution XPS spectra for C1s and N1s of the electrode material are also shown in figure 5.15. The presence of CDs and SWCNTs in the electrode material justifies the peaks obtained by deconvoluting C1s spectra, whereas, the presence of nitrogen in the CDs (N-doped) verifies the peaks obtained by the high resolution spectra the N1s as shown in figure 5.15a and b, respectively. The peaks at 284.7, 285.8 and 288.6 eV in the plot presented in the top section of figure 5.15a correspond to $\mathrm{C-C}$,

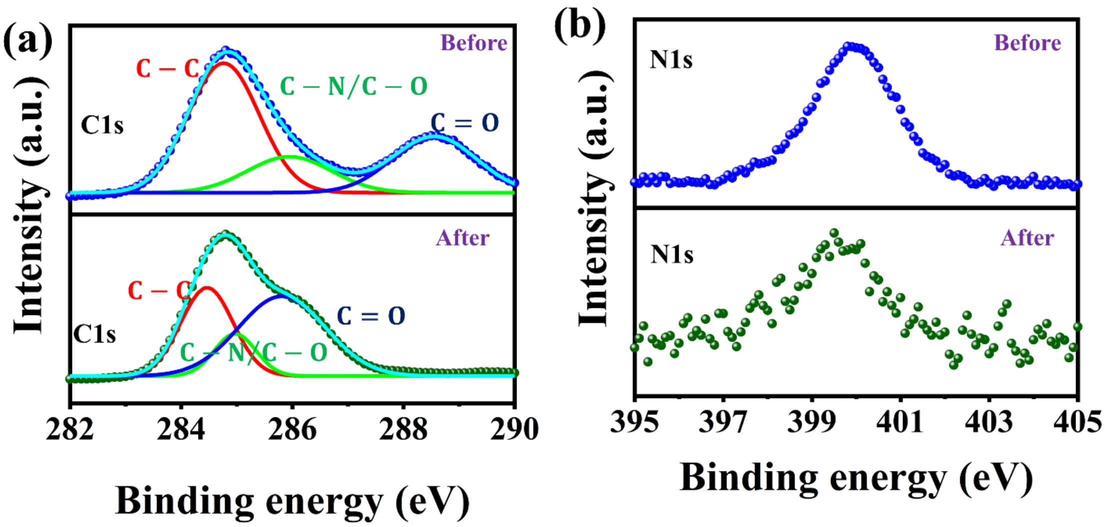

Figure 5.15. High resolution XPS spectra of (a) C1s and (b) N1s before and after the electrochemical reaction.

$\mathrm{C-N/C-O, C=O}$, respectively [22, 61]. However, after the electrochemical treatment, the peaks got blue shifted as shown in the bottom section of the figure 5.15a. Similarly, it is observed from figure 5.15b, that the peak in the N1s spectrum also witnesses a blue shift after the charging-discharging cycles. The peak related to $\mathrm{C-N-C}$ at 399.9 eV [22] gets blue shifted to 399.56 eV after the electrochemical treatment of the electrode material.

5.4. Conclusions

This chapter reports the fabrication of CD enhanced SWCNT/ZnO hybrid electrode for supercapacitor devices. The optical properties of the CDs and ZnO have been utilized to develop a UV-responsive hybrid supercapacitor. The working mechanism of the supercapacitor has also been explored to identify the contributions from EDL and pseudocapacitance to the overall capacitance of the system. Dunn method was used to calculate these contributions. It was observed that the EDLC and the pseudocapacitance contribution towards the areal capacitance were 69.35 and 30.65%, respectively. Due to the presence of diffusion-controlled pseudocapacitance (intercalation pseudocapacitance) in the system, the electrolytic ions' diffusivity into the electrode material was also calculated. The values for the same were obtained to be 0.13 and 0.14 mm^2/s for the oxidation peaks, whereas 1 and 0.07 mm^2/s for the reduction peaks, respectively. Moreover, a detailed analysis of the reaction mechanism was also performed, and the confirmation of the intercalation of K$^+$ ions in the defects of ZnO was also established by the XPS, PL, and TRPL analysis of the sample before and after the electrochemical reactions. The device performance was further analyzed. It was observed that the areal capacitance got enhanced by 41.38, 23.23, 19.28, and 6.79% in the presence of UV light at 50, 200, 400, and 1000 mV/s scan-rates, respectively. The photo-charging and galvanostatic discharging were also examined at different current density values of 1.25, 3.75, 6.5, 15, 40, and 65 µA/cm^2. The device showed good sustainability up to 800 charging-discharging cycles. The calculated photo-charged areal capacitance values at 1.25 and 65 µA/cm^2 were observed to be 1.53 and 0.09 mF/cm^2, whereas the values of areal energy density and areal power density at these two current density values were 19.85×10^{-3} and 1.56×10^{-3} µWh/cm^2, and 0.0953 and 5.93 µW/cm^2, respectively.

References

[1] R. Sinha, A. Bisht, S. Rarotra, T.K. Mandal, Industrial & Engineering Chemistry Research, 59 (2020) 1737.

[2] Y. Jiang, J. Liu, Energy & Environmental Materials, 2 (2019) 30.

[3] F. Zhang, Y. Lu, X. Yang, L. Zhang, T. Zhang, K. Leng, Y. Wu, Y. Huang, Y. Ma, Y. Chen, Small, 10 (2014) 2285.

[4] J. Zhou, J. Yu, L. Shi, Z. Wang, H. Liu, B. Yang, C. Li, C. Zhu, J. Xu, Small, 14 (2018) 1803786.

[5] U. Mahanta, S. Choudhury, R.P. Venkatesh, S. SarojiniAmma, S.A. Ilangovan, T. Banerjee, ACS Sustainable Chemistry & Engineering, 8 (2020) 372.

[6] R. Sahoo, T.H. Lee, D.T. Pham, T.H.T. Luu, Y.H. Lee, ACS Nano, 13 (2019) 10776.

[7] M. Salanne, B. Rotenberg, K. Naoi, K. Kaneko, P.L. Taberna, C.P. Grey, B. Dunn, P. Simon, Nature Energy, 1 (2016) 16070.

[8] M. Toupin, T. Brousse, D. Bélanger, Chemistry of Materials, 16 (2004) 3184.

[9] S. Wang, C. Sun, Y. Shao, Y. Wu, L. Zhang, X. Hao, Small, 13 (2017) 1603330.

[10] Y. Rangom, X. Tang, L.F. Nazar, ACS Nano, 9 (2015) 7248.

[11] A. Dixit, S. Middya, S. Mitra, S. Maity, M. Bhattacharjee, D. Bandyopadhyay, The Journal of Physical Chemistry C, 123 (2019) 195.

[12] Y. Koo, V.N. Shanov, S. Yarmolenko, M. Schulz, J. Sankar, Y. Yun, Langmuir, 31 (2015) 7616.

[13] N. Zhang, Y. Li, J. Xu, J. Li, B. Wei, Y. Ding, I. Amorim, R. Thomas, S.M. Thalluri, Y. Liu, G. Yu, L. Liu, ACS Nano, 13 (2019) 10612.

[14] P. Yang, Y. Ding, Z. Lin, Z. Chen, Y. Li, P. Qiang, M. Ebrahimi, W. Mai, C.P. Wong, Z.L. Wang, Nano Letters, 14 (2014) 731.

[15] S. Wang, L. Gai, H. Jiang, Z. Guo, N. Bai, J. Zhou, Journal of Materials Chemistry A, 3 (2015) 21257.

[16] B.D. Boruah, B. Wen, S. Nagane, X. Zhang, S.D. Stranks, A. Boies, M. De Volder, ACS Energy Letters, 5 (2020) 3132.

[17] B.D. Boruah, A. Misra, ACS Applied Energy Materials, 2 (2019) 278.

[18] S. Ahmad, C. George, D.J. Beesley, J.J. Baumberg, M. De Volder, Nano Letters, 18 (2018) 1856.

[19] X. Xu, S. Li, H. Zhang, Y. Shen, S.M. Zakeeruddin, M. Graetzel, Y.-B. Cheng, M. Wang, ACS Nano, 9 (2015) 1782.

[20] S. Dhar, T. Majumder, S.P. Mondal, ACS Applied Materials & Interfaces, 8 (2016) 31822.

[21] R. Sinha, A.P. Bidkar, R. Rajasekhar, S.S. Ghosh, T.K. Mandal, The Canadian Journal of Chemical Engineering, 98 (2020) 194.

[22] R. Sinha, N. Roy, R. Rajasekhar, A. Karnawat, T.K. Mandal, Journal of Environmental Chemical Engineering, 9 (2021) 104971.

[23] R. Sinha, N. Roy, T.K. Mandal, ACS Applied Materials & Interfaces, 12 (2020) 33428.

[24] S. Sahoo, A.K. Satpati, P.K. Sahoo, P.D. Naik, ACS Omega, 3 (2018) 17936.

[25] S. Zhu, Q. Meng, L. Wang, J. Zhang, Y. Song, H. Jin, K. Zhang, H. Sun, H. Wang, B. Yang, Angew. Chem., Int. Ed., 52 (2013) 3953.

[26] F. Teng, W. Ouyang, Y. Li, L. Zheng, X. Fang, Small, 13 (2017) 1700156.

[27] R.K. Agrawalla, R. Paul, P.K. Sahoo, A.K. Chakraborty, A.K. Mitra, International Journal of Smart and Nano Materials, 5 (2014) 180.

[28] S.K. Bajpai, A. D'Souza, B. Suhail, International Nano Letters, 9 (2019) 203.

[29] J. Ghosh, R. Ghosh, P.K. Giri, Sens. Actuators, B, 254 (2018) 681.

[30] J. Sann, J. Stehr, A. Hofstaetter, D.M. Hofmann, A. Neumann, M. Lerch, U. Haboeck, A. Hoffmann, C. Thomsen, Physical Review B, 76 (2007) 195203.

[31] S. Meti, M.R. Rahman, M.I. Ahmad, K.U. Bhat, Applied Surface Science, 451 (2018) 67.

[32] R. Zhang, P.-G. Yin, N. Wang, L. Guo, Solid State Sciences, 11 (2009) 865.

[33] Ü. Özgür, Y.I. Alivov, C. Liu, A. Teke, M.A. Reshchikov, S. Doğan, V. Avrutin, S.J. Cho, H. Morkoç, Journal of Applied Physics, 98 (2005) 041301.

[34] A. Muravitskaya, A. Rumyantseva, S. Kostcheev, V. Dzhagan, O. Stroyuk, P.-M. Adam, Opt. Express, 24 (2016) A168.

[35] M.S. Jang, M.K. Ryu, M.H. Yoon, S.H. Lee, H.K. Kim, A. Onodera, S. Kojima, Current Applied Physics, 9 (2009) 651.

[36] W. Bousslama, B. Sieber, H. Elhouichet, B. Gelloz, A. Addad, M. Férid, Journal of Physics D Applied Physics, 46 (2013) 505104.

[37] V.A. Chhabra, R. Kaur, N. Kumar, A. Deep, C. Rajesh, K.-H. Kim, RSC Advances, 8 (2018) 11446.

[38] D. Das, P. Mondal, RSC Advances, 4 (2014) 35735.

[39] B. Allabergenov, U. Shaislamov, H. Shim, M.-J. Lee, A. Matnazarov, B. Choi, Opt. Mater. Express, 7 (2017) 494.

[40] K. Brezesinski, J. Wang, J. Haetge, C. Reitz, S.O. Steinmueller, S.H. Tolbert, B.M. Smarsly, B. Dunn, T. Brezesinski, J. Am. Chem. Soc., 132 (2010) 6982.

[41] C. Cheng, A.H.W. Ngan, ACS Nano, 9 (2015) 3984.

[42] B. Deka Boruah, A. Mathieson, S.K. Park, X. Zhang, B. Wen, L. Tan, A. Boies, M. De Volder, Advanced Energy Materials, n/a (2021) 2100115.

[43] V. Augustyn, J. Come, M.A. Lowe, J.W. Kim, P.-L. Taberna, S.H. Tolbert, H.D. Abruña, P. Simon, B. Dunn, Nature Materials, 12 (2013) 518.

[44] J. Shao, X. Zhou, Q. Liu, R. Zou, W. Li, J. Yang, J. Hu, Journal of Materials Chemistry A, 3 (2015) 6168.

[45] D.Y.W. Yu, C. Fietzek, W. Weydanz, K. Donoue, T. Inoue, H. Kurokawa, S. Fujitani, Journal of The Electrochemical Society, 154 (2007) A253.

[46] S. Shi, X. Zhuang, B. Cheng, X. Wang, Journal of Materials Chemistry A, 1 (2013) 13779.

[47] B.D. Boruah, A. Maji, A. Misra, ACS Applied Materials & Interfaces, 10 (2018) 15864.

[48] H. Kim, J. Yoon, G. Lee, S.-h. Paik, G. Choi, D. Kim, B.-M. Kim, G. Zi, J.S. Ha, ACS Applied Materials & Interfaces, 8 (2016) 16016.

[49] W.-W. Liu, Y.-Q. Feng, X.-B. Yan, J.-T. Chen, Q.-J. Xue, Advanced Functional Materials, 23 (2013) 4111.

[50] J.J. Yoo, K. Balakrishnan, J. Huang, V. Meunier, B.G. Sumpter, A. Srivastava, M. Conway, A.L. Mohana Reddy, J. Yu, R. Vajtai, P.M. Ajayan, Nano Letters, 11 (2011) 1423.

[51] W. Wang, S. Guo, I. Lee, K. Ahmed, J. Zhong, Z. Favors, F. Zaera, M. Ozkan, C.S. Ozkan, Scientific Reports, 4 (2014) 4452.

[52] H.-S. Kim, J.B. Cook, H. Lin, Jesse S. Ko, Sarah H. Tolbert, V. Ozolins, B. Dunn, Nature Materials, 16 (2017) 454.

[53] G.G. Guillén, M.I.M. Palma, B. Krishnan, D. Avellaneda, G.A. Castillo, T.K.D. Roy, S. Shaji, Materials Chemistry and Physics, 162 (2015) 561.

[54] T.K. Pathak, A. Kumar, C.W. Swart, H.C. Swart, R.E. Kroon, RSC Advances, 6 (2016) 97770.

[55] S. Bai, L. Chen, S. Chen, R. Luo, D. Li, A. Chen, C.C. Liu, Sensors and Actuators B: Chemical, 190 (2014) 760.

[56] M. Wang, L. Jiang, E.J. Kim, S.H. Hahn, RSC Advances, 5 (2015) 87496.

[57] S.-S. Li, Y.-K. Su, RSC Advances, 9 (2019) 2941.

[58] L.Q. Wu, Y.C. Li, S.Q. Li, Z.Z. Li, G.D. Tang, W.H. Qi, L.C. Xue, X.S. Ge, L.L. Ding, AIP Advances, 5 (2015) 097210.

[59] M. Kwoka, A. Kulis-Kapuscinska, D. Zappa, E. Comini, J. Szuber, Nanotechnology, 31 (2020) 465705.

[60] Y. Dall'Agnese, M.R. Lukatskaya, K.M. Cook, P.-L. Taberna, Y. Gogotsi, P. Simon, Electrochemistry Communications, 48 (2014) 118.

[61] Y. Han, B. Tang, L. Wang, H. Bao, Y. Lu, C. Guan, L. Zhang, M. Le, Z. Liu, M. Wu, ACS Nano, 14 (2020) 14761.

Chapter 6

Summary and future scopes

Contents

6.1. Summary

In a nutshell, the thesis uncovers different precursor materials for synthesizing carbon dots (CDs). Three different synthesis techniques have been employed to produce the CDs. Owing to the CDs' photoluminescence (PL) property, they were exploited in PL-based sensing and bioimaging applications. Not only this, the favourable band gaps of the CDs helped to use them in other applications such as UV-photodetection and photo-responsive energy storage systems. In this regard, CDs were attached with other semiconductor materials like ZnO and SWCNT to get better performances. Apart from the synthesis and applications of the CDs, this thesis also discusses the sensing as well as the energy storage mechanisms. The detailed conclusions of the individual technical chapters are elaborated on below.

After introducing the objectives in the first chapter, the second chapter (first technical chapter) reports the facile synthesis of CDs from potato precursors using a simple heating reaction technique. Without further refining and stabilizing, the synthesized CD particles showed good optical properties with an average diameter of 5.97 nm and a quantum yield (QY) of 6.08% at 345 nm. The luminescent property of the synthesized CDs was used to detect heavy metals in the water sample, and the CDs showed a good selectivity and sensitivity towards Cr^{6+} and Fe^{3+} ions with a detection limit of 0.012 μM and 0.000 549 μM for Cr^{6+} and Fe^{3+}, respectively. The feasibility of the sensing system was also tested in real water samples. In addition, the low-toxic nature of the CDs allowed us to use them in bioimaging applications as well.

The third chapter (second technical chapter) focuses on the applications of N-doped CDs, synthesized from cigarette-tobacco by microwave assisted synthesis technique. The synthesized CDs were used in PL-based sensing applications by detecting PA in water samples. The obtained limit of detection (LOD) value for PA sensing is reported to be 140 nM (32.1 ppb). In this case also, the feasibility in real water samples was successfully tested. The PL and TRPL (time-resolved photoluminescence) characterization of the samples helped to identify the sensing mechanism, which was a combination of charge transfer complex and inner filter effect. Further, the CDs were attached with multi-walled carbon nanotube (MWCNT) to synthesize CD-MWCNT nanocomposite, which showed UV-responsive characteristics. The rise and decay time of the UV responsive nanocomposite were calculated from the transient response, and these values are 0.38 s and 0.42 s, respectively. An understanding of the charge transfer mechanism through the composite has also been obtained from this chapter.

The fourth chapter (third technical chapter) reports the fabrication of a flexible, self-powered Schottky diode based UV-photodetector. This photodetector was fabricated by growing CD decorated ZnO nanorods on graphite-coated paper substrate. The transient response of the photodetector at self-powered condition was used to calculate the response time and recovery time of the diode, and these calculated values are ~2 and ~3.2 s, respectively. The responsivity and the specific detectivity of the fabricated UV detector have been calculated as 9.57 mA/W and 4.27×10^{8} Jones, respectively, at a 330 nm wavelength. Moreover, a probable mechanism for the photodetection in self-powered conditions has also been discussed.

The fifth chapter (fourth technical chapter) explores the synthesis of CD-enhanced SWCNT/ZnO hybrid electrode for an optically responsive supercapacitor. The working mechanism of the supercapacitor was examined to identify the contributions from electric double layer capacitance (EDLC) and pseudocapacitance to the overall capacitance of the system. It was observed that the EDLC and the pseudocapacitance contribution towards the overall capacitance were 69.35 and 30.65%, respectively. Moreover, a detailed analysis of the reaction mechanism was also done. The confirmation of the intercalation of K^+ ions in the defects of ZnO was established by the XPS, PL, and TRPL analysis of the sample before and after the electrochemical reactions. The device performance was also analyzed under dark and illuminated conditions. It was observed that the areal capacitance got enhanced by 41.38, 23.23, 19.28, and 6.79% in the presence of UV light at 50, 200, 400, and 1000 mV/s scan-rates, respectively.

Overall, it can be summarized that CDs were successfully synthesized from different precursor sources using different synthesis techniques. The optical property of the CDs was utilized judiciously in the applications of PL-based sensing, bioimaging, optoelectronics, and energy storage systems.

6.2. Future scopes

The works presented in the technical chapters further open up a wide range of future scopes in the relevant working fields, some of which are referred below.

- The low LODs for Cr^{6+} and Fe^{3+} detection inspires to approach for the fabrication of a portable PL-based device for the detection of other toxic heavy metals as well in real water samples. Moreover, the low toxicity and the bioimaging application further open up the possibility to use the CDs in in-vivo imaging applications.
- The photo-responsive property of the CD-MWCNT nanocomposite can be explored in the field of photocatalysis as well. Also, the ability of the

nanocomposite to detect UV light can further be used to fabricate carbon material-based portable devices for UV-photodetection. Moreover, the possibility of increasing the QY of the CDs can be perceived as a scope for future work in the fields of light-emitting diodes (LEDs) and bioimaging applications. Therefore, the ability of the CDs to be used in different areas of applications has opened up a vast range of scopes for researchers.

- Investigation of other metal oxides along with CDs for the UV-photodetection applications to examine for a higher detectivity and responsivity values can be perceived as a potential future scope. Moreover, enhancing the sustainability of the device at more bending cycles can also be a challenging task to look forward to.
- The usage of photon energy in supercapacitor applications sets up a good foundation for researchers to work on renewable energy usage processes. Moreover, tuning the bandgap of the electrode materials or the usage of visible light-responsive materials would definitely play a major role in applying this technique in industrial applications as well.

Annexure I

Relative contents of N, O, and C from XPS:

The formula used to calculate this value is as follows [1]:

$$C_x = (\frac{I_x}{S_x}) / \sum (\frac{I_i}{S_i})$$

where, C is atomic concentration of element; I is the integrated area of each element obtained from XPS; S is sensitivity factor for each element; x is type of element; i is the number of element.

Data note on cyclic voltammetry measurement:

To calculate the HOMO and LUMO energy levels of the CDs were calculated by performing cyclic voltammetry (CV) with a standard three-electrode system. Simple graphite rod was used as the working electrode, a platinum wire was used as the counter electrode, and Ag/AgCl was considered as the reference electrode. CV was recorded in DI-water containing 0.5 mg/mL CDs and 0.1 M KCl as the supporting electrolyte [2, 3].

Calculation of photovoltaic parameters:

The following formulae were used to calculate the fill factor (FF) and the efficiency values [4, 5].

$$FF = \left(\frac{V_{mp} I_{mp}}{V_{OC} I_{SC}} \times 100\right) \%$$

$$Efficiency = (\frac{FF \times V_{OC} I_{SC}}{A \times P_{in}} \times 100)\%$$

Here, V_{OC} refers to the open circuit voltage, I_{SC} corresponds to short circuit current, V_{mp} refers to the maximum voltage and I_{mp} denotes the maximum current.

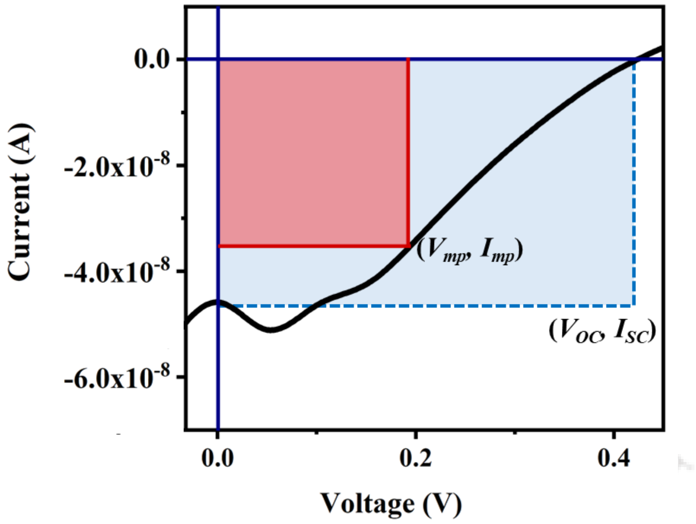

Figure A1. Current vs. voltage plot to identify V_{OC}, I_{SC}, V_{mp}, and I_{mp}.

Table A1. Photovoltaic Parameters of the Fabricated Devices

V_{OC} (V)	I_{SC} (A)	V_{mp} (V)	I_{mp} (A)	FF (%)	Efficiency (%)
0.42	4.6×10^{-8}	0.193	3.5×10^{-8}	35.23	0.00034

Calculations of areal capacitance, areal energy density, and areal power density:

The following formulae were used to calculate all the parameters related to the supercapacitor [6],

Areal capacitance from CV plot $(C_{CV}) = \frac{1}{Av(V_f - V_i)} \int_{V_i}^{V_f} I\, dV$

Areal capacitance from charge-discharge plot $(C_{CD}) = \frac{I\Delta t}{A(V_f - V_i)}$

Areal energy density $(E_A) = \frac{1}{2} \times C_{CD} \times \frac{(V_f - V_i)^2}{3600}$

Areal power density$= \frac{E_A}{\Delta t} \times 3600$

Where, A, ν, V_f, V_i, I, Δt refer to the total active area, scan rate, final voltage limit, initial voltage limit, and total current, respectively.

References

[1] S.K. Das, R. Gawas, S. Chakrabarty, G. Harini, R. Patidar, K. Jasuja, The Journal of Physical Chemistry C, 123 (2019) 25412.

[2] S. Han, T. Chang, H. Zhao, H. Du, S. Liu, B. Wu, S. Qin, Nanomater., 7 (2017) 176.

[3] S. Zhu, Q. Meng, L. Wang, J. Zhang, Y. Song, H. Jin, K. Zhang, H. Sun, H. Wang, B. Yang, Angew. Chem., 125 (2013) 4045.

[4] A. Eibeck, D. Nurkowski, A. Menon, J. Bai, J. Wu, L. Zhou, S. Mosbach, J. Akroyd, M. Kraft, ACS Omega, 6 (2021) 23764.

[5] A.I. Kanareykin, IOP Conference Series: Earth and Environmental Science, 808 (2021) 012018.

[6] B.D. Boruah, A. Maji, A. Misra, ACS Applied Materials & Interfaces, 10 (2018) 15864.

Annexure II

Publications, Patent and Conferences

Publications

From Thesis:

- A Facile Fynthesis of Nontoxic Luminescent Carbon Dots for Detection of Chromium and Iron in Real Water Sample and Bio-imaging. **Rupam Sinha,** Anil P. Bidkar, Ravula Rajasekhar, Siddhartha S. Ghosh and Tapas K. Mandal, ***Can. J. Chem. Eng.***, 98, 194-204. **DOI:** 10.1002/cjce.23630

- N-Doped Carbon Dot from Cigarette-Tobacco: Picric Acid Sensing in Real Water Sample and Synthesis of CD-MWCNT Nano-Composite for UV-Photodetection. **Rupam Sinha,** Nirmal Roy, Ravula Rajasekhar, Aabhas Karnawat and Tapas K. Mandal, ***J. Env. Chem. Eng.***, 9, 104971, 2021. **DOI:** 10.1016/j.jece.2020.104971

- Growth of Carbon Dot-Decorated ZnO Nanorods on a Graphite-Coated Paper Substrate to Fabricate a Flexible and Self-Powered Schottky Diode for UV Detection. **Rupam Sinha**, Nirmal Roy and Tapas K. Mandal, ***ACS Appl. Mater. Interfaces***, 12, 33428-33438, 2020. **DOI:** 10.1021/acsami.0c10484

- SWCNT/ZnO nanocomposite decorated with carbon dots for photoresponsive supercapacitor applications.” **Rupam Sinha**, Nirmal Roy and Tapas K. Mandal, *Chem. Engg. J.* 431, 133915, 2022. DOI: 10.1016/j.cej.2021.133915

- An Appraisal of Future Prospects of Carbon Dots._**Rupam Sinha** and Tapas K. Mandal. (*Manuscript under preparation*)

Outside Thesis:

- Continuous Semi-Micro Reactor Prototype for the Electrochemical Reduction of CO_2 into Formic Acid. **Rupam Sinha**, Agam Bisht, Saptak Rarotra and Tapas K. Mandal, ***Ind. Eng. Chem. Res.***, 59, 1737−1745, 2020. **DOI:** 10.1021/acs.iecr.9b03304

- Highly Sensitive Room Temperature CO Gas Sensor Based on MWCNT-PDDA Composite. Nirmal Roy, **Rupam Sinha**, Thomas T. Daniel, Harshal B. Nemade and Tapas K. Mandal, ***IEEE Sens. J.***, 2020. **DOI:** 10.1109/JSEN.2020.3004994

- Synthesis of MoS_2-CuO nanocomposite for room temperature acetone sensing application. Nirmal Roy, **Rupam Sinha**, Harshal B. Nemade and Tapas K. Mandal, ***J. Alloy. Compd.***, 2022. **DOI:** 10.1016/j.jallcom.2022.164891

- Room Temperature Synthesis of Carbon Dots with Tunable Gap Energy and Particle Size from Glucose. **Rupam Sinha** and Tapas K. Mandal. (*Manuscript under process*)

Patent

- Paper based flexible and self-powered UV photodetector. **Rupam Sinha**, Nirmal Roy, and Tapas K. Mandal, ***202031051178***, 2020.

Conferences

- Paper based flexible and self-powered UV photodetector, **Rupam Sinha**, Nirmal Roy and Tapas K. Mandal, ***Advances in Sustainable Research for Energy and Environmental Management (ASREEM-2021),*** SVNIT Surat, India. (Oral)

- Cigarette: A source of photoluminescent N-doped carbon dots showing potential in photo-responsive application and explosive material sensing. **Rupam Sinha**, Nirmal Roy, Ravula Rajasekhar and Tapas K Mandal, ***International Conference on Advances in Chemical Engineering-2020 (AdChE-2020),*** UPES, Uttarakhand, India. (Oral)

- Synthesis of N-doped carbon dots from cigarette and its applications in picric acid and UV detection. **Rupam Sinha**, Nirmal Roy, Ravula Rajasekhar and Tapas K Mandal, ***6th International Conference on Advanced Nanomaterial and Nanotechnology (ICANN-2019)***, 2019, IIT Guwahati, India. (Poster)

- A Facile Synthesis of Nontoxic Luminescent Carbon Dots for Simultaneous Detection of Cr^{6+} and Fe^{3+} Ions. **Rupam Sinha**, Ravula Rajasekhar and Tapas

K. Mandal, ***TEQIP III Sponsored 1st National Student Conference on Advances in Chemical Engineering 2019***, AEC, India. (Oral)

- Carbon dots photoluminescence technique to detect total Chromium in industrial wastewater, **Rupam Sinha**, Ravula Rajasekhar and Tapas K. Mandal, ***The International Nanotech & nanoscience Conference and Exhibition Nanotech France 2019***. DOI: https://doi.org/10.26799/cp-nanotechfrance2019.

- Utilization of photoluminescent carbon dots for detecting Cr^{6+} ions. **Rupam Sinha**, Ravula Rajasekhar and Tapas K. Mandal, ***12th International Conference on Complex Fluids and Soft Matter (COMPFLU -2018)***, December 6 – 9, 2018, IIT Roorkee, India. (Poster)

- Electrochemical reduction of CO_2 into formic acid using Sn electrocatalyst as a cathode: A study on pH effect. **Rupam Sinha**, Agam Bisht and Tapas K. Mandal, ***Research Conclave 2018***, March 8 – 11, 2018, IIT Guwahati, India. (Poster)

Awards and Acknowledgements

Best Oral Presentation Award, ***Advances in Sustainable Research for Energy and Environmental Management (ASREEM-2021),*** SVNIT Surat, India. Paper based flexible and self-powered UV photodetector, **Rupam Sinha**, Nirmal Roy and Tapas K. Mandal.

SARDAR VALLABHBHAI NATIONAL INSTITUTE OF TECHNOLOGY
Surat 395007 - India

CERTIFICATE OF APPRECIATION

This is to certify that ***Rupam Sinha*** having ASREEM ID **ASIN0017** has achieved Best Oral Presentation Award under category "***Interfacial Engineering and Energy Technology***" at Virtual International Conference on **Advances in Sustainable Research for Energy and Environmental Management (ASREEM-2021)** organized by Department of Chemical Engineering, Sardar Vallabhbhai National Institute of Technology, Surat (India) on August 06 – 08, 2021.

Dr. Arvind K. Mungray
Dr. V. N. Lad
Dr. Alka A. Mungray
Dr. M. Chakroborty
Dr. Jogender Singh
(Organizing Secretaries)

Best Presentation Award, ***TEQIP III Sponsored 1st National Student Conference on Advances in Chemical Engineering 2019***, AEC, India. A Facile Synthesis of Nontoxic Luminescent Carbon Dots for Simultaneous Detection of Cr^{6+} and Fe^{3+} Ions, **Rupam Sinha**, Ravula Rajasekhar and Tapas K. Mandal.

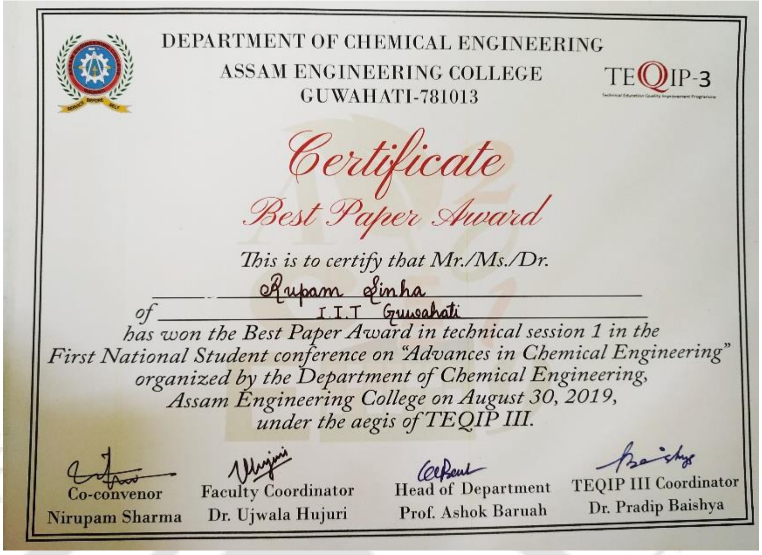

DEPARTMENT OF CHEMICAL ENGINEERING
ASSAM ENGINEERING COLLEGE
GUWAHATI-781013

TEQIP-3

Certificate
Best Paper Award

This is to certify that Mr./Ms./Dr. Rupam Sinha
of I.I.T Guwahati
has won the Best Paper Award in technical session 1 in the First National Student conference on "Advances in Chemical Engineering" organized by the Department of Chemical Engineering, Assam Engineering College on August 30, 2019, under the aegis of TEQIP III.

Co-convenor
Nirupam Sharma

Faculty Coordinator
Dr. Ujwala Hujuri

Head of Department
Prof. Ashok Baruah

TEQIP III Coordinator
Dr. Pradip Baishya

Invited speaker, ***Indo-UK Joint Webinar on Current Trends in Chemical Technology and Materials Development, jointly organized by Indian Institute of Technology Guwahati, Assam, India and University of Aberdeen, United Kingdom***, Growth of Carbon Dot-Decorated ZnO Nanorods on a Graphite-Coated Paper Substrate to Fabricate a Flexible and Self-Powered Schottky Diode for UV Detection. **Rupam Sinha**, Nirmal Roy and Tapas K. Mandal.

1495 UNIVERSITY OF ABERDEEN
CELEBRATING 525 YEARS 1495 – 2020

Indian Institute of Technology Guwahati

Indo-UK Joint International Webinar on
Current Trends in Chemical Process Technology and Materials Development
19 — 20 August 2020

Certificate of Appreciation

This certificate is presented to **Mr. Rupam Sinha** from Indian Institute of Technology Guwahati, India for delivering a speech titled **Growth of Carbon Dot-Decorated ZnO Nanorods on a Graphite-Coated Paper Substrate to Fabricate a Flexible and Self-Powered Schottky Diode for UV Detectiones** in the Indo-UK Joint International Webinar on **Current Trends in Chemical Process Technology and Materials Development**. The Webinar was jointly organized by Indian Institute of Technology Guwahati, Assam, India and University of Aberdeen, United Kingdom.

Prof. Tapas K Mandal
Webinar Convener, IN

Aniruddha
Dr. Aniruddha Majumder
Webinar Convener, UK

Dr. Raghvendra Gupta
Webinar Convener, IN

Jiong
Dr. Jiang Long
Webinar Convener, UK